The Pennsylvania State University
The Graduate School

DESIGN, CONTROL, AND ACOUSTICS OF A MARINE HYDROKINETIC CYCLOTURBINE VEHICLE

A Dissertation in
Aerospace Engineering
by
Margalit Zipora Goldschmidt

Submitted in Partial Fulfillment
of the Requirements
for the Degree of

Doctor of Philosophy

December 2020

The dissertation of Margalit Zipora Goldschmidt was reviewed and approved by the following:

Michael Jonson
Assistant Research Professor, Applied Research Laboratory
Dissertation Co-Advisor, Co-Chair of Committee

Joseph Horn
Professor of Aerospace Engineering
Dissertation Co-Advisor, Co-Chair of Committee

George Lesieutre
Associate Dean for Research
Committee Member

Mary Frecker
Professor of Mechanical Engineering
Committee Member

Amy Pritchett
Professor of Aerospace Engineering
Head of the Department of Aerospace Engineering

Abstract

A marine hydrokinetic (MHK) cycloturbine is a renewable electric power generation system used in rivers or tidal environments to address the need for electricity in remote regions. MHK cycloturbines have foils oriented perpendicular to the flow in a paddlewheel configuration. Lift from these foils produces torque to turn the turbine and a generator which in turn produces power. Due to the high cost associated with MHK system operation and maintenance, design of a novel MHK vehicle that can self-deploy and maneuver is a critical objective. By powering the turbines and using pitching foils for control, a maneuverable system can be designed. Initial feasibility studies demonstrate that a four turbine design with stacked counter-rotating turbines provides the best vehicle control and performance.

A detailed simulation model is developed to understand the vehicle dynamics and assist in the design of controllers. The simulation model solves the six degree-of-freedom rigid body equations of motion for the MHK vehicle subject to hydrodynamic lift and drag forces, hydrostatic forces, and the propulsive forces from the turbines. The turbine propulsive force model is matched to computational fluid dynamics analysis and experimental data for a 1/5.56 scale single turbine Rapid Prototype Device and a Subscale Demonstrator. Global feedback controllers are initially designed by applying classical control methods to an approximate linear model of the system dynamics. More sophisticated controllers that take into account system nonlinearities are subsequently designed to increase vehicle maneuverability and performance using nonlinear dynamic inversion.

In addition to control of the vehicle dynamics, acoustic control is also desired. The cycloturbines are sources of radiated acoustics underwater. Acoustic control is important to curtail the vehicle's vibrations, which reduces the vehicle's fatigue for longer deployment, as well as the acoustic signature, which potentially prevents harmful effects on aquatic life. A method of reducing the radiated acoustics of the vehicle is determined for tones at blade rate frequency and multiples, by means of clocking the blades between turbines. This work is validated experimentally on a Subscale Demonstrator in a reverberant tank.

Table of Contents

List of Figures

List of Tables

List of Symbols

a	acceleration
a_0	speed of sound in water
A	capture area, drag area (Chapter 3)
	stability derivative matrix (Chapter 4)
A_{tube}	cross-sectional area of tube
AR	aspect ratio
b	foil span
B	control derivative matrix
$\vec{B}$	buoyancy force
B^+	pseudo inverse matrix
BR	blade rate
c	foil chord
C	Theodorsen's function
C_D	coefficient of drag
C_L	coefficient of lift
$C(s)$	controller model
d	turbine offset distance from center of mass
dB	decibel
D	drag force (Chapters 2, 3)
	dipole amplitude (Chapter 5)
D_{turb}	turbine diameter
e	Oswald efficiency factor (Chapter 3)
	tracking error (Chapter 4)
E	Young's Modulus
f	frequency
f_{bp}	blade passage frequency
f_δ	blockage effect function

F	force (Chapters 2, 3)
	hydrodynamic force (Chapter 5)
$\tilde{F}$	fluctuating component of hydrodynamic force
F_{ij}	force acting on link j by link i
F_{SSD}	total force from subscale turbine
g	gravitational acceleration
$H_n^{(2)}$	Hankel functions of the second kind
I_G	mass moment of inertia
I_{XX}	rolling moment of inertia
I_{YY}	pitching moment of inertia
I_{ZZ}	yawing moment of inertia
I_{XZ}	product of inertia
I	sound intensity
J	advance coefficient
k	wave number, ω / a_0
k_{red}	reduced frequency
K	vehicle roll moment (Chapter 3)
	stiffness (Chapter 5)
K_D	derivative gain
K_I	integral gain
K_P	proportional gain
K_Q	propeller torque coefficient
K_T	propeller thrust coefficient
l	distance from pivot to c.g.
l_i	outward surface normal
L	lift force
L_{tube}	tube length
L_n	link length
L_W	sound power level
m	vehicle mass
$\dot{m}$	mass flow rate
M	moment (Chapters 2, 3)
	vehicle pitch moment (Chapter 3)
n	rotation rate
N	vehicle yaw moment
N_b	number of foils
N_{DOF}	number of degrees-of-freedom
N_L	number of links
N_J	number of joints

O	octopole amplitude
OS	overshoot
p_N, p_E, p_D	position in North-East-Down coordinates
p	acoustic pressure
p_0	ambient acoustic pressure
$\hat{p}$	complex amplitude of acoustic pressure
P	roll rate
P_i	induced power required
$P(s)$	plant model
q_{turb}	cyclorotor torque
q	dynamic pressure
$\vec{q}$	rigid body translations and rotations
Q	pitch rate (Chapter 3)
	quadrupole amplitude (Chapter 5)
r	distance to force (Chapter 2)
	desired trajectory (Chapter 4)
R	yaw rate (Chapter 3)
	radial distance from source to a receiver (Chapter 5)
R_{turb}	turbine radius
R_{ij}	distance from cg of link j to joint on link i
Re	Reynolds number
S	planform area (Chapter 3)
	surface, monopole amplitude (Chapter 5)
t	time
t_s	settling time
T	thrust magnitude
T_{60}	reverberation time for pressure to reduce 60 dB
T_{ij}	Lighthill stress tensor
TSR	tip speed ratio, $\omega R_{tip}/V_\infty$
u	vehicle control
U	resultant velocity at the cycloturbine, longitudinal velocity (Chapter 3)
	volume velocity (Chapter 5)
v_h	induced velocity at hover
v_i	induced velocity
V	lateral velocity (Chapter 3)
	volume (Chapter 5)
V_{foil}	foil velocity

V_N	normal inflow velocity
V_{ref}	reference velocity
V_T	tangential inflow velocity
V_{tank}	reverberant tank volume
V_{veh}	vehicle velocity
V_∞	inflow velocity
w	velocity in the far wake
W	weight (Chapter 2)
	heave velocity (Chapter 3)
x	vehicle state (Chapter 3)
	receiver location, position (Chapter 5)
X	longitudinal force on the vehicle
y	vehicle output
Y	lateral force on the vehicle
Z	heave force on the vehicle
α	angle-of-attack
$\bar{\alpha}$	mean angle-of-attack
α_{lag}	unsteady phase lag
$\alpha_{unsteady}$	unsteady angle-of-attack
β_{abs}	foil pitching angle in the absolute frame
β_{max}	maximum foil pitching angle
β_{range}	allowable range of β_{max}
δ	blockage effect
θ	circumferential angle (Chapter 3)
	vehicle pitch angle (Chapters 2, 3)
	azimuthal angle to a receiver (Chapter 5)
κ	momentum inflow correction factor
λ	clocking angle
ν	kinematic viscosity of freshwater (Chapter 3)
	auxiliary input (Chapter 4)
ρ	density
ρ_0	density of water
φ	turbine phase angle
φ_n	phase of hydrodynamic force at multiple of blade rate
ϕ	vehicle roll angle (Chapter 3)
	elevation angle to a receiver (Chapter 5)
ϕ_T	phase angle of thrust vector
Φ	transformation matrix

τ	time period for one oscillation
τ_{inflow}	time constant for dynamic inflow
Ψ	thrust angle
ψ	vehicle yaw angle
ω	angular frequency
$\dot{\omega}$	angular acceleration
$_{cb}$	center of buoyancy
$_{cg}$	center of gravity
$_{cp}$	center of pressure
$_{i}$	index
$_{n}$	blade rate multiple
$_{s}$	source index
$_{X,x}$	x-direction component
$_{Y,y}$	y-direction component
$_{Z,z}$	Z-direction component
$_{\delta}$	deflection

Acknowledgments

First and foremost, I would like to acknowledge Dr. Michael Jonson, my research co-advisor, mentor, and friend, without whose encouragement and support this dissertation would not have been possible. His unwavering belief in my potential as a scientist and engineer has carried me through the many challenges I have faced during the completion of this thesis. I would also like to thank my co-advisor Dr. Joseph Horn, whose expertise and insight has been essential in completing this research, particularly his breadth of knowledge in stability and controls. Additionally, I am greatly obliged to my committee members, Dr. George Lesieutre and Dr. Mary Frecker, for their guidance.

This project would not have been possible without the many hardworking individuals who assisted me through various stages of the research. I am especially grateful to the machinists and engineering support staff who provided their time and energy to help me with part manufacture, vehicle assembly, and transport: Ron Ayers, Scott Tokarz, James Mickey, Thomas Juska, John Bodine, Barry Musser, and particularly Michael Prendergast. I am also grateful to Brian Kline and Edward "Rusty" Boone for their work on the electronics; to Dr. Joel Anstrom and Eric Trainum for their support on the vehicle controls; to Dr. Richard Medvitz for providing the CFD; to Jonathan Bechtel for conducting finite element analysis; to Todd Fetteroff and Bill Harvey for their work on drafting; and to Dr. Rhett Jefferies for his design guidance.

I am deeply indebted to the friends that I have made during graduate school, who have been patient listeners, sources of encouragement, and role models. In particular, I thank Dr. Tyler Dare, Dr. Ben Beck, and Dr. Andy Wixom, who were never too busy to explain difficult concepts, get coffee, or to just let me think through ideas on their whiteboards; Dr. Julia Cole, who has infinite patience; and Amber Miller, who is a great listener and friend and has been a voice of reason. I also would like to thank Dr. Amanda Hanford, who has been a wonderful mentor and friend. I'd additionally like to thank Dr. Michelle Denlinger, Dr. Kelilah Wolkowicz, and Dr. Junyi Geng for sharing their doctoral presentations with me in preparation for my defense. The constant support and perspective from these friends has truly sustained me over the past several years.

I would like to thank my family, whose unconditional love and support allowed me to pursue my degree. I am most grateful to my mother, Dr. Lidush Goldschmidt, who is a brilliant and an inspiring woman in STEM, and who pushed me into an Engineering major my freshman year. I am also grateful to my late father, Dr. Yadin Goldschmidt, who always supported and encouraged my interest in science and math, and spent many hours after school helping me with homework or science fair experiments. This thesis is dedicated to him.

I must also thank my mother and father-in-law, Dr. Deborah Liczwek and Dr. David Corbin, for their sage advice and contagious enthusiasm for science. I would also like to thank Ariel and Tirtza, and Andrea, Elise, and Curtis, for letting me vent about my research and offering words of encouragement.

Most importantly, I thank my husband, Dr. David Corbin. He has been a source of support and encouragement throughout this process, and has always pushed me to be the best version of myself. Dave is my best friend and my constant champion and I could have never done this without him by my side.

Finally, I must acknowledge the funding sources for this research: this work was supported by the U.S. Department of Energy's Advanced Research Projects Agency-Energy (ARPA-E) as well as the Ocean Renewable Power Company (ORPC) under Contract Number DE-FOA-0001261. Specifically, I would like to thank ORPC's Jarlath McEntee for his research guidance. I would also like to thank Nathan Hayes and Milo Feinberg from ORPC for aiding this research effort.

The U.S. Government is authorized to reproduce and distribute reprints for Governmental purposes notwithstanding any copyright notation thereon. The views and conclusions contained herein are those of the authors and should not be interpreted as necessarily representing the official policies or endorsements, either expressed or implied, of the U.S. Government.

1 Introduction

1.1 Motivation

In 2017, 1.2 billion people worldwide had little to no access to electricity [1]. This includes a lack of household access to a minimum level of electricity, access that enables economic activity such as mechanical power for agriculture, and access for public services such as health facilities and schools.

Marine Hydrokinetic (MHK) technologies are underwater systems that generate power in order to address the inadequate and costly access to electricity in remote regions. Upwards of 80% of the energy-poor live in remote regions [1]. In the U.S. specifically, there is extensive clean energy potential in tidal hotspots such as Alaska, Washington, and Maine. Additionally, unlike traditional hydroelectric technologies such as dams, MHK power generation systems can be placed anywhere as there is no requirement for a hydrostatic head.

The hydrokinetic approach to generating power is particularly attractive because tidal currents are predictable, with low seasonal and annual variability [2]. There is a large energy potential, and because these systems are renewable, they provide sustainable power production with minimal environmental effects [3].

While a three-blade open turbine has become the most common marine hydrokinetic technology [3], other designs exist that use different principles, such as underwater kites, ducted turbines, or crossflow turbines. Crossflow turbines (or cycloturbines) orient the rotational axis of the rotor parallel to the water surface and orthogonal to the incoming flow field. They use lift forces on rotating foils to turn a generator.

While there are substantial benefits to this kind of renewable energy, the harsh marine environment provides barriers to its operation. Corrosion in seawater requires mechanical parts to either be painted, galvanized, or constructed with corrosion-resistant materials, such as steel. Additionally, debris carried in the current can damage the turbine foils. Because of this environment, MHK cycloturbines require frequent maintenance and repair, which for current systems necessitates the use of a ship, making the process difficult and costly. By turning the MHK cycloturbines into a maneuverable system, the costs and difficulties associated with deployment and repairs could be circumvented. Additionally, noise control during maneuver could decrease vehicle fatigue as well as reduce the noise impact of the MHK on the surrounding marine environment.

In this dissertation, a robust control system is designed for a novel MHK cycloturbine vehicle. Design work on the configuration of the vehicle is conducted as part of this research. Additionally, the vehicle fatigue is decreased and the vehicle's acoustic signature in the marine environment is reduced by design of a novel acoustic controller. This dissertation focuses specifically on reducing the tonal noise at foil passing frequency.

1.2 Background

A MHK cycloturbine is a renewable electric power generation system used in rivers or tidal environments to address the need for electricity in remote regions. MHK cycloturbines (or crossflow turbines) are oriented with the shaft perpendicular to the flow, and use lift forces on rotating foils to turn a generator. This "paddlewheel" configuration is similar to a cyclorotor as is found on some vertical lift aircraft and vertical axis wind turbines (see Fig. 1.1). Despite success in the deployment and operation of crossflow turbines by companies such as the Ocean Renewable Power Company (ORPC), there is a high cost associated with the operation and maintenance of these turbines due to limited accessibility and difficulties in deployment and retrieval. It is therefore desirable to design an MHK system that can self-deploy and maneuver itself by powering the rotors and using pitching foils for control. In this case the maneuvering turbines become similar to a free-flying cyclorotor aircraft.

A literature review is conducted to develop a concept for a maneuvering MHK cycloturbine system. This includes a review of current hydrokinetic power generation technologies, cyclorotors, active foil pitching mechanisms, system modeling and

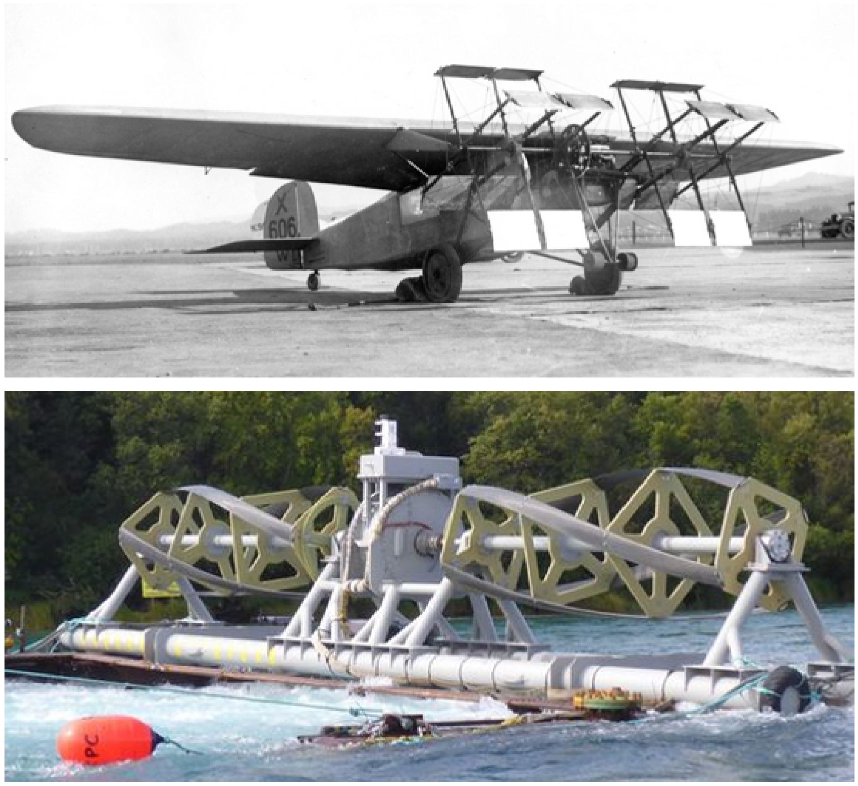

Figure 1.1. Marine Hydrokinetic cycloturbine system vs. cyclorotor aircraft. Top: Schroeder cyclorotor aircraft built in 1930 [4]. Bottom: Ocean Renewable Power Company (ORPC) RivGen™ crossflow turbine system prior to submersion [5].

controls. In respect to the acoustic control of the vehicle and its novelty, a review of prior work done using the method of phase clocking for active noise control is conducted. This dissertation focuses on the design, control, and acoustics of a Marine Hydrokinetic Cycloturbine vehicle; power generation is outside of the scope of this dissertation.

1.2.1 Review of Hydrokinetic Energy Technologies

Hydrokinetic technologies are growing to address the inadequate and costly access to electricity in remote regions. Unlike traditional hydroelectric power generation which requires large dams/reservoirs, marine hydrokinetic technologies can be placed anywhere. In the U.S. specifically, there is extensive renewable energy potential in tidal hotspots such as Alaska, Washington, and Maine. Tidal power is particularly attractive because it is predictable (low seasonal and annual variability)

Figure 1.2. Ocean Renewable Power Company (ORPC) TidGen^{TM} crossflow turbine system [5]. The hydrofoils are skewed to provide smooth operation and improve self-starting.

and has a large energy potential [2]. Additionally, because hydrokinetic technologies are renewable, they provide sustainable power production with minimal negative effects on the environment [6].

While there are many different types of marine hydrokinetic technologies, including turbine and non-turbine systems, this work focuses on cycloturbine (or crossflow turbine) systems. Crossflow turbines orient the rotational axis of the rotor parallel to the water surface and orthogonal to the incoming flow field. The turbines generate power by converting kinetic energy from tidal, river, and ocean currents into mechanical energy via lift and drag on the turbine foils [7].

There are several crossflow turbine systems currently in development or production. The Ocean Renewable Power Company (ORPC) has developed a modular turbine generator unit that can be deployed in rivers (RivGen^{TM}) or tidal environments (TidGen^{TM}) [8]. The tidal generation unit TidGen^{TM} is shown in Fig. 1.2. Currently, these systems are either secured to the seabed with fixed bottom support frames, or suspended in the water with a buoyant tension mooring system [5]. The same is true for other marine hydrokinetic technology competitors [9]. To name specific examples, the Blue Tec (still in conceptual development) can support two to four turbines on a floating platform anchored by cables to the seabed [10] while the Transverse Horizontal Axis Water Turbine fixes the turbines to three columns that are fixed to the ocean floor [11]. In either instance, a support vessel nearby is needed for any operation or maintenance.

To reduce risk and costs associated with the maintenance and repair of MHK vessels, it is desirable to design an MHK system that can self-deploy and maneuver by powering the rotors and using pitching foils for control. Review of current MHK

Figure 1.3. Voith-Schneider propeller on a VectRA 3000 tugboat [12]. The propeller is oriented vertically beneath the ship. Voith-Schneider propellers are mainly used on tugboats.

turbine prototypes and commercial systems [9] shows that no attempts have as yet been made to this end. This leads to a review of current propulsive technologies that could be applied to a maneuvering underwater crossflow turbine system.

1.2.2 Review of Cyclorotor History and Current Technology

Cyclorotors have been used for both Vertical Take-Off and Landing (VTOL) flight and marine applications. The use of cyclorotors has been periodically considered for vertical flight applications, but consistently abandoned in favor of conventional helicopter platforms, since the control mechanisms for a cyclorotor made the vehicles too large and heavy for airborne flight [4]. Cyclorotors have been more successful in marine applications where they are used for ship propulsion and power generation. Two examples of cyclorotors used for ship propulsion are the Kirsten-Boeing propeller and the Voith-Schneider propeller.

In 1926, Kirsten patented his design for a marine cyclo-propeller [14]. His design was supported by William Boeing and is known as the Kirsten-Boeing propeller. These steerable propellers are made of straight foils pitching and rotating about a vertical axis. Controlling the schedule of the pitching foils produces a vectored

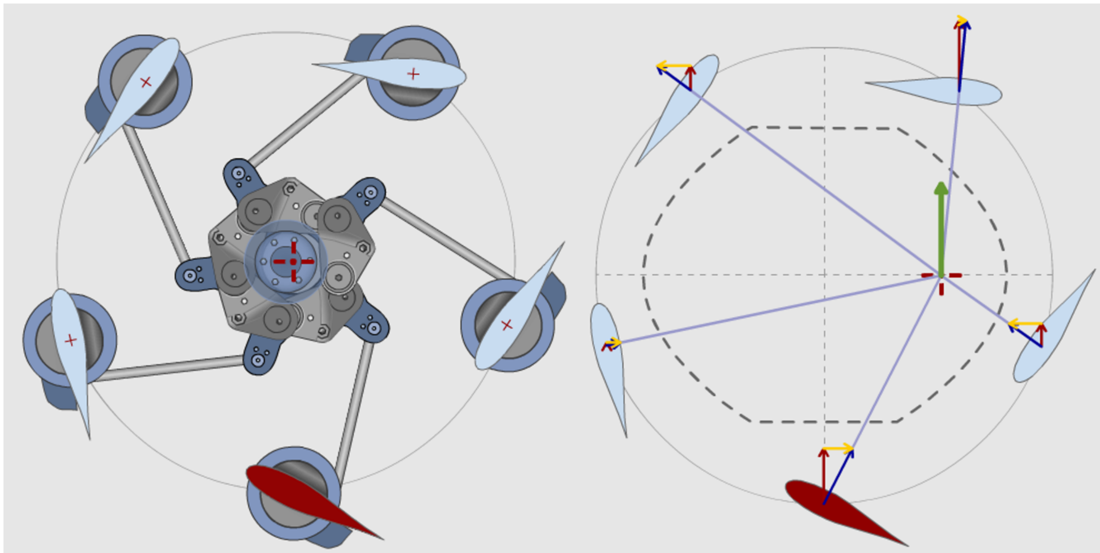

Figure 1.4. Voith-Schneider mechanical actuator mechanism [13]. Left: Kinematics. Right: Hydrodynamic forces. Individual foil lift shown with blue vectors, total thrust shown with green vector.

thrust: the thrust can be vectored in any direction by changing where each foil is at maximum pitch along its circumferential trajectory, i.e. by changing the foil phasing.

The Voith-Schneider propeller is one of the oldest marine cycloidal propellers and is still used today [15]. It is an improvement to Kirsten's design, which was sold to the Voith-Schneider company [16]. The main application of these propellers is in tugboats, where the propeller is oriented vertically beneath the ship (see Fig. 1.3). The foil pitching angle is controlled by the mechanism shown in Fig. 1.4, where the hydrodynamic lift forces on each foil sum to produce a total thrust. The Voith-Schneider cycloidal propellers are optimized for high rotation speeds and high thrust production [17].

Unlike the Kirsten-Boeing propeller, the individual foils in the Voith-Schneider propeller turn 360° around their axis with each turbine revolution rather than only 180° [14]. This is known as prolate cycloidal motion and is described in Fig.1.5. Additionally, the foils in the Kirsten-Boeing propeller have a fixed maximum pitching angle, and so the magnitude of the thrust can only be varied by changing the turbine RPM. Because the thrust magnitude in the Voith-Schneider propeller is additionally controlled by the foil maximum pitch angle, the control mechanism for

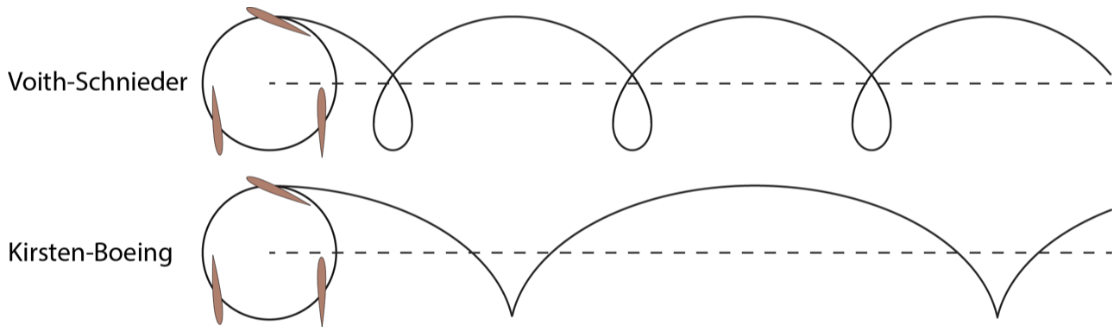

Figure 1.5. Voith-Schneider propeller prolate cycloidal motion vs. Kirsten-Boeing propeller cycloidal motion. The individual foils in the Voith-Schneider propeller turn 360° around their axis with each turbine revolution rather than only 180° [14].

the Voith-Schneider propeller is more complex than the Kirsten-Boeing propeller. Details of active foil pitching mechanism designs will be reviewed in further detail later in this dissertation.

As demonstrated, cycloturbines have been used in marine applications as propellers or as part of a power generation system. Application of cycloturbines has also recently been proposed for use in the micro-air vehicle (MAV) field. Conventional MAVs operate at low Reynolds numbers (bounded by Re between 2.000 and 100,000) where viscous effects in the flow are dominant over the inertial ones, and boundary layers are thick and vulnerable to easy separation [18]. Because separation, transition, and reattachment can all occur in a short chordwise distance, formation of laminar separation bubbles effect the lifting surface characteristics. Since cyclorotor foils see uniform velocities across their span, they suffer less from these low Reynolds number effects that occur on small conventional rotor systems. Many insights on design and control of these systems can be utilized in the design of a maneuverable MHK cycloturbine. Two relevant studies to this end have been conducted at the University of Maryland [18–25] and Seoul National University [26–30].

Researchers at the University of Maryland have developed both quad-rotor and twin-rotor MAV cyclocopters. These vehicles are shown in Fig.1.6. The cyclocopter with two cycloidal rotors employs a conventional tail rotor to balance the vehicle in pitch. Recent efforts have focused on the twin-rotor design as the quad-rotor vehicle was unstable at high thrust levels and untethered stable hover could not be achieved [23]. This was due to excessive coupling among pitch, roll, and yaw

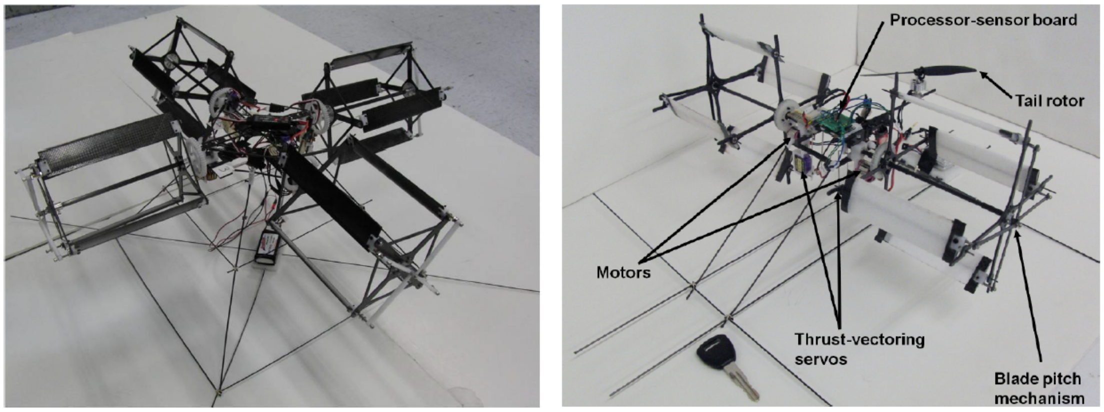

Figure 1.6. University of Maryland cyclocopters [23]. Left: 800 gram quad-rotor cyclocopter. Right: 210 gram twin-rotor cyclocopter.

moments as a result of complex vehicle dynamics and a symmetric structure.

Parametric studies by Benedict and Chopra [19, 21, 22] investigated the effects of foil span, foil number, solidity, foil planform, foil kinematics, chord/radius ratio, and airfoil section. They also investigated the effects of foil stiffness and flow curvature. Several conclusions were made from these studies. First, it was found that foils with shorter spans performed better for the same disk loading, and that this effect was increased for lower pitching amplitudes. It was also found that for a constant solidity, the rotor with fewer foils produced more thrust, and that performance improved for an increased solidity up to approximately 0.4. Higher pitching amplitudes (a maximum of 40° was used in the study) improved power loading, and asymmetric pitching (higher pitch angle at the top of the rotor than at the bottom of the cycle) provided better power loading than symmetric pitching. Additionally, the optimum pitching axis location was found to be between 25-35% of chord.

Of the airfoil sections investigated (all symmetric foils, with varying thickness) it was found that the thickest section investigated (NACA 0015) had the highest power loading [19, 22]. This result was considered somewhat surprising by Benedict and Chopra, since typically thinner airfoils perform better at low Reynolds numbers. They theorized that this may be due to the fact that a thicker airfoil has a higher lift-to-drag ratio over a wide range of angle of attack. Since in a cyclorotor, the blade angle of attack is varied over a large range, a thicker airfoil is perhaps more forgiving. Additionally, stiffer foils were found to produce better efficiency and

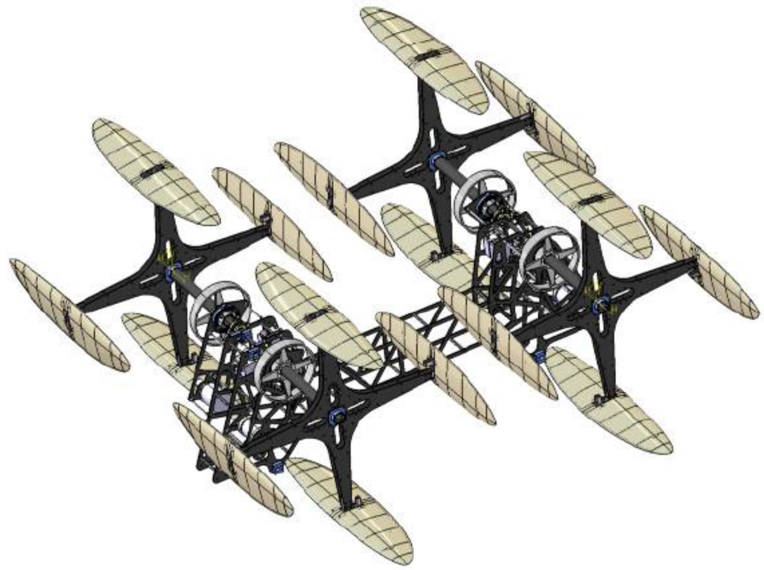

Figure 1.7. Seoul National University designed quadcopter [27]. This design employs four NACA 0018 airfoils per turbine with elliptical planforms.

higher power loadings because of reduced aeroelastic effects.

Similar studies were conducted by researchers at Seoul National University to optimize a quad-rotor cyclocopter (seen in Fig.1.7). Hwang et al. [26–28] investigated various characteristics of cycloidal rotors using two-dimensional and three-dimensional computational fluid dynamics (CFD). These results were in line with those from the University of Maryland. Hwang's most current quad-rotor cyclocopter design employs four NACA 0018 airfoils per turbine with elliptical planforms. While the other planforms investigated were not disclosed, the elliptical planform was given as optimal because of minimized induced drag and reduced required power [27].

These studies influenced many of the design decisions for the maneuverable MHK system in this dissertation, although the MHK vehicle presented in this research has somewhat different design requirements and operating conditions. First, the system can use buoyancy to help lift the system and can vertically offset the center of buoyancy to provide some righting moment for pitch stability and trim. Second, the designed system needs to be efficient while generating power in addition to while propulsing.

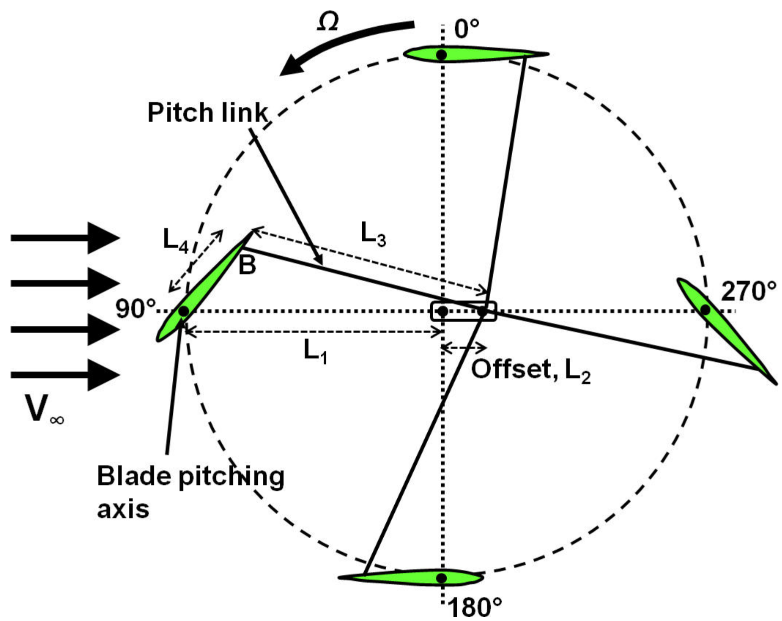

Figure 1.8. Schematic of Vertical Axis Wind Turbine (VAWT) four-bar pitching mechanism [20]. A four-bar linkage system is used to vary the blade pitch amplitude and pitch phasing.

1.2.3 Review of Thrust Vector Control Mechanisms

Dynamically pitching crossflow turbine foils as they move around their axis of rotation has been shown in previous studies to improve turbine efficiency [20,31–33]. Additionally, control of the pitch schedule allows for thrust vectoring: by using either individual foil actuators or a mechanical foil pitching mechanism, the periodic oscillation of the foils about their span axis can be controlled in both amplitude and phase angle.

There are three different types of pitching cycloidal motion: prolate, cycloidal, and curtate. Prolate and cycloidal motion were shown in Fig.1.5 when discussing the Voith-Schneider and the Kirsten-Boeing propellers, respectively. Prolate, or low-pitch cycloidal motion is better suited to hovering and low inflow speeds [34], and thus would be desirable for application in a maneuvering MHK cycloturbine system. Sinusoidal low-pitch control mechanisms have been developed by researchers at the University of Maryland [25], Seoul National University [30], and the National University of Singapore [35]. These mechanisms are called sinusoidal low-pitch systems because the pitch angle variation of the foils over the course of a turbine revolution is very similar to a sine curve [29].

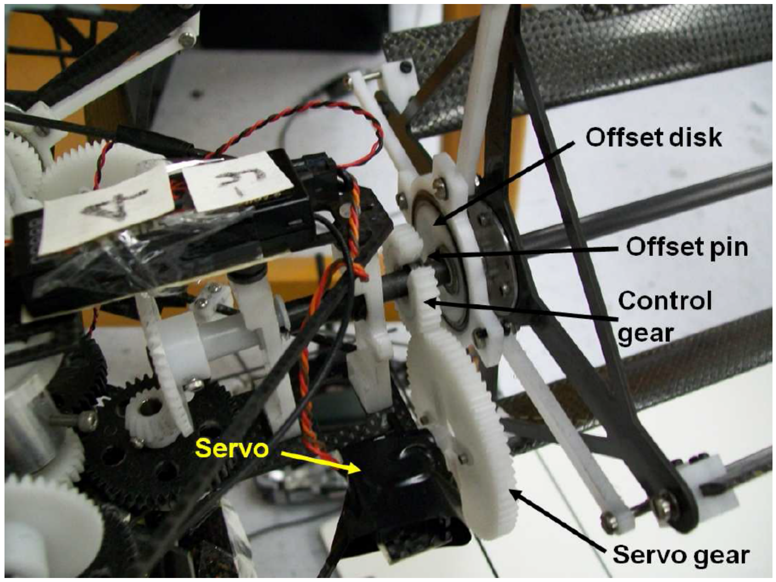

Figure 1.9. University of Maryland micro-air vehicle (MAV) thrust vector control mechanism [18]. An offset disk allows for 360° thrust vectoring capability, but fixes the maximum blade pitch angle.

The University of Maryland low-pitch mechanism is used on an experimental Vertical Axis Wind Turbine (VAWT) designed by Mills, Benedict, and Chopra [25]. The mechanism is designed so that the pitch phasing and the blade pitch amplitude can be easily varied. This is done using a four-bar linkage system (see Fig. 1.8), which simplifies the pitching mechanism that had been commonly used in the 1970s (and which had made variable pitch designs unpopular) [20]. The only power penalty of the linkage system designed is the friction losses from the linkage components. Four characteristic lengths comprise the linkage system: radial distance from the turbine center to the blade quarter chord, the offset link length, pitch link length (which is from the offset link end to a point on the blade), and length between the quarter-chord to this point on the blade. The offset link length controls the maximum blade pitching angle on the blade path. The offset link length and the pitch link length adjust the pitch symmetry.

This design was expanded upon by Benedict [18] through the addition of 360° thrust vectoring capability by twisting an offset disk (see Fig. 1.9). The maximum blade pitch angle in this design is fixed; different offset disks must be used to change the maximum blade pitch angle. The magnitude of the thrust in this design is controlled by varying the turbine RPM.

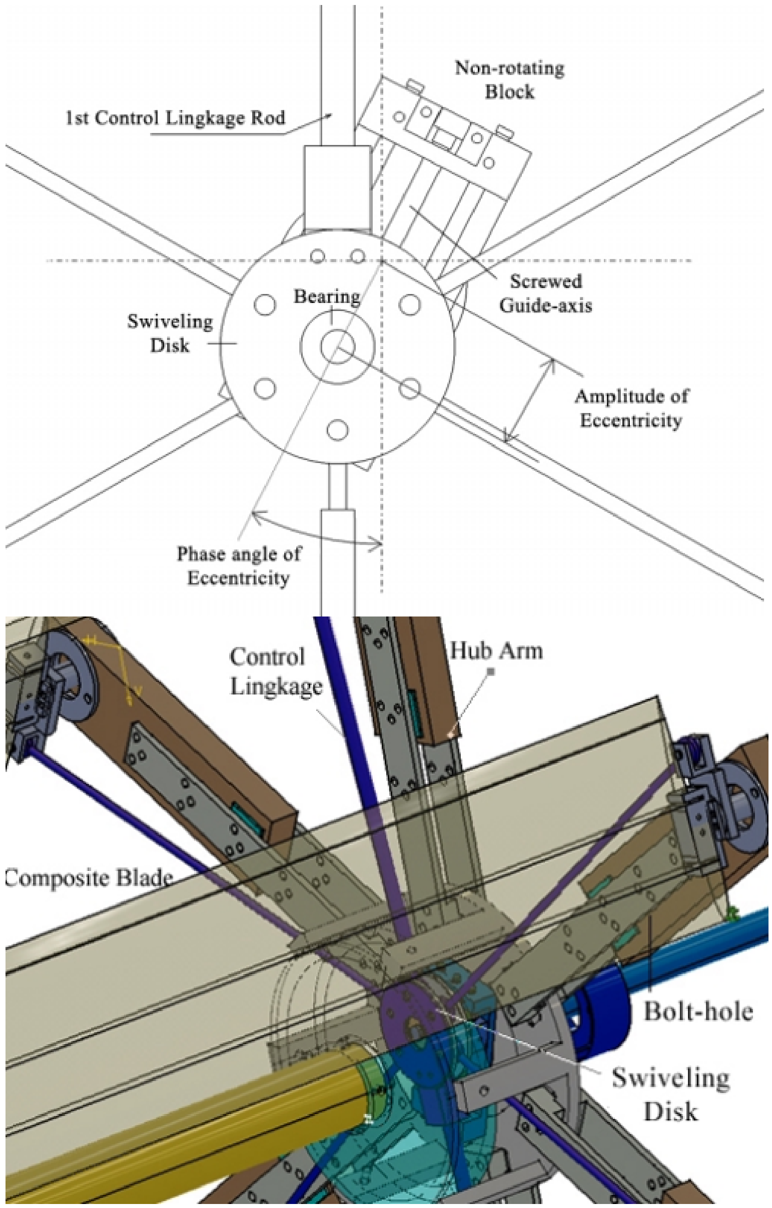

Figure 1.10. Seoul National University thrust vectoring control mechanism [29]. Top: 2D view. Bottom: 3D view. The mechanism uses a swivelling disk to control both the maximum blade pitch angle and the blade pitch phasing.

Kim et al. [29] uses a similar mechanism to control the foil pitch schedule but also controls the magnitude of the thrust by varying the eccentric (offset link length). This mechanism (shown in Fig.1.10) uses a swivelling disk which is centered about the eccentricity point, and gathers all the control linkages on its rim. One control linkage is clamped onto the rim, while the other control linkages are pivoted on the

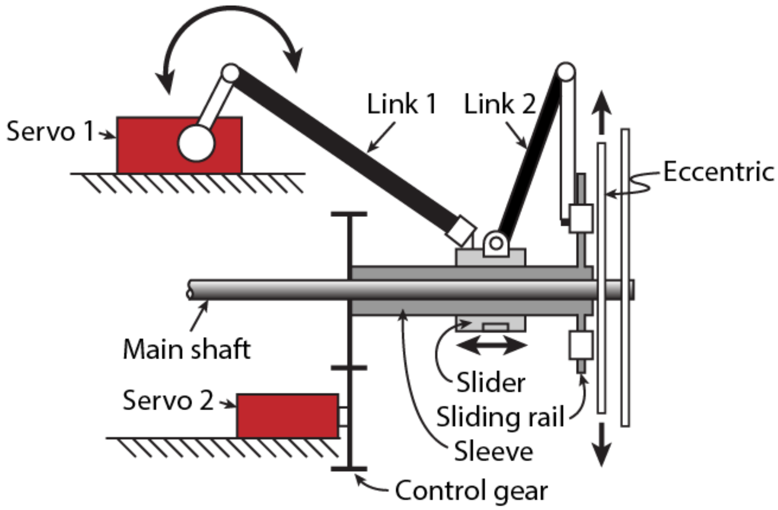

Figure 1.11. University of Singapore micro-air vehicle (MAV) thrust vector control mechanism [35]. Two rotary servos separately control the maximum blade pitch angle and the blade pitch phasing.

rim. The amplitude of the maximum foil pitching angle is controlled by moving the swivelling disk along a screwed guide-axis. A non-rotating block containing the screwed guide-axis can be turned about the turbine shaft, affecting the phase angle.

Finally, Yu et al. [35] developed a control mechanism that consists of two rotary servos that separately control the direction and magnitude of the thrust vector from the pitching foils. The mechanism (shown in Fig. 1.11) is a mixed four bar/five bar mechanism like the mechanism designed by Kim. This design allows for a lighter structure since each blade is not governed by its own eccentric; the turbine blades share a single eccentric.

All of the control mechanisms discussed previously produce a sinusoidal low-pitch motion. Sinusoidal low-pitch active blade control has been shown to enhance the rotor performance over amplified cycloidal motion in laboratory testing [17], but because of limitations in the pitch angle variation, it does not necessarily maximize turbine performance. If individual blade actuators are used, the performance could be improved. For example, Hwang et al. [28] researched optimal blade pitch angle curves for individual blade control and concluded a performance improvement of approximately 25% compared with baseline sinusoidal motion. Optimizing the blade pitch function through individual blade control is an additional consideration when designing a marine hydrokinetic turbine that must both perform as a propulsor and as a power generator.

1.2.4 Review of Cycloturbine System Modeling

Development of a detailed turbine simulation model is necessary to understand the vehicle dynamics and assist in design of controllers. The simulation model solves the six degree-of-freedom rigid body equations of motion for the maneuvering MHK system subject to the hydrodynamic lift and drag forces, hydrostatic forces, and the propulsive forces from the turbines. The model relies on a simplified hydrodynamic analysis of the propulsive forces generated by the turbines, as a function of the foil pitch schedule and vehicle state. Several computational methods to determine the hydrodynamic propulsive forces acting on a cycloturbine are found in the open literature [17, 36–38].

Taniguchi [36] presents a computational method by which to evaluate the performance characteristics of vertical axis cycloidal propellers with semi-elliptic foils. The induced velocity on the cycloturbine is obtained using momentum theory with a modification factor to match the predicted performance to experimental data from a six-bladed vertical axis propeller [39]. Thrust and torque are calculated by integrating the lift and drag forces on each blade using a blade element approach.

Taniguchi's computational method is investigated through a series of experiments by Haberman and Harley [39] over a large range of propeller eccentricity and blade solidity. These experiments show that Taniguchi's method is an adequate predictor of performance characteristics of a cycloidal propeller, with some limitations. The model does not include unsteady effects such as shed vorticity; it assumes that quasi-steady state motion exists. Additionally, the induced velocities are under-predicted in Taniguchi's model. Specifically, Taniguchi assumes uniform inflow over the entire turbine, and that only longitudinal components of the induced velocity contribute to the propeller performance [39]. Therefore, the induced velocity must be determined experimentally or with a higher-order model.

Computational models have since made progress in describing the flow field for a cycloidal propeller. However, they have either been limited by computational power and time to perform, or have sacrificed model fidelity to the physical system [17]. The former is a limitation when running large-scale parametric design studies.

1.2.5 Review of Dynamics Control Methods

To maintain stability and follow a command trajectory in the presence of changing currents and other disturbances, an MHK vehicle would need feedback control. Classical control methods can be used to design controllers to stabilize the MHK vehicle. These controllers provide feedback loops around the vehicle to reduce the effect of variations in vehicle parameters, and are aided by tools such as root locus, Bode, and Nyquist plots. These tools enable visualization of the system dynamics as they are being modified by standard compensators. Compensators can be tuned to simultaneously enhance the transient response while eliminating steady-state error.

However, for complex systems, classical control is limited to a series of single input single output (SISO) designs through successive loop closure. When there are multiple control loops, the design procedure becomes increasingly difficult as there are added gains to be tuned. Additionally, these controllers are not guaranteed to be successful when the dynamics include multiple input multiple output (MIMO) structure, or multiple feedback loops [40]. While classical controllers could work for an MHK vehicle, nonlinear control would outperform linear control in nonlinear operating regions. Therefore, improved vehicle maneuverability is sought by moving from a classical design method (linear and SISO) to a more modern design method (nonlinear and MIMO).

Of the various modern methodologies for control design that could be applied to the MHK vehicle, nonlinear dynamic inversion (NDI) is specifically considered and implemented. NDI is a popular nonlinear control method, applied on the fixed-wing STOVL Harrier [41] and the F-35B STOVL Joint Strike Fighter [42]. It has also gained popularity in application to quadrotor helicopters [43–45].

NDI is based directly on the state-variable model, which provides more information about the system than the black box description used in classical control. Dynamic inversion requires that the controller have a full model of the vehicle nonlinearities. The feedback linearization loop in NDI provides good control performance if there is an accurate model of the system; the plant nonlinearities are ideally canceled in this loop, resulting in perfect linear tracking error dynamics [45]. If the model of the system is not accurate, NDI can be non-robust. NDI is a good candidate for this research, since a simulation model is developed that it is partially

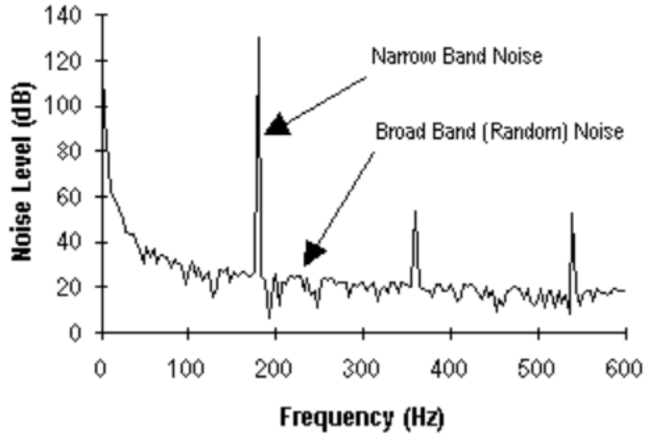

Figure 1.12. Typical noise spectrum [46]. Broadband noise is distributed evenly across the frequency bands, while narrowband noise is concentrated at specific frequencies.

validated by test data.

1.2.6 Review of Noise Control Methods

There are two distinct characteristics to noise sources: broadband noise is distributed evenly across the frequency bands, while narrowband noise is concentrated at specific frequencies (see Fig. 1.12). When the narrowband noise is periodic and consists of a set of tones, it is referred to as "tonal noise". This is common in rotating or repetitive environments. In turbomachinery, tonal noise relating to the blade passage frequency and its multiples varies with the number of blades and rotation speed.

It is desired to control the foil passing noise emitted from the designed MHK vehicle for two reasons. The first is to reduce vibrations associated with blade rate passage. This decreases vehicle fatigue and increases the lifespan of the vehicle. The second reason is to reduce unwanted noise in the surrounding marine environment.

While the effects of man-made noise on fish has yet to be quantified, ship noise has the potential to be particularly intrusive on marine mammal communication and life [47–51]. Ship noise affects marine mammal physical and acoustic behavior, masks communication and echolocation, and increases mammal stress [51].

Erbe et al. conducts a comprehensive literature review of 154 studies that encompass 47 marine mammal species. This review finds that the response to ship noise varies significantly among different species. For example, humpback whales respond strongest to vessels at 127 dB re 1 μPa[1] at 315 Hz 1/3 octave band level[2], while harbor porpoises respond strongest to vessels at 96 dB re 1 μPa at 16 kHz 1/3 octave band level. It is therefore important to consider the radiated noise impact of the entire frequency spectrum as it affects aquaculture.

In this dissertation, an adaptive noise control approach is employed to reduce the radiated acoustics of the MHK vehicle. Adaptive noise control methods attenuate unwanted noise by using another sound source in the system to cancel out the originating noise. An example of this in axial turbomachines is stator-to-stator or rotor-to-rotor indexing (also referred to as vane clocking) [52–54]. Stator vane clocking is when the circumferential position of the stator blades relative to a downstream stator are shifted. By optimizing the mutual circumferential position between two stators in a stator-rotor-stator interaction in a turbomachine, the tonal noise can be decreased [54]. This method is extended for co-rotating fans [55], as well as two-stage rotor-to-rotor clocking [56] which influences noise emission more than stator vane clocking. Auman [55] investigates the acoustic effect of a slowly co-rotating upstream rotor on a downstream rotor, specifically to reduce blade rate tones. Experimental results from this work validate that for some cases slow co-rotation does reduce sound pressure levels by about 5 dB. Alternatively, Blaszczak analyzes the contribution of two-stage rotor-to-rotor circumferential clocking to noise reduction. A 10 dB reduction of the sound pressure levels is found for rotor-to-rotor indexing, *for identical rotor geometry.* Applying the indexing effect to modern gas turbines with varying rotor-to-rotor geometry would be a challenge. Additionally, optimal stator-to-stator or rotor-to-rotor indexing is determined prior to turbomachine operation, and is not performed in situ.

While this method has been applied to axial turbomachines, an example of application to a cycloturbine was not found in the open literature. Therefore tonal noise reduction control using turbine clocking on a cycloturbine vehicle is assumed to be novel.

As with axial flow turbomachinery, cycloturbines could use clocking by adjusting the rotation rates of the various turbines used in the system to attenuate tonal

[1]Ship noise source levels are typically given as a sound pressure level (SPL) quantity in the far-field. Propagation loss is typically modeled and a loss term is added, yielding a sound pressure level referenced to a distance of 1 m from the source. SPL is therefore expressed in dB relative to 1 μPa (at 1 m.)

[2]Octave Band measurements determine the frequency composition of a sound field.

noise generated by the turbines. If such an approach were feasible, it could readily be applied to a maneuverable MHK turbine design that has independent control of multiple cycloturbines. This approach could be applied to both maneuvering and power generation modes.

1.3 Objectives

There are two main objectives for this dissertation.

The first objective of this work is to design a robust control system for a novel MHK cycloturbine vehicle and validate it in simulation and experimentally. The results of small-scale vehicle simulation and testing reveal the behavior of the system under expected flow conditions and how the designed controllers perform under those conditions. This objective is achieved through the following procedure.

1. Determine a mechanical design to effectively maneuver and control an MHK crossflow turbine vehicle:
    (a) Review similar design attempts from literature
    (b) Establish control authority for primary degrees of freedom
    (c) Determine general design from trade-offs of candidate configurations
    (d) Design a mechanism for control of the foil pitching motion
2. Develop a six degree-of-freedom simulation model of the vehicle:
    (a) Solve the six degree-of-freedom rigid body equations of motion for the MHK vehicle subject to the hydrodynamic drag forces, hydrostatic forces, and the propulsive forces from the turbines
    (b) Match the turbine propulsive force model to two-dimensional and three-dimensional CFD of the vehicle
    (c) Tune the turbine propulsive force model to experimental data, specifically a small-scale single turbine Rapid Prototype Device (RPD) and Subscale Demonstrator (SSD) vehicle
3. Design a controller for the vehicle:
    (a) Initially use classical control methods to design controllers

(b) Use more modern nonlinear dynamic inversion method for robust control and increased vehicle maneuverability

(c) Simulate the performance of the vehicle controllers

The second objective of this research is to design a novel acoustic controller that reduces the radiated acoustics and vibrations of the vehicle at foil passing frequency and multiples. This reduces the tonal noise impact of the vehicle in the marine environment, as well as reduces the vehicle fatigue caused by vibration. This objective is achieved through the following procedure.

1. Model radiated acoustics of MHK vehicle and develop method to minimize radiated sound power:

    (a) Model acoustics of MHK vehicle using aerodynamic sound theory and turbine propulsive force model

    (b) Determine relationship between turbine steady force vector and fluctuating pressure

    (c) Determine method to minimize sound power for all possible maneuvers

    (d) Assess sensitivity of sound power to acoustic reduction method

2. Validate tonal noise reduction experimentally:

    (a) Establish baseline sound power levels with single turbine testing in controlled environment

    (b) Establish baseline sound power levels with small-scale vehicle testing in controlled environment

    (c) Validate controller with small-scale vehicle testing in controlled environment using load cells

This second objective focuses on determination of an acoustic method to reduce radiated acoustics and vibration for the MHK cycloturbine vehicle. Reduction of blade rate tones will extend the operating life of the vehicle in the marine environment as well as reduce its environmental impact.

1.4 Structure of Dissertation

This dissertation focuses on the design, control, and validation of a self-deploying MHK crossflow turbine system. The remaining chapters of this dissertation, which cover the work required to design, model, simulate, and test the vehicle are outlined below.

Chapter 2: Mechanical Design and Configuration of a Marine Hydrokinetic Cycloturbine Vehicle

1. This work assesses the static force and moment balance of different deployable MHK turbine configurations, for vehicle design down-select. A general design is established by analyzing the trade-offs of each potential configuration. Details of a mechanical foil pitching mechanism are discussed for a single-turbine RPD and SSD. The experimental setup for the RPD and SSD are additionally detailed.

2. A portion of this work is published in the proceedings of the 2017 American Helicopter Society (AHS) International 73$^{\text{rd}}$ Annual Forum and Technology Display.

Chapter 3: Modeling of the Marine Hydrokinetic Cycloturbine Vehicle Dynamics

1. This work develops the model of the vehicle dynamics for the MHK crossflow turbine vehicle, subject to hydrodynamic forces, hydrostatic forces, and the propulsive forces from the turbines. The turbine force model is tuned using CFD and experimental results from a single turbine RPD and an SSD.

2. This work is accepted for publication in the IEEE Journal of Oceanic Engineering.

Chapter 4: Control Design for the Marine Hydrokinetic Cycloturbine Vehicle

1. Initial controllers are designed using classical control methods. The final controllers use nonlinear dynamic inversion to account for the nonlinearities of the system and increase the vehicle maneuverability. The performance of the controllers are compared and assessed.

2. This work is in preparation for publication to the Elsevier Journal of Control Engineering Practice.

Chapter 5: Tonal Noise Reduction for a Marine Hydrokinetic Cycloturbine Vehicle

1. A model of the vehicle's radiated acoustics and vibrations at multiples of foil passage frequency is determined. Different vehicle maneuvers are simulated, and a control method is determined to reduce sound power. This method is applied experimentally on an SSD in the Applied Research Laboratory Reverberant Tank. Experimental testing provides validation of tonal noise reduction using turbine clocking.

2. This work is published in the proceedings of the 2017 and 2019 International Mechanical Engineering Conference and Exhibition, and accepted for publication in the American Society of Mechanical Engineers (ASME) Journal of Vibrations and Acoustics.

Chapter 6: Conclusions and Recommendations for Future Work

1. The results from this research are summarized. Continued efforts expanding on the work performed are explored. Future work includes the design and application of an acoustic controller, and experimental validation of the nonlinear dynamic inversion controllers.

2 Mechanical Design and Configuration of a Marine Hydrokinetic Cycloturbine Vehicle [1]

2.1 Overview

A notional vehicle layout is defined to establish control authority for primary degrees of freedom; dimensions and locations of main components including turbines, generators, mooring system, etc. are specified; weight and volume estimates of the components are determined using the Ocean Renewable Power Company (ORPC) RivGen™ MHK system [57]; and the expected operating conditions are defined. The primary degrees of freedom desired to be controlled are thrust, lift, and yaw in order to maneuver the system to a desired location. Pitch control and roll control are also desirable, but not absolutely necessary if the system is inherently stable in these axes, which is possible for underwater vehicles by having the center of buoyancy vertically offset above the center of mass (a hydrostatic righting moment). No side force generation is needed, rather the yaw system would steer the vehicle to its desired location.

As the cycloturbine spins, a torque reaction will generate a pitching moment on the structure. A lack of pitch control would lead to uncertainty in trim and dynamic response of the system pitch attitude. For the vehicle to be in equilibrium, this torque therefore must be balanced by a hydrostatic moment or some other force or torque-generating component. Shrestha [23] had success using a two-turbine system with side-by-side turbines turning in the same direction and a tail rotor

[1] The work presented in this chapter is published in the proceedings of the 2017 AHS International 73rd Annual Forum and Technology Display.

to counter pitching moment due to the torque reaction. Hwang's [27] design had success using a four-turbine configuration. Both of these designs were validated in flight tests. In this chapter, different pitch control methods are discussed to determine an optimal MHK vehicle design.

Once an optimal MHK vehicle design is selected, a single turbine Rapid Prototype Device (RPD) and Subscale Demonstrator (SSD) are built for experimental work. Design parameters for these devices are provided.

2.2 Technical Approach

A Graphical User Interface (GUI) tool is developed in MATLAB to understand and analyze the pitch balance of the vehicle in typical operating conditions (see Fig. B.1). The tool analyzes the force and moment balance in detail for different vehicle configurations. Initially, hydrostatic pitch balance is investigated through the use of an overhead buoyancy pod and base weight as shown in Fig. 2.1. The center of the coordinate system is located at the center of the turbines. The Z-axis is positive down, and the X-axis is positive forward. The sum of the moments is equal to:

$$\sum \vec{r}_i \times \vec{F}_i + \vec{M}_i = 0 \tag{2.1}$$

where F_i are the lift, weight, buoyancy, thrust, and drag forces, M_i are the external moments, and r_i are the corresponding distances to where these forces act. The moment balance equation for a cycloturbine configuration is as follows:

$$\begin{aligned}
&(\vec{r}_{cb,pod} \times \vec{B}_{pod}) + (\vec{r}_{cg,pod} \times \vec{W}_{pod}) + (\vec{r}_{cp,pod} \times \vec{D}_{pod}) + \dots \\
&(\vec{r}_{cp,pod} \times \vec{L}_{pod}) + (\vec{r}_{cb,base} \times \vec{B}_{base}) + (\vec{r}_{cg,base} \times \vec{W}_{base}) + \dots \\
&(\vec{r}_{cp,base} \times \vec{D}_{base}) + (\vec{r}_{cb,chassis} \times \vec{B}_{chassis}) + \dots \\
&(\vec{r}_{cg,chassis} \times \vec{W}_{chassis}) + (\vec{r}_{cp,chassis} \times \vec{D}_{chassis}) + q_{turb} = 0
\end{aligned} \tag{2.2}$$

where q_{turb} is the torque applied to the turbine. This equation accounts for the buoyancy pod above the turbines, the base weight, and the support chassis for the buoyancy pod.

To simplify initial analysis, it is assumed that the center of buoyancy, center of gravity, and center of pressure coincide for each vehicle component. This is reflected

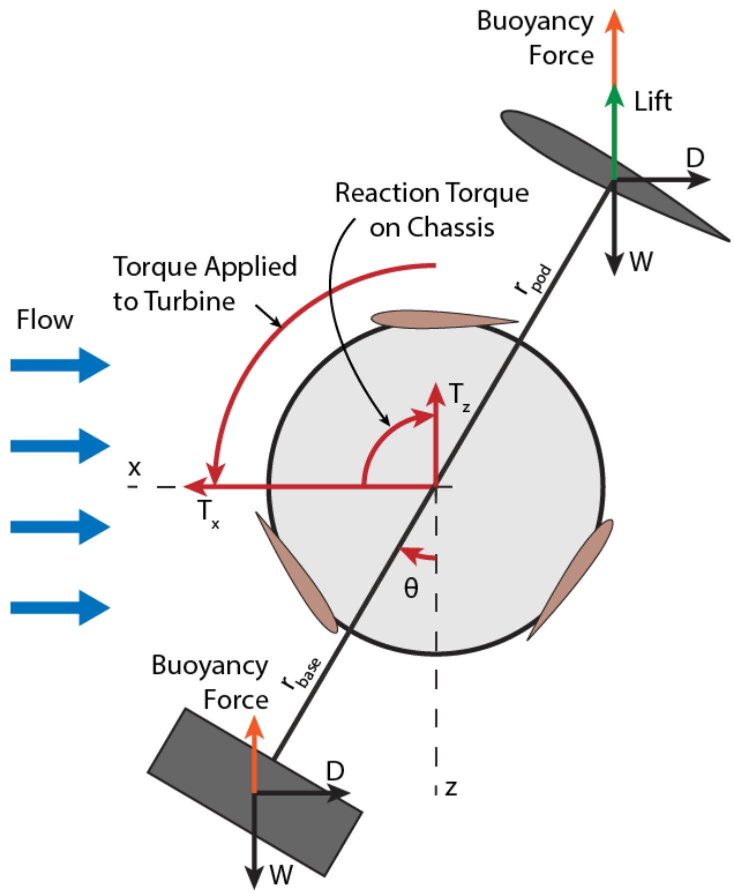

Figure 2.1. Hydrostatic righting moment provided by base weight and buoyancy pod.

in the reduced moment balance equation:

$$\begin{aligned}
&[r_{pod}(B_{pod} - W_{pod} + L_{pod}) + r_{base}(W_{base} - B_{base}) + \dots \\
&r_{chassis}(B_{chassis} - W_{chassis})] \sin\theta + \dots \\
&[-r_{pod}D_{pod} + r_{base}D_{base} - r_{chassis}D_{chassis}] \cos\theta = -q_{turb}
\end{aligned} \tag{2.3}$$

where θ is defined as the pitch attitude of the MHK system. The terms in Eqn. 2.3 can be rearranged to solve for the pitch attitude. First, new variables are defined to simplify the final solution:

$$
\begin{aligned}
A =& r_{pod}(B_{pod} - W_{pod} + L_{pod}) + r_{base}(W_{base} - B_{base}) + \dots \\
& r_{chassis}(B_{chassis} - W_{chassis}) \\
B =& - r_{pod}D_{pod} + r_{base}D_{base} - r_{chassis}D_{chassis} \\
C =& - q_{turb} \\
& A\sin\theta + B\cos\theta = C
\end{aligned}
\tag{2.4}
$$

Next, $\cos\theta$ is replaced with its alternate definition:

$$
A\sin\theta + B\sqrt{1-\sin^2\theta} = C \tag{2.5}
$$

Using algebra and the quadratic formula, the pitch attitude can be determined:

$$
\begin{aligned}
& B\sqrt{1-\sin^2\theta} = C - A\sin\theta \\
& B^2 - B^2\sin^2\theta = C^2 + A^2\sin^2\theta - 2AC\sin\theta \\
& (A^2+B^2)\sin^2\theta - 2AC\sin\theta + (C^2 - B^2) = 0 \\
& \sin\theta = \frac{2AC \pm \sqrt{4A^2C^2 - 4(A^2+B^2)(C^2-B^2)}}{2(A^2+B^2)} \\
& \theta = \sin^{-1}\left(\frac{2AC \pm \sqrt{4A^2C^2 - 4(A^2+B^2)(C^2-B^2)}}{2(A^2+B^2)}\right)
\end{aligned}
\tag{2.6}
$$

Of the two solutions for pitch angle, the only solution that is valid for pitch is:

$$
\theta = \sin^{-1}\left(\frac{2AC + \sqrt{4A^2C^2 - 4(A^2+B^2)(C^2-B^2)}}{2(A^2+B^2)}\right). \tag{2.7}
$$

The full scale turbine and chassis values used to compute the parameters in this equation are derived from the ORPC RivGen$^{\text{TM}}$. User-defined estimates are used to determine buoyancy pod and/or base weight parameters (size and offset distance from vehicle center) necessary to maintain small values of pitch attitude. The main drag components and their contributions to the total drag area are listed in Table 2.1. The drag is calculated at a speed of 2.25 m/s.

It is shown in Fig. 2.2 that a large offset distance for the base and buoyancy pod, a heavy base weight, and large buoyancy volume are needed to balance the torque with a hydrostatic moment. A large hydrostatic righting moment leads to high frequency oscillations and lower damping in pitch dynamics [58]. For this

Table 2.1. Estimates of main drag components for configuration study

Component	Drag Area	Comment
Buoyancy Pod	0.1 m^2	NACA 0020 airfoil $C_D = 0.009$, Frontal area = 10.5 m^2
Support Chassis	5.1 m^2	Cylindrical pipe Length = 20.5 m, Diameter = 0.25 m
Turbine Shafts	2.0 m^2	Cylindrical pipe Length = 8.20 m, Diameter = 0.25 m
Electronics Enclosure	2.0 m^2	Rough estimate
Base Support	1.6 m^2	Bluff body estimate $C_D = 0.80$, Length = 8.20 m, Height = 0.25 m

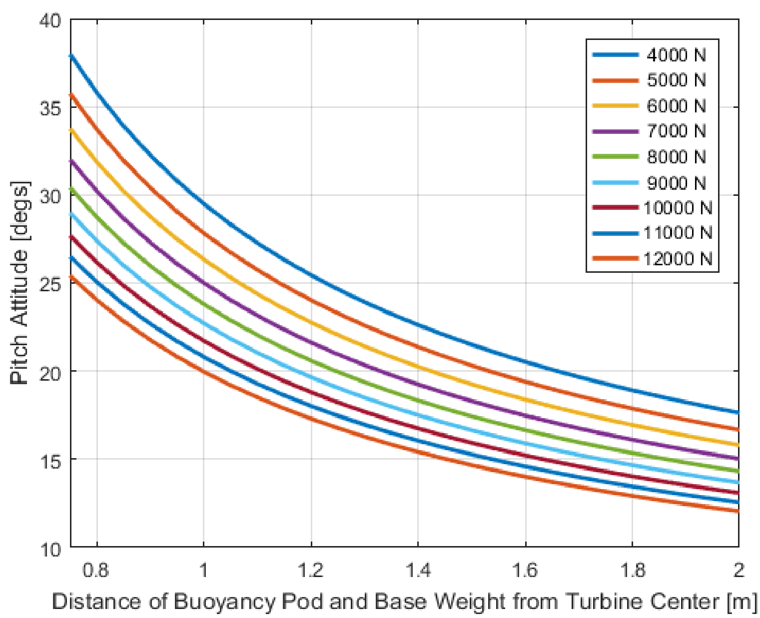

Figure 2.2. Sensitivity of pitch attitude to offset distance and net weight of base weight and buoyancy pod.

reason, several design alternatives are investigated. These alternatives include: two counter-rotating rotors, four counter-rotating rotors, a tail rotor, control surfaces, and vertically offset side thrusters.

2.3 Configuration Study

Estimates for torque, thrust and lift are obtained from two-dimensional computational fluid dynamics (CFD) results of the turbine operating through a range of tip speed ratios (TSRs) and foil actuation schemes for both two and four turbine systems. The resultant forces of the two-dimensional CFD are then used in the stability and control predictions for the varying conceptual designs. The CFD is performed in a manner consistent with previous CFD performed on the ORPC MHK turbine [59]. In the current work, the CFD is extended to implement sinusoidal pitching motion for the individual foils.

The results of the qualitative analysis done in this section are summarized in Tables 2.2 and 2.3. Table 2.2 summarizes the control authority for each option investigated, while Table 2.3 evaluates the pitch control benefits or disadvantages of each design. Table 2.3 shows that a four-turbine configuration is most beneficial for this project, despite the high cost. The pitch axis is controlled in forward flight, hover, and reverse flight, and there is an added benefit in power generation.

2.3.1 Twin-Rotor Cyclocopter

The first concept investigated is a two-turbine configuration with counter-rotating rotors. The pitch of the foils controls the direction of the thrust vector, regardless of the direction of rotation. This is shown in Fig. 2.3. In other words, the two turbines can rotate in opposite directions, but still be thrusting in the same direction. Therefore, the magnitude and direction of the thrust for this vehicle would be controlled by the turbine rotation rate and the foil pitching schedule. Figure 2.4 shows the control strategy for the two-turbine configuration. Roll and yaw are controlled by differential lift and thrust, respectively, on the two turbines. The pitching moments due to torque should approximately balance due to counter-rotation, but this system does not have pitch control. There may be variation in the torque between the two motors as well as different local velocities along the span of the vehicle in a tidal environment. These factors could contribute to unpredictable pitch behavior or even instability.

Table 2.2. Summary of control authority for different vehicle configurations

Pitch Control Option	Thrust	Pitch	Roll	Yaw
Two counter-rotating rotors	Magnitude and direction determined by turbine RPM and foil pitching schedule	No control	Differential lift on turbines	Differential thrust on turbines
Tail Rotor	Magnitude and direction determined by turbine RPM and foil pitching schedule	Controlled by tail rotor	Differential lift on turbines	Differential thrust on turbines
Control surfaces	Magnitude and direction determined by turbine RPM and foil pitching schedule	Controlled by surfaces	Differential lift on turbines	Differential thrust on turbines
Vertically offset side thrusters	Magnitude and direction determined by turbine RPM and foil pitching schedule, also from thrusters	Controlled by thrusters	Differential lift on turbines	Differential thrust on turbines
Four counter-rotating rotors	Magnitude and direction determined by turbine RPM and foil pitching, also from second set of turbines	Counter-rotate to minimize torque reaction, differential thrust (top/bottom) controls pitch	Differential lift on turbines	Differential thrust on turbines

Table 2.3. Summary of advantages and disadvantages for different vehicle configurations

Pitch Control Option	**Cost**	**Pitch axis controlled in forward flight**	**Pitch axis controlled in hover/reverse flight**	**Torque balance method provides benefits beyond maneuvering**
Two counter-rotating rotors	Low			
Tail rotor	Medium	✓	✓	
Control surfaces	Low	✓		
Vertically offset side thrusters	Medium	✓	✓	Contributes to forward thrust
Four counter-rotating rotors	High	✓	✓	Efficiency increase in power generation

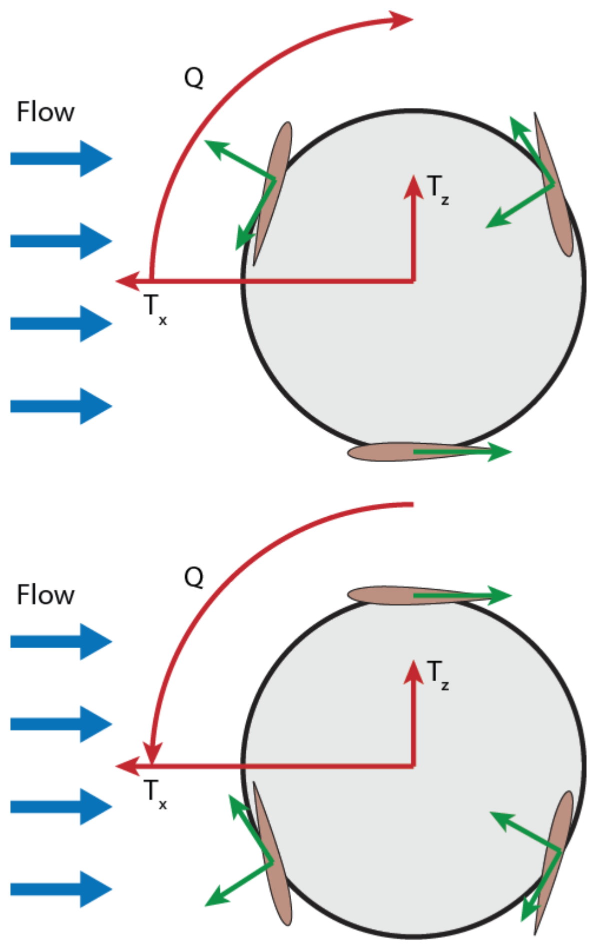

Figure 2.3. Foil pitching schedule controls direction of thrust vector. Thrust direction is independent of the direction of turbine rotation.

2.3.2 Twin-Rotor Cyclocopter with Tail Rotor

Another method of pitch control investigated is that of a tail rotor, such as implemented by Shrestha [23]. Figure 2.5 shows the force balance for this control option. The pitch attitude is calculated in the same manner as in Eqn. 2.4:

$$\begin{aligned}
A =& r_{pod}(B_{pod} - W_{pod} + L_{pod}) + r_{base}(W_{base} - B_{base}) + \dots \\
& r_{chassis}(B_{chassis} - W_{chassis}) + D_{tail} r_{tail} \\
B =& - r_{pod} D_{pod} + r_{base} D_{base} - r_{chassis} D_{chassis} - (W_{tail} - B_{tail}) r_{tail} \\
C =& - q_{turb} - T_{tail} r_{tail} \\
& A \sin\theta + B \cos\theta = C
\end{aligned} \tag{2.8}$$

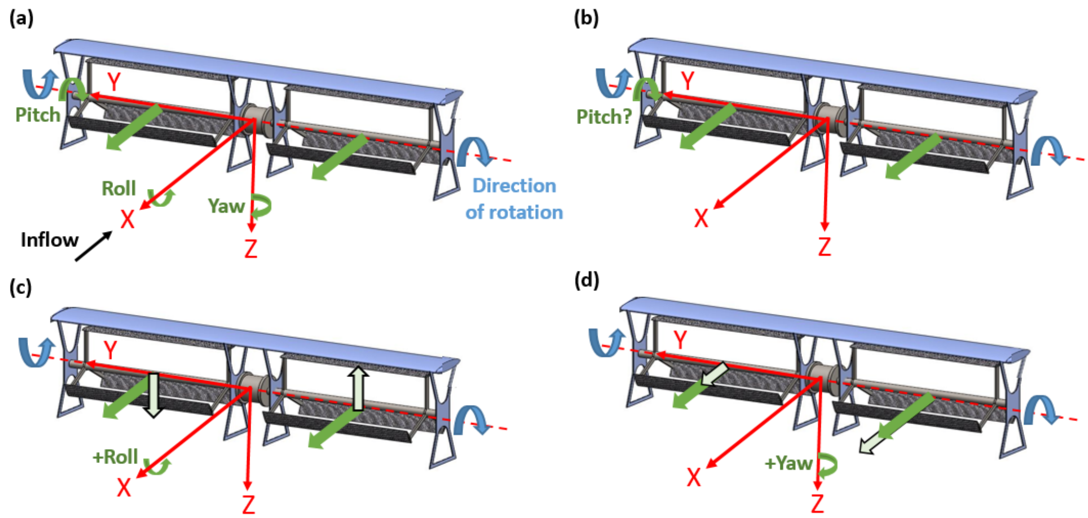

Figure 2.4. Control strategy for two turbine MHK configuration. (a) Definition of pitch, roll, and yaw degrees of freedom; (b) No pitch control from counter-rotating turbines; (c) roll control using differential lift; (d) yaw control using differential thrust.

but including the forces generated by the addition of the tail rotor. It is found that a tail rotor does not require a lot more power to maintain stability, and is simple to implement. However, the tail rotor's only function would be for maneuvering. It does not aid in power generation. Additionally, there is concern that the tail rotor could be damaged in the river or other tidal environment since for the MHK system designed, it would need to have a large moment arm and extend far from the main body of the system.

2.3.3 Twin-Rotor Cyclocopter with Control Surfaces or Side Thrusters

Other control options investigated are control surfaces and vertically offset side thrusters. Figure 2.6 demonstrates the MHK vehicle concept with vertically offset side thrusters. Unlike control surfaces that are only effective in forward flight, vertically offset side thrusters can be used in reverse motion. The side thrusters help with yaw control of the vehicle and also contribute to forward thrust. Additionally, they stabilize the vehicle in pitch with only minimal power required. However, like the tail rotor configuration, these options do not contribute to increased power generation.

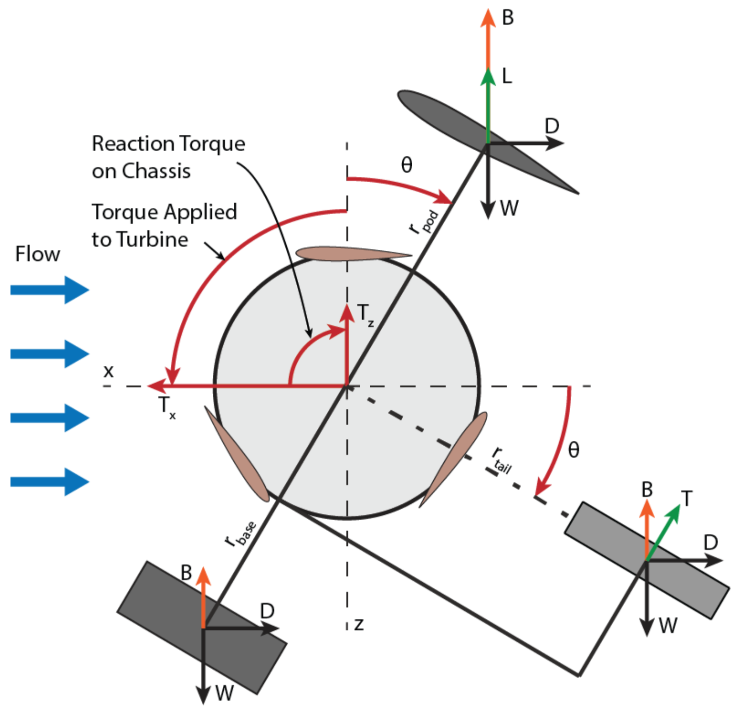

Figure 2.5. Force balance for a tail rotor.

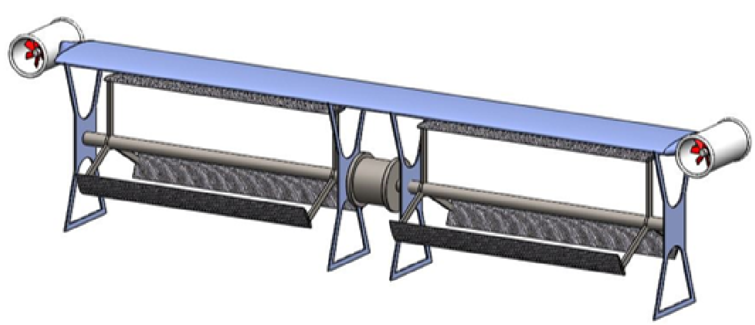

Figure 2.6. Two-turbine configuration with vertically offset side thrusters

2.3.4 Quad-Rotor Cyclocopter

The final control option investigated to add pitch control is to add a second set of turbines, making the system a four-turbine design (see Fig. 2.7). By counter-rotating the turbines, the torque reaction is minimized, and unlike the two-turbine configuration, differential thrust between the top and bottom turbines controls pitch attitude. Figure 2.8 shows the force-body diagram for the four turbine system, with an overhead buoyancy pod and base weight underneath. With a second set

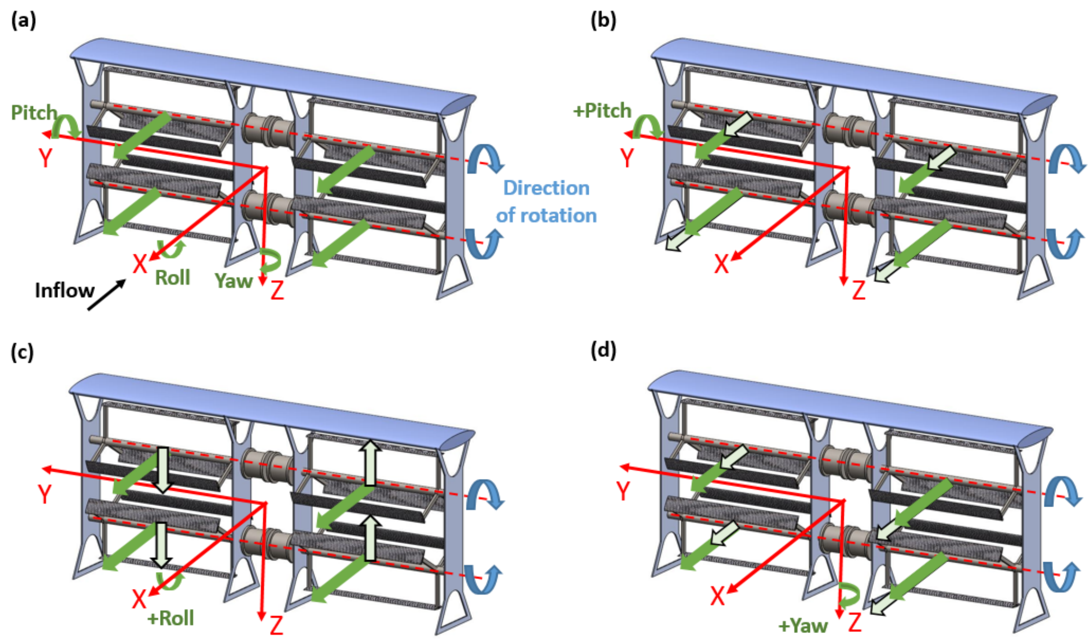

Figure 2.7. Control strategy for four turbine MHK configuration. (a) Definition of pitch, roll, and yaw degrees of freedom; (b) pitch control using differential thrust; (c) roll control using differential lift; (d) yaw control using differential thrust.

of turbines it is found that only a minimal increase in power required is needed to maintain pitch balance. CFD analyses have also suggested there is a benefit in power generation due to favorable interactions between the two turbines which increase the total mass flow in power generation mode. The only caveat for this design is that the actuation of the pitching mechanisms required for this system is more complex and expensive.

2.4 Design of a Rapid Prototype Device (RPD)

A Rapid Prototype Device (RPD) is designed and manufactured to determine the operation and performance of a single turbine. This turbine design is 1/5.56 scale of the turbine used for the ORPC RivGen^{TM} and the intended full-scale vehicle. (The RPD is 1/10 scale of a power generation system that can produce 150kW of power.) The turbine characteristics are summarized in Table 2.4. The testing knowledge gained is used to validate CFD and blade element simulation results of lift, thrust, and torque, as well as to ascertain the effectiveness of a mechanical foil

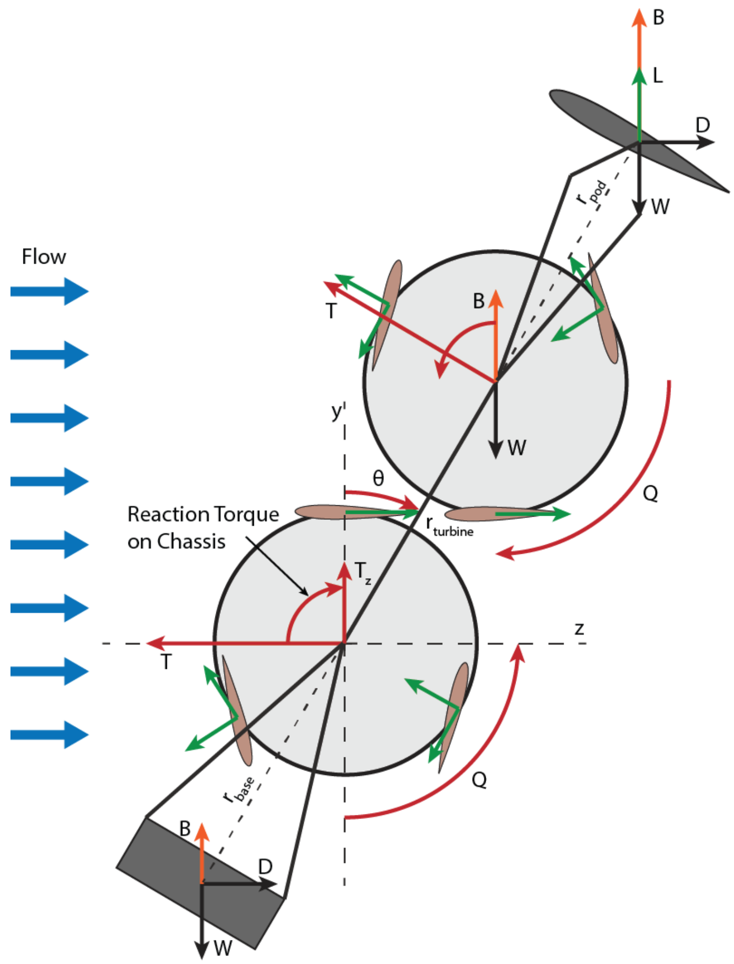

Figure 2.8. Force balance for four turbine configuration in forward flight

pitching mechanism. Additionally, the radiated sound performance for the single turbine is quantified since such information may have an environmental impact on marine mammals and fish. The operation of an MHK cycloturbine vehicle is novel and any difficulties can be addressed with the simpler RPD system. The flow around a single turbine is relevant for validation since most of the flow configuration anticipated for a Subscale Demonstrator do not include significant interactions between the turbines. The three-dimensional flow around the turbine provides an excellent test case for CFD computations of the full three-dimensional flow field.

The RPD has components that are operated in air and in water to avoid using waterproof motors in the rapid prototype. This is achieved using a barge platform (see Fig. 2.9) to hold the motor and many of mechanisms. The axis of the turbine is oriented vertically and submerged below the barge (see Fig. 2.10).

Table 2.4. Turbine characteristics

Description	Full Scale Value	RPD Scale Value	Unit
Foil Span	5000	900	mm
Foil Chord	528	95	mm
Foil Number	3	3	–
Foil Profile	NACA 0018	NACA 0018	–
Turbine Diameter	2500	450	mm
Pitch Amplitude	0-30	9, 30	°
Pitch Phase	0-360	0-360	°

Figure 2.9. Barge for RPD. The barge provides a large surface area to mitigate air drawing, and the solid boundary underneath of the barge also provides a more convenient boundary condition for three-dimensional CFD.

This configuration allows for any thrust to be oriented in the horizontal plane. The barge has an area of 1.83 m^2 which is large enough to float the entire RPD. The turbine generates a vortex that has the potential to draw air from the surface of the water. The barge provides a large surface area to mitigate air drawing. The solid boundary underneath of the barge also provides a more convenient boundary condition for the three-dimensional CFD.

2.4.1 Design of RPD Thrust Vectoring Mechanism

Individual foil actuation is initially investigated to control the pitch schedule of the foils on the turbine. However, it is found from CFD that at the RPD scale, the actuator torque is large. In combination with the required foil pitching speed, this

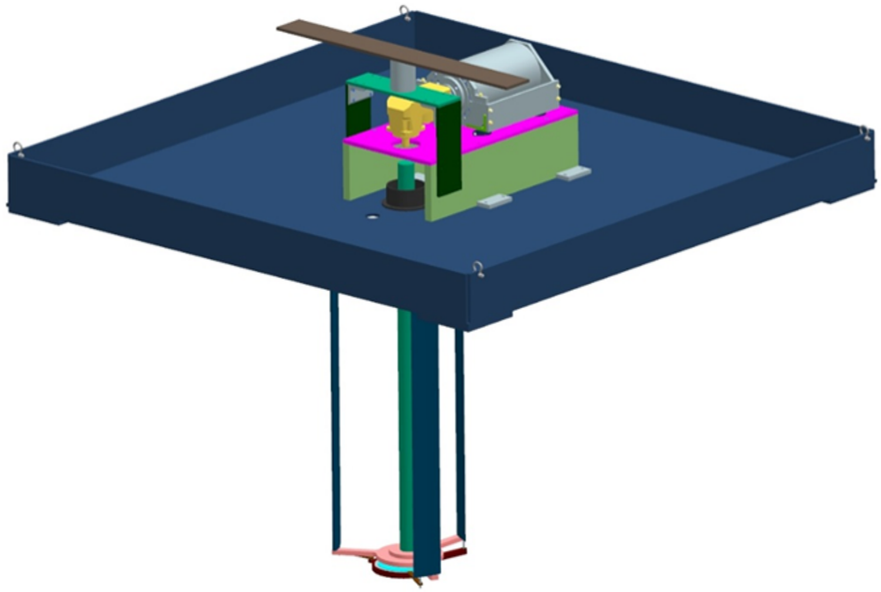

Figure 2.10. Rapid Prototype Device suspended under the barge. The motor, gearbox, and load cell remain dry.

method of foil actuation is beyond state of the art actuators. Scaling shows that if the actuator cannot work at model scale, it will not work at full scale when an n^2 greater torque is required [60]. Therefore, a mechanical foil pitching mechanism is required to vector the thrust.

The design of the foil pitching mechanism is based on a design by Benedict [18], which allows the RPD to have 360° thrust vectoring capability by using an offset disk. For the RPD, two offset disks are used. The first disk provides a maximum foil pitching angle $\beta_{max} = 9°$ for optimum power generation. The second disk provides a maximum foil pitching angle $\beta_{max} = 30°$ for optimum thrust. The foil pitching mechanism is comprised of two bearings: the first installed about the axis of the turbine shaft, and the second installed around the edge of a disk whose central axis is offset from the turbine shaft. The inner bearing allows the main shaft to rotate independently from the offset disk.

Figure 2.11 shows that the offset distance between the center of the disk and the main shaft creates a link in the pitching mechanism for the foils. As shown, link 1 connects the main shaft to the quarter chord of the foil. The length of link 1 is the radius of the turbine. For the RPD, this radius is 225 mm. Link 4 is the distance from the quarter chord of the foil to the three quarter chord of the foil. Link 3

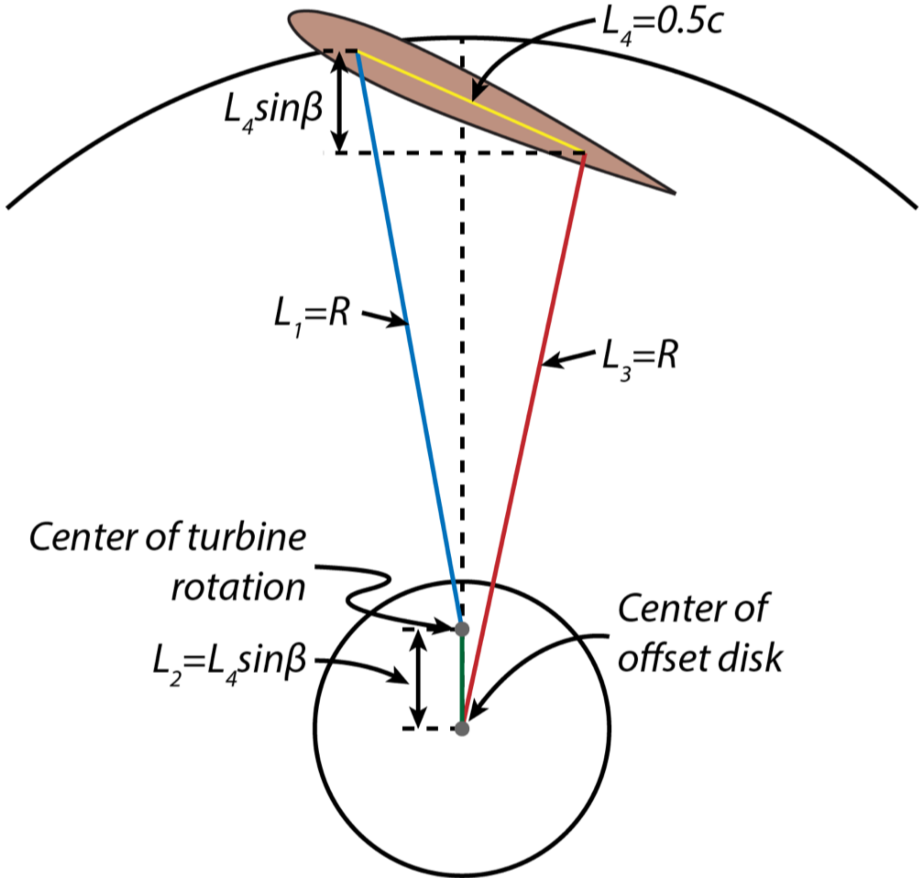

Figure 2.11. Four-bar linkage mechanism for cyclic foil pitching.

connects the three quarter chord point on the foil to the center of the offset disk and is the same length as link 1. Not shown is that this pitch link is rigidly connected to the outer bearing around the edge of the offset disk. This is so that when the main shaft spins, link 1 pulls link 4 and link 3 around with it, but the offset disk remains stationary. Finally, link 2 is the offset distance. From geometry, this link length corresponds to $(1/2)c \sin \beta_{max}$. Therefore, one can control the maximum foil pitching amplitude by altering this length. The maximum foil pitching amplitude affects the magnitude of the thrust vector, as shown in Fig. 2.12.

The twist of the offset disk relative to the central shaft controls the phase of the pitching foils; i.e. where the maximum foil pitch angle occurs along the foil's circumferential trajectory. An illustration of the thrust vectoring for a three-bladed turbine is seen in Fig. 2.13.

In this foil pitching mechanism, the pitch linkages are connected to the offset

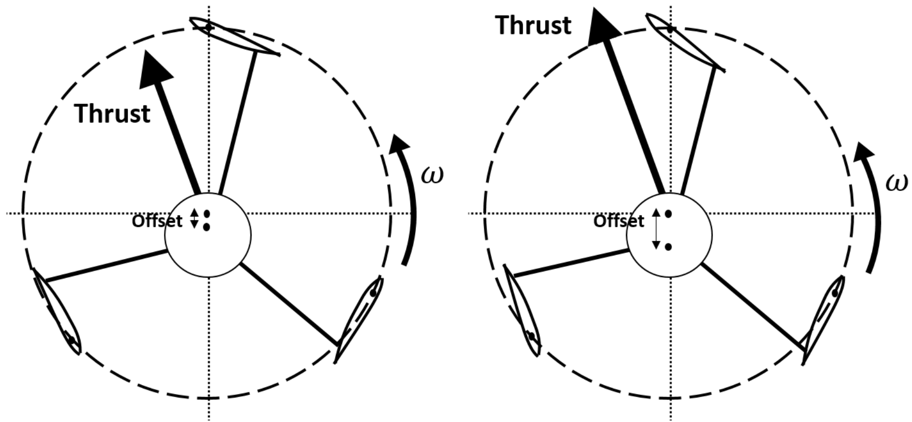

Figure 2.12. Effect of offset link length on foil pitching amplitude. Increased offset corresponds to a greater foil pitching amplitude, and higher thrust. Left: Low pitching amplitude. Right: High pitching amplitude.

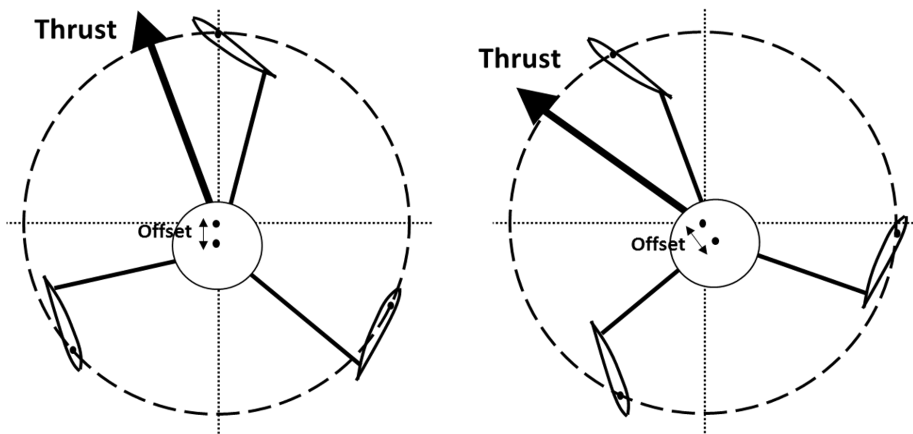

Figure 2.13. Effect of offset twist on foil pitching phase angle. The phase angle is related to the thrust direction.

disk and to the three quarter chord location on the foils. For the system to have one degree-of-freedom (pure rotation), two of the pitch links must be pinned-pinned and one of the pitch links must be rigidly connected to the outside bearing on the offset disk. Figure 2.14 shows the breakdown of links and joints for the foil pitching mechanism. One pitch linkage rigidly connected to the outer bearing of the offset disk results in 8 links and 10 joints. Using Gruebler's equation [61]:

$$N_{DOF} = 3(N_L - 1) - 2N_J \tag{2.9}$$

where $N_L = 8$ is the number of links, and $N_J = 10$ is the number of joints, results

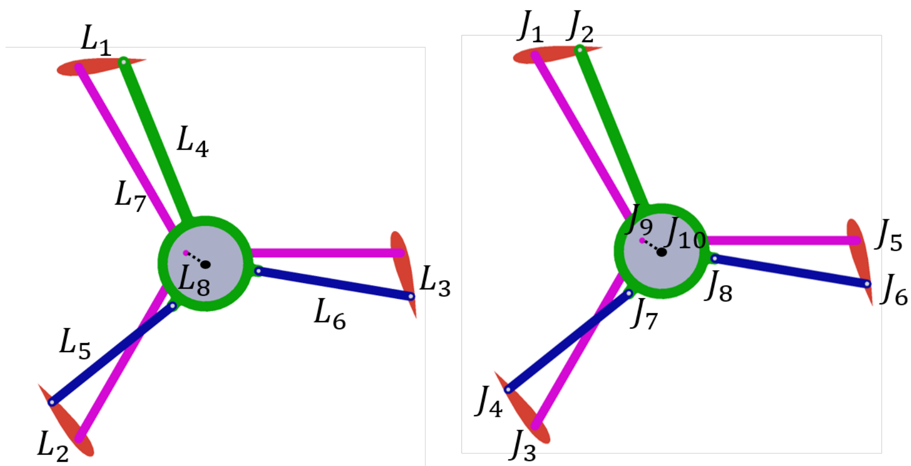

Figure 2.14. The foil pitch schedule of the RPD is controlled using a sinusoidal pitching mechanism that consists of one four-bar and two five-bar mechanisms. Gruebler's formula shows that the pinned-pinned links satisfy the requirement for one degree-of-freedom for pure rotation. Left: L is the number of links. Right: J is the number of joints.

in one degree-of-freedom of pure rotation.

The resulting system is comprised of a crank-rocker type four-bar mechanism mixed with a geared five-bar mechanism, which accomplishes the required sinusoidal variation in foil pitch. A program is written to perform the position, velocity, and acceleration analyses of the linkage mechanism to verify this result. Figure 2.15 demonstrates the cyclic pitching produced from this mechanism for three different maximum foil pitch angles. It should be noted that there is a slight phase shift associated with this mechanism (4° to 5°) that will produce a small lateral thrust force. The application of this mechanism also produces a slight asymmetry between the maximum pitch angle at the top of the foil trajectory versus the bottom of the foil trajectory (about 1°).

Additionally, as the radius of the offset disk increases, there is a slight increase in variation between the foils over their circumferential trajectory (see Fig. 2.16). This is an effect of the five-bar system in the linkage mechanism: there is increased foil-to-foil variation with increasing offset disk radius. Outside of these variations from the ideal kinematics, the linkage mechanism produces the desired sinusoidal pitching schedule.

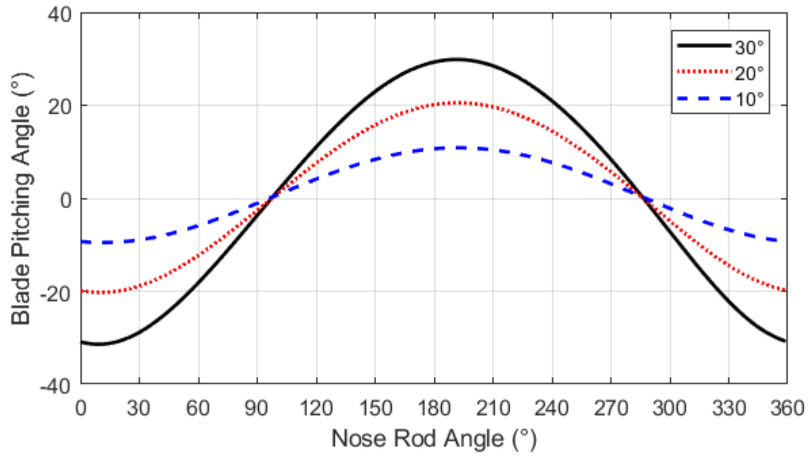

Figure 2.15. Variation of foil pitch angle along the azimuth using linkage mechanism.

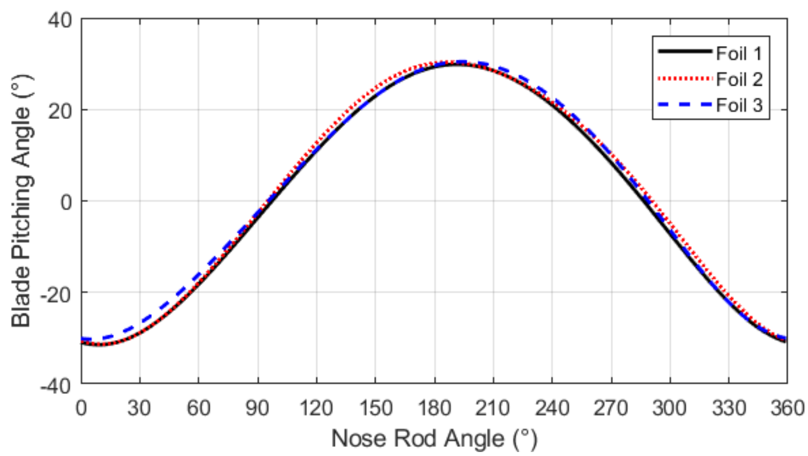

Figure 2.16. Variation of pitch angle between foils at an increased offset disk radius, $\beta_{max} = 30°$.

2.4.2 Inertial and Hydrodynamic Force Consideration for RPD Thrust Vectoring Mechanism

On the RPD, a servo motor provides the adjustment of the thrust vector direction. As with the main motor, the servo motor is located within the barge hold. The shaft penetrates the barge base and connects to a gear train controlling an offset disk (see Fig. 2.17). The gearing is determined based on the static holding torque of the stepper motor available and the torque generated on the offset disk through inertial linkage forces and hydrodynamic forces.

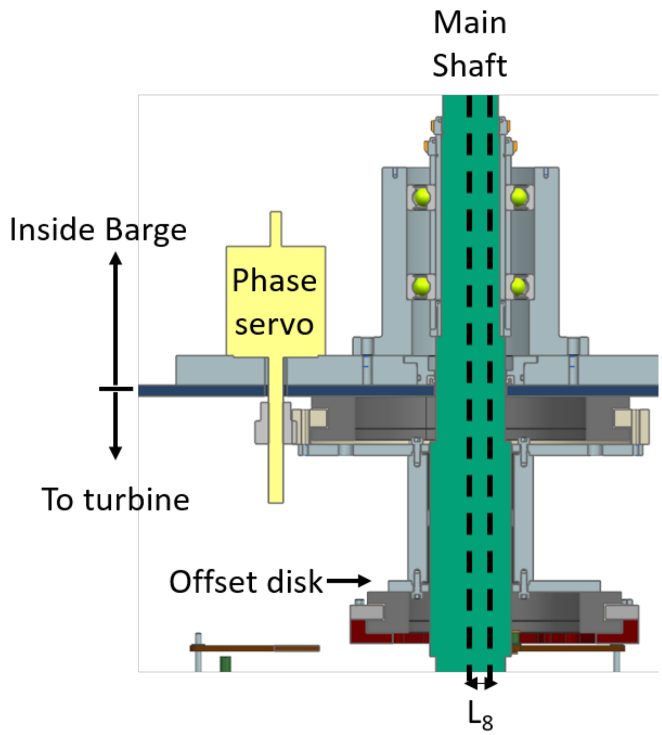

Figure 2.17. Thrust vectoring mechanism for the RPD. The offset disk sets the maximum foil pitching amplitude, while a servo motor with a gear reduction controls the phase angle of the foil pitch schedule. For reference, link 8 from Fig. 2.14 is shown.

The inertial and hydrodynamic forces on the linkage mechanism are considered to determine the holding torque necessary for the offset disk. Hydrodynamic loads are predicted from two-dimensional CFD, and mass and moments of inertia for each linkage in the mechanism are estimated. To determine the inertial forces, a dynamic force analysis is performed using a Newtonian solution method. The dynamic force analysis for the four-bar linkage system is shown in Fig. 2.18. For each linkage, the forces are summed in the vertical and horizontal directions, with the coordinate systems centered at the center of gravity for each linkage, respectively. The torques are also summed for each linkage. This leads to 9 equations and 9 unknowns:

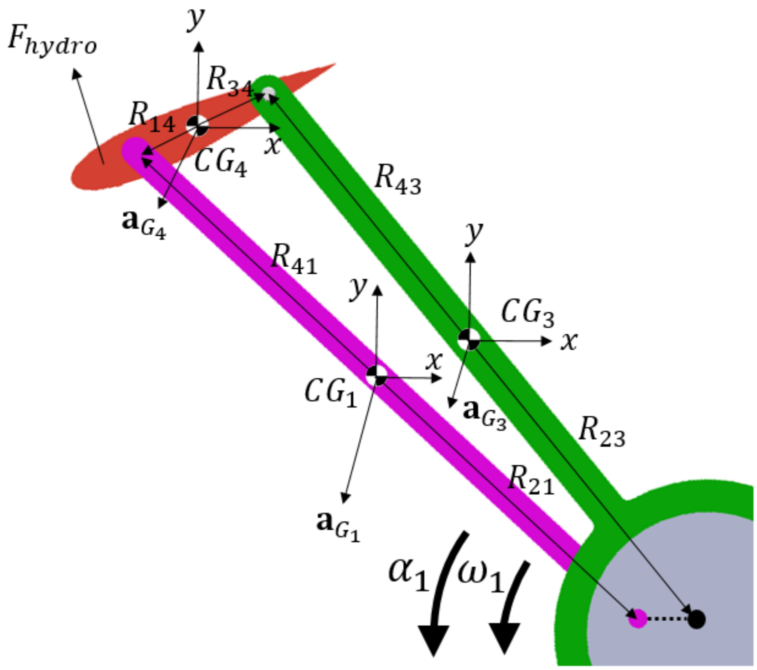

Figure 2.18. Dynamic force analysis of the four-bar linkage system. The inertial and hydrodynamic forces on the linkage mechanism are considered.

$$
\begin{aligned}
F_{21_X} + F_{41_X} &= m_1 a_{G_{1_X}} \\
F_{21_Y} + F_{41_Y} &= m_1 a_{G_{1_Y}} \\
M_{21} + (R_{21_X} F_{21_Y} - R_{21_Y} F_{21_X}) + (R_{41_X} F_{41_Y} - R_{41_Y} F_{41_X}) &= I_{G_1} \dot{\omega}_1 \\
F_{34_X} - F_{41_X} + F_{hydro_X} &= m_4 a_{G_{4_X}} \\
F_{34_Y} - F_{41_Y} + F_{hydro_Y} &= m_4 a_{G_{4_Y}} \\
(R_{34_X} F_{34_Y} - R_{34_Y} F_{34_X}) - (R_{14_X} F_{41_Y} - R_{14_Y} F_{41_X}) + M_{hydro} &= I_{G_4} \dot{\omega}_4 \\
F_{23_X} - F_{34_X} &= m_3 a_{G_{3_X}} \\
F_{23_Y} - F_{34_Y} &= m_3 a_{G_{3_Y}} \\
(R_{23_X} F_{23_Y} - R_{23_Y} F_{23_X}) - (R_{43_X} F_{34_Y} - R_{43_Y} F_{34_X}) &= I_{G_3} \dot{\omega}_3
\end{aligned}
\tag{2.10}
$$

where the subscript notation F_{ij} denotes the force acting on link j by link i, and where M_{21} is a source torque available on the drive link. It is the torque delivered from the ground to link 1 in order to drive it at the kinematically defined accelerations [61]. These equations can furthermore be transformed into matrix form:

$$\begin{bmatrix} 1 & 0 & 1 & 0 & 0 & 0 & 0 & 0 & 0 \\ 0 & 1 & 0 & 1 & 0 & 0 & 0 & 0 & 0 \\ -R_{21_Y} & R_{21_X} & -R_{41_Y} & R_{41_X} & 0 & 0 & 0 & 0 & 1 \\ 0 & 0 & -1 & 0 & 1 & 0 & 0 & 0 & 0 \\ 0 & 0 & 0 & -1 & 0 & 1 & 0 & 0 & 0 \\ 0 & 0 & R_{14_Y} & -R_{14_X} & -R_{34_Y} & R_{34_X} & 0 & 0 & 0 \\ 0 & 0 & 0 & 0 & -1 & 0 & 1 & 0 & 0 \\ 0 & 0 & 0 & 0 & 0 & -1 & 0 & 1 & 0 \\ 0 & 0 & 0 & 0 & R_{43_Y} & -R_{43_X} & -R_{23_Y} & R_{23_X} & 0 \end{bmatrix} \begin{bmatrix} F_{21_X} \\ F_{21_Y} \\ F_{41_X} \\ F_{41_Y} \\ F_{34_X} \\ F_{34_Y} \\ F_{23_X} \\ F_{23_Y} \\ M_{21} \end{bmatrix} = \begin{bmatrix} m_1 a_{G_{1_X}} \\ m_1 a_{G_{1_Y}} \\ I_{G_1}\dot{\omega}_1 \\ m_4 a_{G_{4_X}} - F_{hydro_X} \\ m_4 a_{G_{4_Y}} - F_{hydro_Y} \\ I_{G_4}\dot{\omega}_4 - M_{hydro} \\ m_3 a_{G_{3_X}} \\ m_3 a_{G_{3_Y}} \\ I_{G_3}\dot{\omega}_3 \end{bmatrix} \tag{2.11}$$

which are solved using matrix operations in MATLAB.

This matrix method of force analysis is extended to the five-bar linkages. Let link 5 be the link from the center of the offset disk to the connection point with the pitch link 3 on the offset disk edge. The length of link 5 is the radius of the offset disk. The sum of forces and moments in matrix form is now:

$$\begin{bmatrix} 1 & 0 & 1 & 0 & 0 & 0 & 0 & 0 & 0 & 0 & 0 & 0 \\ 0 & 1 & 0 & 1 & 0 & 0 & 0 & 0 & 0 & 0 & 0 & 0 \\ -R_{21_Y} & R_{21_X} & -R_{41_Y} & R_{41_X} & 0 & 0 & 0 & 0 & 0 & 0 & 1 & 0 \\ 0 & 0 & -1 & 0 & 1 & 0 & 0 & 0 & 0 & 0 & 0 & 0 \\ 0 & 0 & 0 & -1 & 0 & 1 & 0 & 0 & 0 & 0 & 0 & 0 \\ 0 & 0 & R_{14_Y} & -R_{14_X} & -R_{34_Y} & R_{34_X} & 0 & 0 & 0 & 0 & 0 & 0 \\ 0 & 0 & 0 & 0 & -1 & 0 & 1 & 0 & 0 & 0 & 0 & 0 \\ 0 & 0 & 0 & 0 & 0 & -1 & 0 & 1 & 0 & 0 & 0 & 0 \\ 0 & 0 & 0 & 0 & R_{43_Y} & -R_{43_X} & -R_{53_Y} & R_{53_X} & 0 & 0 & 0 & 0 \\ 0 & 0 & 0 & 0 & 0 & 0 & -1 & 0 & 1 & 0 & 0 & 0 \\ 0 & 0 & 0 & 0 & 0 & 0 & 0 & -1 & 0 & 1 & 0 & 0 \\ 0 & 0 & 0 & 0 & 0 & 0 & R_{35_Y} & -R_{35_X} & -R_{25_Y} & R_{25_X} & 0 & 1 \end{bmatrix} \begin{bmatrix} F_{21_X} \\ F_{21_Y} \\ F_{41_X} \\ F_{41_Y} \\ F_{34_X} \\ F_{34_Y} \\ F_{53_X} \\ F_{53_Y} \\ F_{25_X} \\ F_{25_Y} \\ M_{21} \\ M_{25} \end{bmatrix} \dots$$

$$= \begin{bmatrix} m_1 a_{G_{1_X}} \\ m_1 a_{G_{1_Y}} \\ I_{G_1}\dot{\omega}_1 \\ m_4 a_{G_{4_X}} - F_{hydro_X} \\ m_4 a_{G_{4_Y}} - F_{hydro_Y} \\ I_{G_4}\dot{\omega}_4 - M_{hydro} \\ m_3 a_{G_{3_X}} \\ m_3 a_{G_{3_Y}} \\ I_{G_3}\dot{\omega}_3 \\ m_5 a_{G_{5_X}} \\ m_5 a_{G_{5_Y}} \\ I_{G_5}\dot{\omega}_5 \end{bmatrix}. \tag{2.12}$$

Solving these systems of equations, the inertial loading on the disk and the torque generated on the main shaft from the offset point is determined. For the four-bar part of the mechanism, the torque is

$$q_{4bar} = L_2\sqrt{F_{23_X}^2 + F_{23_Y}^2} \tag{2.13}$$

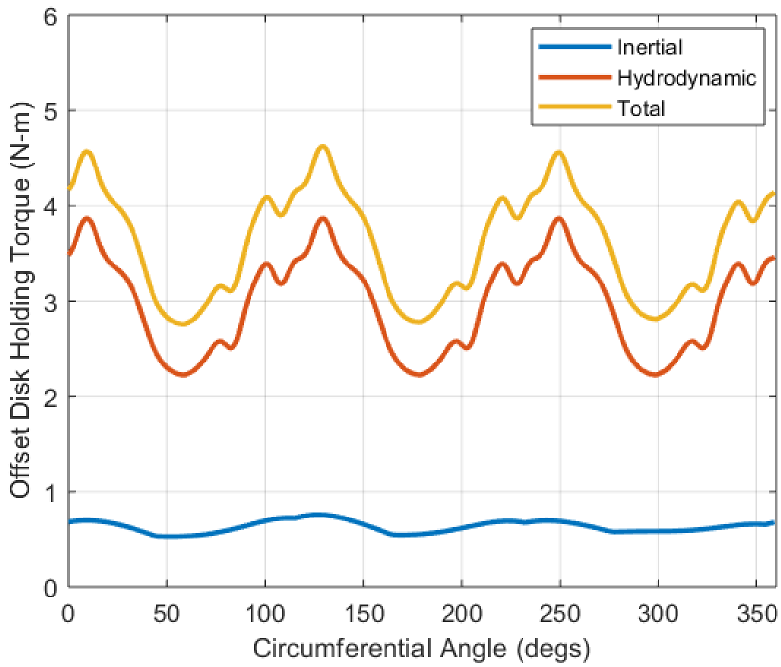

Figure 2.19. Holding torque required for RPD offset disk as a function of turbine circumferential angle. Hydrodynamic loads are obtained from CFD run at a tip speed ratio of 3, and an inflow velocity of 2.25 m/s.

while for the five-bar systems

$$q_{5bar} = L_2\sqrt{F_{25_X}^2 + F_{25_Y}^2} \tag{2.14}$$

where L_2 is the offset distance. Combining these results with two-dimensional CFD results of the hydrodynamic loads at a tip speed ratio of 3 and a velocity of 2.25 m/s, the total holding torque on the offset disk is found (see Fig 2.19). As shown, the hydrodynamic loads dominate the inertial loads and the maximum holding torque is 4.61 N-m.

The stepper motor available for the RPD testing is a Parker Compumotor 83-93 A-series motor. At the desired operating speed of 30 rad/s, the available torque is approximately 1.6 N-m [62]. Because this value is less than the torque necessary to hold the offset disk, a gearing system must be used with a gear ratio of at least 3:1. This gear train is shown in Fig. 2.17. For the RPD, a gear ratio of 12.5:1 is ultimately used.

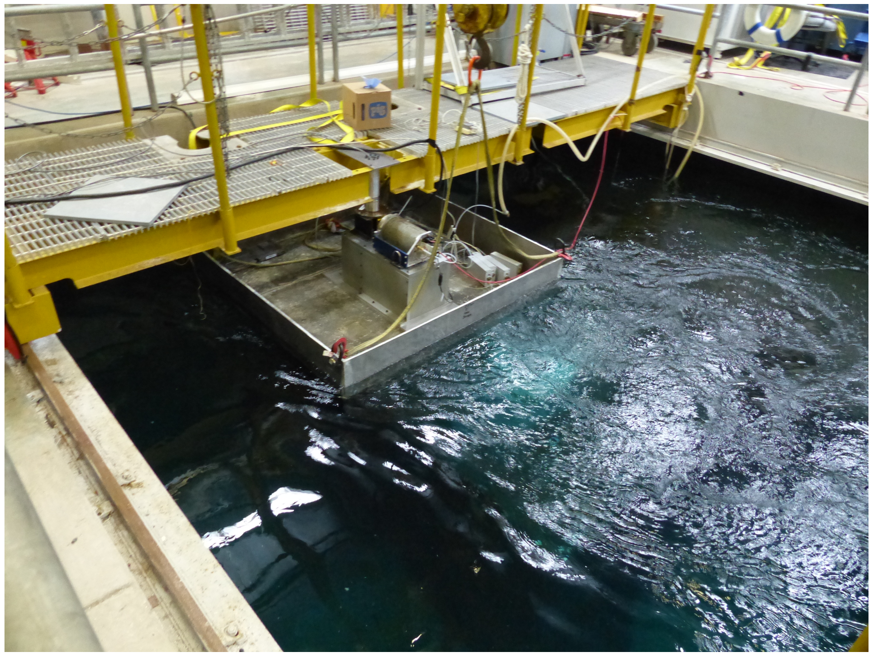

Figure 2.20. Rapid Prototype Device (RPD) in ARL Reverberant Tank test facility. The RPD is constrained to a tank platform to allow measurement of the integrated loads.

2.4.3 Experimental Setup for RPD

The RPD is tested in the Applied Research Laboratory (ARL) Reverberant Tank (see Fig. 2.20) since the facility provides the underwater volume needed to submerge the turbine and is a useful facility for measuring the turbine acoustics. The tank is 8.71 m long, 6.91 m wide, and 5.40 m deep. Because the tank contains a box in one corner, the net fluid volume of the tank is reduced to 298 m^3. The tank has two movable platforms that span the width of the tank. The single turbine of the RPD always generates a torque and must be constrained from turning itself, thus the RPD is fixed to one of tank platforms. Constraining the RPD provides the ability to measure the integrated loads using an existing six degree-of-freedom load cell.

The RPD is assembled in air. This allows easy access to insert the shaft and place the supports and foils. With the motor and gearbox disconnected, the mechanism is exercised by hand to ascertain any binding. Two different offset disks are used that provide a maximum foil pitching amplitude of 9° for power generation mode, and 30° for propulsion mode. Measurements are taken both for a bare shaft, and for the turbine isolated beneath the barge.

The RPD loads are obtained with the test setup shown schematically in Fig.

2.21. The turbine motor, 90° gearbox, stepper motor, and load cell are located inside the barge above the water (see Fig. 2.22). While ideally the whole system should be submerged, waterproof motors could not be acquired for this test.

Turbine phase angle commands are provided to a Parker Compumotor Microstep A-series Drive whose output drives the Parker Compumotor 83-93 A-series stepper motor. An AMTI six degree-of-freedom load cell (Model SP4D-4K-7390), through an AMTI MSA-6 Mini Amplifier, records the loads generated by the RPD at a rate of 2048 Hz with a National Instruments (NI) 9205 card, housed in a NI cDAQ-9188 chassis, and stored on a computer. The chassis is grounded to the RPD. Non-linearity and hysteresis of the load cell is less than 0.3% and crosstalk is less than 2%.

The main motor's encoder data is recorded at a rate of 2048 Hz with an NI 9411 card, also housed in the NI cDAQ-9188 chassis. The main motor that drives the RPD turbine is a 15kW induction motor. An ABB inverter converts the alternating current from a power outlet to direct current, to power the main motor. The 350 volt motor is oriented horizontally and operates at a lower torque and higher speed than is required for the RPD. A right-angled 10:1 gearbox lowers the RPM and increases the torque to the vertically oriented turbine shaft. Double roller bearings provide a clamped end condition for the shaft in the center of the barge. The solid shaft diameter of 50 mm is designed to limit shaft deflection to less than 10 mm when the turbine operates at maximum thrust.

Additionally, a PCB Model 105C02 accelerometer is placed on the bridge next to the RPD to quantify any bridge vibrations that could contaminate the load cell measurements. The accelerometer data is recorded at a rate of 2048 Hz with an NI 9237 card, housed in an NI cDAQ-9188 chassis, and stored on a computer. Figure 2.23 demonstrates the differences in the accelerometer data at a higher RPM before and after the platform is stiffened with I-beams and end clamps. The data additionally shows that the bridge vibrations are independent of the thrust forces produced by pitching foils.

Five Reson TC 4032 hydrophones are used to quantify the radiated sound power from the RPD. The data from the hydrophones is recorded at a rate of 204.8 kHz with an NI 4496 card, housed in an NI PXI-1031 chassis, and stored on a computed. The signal from the hydrophones is conditioned with a Reson EC6073 signal conditioner, powered by a Reson EC 6068 battery. Conlon et al. describes

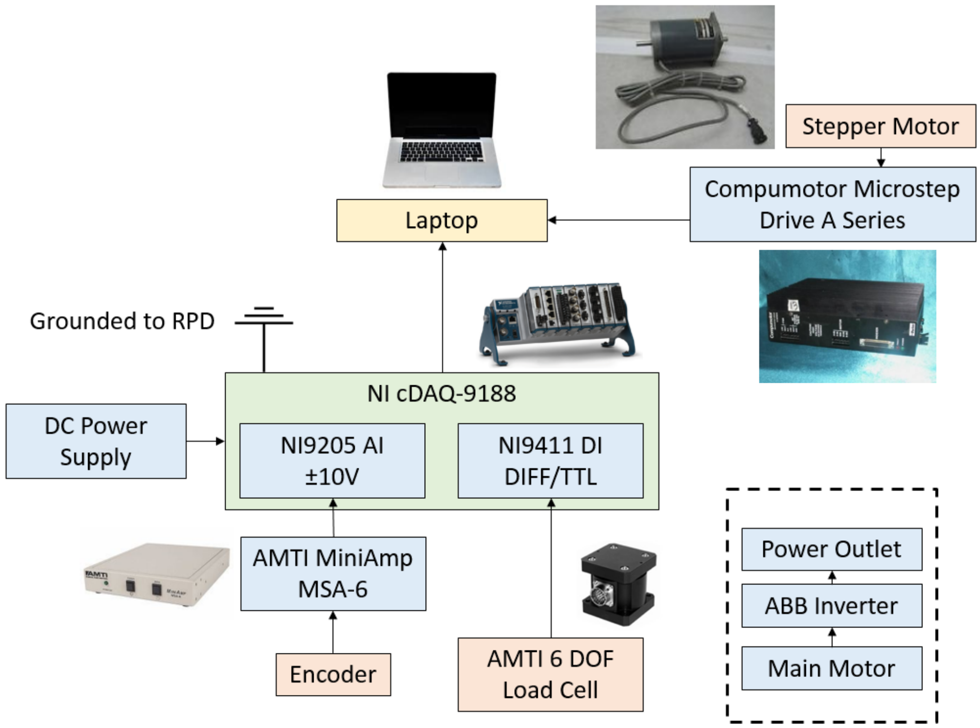

Figure 2.21. Experimental setup for Rapid Prototype Device (RPD).

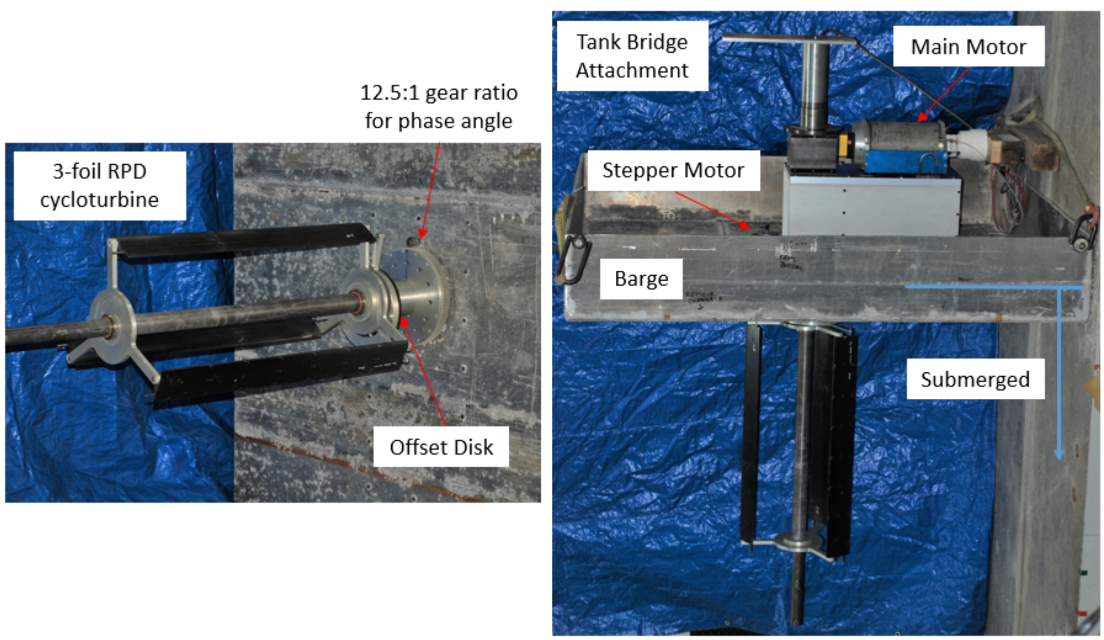

Figure 2.22. RPD prior to submersion in ARL Reverberant Tank test facility. Left: Cycloturbine with mechanical foil pitching mechanism comprising an offset disk. A 12.5:1 gear train is used for torque reduction. Right: The turbine motor, gearbox, stepper motor, and load cell are located inside the barge above the water.

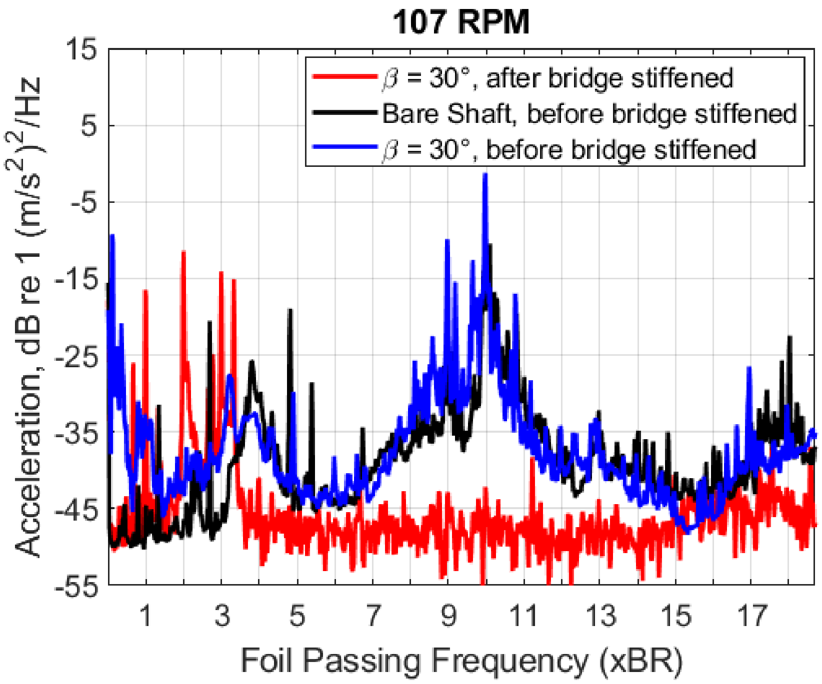

Figure 2.23. Acceleration vs. foil passing frequency at 107 RPM. Stiffening the Reverberant Tank platform reduces vibration effects.

Table 2.5. Tank locations for hydrophones used in reverberant power calculations are all referenced. The origin is the northeast bottom of the tank.

Hydrophone	X (mm)	Y (mm)	Z (mm)
1	51	3610	2740
2	1370	1960	3660
3	2690	305	4570
4	5330	1960	3660
5	4010	5260	2740

the reverberant tank and its acoustic properties and determines a set of optimum hydrophone positions for reverberation measurements [63]. The locations shown in Tab. 2.5 are chosen to provide a mean sound energy level and standard deviation similar to that of a larger set of hydrophones.

As many of the bearings need water for lubrication, testing with the motor and gearbox is done in the water tank. The RPD is run at 6 different rotation rates: 22, 43, 65, 86, 107, and 129 RPM. These rates correspond to 10%, 20%, 30%, 40%, 50%, and 60% of the rated flow velocity of 2.25 m/s, at a high tip speed ratio. Higher RPMs are not acquired because of large bridge vibrations. Refer to

Table 2.6. Subscale Demonstrator turbine properties.

Turbine Property	**Value**
Foil Span	900 mm
Foil Chord	95 mm
Foil Number	3
Foil Profile	NACA 0018
Turbine Diameter	450 mm
Turbine Offset Distance (d_x, d_y, d_z)	(0,1428,386) mm

Appendix A for the RPD test matrices.

Each data point is taken for 30 seconds to obtain good average values. The motor is stopped and the water in the tank is allowed to settle between runs. The load cell is also re-zeroed between runs.

2.5 Design of a Subscale Demonstrator (SSD)

A 1/5.56 scale vehicle called the Subscale Demonstrator (SSD) is designed and built. It consists of four crossflow turbines. The SSD has a span, length, and height of 3960 mm, 1061 mm, and 1464 mm, respectively and is shown in Fig. 2.24. It is designed to generate power with a nominal current of 2 m/s. The turbine characteristics are the same as those for the RPD (see Tab. 2.6). The turbine offset distance magnitude from the center of the vehicle is also provided in Tab. 2.6.

The Ocean Renewable Power Company worked jointly with the Penn State Applied Research Laboratory to design the structure of the vehicle and modify the thrust vectoring mechanism from the RPD. The outer nacelles and central frame supply rigidity for the structure. Additionally, ducted turbines provide an increase in power generation by modifying flow conditions into the rotor [64, 65]. CFD parametric studies of the nacelle and center structure design (both shape and vertical separation distance) is performed by R. Medvitz at the Applied Research Laboratory.

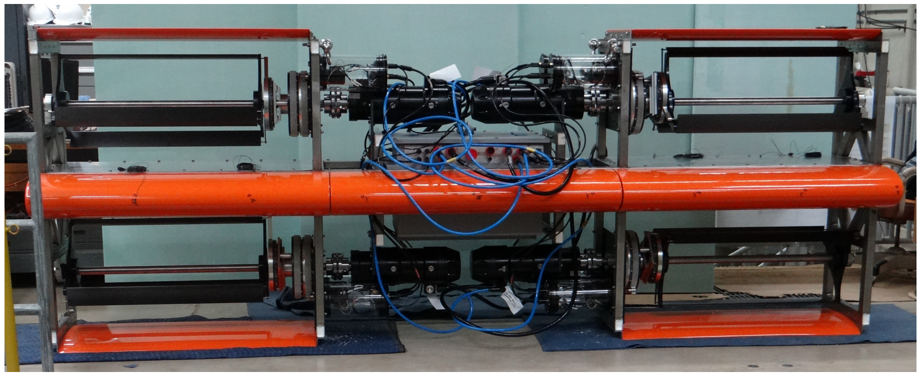

Figure 2.24. Subscale Demonstrator (SSD)

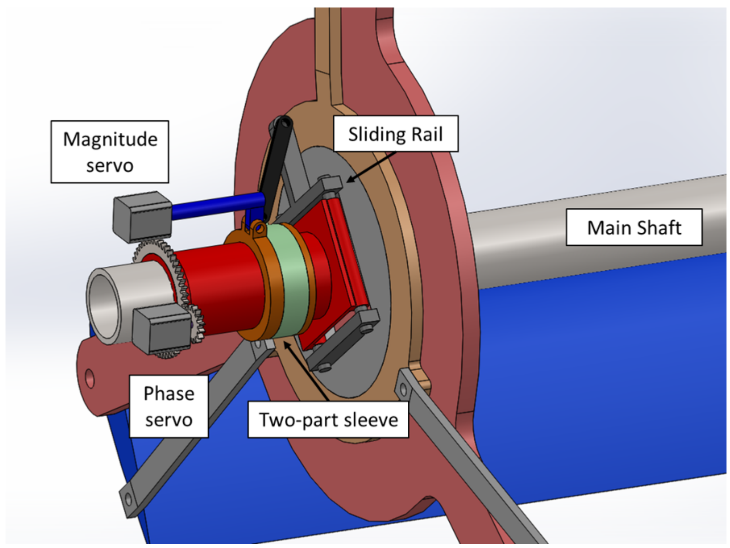

Figure 2.25. Option for amplitude and phase control mechanism based on design from National University of Singapore.

2.5.1 Design of SSD Thrust Vectoring Mechanism

While different offset disks are used for the RPD (see Section 2.4.1), the full scale vehicle must have the capability to change the maximum foil pitching angle built into the mechanism. Hu et al. [66] developed a control mechanism that consists of two rotary servos that separately control the direction and magnitude of the thrust vector from the pitching foils. An example of this mechanism is shown in Fig. 2.25. The servo that controls the magnitude of the thrust vector incorporates a sliding rail and a two-part sleeve.

Due to space constraints, a different design is used for the MHK vehicle in this

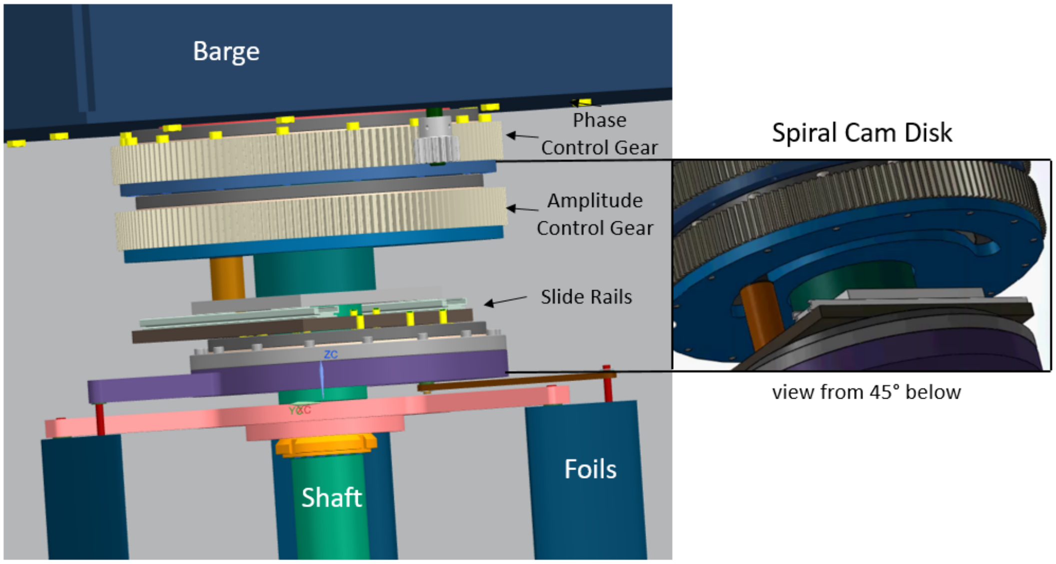

Figure 2.26. Amplitude and phase control mechanism

dissertation to control the magnitude of the thrust vector, albeit inspired by the University of Singapore. The mechanism uses a sliding rail and a slotted spiral cam disk developed by N. Hayes at ORPC (see Fig. 2.26). This disk is attached to a gear train like the one used for the phase control in the RPD. A separate stepper motor is used to control the twist of this gear. Figure 2.27 shows the comparison between the foil pitching mechanism used for the RPD and for the SSD.

2.5.2 SSD Moments of Inertia

The SSD weight and moments of inertia are necessary parameters for simulation and control of the vehicle. The SSD is weighed in-air before Reverberant Tank testing. At this stage, the SSD is fully assembled, with the exception of two syntactic foam blocks that are to be sandwiched between the upper and lower turbines, inside the central frame. The measured weight in-air is 1225 kg (2700 lbs). The wet weight of the vehicle is 272 kg (600 lbs). If the foam blocks are added to the vehicle, there is a predicted added buoyancy of 158 kg (350 lbs). In order for the vehicle to be neutrally buoyant, additional ballasts would be needed.

It is also validated that the center of buoyancy is above the center of mass from submerging the vehicle in the Reverberant Tank: the vehicle has no tendency to pitch about the y-axis.

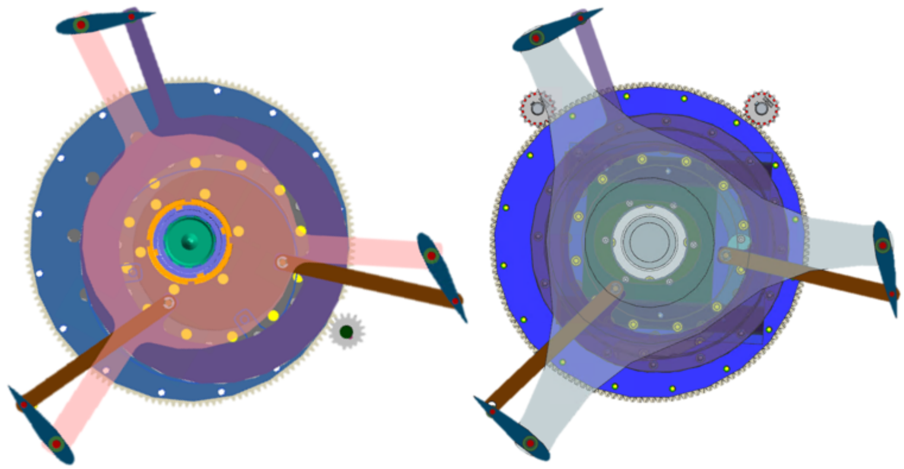

Figure 2.27. Comparison of foil pitching mechanism between the RPD (left) and the SSD (right). The foil pitching mechanism on the SSD allows for variation of the maximum pitching angle in addition to the phase angle. The view shown here is oriented looking down the turbine shaft. The 1/4 chord linkage of both mechanisms is shown as translucent to highlight the differences between the four-bar linkages and the five-bar linkages.

The moments of inertia of the vehicle are estimated from the Computer Aided Design (CAD) model and via inertia swing tests. These tests are carried out to estimate pitch (I_{YY}), roll (I_{XX}) and yaw (I_{ZZ}) moments of inertia. The product of inertia I_{XZ} is assumed to be small due to the symmetry of the vehicle. The predicted moments of inertia from the CAD model are $I_{XX} = 1294$ kg·m^2, $I_{YY} = 186.4$ kg·m^2, and $I_{ZZ} = 1191$ kg·m^2.

A swing test is performed by suspending the SSD from a crane and swinging it about its X- and Y- axes like a simple pendulum (see Fig. 2.28). If two cranes are used to create a torsional pendulum, the moment of inertia about the Z-axis could be obtained. However, two cranes of appropriate height could not be obtained in the testing facility. The moment of inertia about the Z-axis is therefore predicted using the measured moment of inertia about the X-axis, and the predicted moments of inertia about the X- and Z-axes from the CAD model: $I_{ZZ,pred.} = I_{XX,meas.}(I_{ZZ,cad}/I_{XX,cad})$.

To calculate the mass moment about the centroid of the vehicle, the moments about the pivot point are summed:

$$(I_G + ml^2)\ddot{\phi} + mgl\sin(\phi) = 0 \tag{2.15}$$

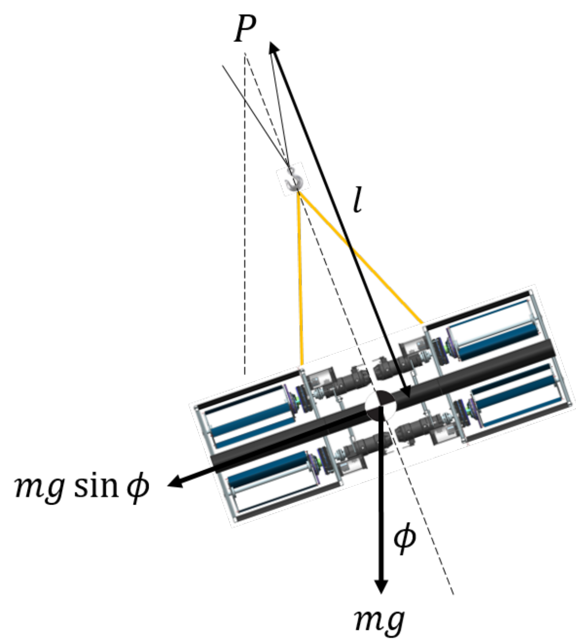

Figure 2.28. Measuring SSD mass moment of inertia as a simple pendulum. Note dimensions and angles are not to scale.

Table 2.7. SSD inertia testing data

Moment of Inertia Measured	Time for 5 Osc (s)	τ (s)
I_{XX}	16.95	3.390
I_{XX}	16.81	3.362
I_{XX}	16.48	3.296
I_{YY}	14.36	2.872
I_{YY}	14.74	2.948
I_{YY}	14.42	2.884

where for small angles $\phi < 20°$, $\sin(\phi) \approx \phi$. If we assume that $\phi = \phi_{MAX}\cos(2\pi f t)$ and thus $\ddot{\phi} = -4\pi^2 f^2 \phi_{MAX}(2\pi f t)$, then this equation can be reduced and rearranged to solve for the mass moment of inertia:

$$I_G = \frac{mgl\tau^2}{4\pi^2} - ml^2 \tag{2.16}$$

where $\tau = 1/f$ or the time period for one oscillation. The time period for one oscillation is found by recording the time for the SSD to oscillate as a result of a small push (see Table 2.7). The distance from the pivot point to the center of gravity is measured from the crane hub, where the rocking is observed to occur.

Table 2.8. Subscale Demonstrator vehicle properties.

Vehicle Property	**Value**
Total Mass	1225 kg
Total Volume	0.93 m^3
Span, width, height	3960, 1061, 1464 mm
Center of gravity (estimated)	0, 0, 20 mm
Center of buoyancy (estimated)	0, 0, 0 mm
Pitching moment of inertia I_{YY}	153.5 kg·m^2
Rolling moment of inertia I_{XX}	1884 kg·m^2
Yawing moment of inertia I_{ZZ}	1734 kg·m^2
Product of inertia I_{XZ} (estimated)	0

The final estimated values along with total mass and location of center of gravity are reported in Tab. 2.8. The center of gravity and center of buoyancy are estimated using the CAD model. The pitching moment of inertia determined experimentally is lower than predicted by the CAD model (153.5 kg·m^2 versus 186.4 kg·m^2), the rolling moment of inertia determined experimentally is higher than predicted by the CAD model (1884 kg·m^2 versus 1294 kg·m^2) and the yawing moment of inertia determined experimentally is higher than predicted by the CAD model (1734 kg·m^2 versus 1191 kg·m^2).

2.5.3 Experimental Setup for SSD

The SSD is tested in the ARL Reverberant Tank (see Fig. 2.29). The tank has two movable platforms that span the width of the tank. The SSD is fixed to a steel support frame that is clamped to the platforms. The platforms are additionally clamped to the side rails of the tank to reduce vibrations. Constraining the SSD provides the ability to measure the integrated loads; a dynamometry system with six strain load cells is used to measure the forces and moments produced from the vehicle (see Fig. 2.30). The SSD forces are determined from the sum of forces using the geometry and numbering from Fig. 2.30:

$$\begin{aligned} F_X &= (F_1 + F_4)\sin\theta_{dyno,X} \\ F_Y &= -F_6 \sin\theta_{dyno,Y} \\ F_Z &= -(F_2 + F_3 + F_5 + (F_1 + F_4)\cos\theta_{dyno,X} + F_6\cos\theta_{dyno,Y}) \end{aligned} \tag{2.17}$$

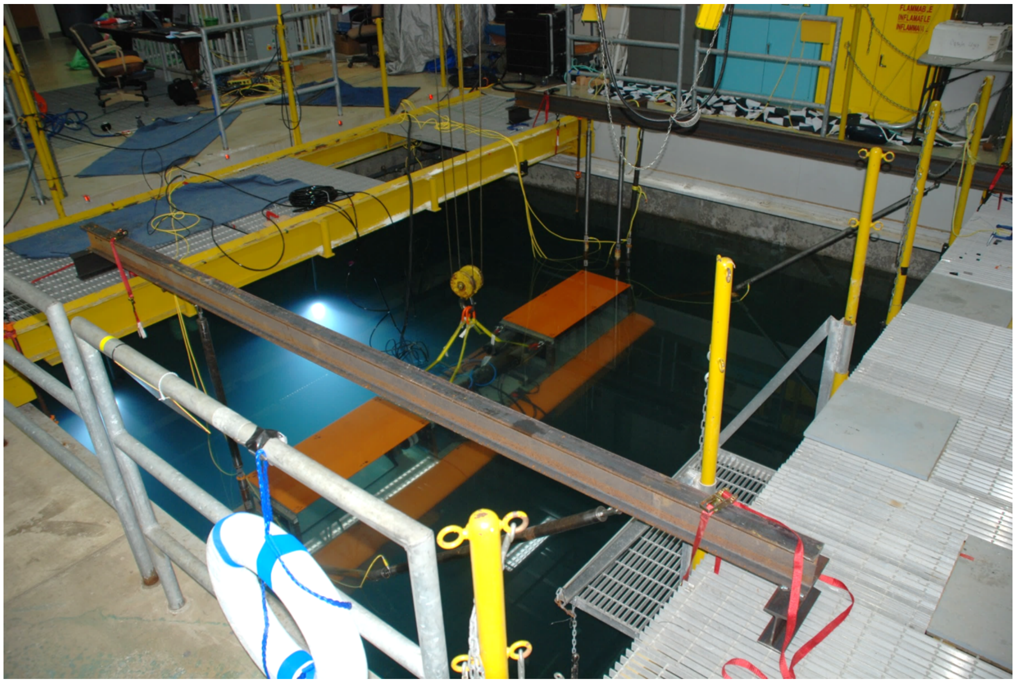

Figure 2.29. SSD in ARL Reverberant Tank test facility. The SSD is fixed to a steel support frame that is clamped to the tank platforms.

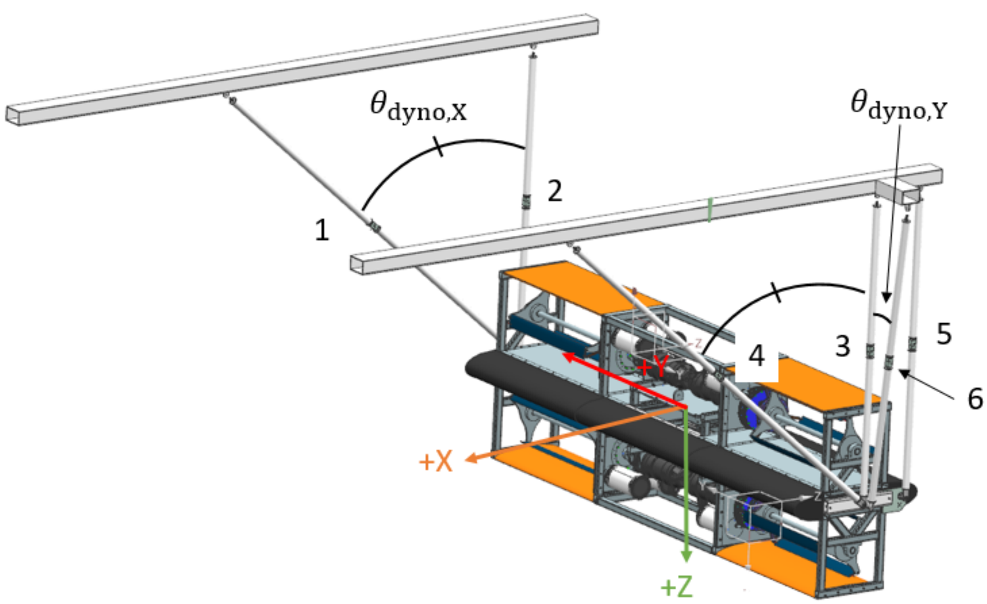

Figure 2.30. SSD Dynamometry System. Six strain load cells are used to measure the forces and moments produced from the vehicle.

Table 2.9. Subscale Demonstrator dynamometry moment distances.

Distance	Value (m)
$d_{dyno,1Y}$	2.074
$d_{dyno,4Y}$	2.074
$d_{dyno,5X}$	0.365
$d_{dyno,1Z}$	2.074
$d_{dyno,2Z}$	2.074
$d_{dyno,3Z}$	2.074
$d_{dyno,4Z}$	2.074
$d_{dyno,5Z}$	2.074
$d_{dyno,6Z}$	2.074

where $\theta_{dyno,X} = 49.6°$ and $\theta_{dyno,Y} = 9.2°$. For this summation, the force vectors originate at the SSD and are directed along the load cell linkages towards the dynamometry frame. The origin of the coordinate system is centered on the SSD. The moments are determined from

$$\begin{aligned}
M_X &= F_4 d_{dyno,4Z} \cos\theta_{dyno,X} + F_6 d_{dyno,6Z} \cos\theta_{dyno,Y} + F_5 d_{dyno,5Z} + \dots \\
&\quad F_3 d_{dyno,3Z} - F_2 d_{dyno,2Z} - F_1 d_{dyno,1Z} \cos\theta_{dyno,X} \\
M_Y &= -F_5 d_{dyno,5X} \\
M_Z &= F_4 d_{dyno,4Y} \sin\theta_{dyno,X} - F_1 d_{dyno,1Y} \sin\theta_{dyno,X}
\end{aligned} \tag{2.18}$$

where the distances to the forces in X, Y, and Z are listed in Tab. 2.9.

Figure 2.31 shows the experimental setup for the SSD testing. The electronics enclosure on the vehicle is supplied with 480V of power, and 41.4 kPa (6 psi) of model pressure to prevent leaks. The electronics enclosure contains four Advanced Motion Inverters for the four turbine motors, and two power supplies for the four main motors and eight stepper motors. The forces and moments produced by the SSD are measured with a dynamometry system that contains six HRS-3K load cells. The loads are recorded at a rate of 2048 Hz with a National Instruments (NI) 9237 card, housed in an NI cDAQ-9188 chassis, and stored on a computer. In addition to load cell measurements, three accelerometers are placed on the two bridges to quantify any bridge vibrations that could contaminate the load cell measurements. The accelerations are recorded at a rate of 2048 Hz with an NI 9237 card, also housed in the NI cDAQ-9188 chassis. The chassis is grounded to the steel frame.

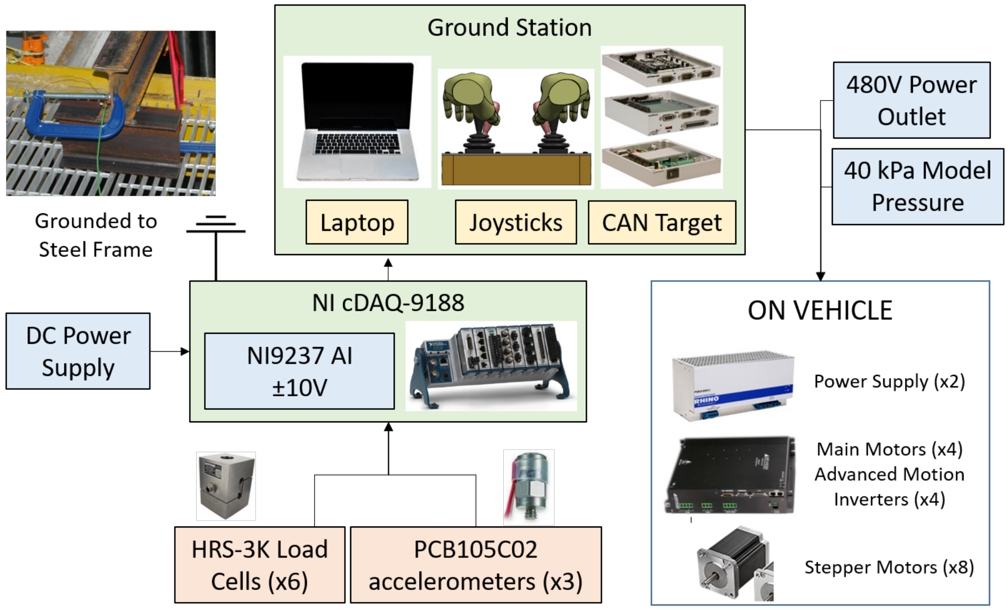

Figure 2.31. Experimental setup for SSD.

In addition to these measurements, stepper motor angle and main motor shaft rate are recorded with a Controller Area Network (CAN) bus target. The CAN Target PC is located off-vehicle at the ground station. This is done so that quick changes to the control code can be made without retrieving the vehicle. The final vehicle is designed to have the CAN Target on-board.

The SSD is assembled in air. With the motors running at a low RPM, the thrust vectoring mechanism is exercised by the stepper motors to ascertain any binding. Because many of the bearings need water for lubrication, testing at higher RPMs with the main motors is done in the water tank.

The test matrices for the SSD steady state load testing are documented in Tabs. A.4 and A.5. The test matrix for the bare shaft testing is also documented in Appendix A. Sixty seconds of data is taken at each test condition. The motors are stopped and the water in the tank is allowed to settle between runs. The load cells are also re-zeroed between runs.

Only three turbines are used for SSD testing, since only three of the four main motors are functional; the bottom port turbine is not operational. The main motors are waterproof three phase AC electric motors manufactured by IKM. Slip is an important consideration for these motors: slip occurs when there difference between the synchronous speed and the speed of the rotor magnetic field. According to the

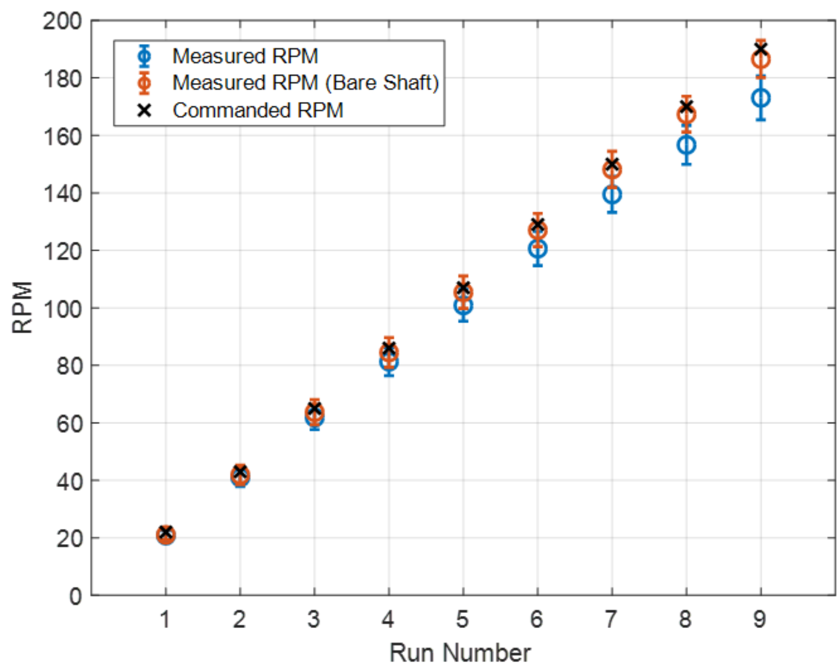

Figure 2.32. Comparison between commanded and measured RPM for the top port turbine of the SSD, at a maximum foil pitching angle of 30°. There is less slip with the bare shaft due to the decreased forces and torque. There is a greater effect of slip at higher RPMs.

motor specification sheet, at a supply frequency of 60 Hz the rated speed is 1700 RPM. For these 4 pole motors, this results in a slip of approximately 5%. Slip is a key factor, as the greater the load or torque, the greater the slip. This is reflected in the acquired data. There is a difference between the commanded RPM and the measured RPM due to slip in the induction motors. This difference is more sizable with the foils on than with the bare shaft, and has a greater effect at higher RPMs (see Fig. 2.32 and corresponding Tab. 2.10). The data shown in the figure and tabulated is for the top port turbine thrusting forward at a maximum pitching angle of 30 degrees.

In addition to motor slip, it is also observed that there is RPM drift over the longer runs. Figure 2.33 shows this drift over 500 seconds. In this figure, the motor feedback RPM is in black. A 5 second moving average filter is applied and the result is shown in red. The RPM is observed to drift up by approximately 2 RPM over the course of this example test. This drift is probably caused by turbulence in the tank.

Table 2.10. SSD commanded RPM vs. measured RPM

Run	Commanded RPM	Measured RPM Mean ± Std. Dev.	Measured RPM (Bare Shaft) Mean ± Std. Dev.
1	22	20.8 ± 1.7	21.0 ± 1.8
2	43	41.0 ± 3.2	41.9 ± 3.3
3	65	61.8 ± 4.2	63.7 ± 4.4
4	86	81.3 ± 4.9	84.5 ± 5.2
5	107	100.9 ± 5.5	105.4 ± 5.7
6	129	120.6 ± 5.9	127.1 ± 5.8
7	150	139.5 ± 6.3	148.2 ± 6.3
8	170	156.7 ± 6.8	167.4 ± 6.2
9	190	173.1 ± 7.6	186.6 ± 6.5

2.6 Concluding Remarks

The results of the qualitative analysis done in Section 2.3 are summarized in Tables 2.2 and 2.3. Table 2.2 summarizes the control authority for each option investigated, while Table 2.3 evaluates the pitch control benefits or disadvantages of each design. From Table 2.3, we find that a four-turbine configuration is most beneficial for this project, despite the high cost. The pitch axis is controlled in forward flight, hover, and reverse flight, and there is an added benefit in power generation from this method.

A 1/5.56 scale single turbine Rapid Prototype Device (RPD) and Subscale Demonstrator (SSD) are designed and built for experimental testing. A thrust vectoring mechanism is designed to control the propulsive forces from the vehicle turbines. The experimental setup and test matrices are discussed.

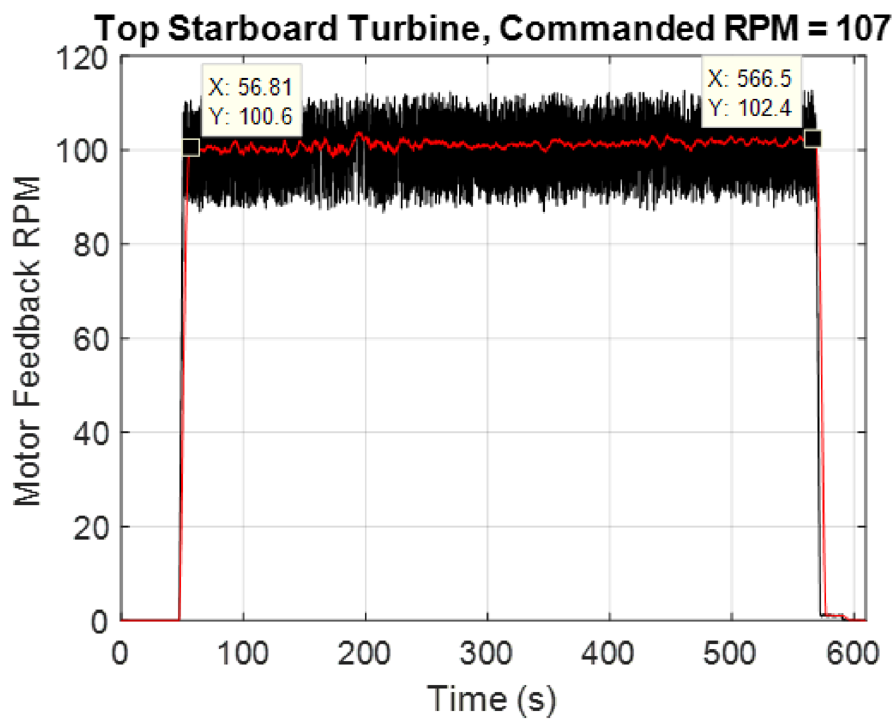

Figure 2.33. Observed drift in RPM for SSD top starboard turbine motor. The RPM drifts up by approximately 2 RPM over the 500 second run. This drift is probably caused by turbulence in the tank.

3 Modeling of the Marine Hydrokinetic Cycloturbine Vehicle Dynamics [1]

3.1 Overview

A detailed turbine simulation model is necessary to understand the MHK vehicle dynamics and assist in the design of the vehicle controllers. The simulation model solves the six degree-of-freedom rigid body equations of motion for the maneuvering MHK system subject to the hydrodynamic drag forces, hydrostatic forces, and the propulsive forces from the turbines (see Fig. 3.1). The model uses a simplified hydrodynamic analysis of the propulsive forces generated by the cycloturbines, as a function of the foil pitch schedule and vehicle state. The turbine propulsive forces and moments are calculated as the time-averaged foil forces over one turbine revolution using an azimuthally averaged blade element approach. The fundamental approach is derived from simulations used to model trochoidal propellers [17, 36]. The turbine force model is tuned to two-dimensional and three-dimensional computational fluid dynamics (CFD) and experimental single turbine Rapid Prototype Device (RPD) data.

3.2 Rigid Body Equations of Motion

A nonlinear dynamics model for simulation and analysis is developed by combining hydrodynamic force and moment models with flat-earth vector equations of motion

[1] The work presented in this chapter is accepted for publication by the IEEE Journal of Oceanic Engineering.

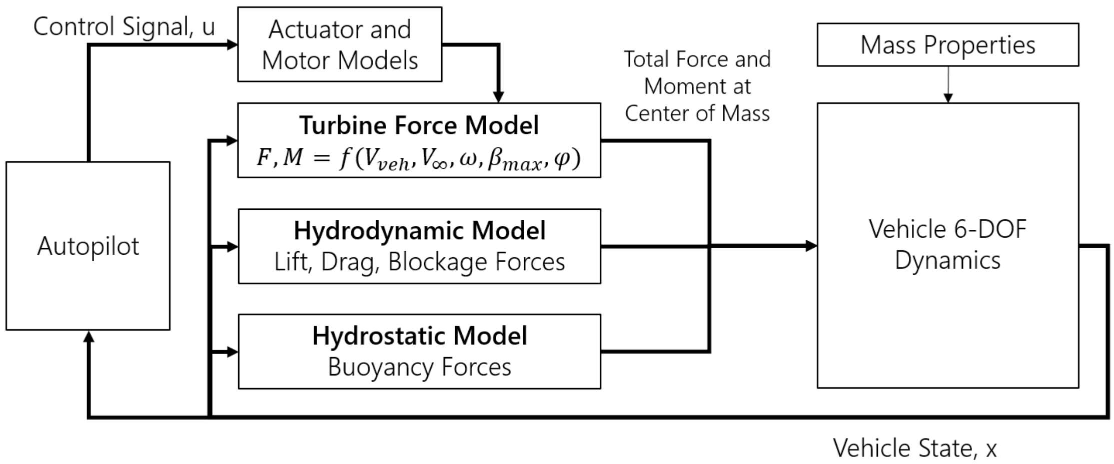

Figure 3.1. Flowchart of turbine dynamics simulation model. The simulation model solves the six degree-of-freedom rigid body equations of motion for the maneuvering MHK system subject to the hydrodynamic drag forces, hydrostatic forces, and the propulsive forces from the turbines.

for a rigid body in six degrees-of-freedom. The system is described in state-space form by

$$\begin{aligned} \dot{\vec{x}} &= f(\vec{x}, \vec{u}) \\ \vec{y} &= h(\vec{x}) \end{aligned} \tag{3.1}$$

with state $x(t)$, control input $u(t)$, and output $y(t)$. The output equation relates the states to physically measurable quantities. The components of this equation are defined more explicitly as [40] [2]

[2]Note: $c\phi$,$c\theta$,$c\psi$, $s\phi$, $s\theta$, $s\psi$, and $t\theta$ represent $\cos\phi$,$\cos\theta$, $\cos\psi$,$\sin\phi$,$\sin\theta$, $\sin\psi$ and $\tan\theta$, respectively.

$$
\begin{aligned}
\dot{\vec{x}} &= [\dot{p_N}, \dot{p_E}, \dot{p_D}, \dot{\phi}, \dot{\theta}, \dot{\psi}, \dot{U}, \dot{V}, \dot{W}, \dot{P}, \dot{Q}, \dot{R}]^T \\
f(\vec{x}, \vec{u}) &= \begin{bmatrix}
Uc\theta c\psi + V(s\phi s\theta c\psi - c\phi s\psi) + W(s\phi s\psi + c\phi s\theta c\psi) \\
Uc\theta s\psi + V(c\phi c\psi + s\phi s\theta s\psi) + W(c\phi s\theta s\psi - s\phi c\psi) \\
Us\theta - Vs\phi c\theta - Wc\phi c\theta \\
P + Qs\phi t\theta + Rc\phi t\theta \\
Qc\phi - Rs\phi \\
Qs\phi \sec\theta + Rc\phi \sec\theta \\
RV - QW - gs\theta + \frac{X}{\mathrm{m}} \\
-RU + PW + gs\phi c\theta + \frac{Y}{\mathrm{m}} \\
QU - PV + gc\phi c\theta + \frac{Z}{\mathrm{m}} \\
\frac{I_{XZ}(I_X - I_Y + I_Z)PQ - [I_Z(I_Z - I_Y) + I_{XZ}^2]QR + KI_Z + NI_{XZ}}{I_X I_Z - I_{XZ}^2} \\
\frac{(I_Z - I_X)PR - I_{XZ}(P^2 - R^2) + M}{I_Y} \\
\frac{-I_{XZ}(I_X - I_Y + I_Z)QR + [I_X(I_X - I_Y) + I_{XZ}^2]PQ + KI_{XZ} + NI_X}{I_X I_Z - I_{XZ}^2}
\end{bmatrix} \\
\vec{y} &= [h(U, W, P, Q, R)]^T
\end{aligned}
\tag{3.2}
$$

where X, Y, and Z are the longitudinal, lateral, and heave forces produced on the vehicle, while K, M, and N are the roll, pitch, and yaw moments produced on the vehicle, respectively. These forces and moments are themselves nonlinear functions of the vehicle states and controls. The vehicle states are defined as

$$\vec{x} = [p_N, p_E, p_D, \phi, \theta, \psi, U, V, W, P, Q, R]^T \tag{3.3}$$

where the vehicle position is described in North-East-Down (NED) coordinates by p_N, p_E, p_D and the attitude is described by the Euler angles for roll, pitch, and yaw– ϕ, θ, and ψ, respectively. The longitudinal, lateral, and heave velocity states are given by U, V, and W, and the roll, pitch, and yaw attitude rates are given by P, Q, and R. Refer to Fig. 3.2 for system orientation and definition.

The output equation relates the states to physically measurable quantities. In the context of NDI control design, the output vector, $y(t)$, is the vector of controlled variables that we want to follow a reference command. In this particular application, the controlled variables are:

$$\vec{y} = [U, \dot{Z}, \dot{\phi}, \dot{\theta}, \dot{\psi}] \tag{3.4}$$

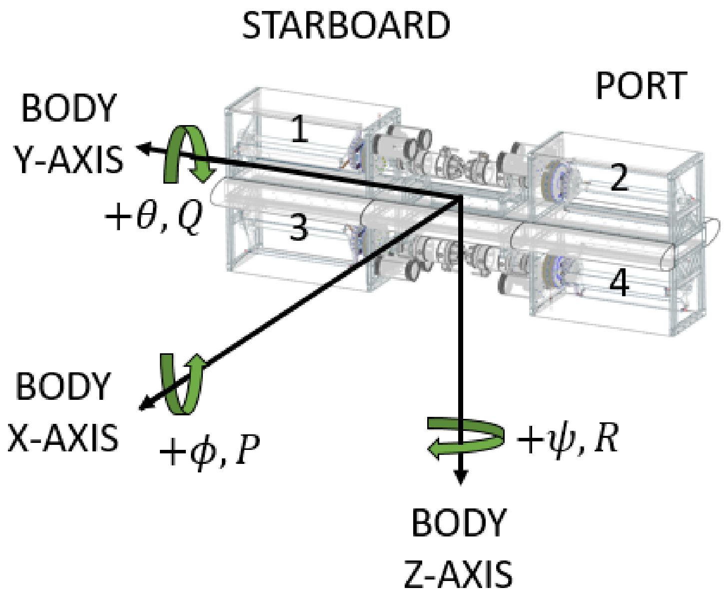

Figure 3.2. Definition of body axes and states. The upper turbines rotate counter to the lower turbines. The turbines are assigned numbers 1-4 for reference.

Note that these controlled variables linearize to a subset of the vehicle state:

$$\vec{y} \approx [U, W, P, Q, R]. \tag{3.5}$$

3.3 Hydrodynamic Model

The hydrodynamic model calculates the lift and drag for each vehicle component using the local velocity at each component. The local velocity is used to determine the angle-of-attack of each component.

Two-dimensional CFD analysis shows that the nacelles and center structure produce a lifting force at positive angles-of-attack. The lift from CFD is non-dimensionalized using dynamic pressure and planform area to determine the 2D coefficient of lift

$$C_{L,2D} = \frac{L}{\frac{1}{2}\rho V_{ref}^2 S} \tag{3.6}$$

where the reference velocity V_{ref} is 2.25 m/s, and S is the planform area of the vehicle component (4.20 m^2 for the center nacelle and 0.67 m^2 for each of the four outer nacelles). Plotting the coefficient of lift versus the angle-of-attack provides the 2D lift-curve slope. For the entire system, this lift-curve slope is 5.36 1/rad. As reference, thin airfoil theory states that the 2D lift-curve slope for a thin airfoil is 6.28 1/rad. Clearly, the nacelles and center structure provide a good amount of lift.

The 2D lift-curve slope is corrected for 3D finite span effects [67]

$$a_{3D} = \frac{a_{2D}}{1 + \frac{a_{2D}}{\pi e AR}} \tag{3.7}$$

using the aspect ratio of each vehicle component (3.74 for the center nacelle and 2.13 for each of the four outer nacelles) and an assumed Oswald efficiency factor of 0.8. The 3D lift-curve slope is then 3.40 1/rad for the center nacelle and 2.671/rad for each of the four outer nacelles. The 3D lift-curve slope is used to calculate the coefficient of lift, which is in turn used to calculate the lift force acting at the aerodynamic center of the vehicle. The aerodynamic center is assumed to act at the quarter-chord of the center structure.

The induced drag is also accounted for by this model. The coefficient of induced drag is found using

$$C_{Di,3D} = \frac{C_{L,3D}^2}{\pi e AR}. \tag{3.8}$$

where $C_{L,3D}$ is the coefficient of lift corrected for 3D finite span effects (determined from the 3D lift-curve slope). The aspect ratios for each vehicle component and the assumed Oswald efficiency factor are listed above.

The induced drag is added to the form drag to produce the total drag of the vehicle. The form drag force for each component is calculated using

$$D = \frac{1}{2}\rho V^2 A C_D \tag{3.9}$$

where A is the drag area and V is the local relative velocity. The drag area is a sinusoidal function of angle-of-attack:

$$A = A_{front}\cos(\alpha) + A_{top}\sin(\alpha). \tag{3.10}$$

The form drag forces included in the model are for the upper and lower nacelles, the turbine shafts, the main motors, and the center structure. The coefficient of drag is assumed to be 1 for the turbine shafts and main motors due to their cylindrical shape, while a drag coefficient of 1.06 [68] is assumed for the center structure and the nacelles, due to their cross section being closer to a discus.

3.4 Hydrostatic Model

The buoyancy of the vehicle is simply calculated using the density of the water, gravitational acceleration, and the volume of the vehicle: $F_B = -\rho g V$. The volume of the Subscale Demonstrator (SSD) is listed in Tab 2.8, which results in an upward buoyancy force of 9119 N. This buoyancy force acts at a center of buoyancy which is above the center of gravity, due to the distribution of the electronics in the central enclosure. The center of gravity of the vehicle is estimated from a computer-aided design (CAD) model, while the center of buoyany is assumed to be at the center of the vehicle due to symmetry. The current model lists the center of buoyancy as 20 mm above the center of gravity. A vertical offset of the center of buoyancy above the center of gravity provides some hydrostatic righting moment for pitch stability and trim.

More buoyancy can be added to the vehicle by adding syntactic foam blocks in the center structure between the upper and lower turbines. These blocks would add a buoyancy volume of 0.263 m^3, or 2574 N of buoyancy force. According to prediction, the blocks would also add a weight of 1030 N to the Subscale Demonstrator. Increased buoyancy can help lift the system, so that the vehicle doesn't have to work as hard to rise or dive.

3.5 Inflow Model

An accurate inflow model is needed to predict the hydrodynamic loads on the cycloturbine. Particle Image Velocimetry (PIV) measurements performed by Benedict et al. [18] show that the flow inside a cycloturbine is extremely complicated and hard to be represented accurately by a fluid mechanics model. Benedict investigates two different inflow models based on momentum theory: a single streamtube model where the entire turbine is immersed in a single streamtube and a double-multiple streamtube model where the turbine is divided into a number of streamtubes and also the influence of the upper half of the turbine on the lower half is taken into account [18]. The double-multiple streamtube model predicts propulsive forces

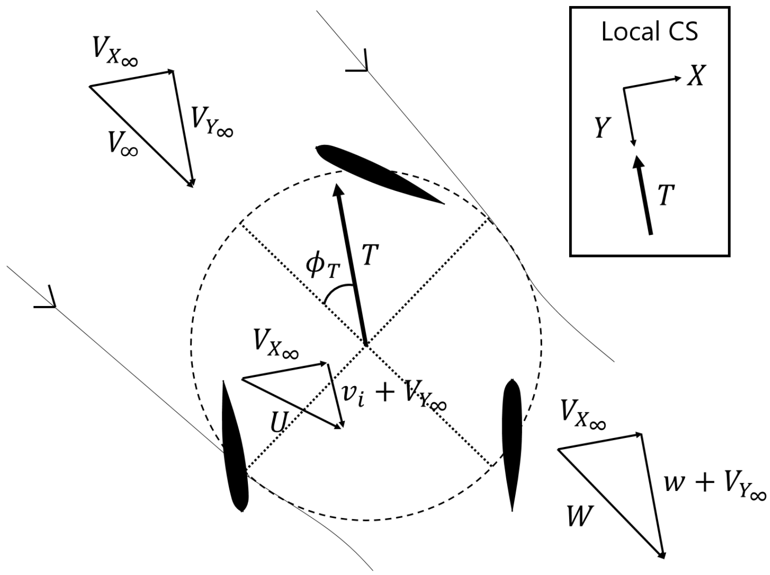

Figure 3.3. Single streamtube inflow model for the momentum analysis of a cycloturbine in forward flight. The local coordinate system to the turbine has the Y-direction parallel to the thrust vector and the X-direction orthogonal to the thrust vector.

that better agree with forces predicted from CFD. It is theorized that the single streamtube model has lower accuracy because it does not include the effect of the induced inflow from the upper half of the turbine on the lower half. A single streamtube model is used for the current work due to its reduced complexity and fast computation time. Additionally, the model is tuned to forces predicted by CFD and experimental results to improve accuracy.

Inflow for the current model is calculated using a momentum theory inflow solution based on helicopter modified momentum theory. When a helicopter is in forward flight, the rotor disk is tilted forward at an angle-of-attack relative to the inflow. Due to the loss of axisymmetry under this condition, the simple helicopter momentum theory is modified to account for the complex nature of the rotor flow in forward flight [69]. This is a single streamtube model as shown in Fig. 3.3. The mass flow rate, $\dot{m}$, through the cycloturbine is

$$\dot{m} = \rho A U \tag{3.11}$$

where A is the capture area of the turbine and U is the resultant velocity at the cycloturbine. For a cycloturbine, the capture area is rectangular. The resultant velocity at the cycloturbine is

$$U = \sqrt{V_{X\infty}^2 + (V_{Y\infty} + v_i)^2}. \tag{3.12}$$

This equation includes the free stream velocity components in the direction of (V_Y) and perpendicular to (V_X) the current thrust vector. The induced velocity v_i is assumed to always be parallel to the thrust vector. The application of conservation of momentum in a direction parallel to the thrust, T, of the cycloturbine gives

$$\begin{aligned} T &= \dot{m}(w + V_{Y\infty}) - \dot{m}V_{Y\infty} \\ &= \dot{m}w \end{aligned} \tag{3.13}$$

where w is the velocity in the far wake. The application of conservation of energy gives

$$\begin{aligned} P_i &= T(v_i + V_{Y\infty}) \\ &= \frac{1}{2}\dot{m}(w + V_{Y\infty})^2 - \frac{1}{2}\dot{m}V_{Y\infty}^2 \\ &= \frac{1}{2}\dot{m}(w^2 + 2wV_{Y\infty}) \end{aligned} \tag{3.14}$$

where P_i is the induced power required. Combination of Eqns. 3.13 and 3.14 finds that $w = 2v_i$. Therefore,

$$\begin{aligned} T &= 2\dot{m}v_i \\ &= 2(\rho A U)v_i \\ &= 2\rho A v_i\sqrt{V_{X\infty}^2 + (V_{Y\infty} + v_i)^2} \end{aligned} \tag{3.15}$$

and the induced velocity, v_i, can be found by solving

$$v_i = \frac{v_h^2}{\sqrt{(V_{X\infty})^2 + (V_{Y\infty} + v_i)^2}} \tag{3.16}$$

where the inflow velocity is resolved via fixed point iteration. The induced flow components are based on the direction of the thrust vector and the vehicle speed:

$$\begin{aligned} V_{X\infty} &= V_{veh,x}\cos\phi_T - V_{veh,y}\sin\phi_T \\ V_{Y\infty} &= V_{veh,x}\sin\phi_T + V_{veh,y}\cos\phi_T \end{aligned} \tag{3.17}$$

where ϕ_T is the phase angle of the thrust vector and $V_{veh,x}$, $V_{veh,y}$ are the vehicle speed in the X- and Y- directions, respectively. The induced velocity at hover, v_h

is the change in air speed induced by the turbine blades with respect to the free stream velocity. It is defined as

$$v_h = \sqrt{\frac{\kappa T}{2\rho A}} \tag{3.18}$$

where κ is an inflow correction factor to account for non-uniformity of induced velocity over the foil length. For reference, the inflow correction factor is typically 1.15 for helicopters. This is also the value used in Benedict's analysis mentioned earlier. Alternatively, Taniguchi [36] estimated the value of κ for a cycloturbine to be 1.176. This value is modified to 1.321 from experiments on a six-bladed cyclo-propeller conducted by Haberman and Harley [39]. In the model used in this paper, the correction factor is used as a tuning factor to better match 2D and 3D CFD results.

3.5.1 Dynamic Inflow

The model computation time can be reduced by using dynamic inflow. As will be discussed, the model runs faster with dynamic inflow because it only has to iterate on quasi-steady inflow for each time step, rather than additionally iterating on inflow and thrust.

The model is improved by representing the induced inflow at the rotor in a series of first order differential equations in the time domain. The state-space model is revised to include the components of the inflow velocity to each of the four cycloturbines:

$$\vec{x} = [p_N, p_E, p_D, \phi, \theta, \psi, U, V, W, P, Q, R, V_{1X}, V_{1Y}, V_{2X}, V_{2Y}, V_{3X}, V_{3Y}, V_{4X}, V_{4Y}]^T \tag{3.19}$$

where the X and Y components of the inflow velocity are defined in Fig. 3.3. The dynamic inflow model first resolves the quasi-steady inflow via the momentum theory inflow solution (see Eq. 3.16)

$$\vec{v}_{i,qs} = [v_i \sin(\phi_T), v_i \cos(\phi_T)]^T \tag{3.20}$$

then computes derivatives of the X and Y components of inflow velocity. The derivatives are found using a time constant based on Pitt-Peters theory [70], which states that the time constant for uniform inflow is a multiple of a gain and an apparent mass term

$$\tau_{inflow} = \frac{1}{2}\frac{128}{75\pi}\frac{R_{turb}}{V_{tot}} \tag{3.21}$$

where

$$V_{tot} = \sqrt{(V_{X_\infty})^2 + (V_{Y_\infty} + v_i)^2} \tag{3.22}$$

and the coefficient $128/75\pi$ is for rotors with twisted blades [71]. The derivatives of the inflow velocity are therefore

$$[\dot{V}_{turb,X}, \dot{V}_{turb,Y}]^T = \frac{1}{\tau_{inflow}}(\vec{v}_{i,qs} - [V_{turb,X}, V_{turb,Y}]^T) \tag{3.23}$$

and can be included in the equations of motion

$$\dot{\vec{x}} = f(\vec{x}, \vec{u}). \tag{3.24}$$

3.6 Propulsive Force Model

The simulation model relies on a simplified hydrodynamic analysis of the propulsive forces generated by the turbines, as a function of the foil pitch schedule and vehicle state. The turbine propulsive forces and moments are calculated as the time-averaged foil forces over one turbine revolution using an azimuthally averaged blade element approach. The fundamental approach is derived from computational methods used to determine the hydrodynamic propulsive forces acting on a cycloturbine [17, 36–38].

The first step in calculating the foil hydrodynamic forces is by calculating the section angle-of-attack. Figure 3.4 shows a schematic of the velocities used to calculate the steady angle-of-attack. The velocity of the foil relative to the fluid is computed by summing the velocity of the vehicle, the induced velocity, and the rotational velocity of the turbine:

$$\vec{V}_{foil} = \vec{V}_{veh} + \vec{v}_i + \vec{\omega} \times \vec{R} \tag{3.25}$$

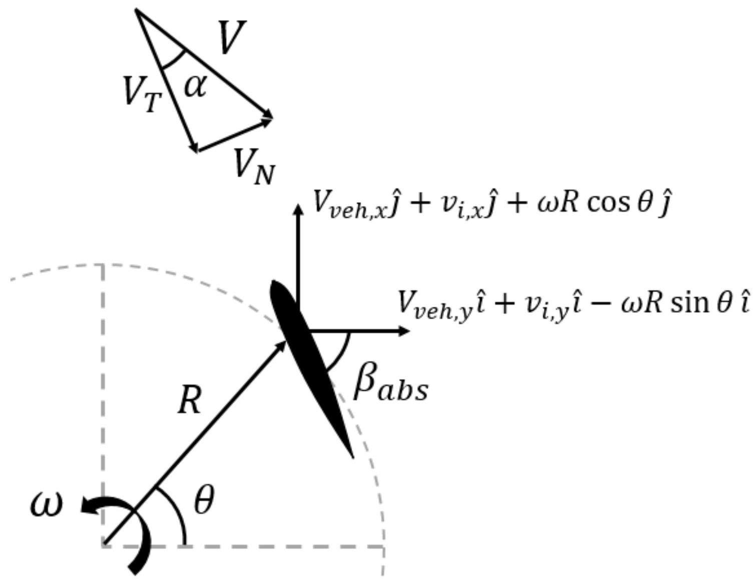

Figure 3.4. Schematic showing the angles and velocities used to formulate the steady section angle-of-attack.

where R is the radius of the turbine, and ω is the rotational rate of the turbine. The angle-of-attack is then calculated

$$\alpha = \tan^{-1}\frac{V_N}{V_T} \tag{3.26}$$

where the velocity normal to the foil axis, V_N, is defined as

$$\begin{aligned} V_N =&(V_{veh,x} + v_{i,x} - \omega R\sin\theta)\sin\beta_{abs}\hat{\imath} + \dots \\ &(V_{veh,y} + v_{i,y} + \omega R\cos\theta)\cos\beta_{abs}\hat{\jmath} \end{aligned} \tag{3.27}$$

and the velocity tangential to the foil axis, V_T, is defined as

$$\begin{aligned} V_T =&(V_{veh,x} + v_{i,x} - \omega R\sin\theta)\cos\beta_{abs}\hat{\imath} - \dots \\ &(V_{veh,y} + v_{i,y} + \omega R\cos\theta)\sin\beta_{abs}\hat{\jmath}. \end{aligned} \tag{3.28}$$

The angle-of-attack is used to determine the coefficient of lift from complete non-linear look-up tables that provide lift and drag coefficients for NACA 0015 airfoils over 360° angles of attack and Reynolds numbers between 10,000 and 5,000,000 [72]. Reynolds number is determined by

$$Re = \frac{c|\vec{V}_{foil}|}{\nu} \tag{3.29}$$

where c is the chord of the foil, $|\vec{V}_{foil}|$ is the magnitude of the foil velocity vector, and ν is the kinematic viscosity. The lift is then calculated

$$L = \frac{1}{2}\rho|\vec{V}_{foil}|^2 cbC_L \tag{3.30}$$

where ρ is the density of the surrounding fluid, b is the span of the foil, and C_L is the coefficient of lift based on the angle-of-attack.

Thus far, the angle-of-attack has been calculated for a steady condition (constant with time). The effects of changing circulation acting upon the cycloturbine foils are also necessary to be included. The unsteady hydrodynamic effect of shed vorticity can have a significant effect on the foil loads since the foils operate at a moderately high reduced frequency ($k_{red} \approx 0.20$). Reduced frequency can be thought of as the number of oscillations that an airfoil undergoes during the time it takes for the airflow to travel across the semi-chord. It is defined here as

$$k_{red} = \frac{\omega c}{2|\vec{V}_{foil}|} \tag{3.31}$$

where ω is the rotation rate of the turbine. The unsteady hydrodynamics have the effect of reducing the magnitude of the lift, and, more significantly, introducing a phase lag between the foil motion and the unsteady hydrodynamic forces.

Theodorsen's function is used to model the change in amplitude and phase of the hydrodynamic lift as a result of sinusoidal angle-of-attack. It can be interpreted as a filter that modifies the quasi-steady lift to an unsteady lift depending on the reduced frequency [73]. It is defined as

$$C(k_{red}) = \frac{H_1^{(2)}(k_{red})}{H_1^{(2)}(k_{red}) + iH_0^{(2)}(k_{red})} \tag{3.32}$$

where $H_n^{(2)}(k_{red})$ are Hankel functions of the second kind. The modified angle-of-attack is therefore

$$\alpha_{unsteady} = \bar{\alpha} + |C(k_{red})|\,\bar{\alpha}\sin(\theta + \angle C(k_{red})) \tag{3.33}$$

where the fluctuating component of the unsteady angle-of-attack is modified in the second term using the magnitude and phase of Theodorsen's function. For example, for a reduced frequency of $k_{red} = 0.2$, the unsteady angle-of-attack would lag the steady angle-of-attack by 11° and the magnitude of the lift would be reduced 25%. Further reference in this paper to an unsteady phase lag is defined as follows:

$$\alpha_{unsteady} = \alpha_{steady} + \alpha_{lag}. \tag{3.34}$$

The drag force on the foil is calculated in the same manner as the lift, except the drag coefficient is based on steady hydrodynamics. The lift and drag forces for each foil are converted to forces in the vehicle frame. The forces and moments for each foil are time averaged over one revolution and summed to provide the forces and moments produced by an individual turbine.

3.7 Validation of Propulsive Force Model

Taniguchi [36] presents a computational method by which to evaluate the performance characteristics of vertical axis cycloidal propellers with semi-elliptic blades. The induced velocity on the cycloturbine is obtained using momentum theory with a modification factor to match the predicted performance to experimental data from a six-bladed vertical axis propeller [39]. Thrust and torque are calculated by integrating the lift and drag forces on each blade using a blade element approach.

Taniguchi's computational method is investigated through a series of experiments by Haberman and Harley [39] over a large range of propeller eccentricities (thrust phase angles) and blade solidities. These experiments show that Taniguchi's method is an adequate predictor of performance characteristics of a cycloidal propeller, with some limitations. The model does not include unsteady effects such as shed vorticity; it assumes that quasi-steady state motion exists. Additionally, the induced velocities are underpredicted in Taniguchi's model. Specifically, Taniguchi assumes that the induced velocity is constant over the blade span, and that only longitudinal components of the induced velocity contribute to the propeller performance [39]. Therefore, the induced velocity must be determined experimentally or with a higher-order model.

The turbine force model outlined in this paper produces similar trends as Taniguchi's computational method for evaluating crossflow turbine performance,

Table 3.1. Turbine Force Model Tuning

Basis of Tuning Factor	κ	α_{lag}
2D CFD	0.87	-25°
3D CFD	1.40	-28°
Experimental RPD	1.40	n/a
Experimental SSD	1.40	-10°

with some discrepancies. Figure 3.5 shows the propeller thrust coefficient ($K_T = T/\rho n^2 D_{turb}^3 b$), propeller torque coefficient ($K_Q = Q/\rho n^2 D_{turb}^4 b$), and efficiency ($(K_T/K_Q)(J/2)$) as a function of advance coefficient ($J = V_{veh,x}/n\pi D_{turb}$) for a vertical axis propeller at an eccentricity of 0.6 and a rotor solidity ($\sigma = n_{turb}c/\pi D_{turb}$) of 0.133. The performance characteristics are compared for the Taniguchi method versus the turbine simulation model. The simulation model developed is more complex than Taniguchi's method as it accounts for a prescribed sinusoidal pitch schedule of the foils (instead of a cycloidal schedule as used on trochoidal propellers), uses complete non-linear look-up tables for lift and drag (as opposed to a linear lift and constant drag model), and additionally incorporates unsteady effects modeled by Theodorsen's function. The unsteady effects manifest themselves in the plots in Fig. 3.5. At lower advance coefficients, the reduced frequency increases. As the reduced frequency increases, the magnitude of the lift decreases as a result.

To further tune the model, comparisons to CFD and experimental data are made. Experimental work includes assessment of a single turbine RPD and SSD. The optimal tuning based on each comparison are summarized in Tab. 3.1 for the momentum inflow factor and unsteady phase lag.

3.7.1 Model Comparison to 2D CFD

High resolution Unsteady Reynolds-Averaged Navier Stokes (URANS) analysis is performed to support the design and development of the cycloturbine vehicle. Two-dimensional and three-dimensional unsteady, moving-mesh flow simulations are utilized to assess the device performance. The CFD analyses required simulation of 10-20 turbine rotations using a minimum of 450 timesteps per rotation to obtain an accurate and cycle-to-cycle repeatable solution. Two-dimensional analyses are used for the bulk of the analyses since the significantly smaller mesh sizes (approximately 3×10^5 cells compared to 2.5×10^7 cells for the 3D mesh) provide the timelier

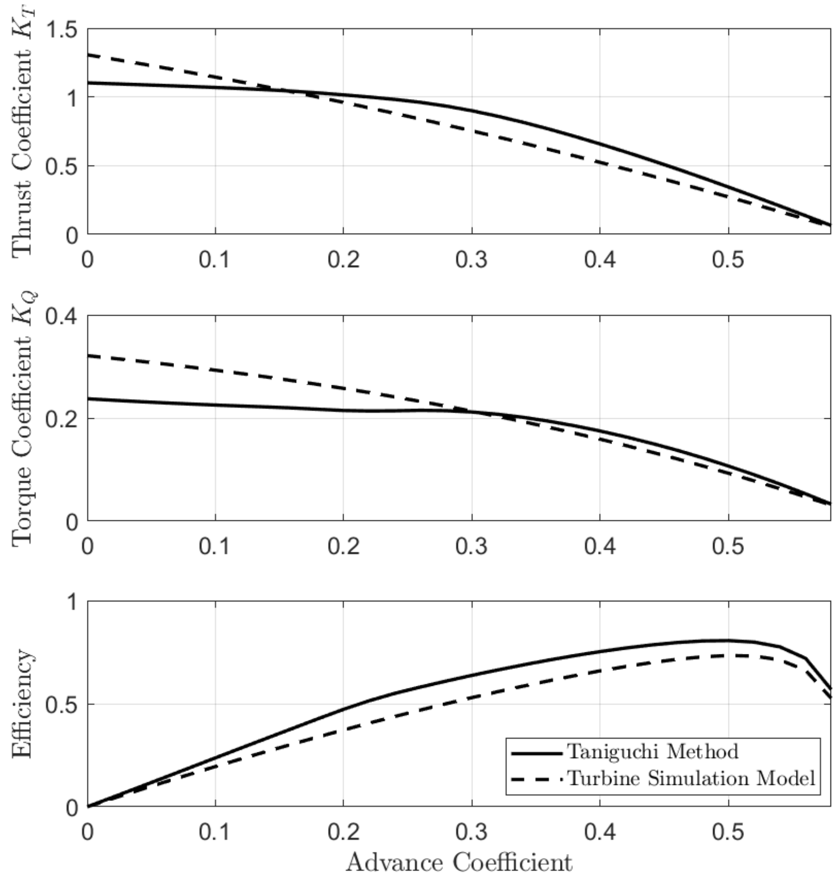

Figure 3.5. Comparison of computed performance characteristics of a vertical axis propeller using the Taniguchi method versus the turbine simulation model. Thrust coefficient, torque coefficient, and efficiency shown versus advance coefficient at an eccentricity of 0.6 and a rotor solidity of 0.133.

solution turn-around needed for design parametric studies. The full 3D model is used to validate and asses select RPD cases. The mesh for the 3D RPD model is shown in Fig. 3.6.

The unsteady CFD analysis is performed using a well-validated, in-house, naval hydrodynamic URANS solver (OVER-REL) in conjunction with dynamic structured overset meshes to resolve the relative motion between geometric components and dynamic foil pitching. This methodology has been previously validated and implemented to assess the ORPC hydrokinetic turbine and is described in detail in Medvitz et al. [59].

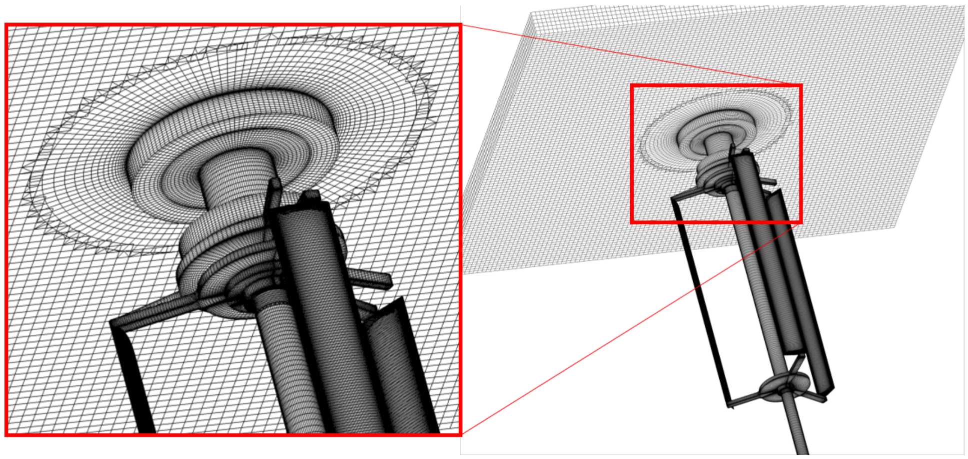

Figure 3.6. The mesh used for the three-dimensional single turbine Rapid Prototype Device and barge to support CFD analyses.

To predict thrust, lift, torque, and control moments, 2D CFD studies are performed over a range of tip speed ratios (TSRs) and maximum foil pitching angles (β_{max}) for a sinusoidal pitch schedule. The proposed turbine has three NACA 0018 foils per turbine, with a turbine solidity of 0.2 (refer to Tab. 2.4 for turbine characteristics).

Since the incorporation of unsteady effects alone into the model has discrepancies with the CFD solutions, the 2D CFD results are used as an empirical basis to tune the momentum inflow correction factor and the unsteady phase lag in the lift computation. Ultimately, a momentum inflow correction factor of 0.87 and an unsteady phase lag of -25° produces the best match to the CFD results based on an iterative method of minimizing the percent difference. Figure 3.7 shows the comparison between the propulsive thrust, power required, and lift force calculated from the simulation model and from the CFD calculations for a 1/5.56 scale model, at a range of tip speed ratios and maximum foil pitching angles. As can be seen in the figure, the thrust, power required, and lift have been matched well to the CFD results. Additionally, this force model runs quickly, and can be incorporated into a real-time six degree-of-freedom simulation model.

It should be noted that these results are for comparisons with 2D CFD. The thrust and lift will be smaller due to 3D effects. For the modeled cycloturbine, it is assumed that the 3D results will be 75% of the 2D results [59]. This is a reasonable penalty due to three-dimensional losses from struts and other features, along with

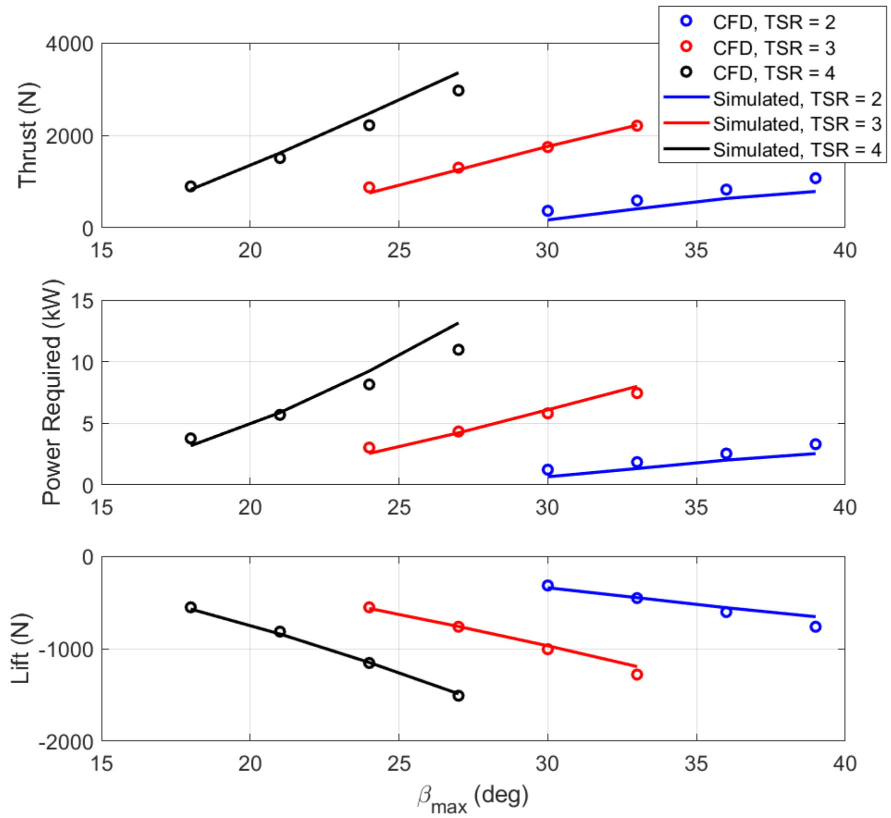

Figure 3.7. Thrust, power required, and lift versus maximum pitching angle, at 0° phase angle. Comparison between turbine force simulation model and two-dimensional CFD at a range of tip speed ratios.

the end section being significantly less efficient. For this 3D loss assumption, the momentum inflow factor that produces simulation results that best match is 1.40, with an unsteady phase lag of -28°.

3.7.2 Model Comparison to RPD and 3D CFD

The RPD is tested in the Applied Research Laboratory (ARL) Reverberant Tank. The experimental setup is discussed in detail in Chapter 2. The test matrices are provided in Appendix A. A four-bar linkage mechanism is used to set the maximum foil pitching angle and phase angle for the sinusoidal pitch schedule (see Fig. 3.8). For the RPD, an offset link length is used to provide a maximum foil pitching amplitude of 30° for propulsion mode. Measurements are taken both for a bare shaft, and for the turbine isolated beneath the barge.

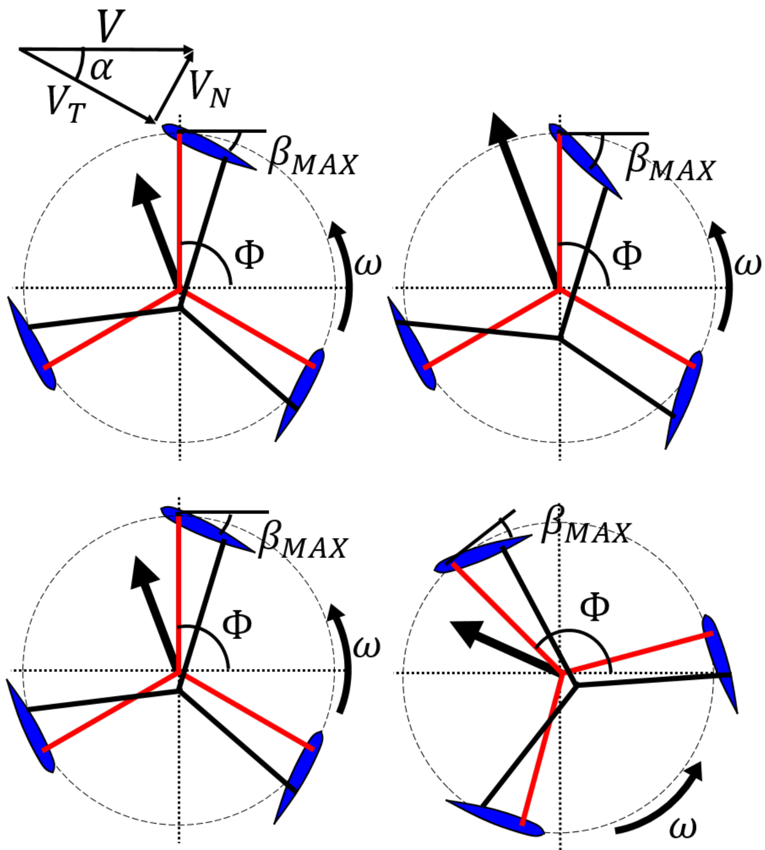

Figure 3.8. Schematic of sinusoidal foil pitching mechanism. Top: The center offset determines the maximum pitching angle, and effectively the magnitude of the thrust. Bottom: The twist of the offset controls the thrust direction by changing the phase angle. The designed mechanism provides 360° thrust vectoring capability.

The results of this experiment are used to further tune the turbine propulsive force model. Figure 3.9 shows the results for the load cell data acquired experimentally at a 30° maximum pitching angle. The mean and standard deviation for data taken on different days for 6 tests are shown up to 107 RPM. Statistics at 127 RPM are not available since only one data point is acquired at this rotation rate. The top plot in Fig. 3.9 shows the total force (sum of thrust and lift) versus turbine RPM, while the bottom plot shows the torque versus turbine RPM. Negative torque corresponds to the torque required. CFD results for 2D and 3D analysis are shown for a Spalart-Allmaras turbulence model [59]. Due to the amount of computation time for 3D CFD, 3D CFD is only computed for the 107 RPM case. As shown, the experimental data agrees well with the 3D CFD results. Additionally, the

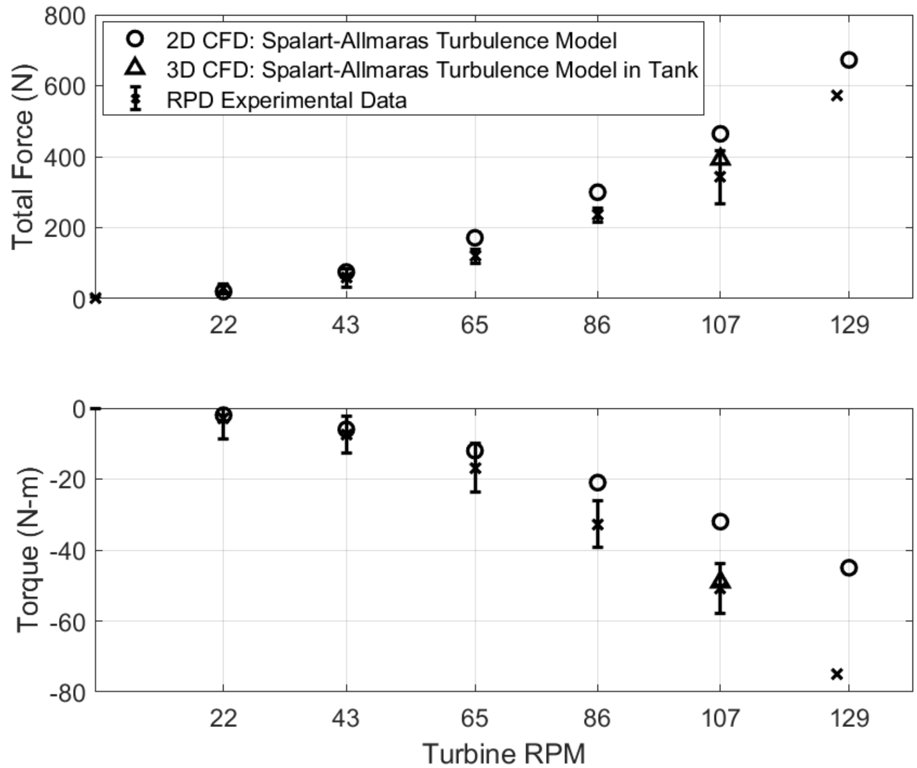

Figure 3.9. Rapid Prototype Device experimental results compared to two-dimensional and three-dimensional CFD, $\beta_{max} = 30°$. Total force and torque are shown as a function of turbine RPM. Negative torque is the torque required. Mean and standard deviation for 6 experimental cases are shown with error bars up to 107 RPM. Only one test case was performed at 127 RPM.

experimental data also matches the trends from the 2D CFD results.

Based on these results, the six degree-of-freedom turbine dynamics model is further revised. The momentum inflow factor that produces simulation results that best match the experimental RPD data is 1.40. The unsteady phase lag is not tuned since the direction of the force vector could not be resolved from the RPD experiment.

3.7.3 Model Comparison to SSD

The SSD is tested in the ARL Reverberant Tank (see Fig. 2.29). The experimental setup is discussed in detail in Chapter 2. The test matrices are provided in Appendix A. To provide good average values, data is taken for sixty seconds for each test

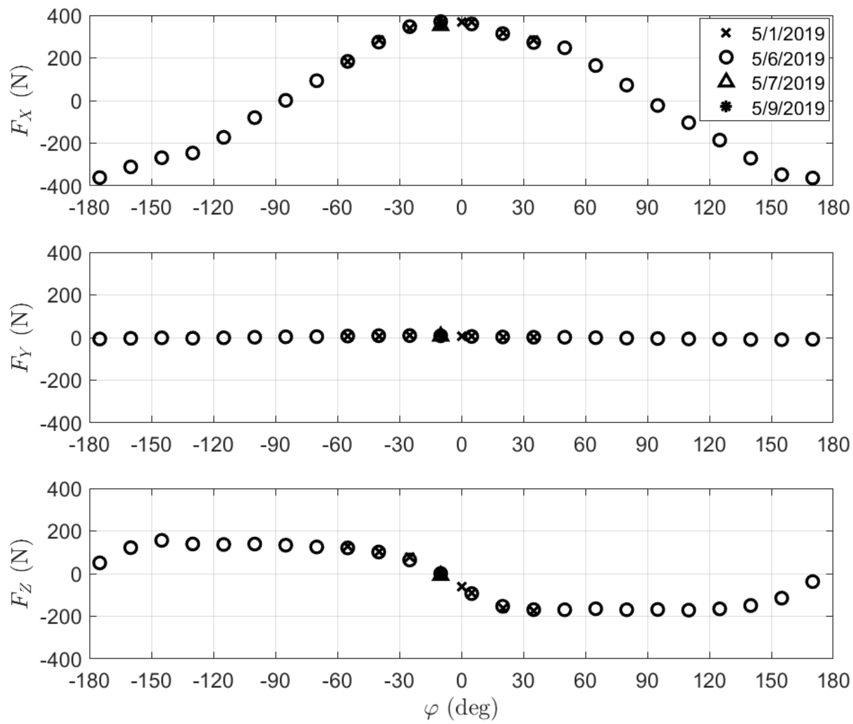

Figure 3.10. Experimental turbine force variation as a function of phase angle, for a constant maximum foil pitching angle of 30°. Data shown is for the top port turbine on the Subscale Demonstrator, at a rotation rate of 107 RPM. Data from different test days are overlaid to demonstrate the repeatability of the experimental results. The coordinate system is defined in Fig. 3.2.

condition.

The results of this experiment are used to further tune the turbine propulsive force model. Figure 3.10 shows the variation of turbine forces for the top port turbine, as the phase angle is varied circumferentially (refer to Fig. 3.11 for phase angle relationship definition to thrust direction). Data from different test days are overlaid on the figure to demonstrate the repeatability of the experimental results. It is clear that the forces in the Z-direction are affected by blockage from the outer nacelles and center nacelle.

In order to tune the turbine force model to the experimental SSD results, the SSD forces are scaled up to a higher operating RPM. The turbine force model predicts loads for a vehicle running at a design RPM of 286 (or 30 rad/s). The total turbine force magnitude from the SSD scales nondimensionally according to

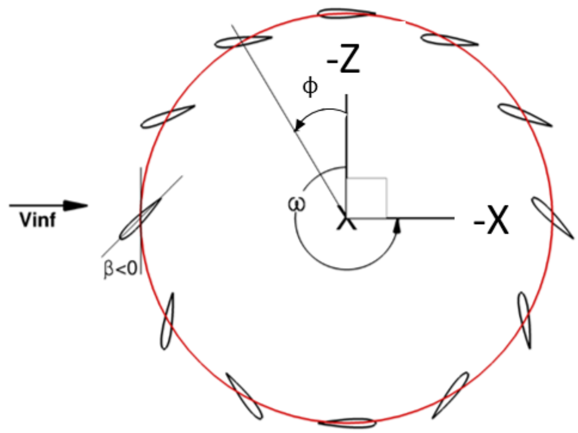

Figure 3.11. Phase angle definition.

the power law

$$\frac{F_{SSD}}{\rho n^2 D_{turb}^4} = 3.96 \left(\frac{\omega R_{turb} c}{\nu}\right)^{-0.022} \tag{3.35}$$

where D_{turb} and R_{turb} are the turbine diameter and radius, respectively, and n is the turbine rotation rate. The coefficients of the fit were determined using least squares minimization. This fit shows that there is very little Reynolds number dependence. Scaling up to 286 RPM from the experimental RPM allows for comparison between the turbine force model and the experimental data.

The momentum inflow factor in the turbine force model that provides the best fit to the experimental SSD data from tuning is 1.4. This is comparable to the momentum inflow factor obtained from the RPD experimental data. Additionally, it is clear from the SSD experimental data that the unsteady phase lag is 10°. The unsteady phase lag is improved for the SSD over the RPD ($\alpha_{lag} = -10°$ vs $\alpha_{lag} = -28°$, respectively). This may be due to the ducting of the turbines. The RPD is an open turbine while the SSD has ducted turbines. The nacelles and center structure increase the flow through the turbines, and improve turbine performance, even though they create blockage.

The blockage effect in the Z-direction is modeled by

$$\delta_Z = \frac{F_{Z,SSD} - F_{Z,veh}}{F_{Z,turbine}} \tag{3.36}$$

where $F_{Z,SSD}$ is the Z-direction force produced from the turbine on the experimental

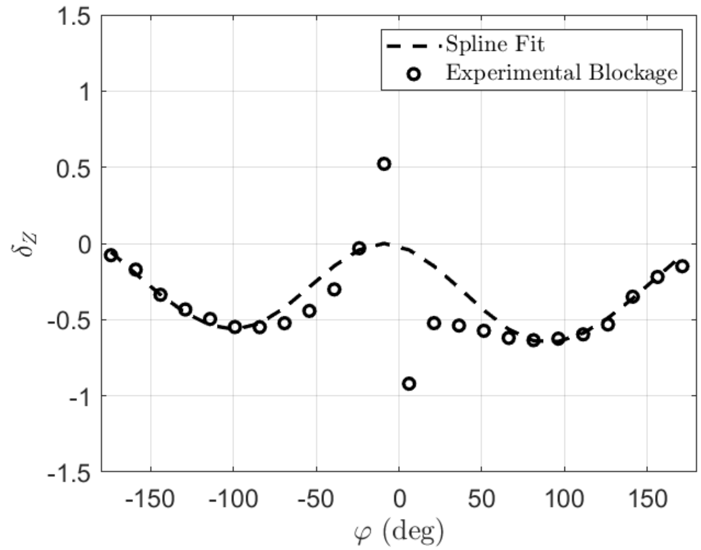

Figure 3.12. Blockage effect in the Z-direction, as a function of the phase angle. A spline fit is used to smooth out discontinuities.

SSD, $F_{Z,veh}$ is the total predicted vehicle force in the Z-direction, and $F_{Z,turbine}$ is the turbine force in the Z-direction. This parameter is essentially a measure of how much blockage, as a fraction of the turbine force, should be added to the total predicted vehicle force to produce the experimental results.

The blockage is then determined as a function of the thrust angle using a cubic spline fit to smooth out discontinuities. This blockage effect is plotted in Fig. 3.12. When the turbine thrusts forward, there is no effect of blockage. As the turbine starts to thrust down or up, a larger percentage of the turbine thrust must be subtracted from the total force to match the experimental data. Note that the blockage effect is greater when thrusting into the center structure versus thrusting towards a nacelle. The maximum blockage is 65% of the turbine thrust force. Figure 3.13 shows the comparison between the SSD experimental data (scaled to 286 RPM) versus the turbine force model for the same conditions. The mean difference between the model and the experimental forces in the X-direction is 272 N, while the mean difference between the model and the experimental forces in the Z-direction is 141 N.

The turbine force model predicts a maximum forward thrust from each turbine at 286 RPM with no current to be approximately 2.9 kN and a maximum lift (with no pitch-back) of approximately 1.2 kN. With four turbines, this equates to a

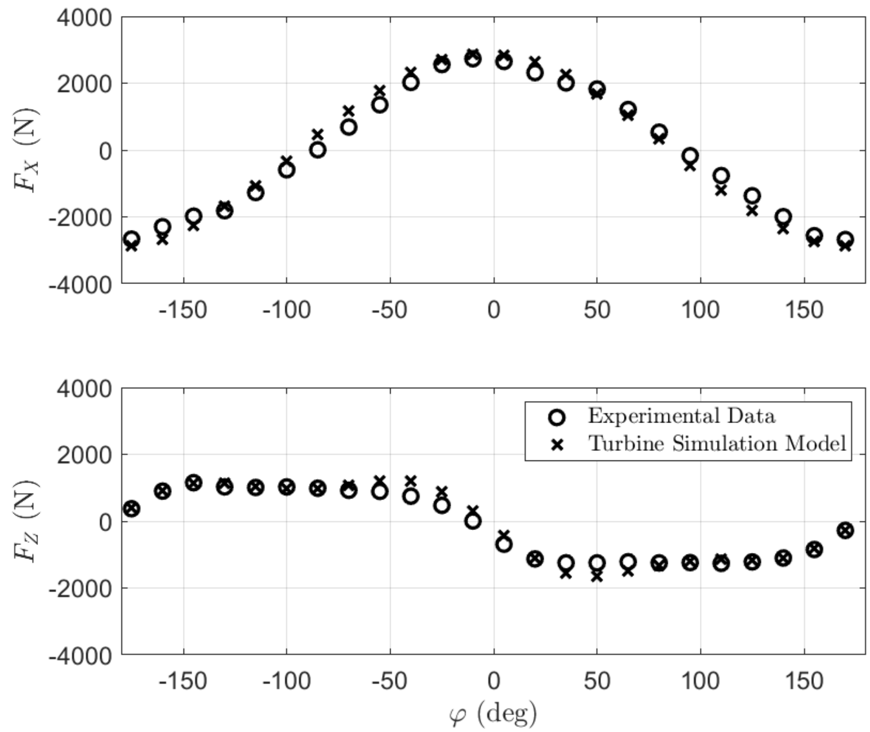

Figure 3.13. X-direction and Z-direction forces versus phase angle. Comparison shown between SSD top port turbine data for $\beta_{max} = 30°$ scaled to 286 RPM and the turbine force simulation model.

maximum forward thrust at 286 RPM of 11.6 kN and a maximum lift of 4.8 kN. If the SSD is pitched back, more lift force can be generated.

3.8 Concluding Remarks

A model to determine the forces and moments produced on and by a maneuverable marine hydrokinetic vehicle is developed. The model solves the six degree-of-freedom rigid body equations of motion for the vehicle subject to hydrodynamic lift and drag forces, hydrostatic forces, and propulsive forces through the turbine. The hydrodynamic model includes lift, induced drag, and form drag calculated from theory. The hydrostatic model includes the vehicle buoyancy forces. The inflow through the turbines is modeled as a single streamtube. The turbine propulsive force model is tuned to 2D and 3D CFD, and further to experimental data.

The simulation model developed runs very quickly, converging on a trim condition in less than a minute. The 3D CFD (which has much higher fidelity than the 2D CFD when comparing to experimental data) takes much longer to converge. For the single 3D CFD case, it took about 9 days to run 30 revolutions with 450 steps/rev. This was the number of revolutions needed to reach a cyclic-repeatable solution.

The simulation model is developed to simulate the response of the vehicle to different input commands and design vehicle controllers. The fast computation time of the simulation model is conducive to this future effort.

4 Simulation and Control Design for the Marine Hydrokinetic Cycloturbine Vehicle [1]

4.1 Overview

In this chapter, global feedback controllers are initially designed by applying classical control methods to an approximate linear model of the system dynamics. A higher performing nonlinear controller is designed using the nonlinear dynamic inversion (NDI) method. NDI takes into account the nonlinearities of the MHK system and therefore is suitable for a wide range of operating conditions. The response of the classical and NDI controllers to speed, depth, roll, pitch, and yaw commands are evaluated and compared in simulation. The classical controller outperforms the NDI controller for small amplitude maneuvers, although the degradation with NDI is minor. However, in the nonlinear operating regime the NDI controller outperforms the classical controller and the classical controller exhibits instability.

4.2 Control Design using Classical Control Methods

Linearized small-perturbation equations are used to understand the flight dynamics of the vehicle and the stability of its motion. The linear equations are derived for steady-state conditions that are important for control system design, such as steady level flight, turning flight, pull-up, and steady roll.

The linear equations are obtained by performing gradient operations on the

[1] The work presented in this chapter is in preparation for submission to the Elsevier Journal of Control Engineering Practice.

force and moment equations of motion. These gradient operations produce partial derivatives of the hydrodynamic forces and moments with respect to the state and control variables. The linear time-invariant model is represented in state-space form as

$$\dot{\vec{x}} = A\vec{x} + B\vec{u} \tag{4.1}$$

where $\vec{x}$ is the state vector, $\vec{u}$ is the control input vector, and A and B are the stability and control dimensional derivative matrices, respectively.

The stability and control derivative matrices capture the force and moment effects. Control derivatives include the change in forces and moments due to changes in the controls while stability derivatives capture the change in forces and moments due to changes of state.

The control derivatives are related to the control inputs. The nondimensional inputs in $\vec{u}$ are defined as the thrust, lift, roll, pitch, and yaw controls for the vehicle:

$$\vec{u} = [u_X, u_Z, u_K, u_M, u_N]^T \tag{4.2}$$

with a notional range of -1 to 1. Each of these controls represent a combination of adjustments to the sinusoidal foil pitch variations on the four turbines. Each turbine has individual controls for maximum foil pitching angle which changes the magnitude of its thrust, and foil phase angle, which changes the direction of the thrust in the up/down direction. For example, u_X adjusts the maximum pitching angle of the foils so that the thrust is increased or decreased equally for all four turbines. The u_N control causes a difference in the thrust magnitude between the starboard side turbines (1 and 3) and the port side turbines (2 and 4), such that it generates a yaw moment about the vehicle center of mass. Pitch control, u_M, works similarly through difference in thrust between the top turbines (1 and 2) and the bottom turbines (3 and 4). Vertical and roll control, u_Z and u_K, make use of the phase changes in the turbines. Note that there is no direct side force control on the vehicle (i.e. u_Y does not exist).

The controls are mixed to obtain the actuator commands (maximum foil pitching angle and phase angle) for each of the four turbines:

$$
\begin{aligned}
\beta_{max1} &= \beta_{range}(u_X - u_M - u_N) \\
\varphi_1 &= \varphi_{range}(u_Z + u_K) \\
\beta_{max2} &= \beta_{range}(u_X - u_M + u_N) \\
\varphi_2 &= \varphi_{range}(u_Z - u_K) \\
\beta_{max3} &= \beta_{range}(u_X + u_M - u_N) \\
\varphi_3 &= \varphi_{range}(u_Z + u_K) \\
\beta_{max4} &= \beta_{range}(u_X + u_M + u_N) \\
\varphi_4 &= \varphi_{range}(u_Z - u_K)
\end{aligned}
\tag{4.3}
$$

where $\beta_{range} = 0.6981$ rad (40°) is the maximum range of foil pitching angle and $\varphi_{range} = 0.7854$ rad (45°) is set as the maximum range of turbine phase angle. As stated earlier, the controls are scaled to range from -1 to 1.

The signs in the equations are based on the location of the turbine relative to the body axes. For example, for turbine 1 (the top starboard turbine, per Fig. 3.2) a forward thrust vector would produce a positive force in the X-direction, a negative moment about the pitch axis, and a negative moment about the yaw axis.

The turbine propulsive force model developed and tuned to experiments (see Chapter 3) is then applied to determine the individual turbine forces and moments generated given these actuator commands. The individual turbine forces and moments are summed together with the hydrodynamic and hydrostatic forces and moments to produce the total forces and moments on the vehicle (X, Y, Z, K, M, N).

Classical control methods can only be used if there is an approximately linear relationship between the control adjustments and the vehicle states. This is the main motivation employing the control mixing in Eq. 4.3 with a limited range in foil phase angle. For example, if the phase were allowed to run through 360°, there would be a nonlinear relationship of the controls to the system dynamics. Thus, for classical control to be effective, the system must be close to neutrally buoyant so that the thrust does not have to vary from vertical to forward directions. Even then there will be difficulties in hovering the vehicle as will be shown below.

To better compare the performance of classical control to NDI control, additional buoyancy is added to the Subscale Demonstrator (SSD). More buoyancy can be added to the vehicle by adding syntactic foam blocks in the center structure between the upper and lower turbines. These blocks would add a buoyancy volume of 0.247

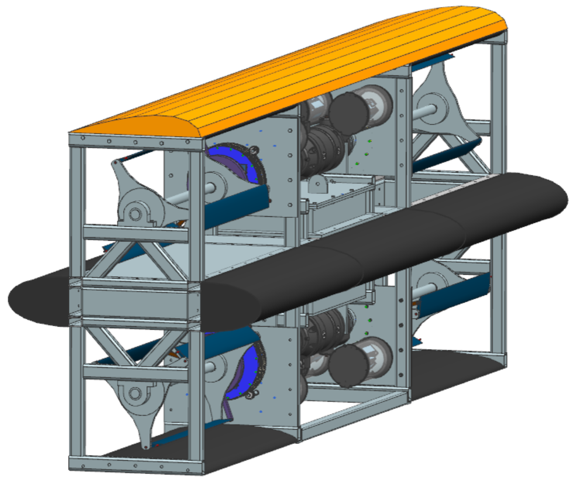

Figure 4.1. Addition of buoyancy to the SSD. Syntactic foam blocks are inserted in the center structure between the upper and lower turbines. An upper buoyancy pod runs the length of the vehicle. It's shape adds hydrodynamic lift in addition to buoyancy.

m^3, or 2415 N of buoyancy force. According to prediction, the blocks would also add a weight of 1160 N to the SSD. Additional buoyancy and lift is added with the addition of a syntactic foam upper buoyancy pod: this adds a buoyancy volume of 0.125 m^3, or 1222 N of buoyancy force, while adding 586 N of weight. The pod is flat on one side to sit flush against the upper nacelles, while the other side has a streamlined shape (see Fig. 4.1).

Increased buoyancy can help lift the system, so that the vehicle does not need to generate any vertical component of thrust if it is not rising or diving (if neutrally buoyant). The syntactic foam blocks and upper pod make the vehicle have a total volume of 1.3 m^3 and a new total mass of 1403 kg (refer to original values in Tab. 2.6 for comparison). The upper buoyancy pod is also predicted to shift the center of buoyancy further up above the center of gravity (from 2 cm to 10 cm according to a computer aided design model). Additionally, the upper buoyancy pod contributes to the hydrodynamic lift of the vehicle. The curved upper slope of the buoyancy pod is modeled after the NACA 2412 airfoil. The NACA 2412 airfoil lookup tables are incorporated into the model in order to calculate the contribution of the pod to vehicle lift and drag.

Using the linearized dynamics model, the control input to the vehicle is found from

$$u(t) = K_P e(t) + K_I \int e(t)dt + K_D \frac{de}{dt} \tag{4.4}$$

where $e(t)$ is the tracking error and K_P, K_I, K_D are the proportional, integral, and derivative gains, respectively. By taking the Laplace transform of this equation, the transfer function of the PID controller is found

$$C(s) = K_P + \frac{K_I}{s} + K_D s \tag{4.5}$$

and the PID compensators are designed. The proportional gain proportionally increases the control signal to the error level. Integral action is used to reduce steady-state error, while derivative action is used to improve the settling time and stability of the system.

The controllers are designed using successive loop closure. The fundamental approach behind this method is to successively close several simple feedback loops around the open loop plant dynamics rather than design a single, and more complex, multiple input multiple output (MIMO) system [74]. Figure 4.2 shows the successive loop closure design for this system. Note that the command trajectories to depth, roll, pitch, and yaw rate ($\dot{r}$) pass through a first order filter and then are integrated to obtain the desired trajectory, r.

PID control is first found for the yaw angle due to yaw control. The compensator is tuned by interacting with the root locus plots of the open-loop system. Design requirements are set for a damping ratio greater than 0.7, and a percent overshoot less than 20%. The yaw feedback loop is appended to the system, and the controller for the roll angle due to roll control is subsequently designed. The next feedback loop designed is for the pitch angle due to pitch control, and finally the down displacement of the vehicle due to lift.

The PID controller gains are summarized in Tab. 4.1. The response of the compensators to an input step command are shown in Tab. 4.2.

Note that the classical controller is designed for a dynamics model that is linearized from a single operating point. Table 4.1 shows the gains for when the dynamics model is linearized about a forward velocity of 1 m/s and a depth of 24 m, for a turbine rotation rate of 286 RPM. These controllers could work at other operating points. For example, at an operating point where the forward velocity is 1.5 m/s vs. 1 m/s, the same gains as shown in Tab. 4.1 could be used. The response

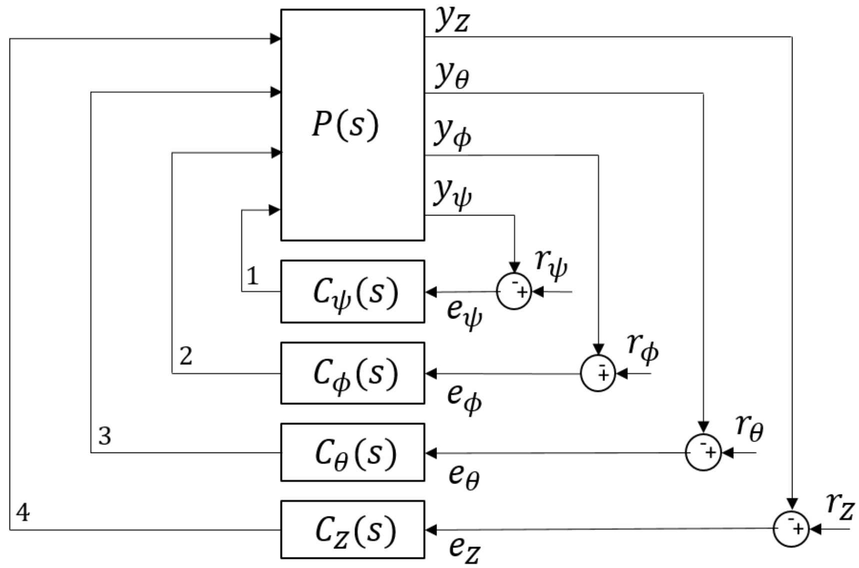

Figure 4.2. Four-stage successive loop closure design for Subscale Demonstrator (which is the plant $P(s)$). Controllers in the Laplace domain, $C(s)$, are designed for roll, pitch, yaw, and depth control. The innermost loop tracks the vehicle yaw, the next outer loop tracks the vehicle roll, the next outer loop tracks the vehicle pitch, and the outermost loop tracks the down displacement of the vehicle.

Table 4.1. Classical controller gains. These gains are determined from a dynamics model linearized about a forward velocity of 1 m/s, a turbine rotation rate of 286 RPM, and a depth of 24 m.

State	K_P **(1/rad)**	K_I **(1/(rad·s))**	K_D **(1/(rad/s))**
Yaw ψ	1.39	1.96	0.25
Roll ϕ	3.74	5.20	0.71
Pitch θ	0.81	1.66	0.12
Depth p_D	2.47	2.27	0.64

of the compensators to different input commands is different, as summarized in Tab. 4.3.

Gain scheduling could be used to set the gains for other operating points. For example, the gains for linearization about a different operating point (linearization about a turbine rotation rate of 236 RPM vs. 286 RPM) are shown in Tab. 4.4, with response to input step commands summarized in Tab. 4.5. An additional benefit of NDI control is that it does not have to consider only one operating point.

Table 4.2. Controller response to a unit step in the control input. The dynamics model was linearized about a forward velocity of 1 m/s and a depth of 24 m. The turbine rotation rate is 286 RPM.

State	**% OS**	t_s **(s)**
Yaw ψ	18.7	1.97
Roll ϕ	15.5	1.98
Pitch θ	6.1	1.77
Depth p_D	16.0	2.78

Table 4.3. Controller response to a unit step in the control input. The dynamics model was linearized about a forward velocity of 1.5 m/s and a depth of 24 m. The turbine rotation rate is 286 RPM.

State	**% OS**	t_s **(s)**
Yaw ψ	17.6	2.00
Roll ϕ	12.5	1.85
Pitch θ	8.0	2.05
Depth p_D	13.2	2.62

4.3 Control Design using Nonlinear Dynamic Inversion (NDI)

Dynamic inversion could be applied to the linear system to simplify the design of the compensators and improve the tracking accuracy of the closed-loop system. However, as discussed above, if we would like the MHK vehicle to be controlled in hover and without neutral buoyancy, we need to account for nonlinearities in the system dynamics. To this end, a nonlinear dynamic inversion controller is designed.

The control architecture for the nonlinear dynamic inversion controller is depicted in Fig. 4.3, where r is a desired trajectory, $\dot{r}$ is a feedforward term to improve error tracking, e is the tracking error, and ν is an auxiliary input that is selected to stabilize the error dynamics. The outer loop tracks the error, and any linear design technique can be used for its design. This is because the inner control loop, called the feedback linearization loop, is nonlinear; the inner loop control contains a model of the vehicle dynamics.

Table 4.4. Classical controller gains for linearization about a different operating point. These gains are determined from a dynamics model linearized about a forward velocity of 1 m/s, a turbine rotation rate of 236 RPM, and a depth of 24 m.

State	K_P **(1/rad)**	K_I **(1/(rad·s))**	K_D **(1/(rad/s))**
Yaw ψ	2.28	1.60	0.25
Roll ϕ	4.89	-	0.24
Pitch θ	0.60	1.22	0.06
Depth p_D	2.89	1.90	0.54

Table 4.5. Controller response to a unit step in the control input. The dynamics model was linearized about a forward velocity of 1 m/s and a depth of 24 m. The turbine rotation rate is 236 RPM.

State	**% OS**	t_s **(s)**
Yaw ψ	15.9	2.41
Roll ϕ	13.2	0.96
Pitch θ	5.0	1.93
Depth p_D	15.0	3.30

Initially, the controller is analyzed and designed using the individual turbine forces as the controls. This is done because it makes the system affine in the controls. The dynamics can thus be written as

$$\dot{\vec{x}} = f(\vec{x}) + g(\vec{x})\vec{F} \tag{4.6}$$

where

$$\vec{F} = [X, Z, K, M, N] \tag{4.7}$$

and for the sake of design it is assumed that the Y-direction force is equal to zero. The dynamics can then be rewritten as

$$\dot{\vec{x}} = f(\vec{x}) + g(\vec{x})(\vec{F}_{prop} - \vec{F}_{veh}) \tag{4.8}$$

where F_{veh} represents the vehicle drag, buoyancy, and buoyancy pod lift forces and moments and F_{prop} are the propulsive forces that can be controlled via the foil

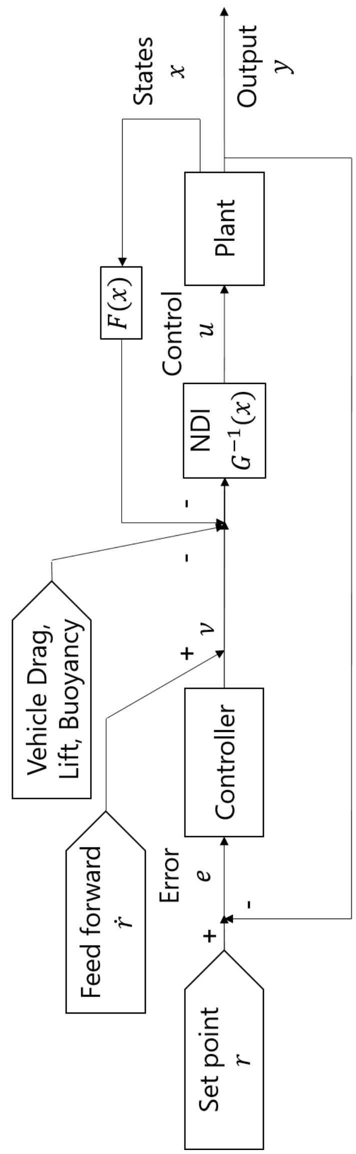

Figure 4.3. High-level control architecture for nonlinear dynamic inversion (NDI).

pitch schedule. The controller is then

$$\vec{u} = g^{-1}(\vec{x})[\vec{\nu} - f(\vec{x}) - \vec{F}_{veh}] \tag{4.9}$$

where ν is known as the "pseudo-control" vector. This control requires that the matrix $g(x)$ be invertible for all feasible state values.

In Eq. 4.9, the individual turbine forces are used as the controls. The individual turbine propulsive forces are assumed to be only in the X and Z directions (a total of eight controls for four cycloturbines). Since this violates the assumption of a square system (there are more control inputs than system outputs), the control dimension is reduced using the pseudo inverse technique.

The desired thrust magnitude and direction for each turbine is then computed from the individual turbine forces. The turbine propulsive force model is inverted to find the relationships between the thrust magnitude and direction, and the maximum foil pitching angle and phase angle per turbine. The relationships are nonlinear, and vary with inflow and turbine RPM, but can be simplified. Analytical expressions are approximated for these relationships.

Finally, outer loop controllers are designed for tracking the relative velocity, the depth, and the vehicle roll, pitch, and yaw. Proportional-integral-derivative gains are selected using the characteristic polynomial of the error dynamics, which will be described in Section 4.3.3.

The controllers are evaluated in simulation to different input commands. The performance is compared to the response of the classical controllers for the neutrally buoyant system detailed in Section 4.2. The performance is also evaluated for the negatively buoyant SSD, where classical controllers fail.

4.3.1 Control Allocation

The first step in the outlined NDI approach is to define the controls as the individual turbine forces. With eight controls, the assumption of a square system is violated, since there are more control inputs than there are degrees-of-freedom to be controlled. In other words, there are many ways that the eight control inputs can be combined to produce the five desired outputs.

The system is described in state-space form by [2] [3]

[2] $\mathrm{c}\theta, \mathrm{s}\theta, \mathrm{t}\theta$ denote respectively $\cos\theta, \sin\theta, \tan\theta$

[3] $I_{XZ} = 0$ for the MHK vehicle

$$
\begin{bmatrix} \dot{p_N} \\ \dot{p_E} \\ \dot{p_D} \\ \dot{\phi} \\ \dot{\theta} \\ \dot{\psi} \\ \dot{U} \\ \dot{V} \\ \dot{W} \\ \dot{P} \\ \dot{Q} \\ \dot{R} \end{bmatrix}
=
\begin{bmatrix}
U\mathrm{c}\theta\mathrm{c}\psi + V(\mathrm{s}\phi\mathrm{s}\theta\mathrm{c}\psi - \mathrm{c}\phi\mathrm{s}\psi) + W(\mathrm{s}\phi\mathrm{s}\psi + \mathrm{c}\phi\mathrm{s}\theta\mathrm{c}\psi) \\
U\mathrm{c}\theta\mathrm{s}\psi + V(\mathrm{c}\phi\mathrm{c}\psi + \mathrm{s}\phi\mathrm{s}\theta\mathrm{s}\psi) + W(\mathrm{c}\phi\mathrm{s}\theta\mathrm{s}\psi - \mathrm{s}\phi\mathrm{c}\psi) \\
U\mathrm{s}\theta - V\mathrm{s}\phi\mathrm{c}\theta - W\mathrm{c}\phi\mathrm{c}\theta \\
P + Q\mathrm{s}\phi\mathrm{t}\theta + R\mathrm{c}\phi\mathrm{t}\theta \\
Q\mathrm{c}\phi - R\mathrm{s}\phi \\
Q\mathrm{s}\phi\sec\theta + R\mathrm{c}\phi\sec\theta \\
RV - QW - g\mathrm{s}\theta \\
-RU + PW + g\mathrm{s}\phi\mathrm{c}\theta \\
QU - PV + g\mathrm{c}\phi\mathrm{c}\theta \\
\frac{-(I_Z - I_Y)QR}{I_X} \\
\frac{(I_Z - I_X)PR}{I_Y} \\
\frac{(I_X - I_Y)PQ}{I_Z}
\end{bmatrix}
+
\begin{bmatrix}
0 & 0 & 0 & 0 & 0 & 0 & 0 & 0 \\
0 & 0 & 0 & 0 & 0 & 0 & 0 & 0 \\
0 & 0 & 0 & 0 & 0 & 0 & 0 & 0 \\
0 & 0 & 0 & 0 & 0 & 0 & 0 & 0 \\
0 & 0 & 0 & 0 & 0 & 0 & 0 & 0 \\
0 & 0 & 0 & 0 & 0 & 0 & 0 & 0 \\
\frac{1}{\mathrm{m}} & 0 & \frac{1}{\mathrm{m}} & 0 & \frac{1}{\mathrm{m}} & 0 & \frac{1}{\mathrm{m}} & 0 \\
0 & 0 & 0 & 0 & 0 & 0 & 0 & 0 \\
0 & \frac{1}{\mathrm{m}} & 0 & \frac{1}{\mathrm{m}} & 0 & \frac{1}{\mathrm{m}} & 0 & \frac{1}{\mathrm{m}} \\
0 & \frac{d_y}{I_X} & 0 & \frac{-d_y}{I_X} & 0 & \frac{d_y}{I_X} & 0 & \frac{-d_y}{I_X} \\
\frac{-d_z}{I_Y} & 0 & \frac{-d_z}{I_Y} & 0 & \frac{d_z}{I_Y} & 0 & \frac{d_z}{I_Y} & 0 \\
\frac{d_y}{I_Z} & 0 & \frac{-d_y}{I_Z} & 0 & \frac{d_y}{I_Z} & 0 & \frac{-d_y}{I_Z} & 0
\end{bmatrix}
\begin{bmatrix} F_{X1} \\ F_{Z1} \\ F_{X2} \\ F_{Z2} \\ F_{X3} \\ F_{Z3} \\ F_{X4} \\ F_{Z4} \end{bmatrix}
\tag{4.10}
$$

where d_y, d_z are the distances the individual turbines are offset from the center of mass. As defined in Eq. 3.2 in Chapter 3, the first vector after the equal sign corresponds to $f(\vec{x})$. The matrix that the turbine forces are multiplied by is $g(\vec{x})$. Note that in this form $g(\vec{x})$ is not actually a function of vehicle state. It is a constant matrix. Therefore, given the system

$$\begin{bmatrix} \frac{X}{\mathrm{m}} \\ \frac{Z}{\mathrm{m}} \\ \frac{K}{I_X} \\ \frac{M}{I_Y} \\ \frac{N}{I_Z} \end{bmatrix} = \begin{bmatrix} \frac{1}{\mathrm{m}} & 0 & \frac{1}{\mathrm{m}} & 0 & \frac{1}{\mathrm{m}} & 0 & \frac{1}{\mathrm{m}} & 0 \\ 0 & \frac{1}{\mathrm{m}} & 0 & \frac{1}{\mathrm{m}} & 0 & \frac{1}{\mathrm{m}} & 0 & \frac{1}{\mathrm{m}} \\ 0 & \frac{d_y}{I_X} & 0 & \frac{-d_y}{I_X} & 0 & \frac{d_y}{I_X} & 0 & \frac{-d_y}{I_X} \\ \frac{-d_z}{I_Y} & 0 & \frac{-d_z}{I_Y} & 0 & \frac{d_z}{I_Y} & 0 & \frac{d_z}{I_Y} & 0 \\ \frac{-d_y}{I_Z} & 0 & \frac{d_y}{I_Z} & 0 & \frac{-d_y}{I_Z} & 0 & \frac{d_y}{I_Z} & 0 \end{bmatrix} \begin{bmatrix} F_{X1} \\ F_{Z1} \\ F_{X2} \\ F_{Z2} \\ F_{X3} \\ F_{Z3} \\ F_{X4} \\ F_{Z4} \end{bmatrix} \tag{4.11}$$

the individual turbine forces that yield the desired vehicle forces and moments must be determined.

One way to reduce the control dimension is to allocate the controls using the pseudo inverse method. If we define from the previous equation a matrix B as

$$B = \begin{bmatrix} \frac{1}{\mathrm{m}} & 0 & \frac{1}{\mathrm{m}} & 0 & \frac{1}{\mathrm{m}} & 0 & \frac{1}{\mathrm{m}} & 0 \\ 0 & \frac{1}{\mathrm{m}} & 0 & \frac{1}{\mathrm{m}} & 0 & \frac{1}{\mathrm{m}} & 0 & \frac{1}{\mathrm{m}} \\ 0 & \frac{d_y}{I_X} & 0 & \frac{-d_y}{I_X} & 0 & \frac{d_y}{I_X} & 0 & \frac{-d_y}{I_X} \\ \frac{-d_z}{I_Y} & 0 & \frac{-d_z}{I_Y} & 0 & \frac{d_z}{I_Y} & 0 & \frac{d_z}{I_Y} & 0 \\ \frac{-d_y}{I_Z} & 0 & \frac{d_y}{I_Z} & 0 & \frac{-d_y}{I_Z} & 0 & \frac{d_y}{I_Z} & 0 \end{bmatrix} \tag{4.12}$$

the pseudo inverse solution is obtained by selection of a specific right inverse B^+ which yields a unique control input vector that provides $\dot{\vec{x}}$ while also having the minimum Euclidean norm of a weighted input vector [75]. The criteria for the right inverse B^+ are

$$
\begin{aligned}
BB^+B &= B \\
B^+BB^+ &= B^+ \\
(BB^+)^* &= BB^+ \\
(B^+B)^* &= B^+B
\end{aligned}
\tag{4.13}
$$

which are known as the Moore-Penrose conditions. For this application, this produces

$$
B^+ = \frac{1}{4}\begin{bmatrix}
1 & 0 & 0 & -1/d_z & -1/d_y \\
0 & 1 & 1/d_y & 0 & 0 \\
1 & 0 & 0 & -1/d_z & 1/d_y \\
0 & 1 & -1/d_y & 0 & 0 \\
1 & 0 & 0 & 1/d_z & -1/d_y \\
0 & 1 & 1/d_y & 0 & 0 \\
1 & 0 & 0 & 1/d_z & 1/d_y \\
0 & 1 & -1/d_y & 0 & 0
\end{bmatrix}
\tag{4.14}
$$

where B^+ is equal to $g^{-1}(x)$ from Eq. 4.9. Therefore, the pseudo inverse technique is used to relate the individual turbine forces to the vehicle forces and moments by

$$
\begin{bmatrix}
F_{X1} \\ F_{Z1} \\ F_{X2} \\ F_{Z2} \\ F_{X3} \\ F_{Z3} \\ F_{X4} \\ F_{Z4}
\end{bmatrix}
= \frac{1}{4}\begin{bmatrix}
1 & 0 & 0 & -1/d_z & -1/d_y \\
0 & 1 & 1/d_y & 0 & 0 \\
1 & 0 & 0 & -1/d_z & 1/d_y \\
0 & 1 & -1/d_y & 0 & 0 \\
1 & 0 & 0 & 1/d_z & -1/d_y \\
0 & 1 & 1/d_y & 0 & 0 \\
1 & 0 & 0 & 1/d_z & 1/d_y \\
0 & 1 & -1/d_y & 0 & 0
\end{bmatrix}
\begin{bmatrix}
X \\ Z \\ K \\ M \\ N
\end{bmatrix}.
\tag{4.15}
$$

The individual turbine forces that produce the desired vehicle forces and moments are used to find the maximum foil pitching angle and phase angle per turbine.

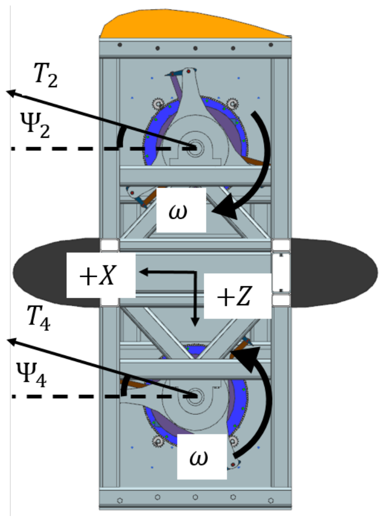

Figure 4.4. Relation between individual turbine forces and turbine rotation direction

4.3.2 Mapping Control Forces to Foil Pitch Commands

The actual foil pitch controls are needed to control the vehicle, which is why mapping the control forces to the foil pitch commands is a necessary step. The individual turbine force commands for the desired trajectory are determined using the psuedo inverse, and the corresponding maximum foil pitching angle and phase angle per turbine can be obtained.

The X- and Z- direction turbine forces are related to the individual turbine thrust magnitude and direction by

$$\begin{aligned} T &= \sqrt{F_X^2 + F_Z^2} \\ \Psi &= \tan^{-1} \frac{F_Z}{F_X} \end{aligned} \tag{4.16}$$

where T is the thrust magnitude and Ψ is the thrust phase angle.

The relationships between the thrust magnitude and direction per turbine and the turbine actuators are determined using the turbine propulsive force model. In the propulsive force model developed, the maximum foil pitching angle and phase angle per turbine are input, and the turbine forces in the X- and Z-directions are determined. For this application, the actuator commands are obtained by inverting the turbine propulsive force model, i.e. the maximum foil pitching angle and phase angle per turbine can be determined by

$$\begin{bmatrix} \beta_{max} \\ \varphi \end{bmatrix} = f(F_X, F_Z, U_{local}, W_{local}, n) \tag{4.17}$$

where F_X and F_Z are turbine forces in the forward and downward directions, U_{local} and W_{local} are the local longitudinal and heave velocities, respectively, and n is the rotation rate of the turbine.

Consider a case where the local longitudinal and heave velocities are zero. The relationships between the thrust magnitude and direction, and the maximum foil pitching angle and turbine phase angle are shown in Fig. 4.5. The turbine data is shown for 286 RPM, which is the target operating rotation rate of the turbines. The relationship between the thrust magnitude and the maximum foil pitching angle is largely dependent on the turbine phase angle. The range of the maximum foil pitching angle is also limited by blade stall. Additionally, the turbine phase angle is linearly related to the thrust direction for this condition, with very little dependence on the maximum foil pitching angle.

The thrust magnitude can be nondimensionalized by the density, the rotation rate of the turbine, and the turbine diameter according to $\rho n^2 D_{turb}^4$. The dependence of the thrust magnitude on turbine phase angle is a result of a blockage effect from the turbine center structure and nacelles (refer to Chapter 3). This dependence can be removed by further dividing the nondimensionalized thrust magnitude by

$$f_\delta(\varphi) = 0.0191 \sin\left(\frac{2\pi\varphi}{3.1460} - \frac{2\pi\varphi}{0.7656}\right) + 0.0819 \tag{4.18}$$

for the top turbines and

$$f_\delta(\varphi) = 0.0223 \sin\left(\frac{2\pi\varphi}{3.3395} - \frac{2\pi\varphi}{0.7733}\right) + 0.0853 \tag{4.19}$$

for the bottom turbines, in radians. These expressions were found by fitting the data to a sinusoidal expression, and minimizing the least-squares cost function. The effect of this fit can be seen for the top port turbine in Fig. 4.6, for a range of RPMs.

The introduction of nonzero local longitudinal and heave velocities changes the relationship between the turbine thrust and the turbine actuators (see Fig. 4.7). Further analysis is conducted to determine the analytical expressions that allow collapse of these curves: the maximum foil pitching angle is shifted

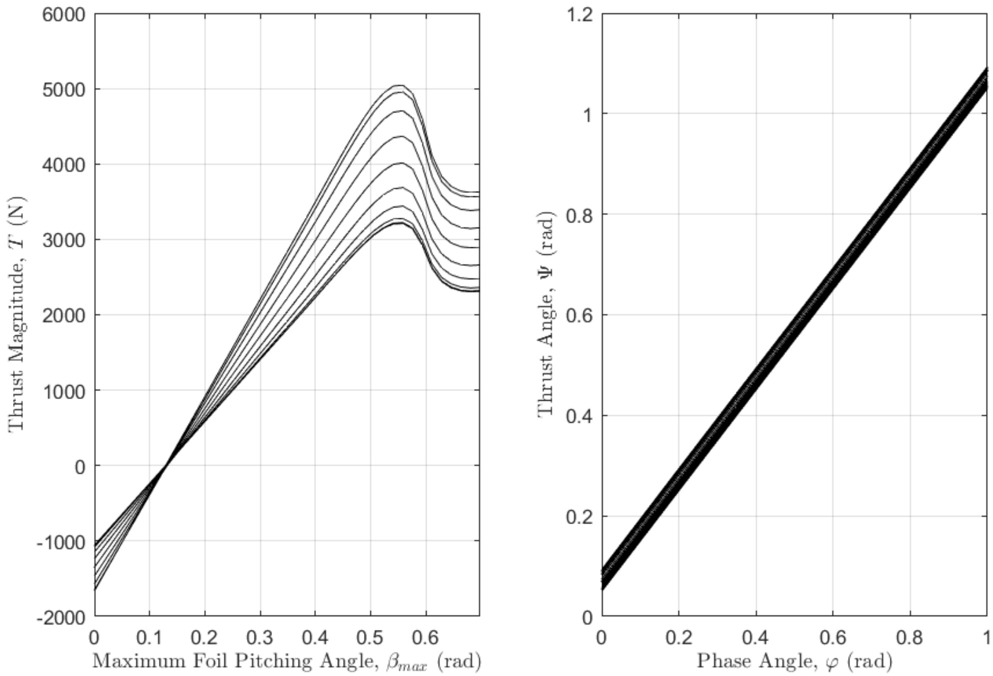

Figure 4.5. Relationships between turbine thrust and turbine controls, for 0 m/s current, 0 m/s vehicle speed, at 286 RPM. Left: Thrust magnitude vs. maximum foil pitching angle, for a range of phase angles from 0 to 90°. There is a strong dependence on phase angle. Right: Thrust direction vs. turbine phase angle, for a range of maximum foil pitching angles from 20 to 40°.

$$\beta_{max} - \frac{U_{local}\cos\varphi + W_{local}\sin\varphi}{nD} \tag{4.20}$$

while the thrust angle is corrected by

$$\frac{\Psi}{(3.3(U_{local} + W_{local})/nD) + 1} + \frac{5W_{local}}{nD} + 0.0773 \tag{4.21}$$

for the top turbines and

$$\frac{\Psi}{(3.3(U_{local} + W_{local})/nD) + 1} + \frac{5W_{local}}{nD} - 0.0773 \tag{4.22}$$

for the bottom turbines to account for their counter-rotation. Application of these corrections allow the curves in Fig. 4.7 to be collapsed to a more compact solution as shown in Fig. 4.8.

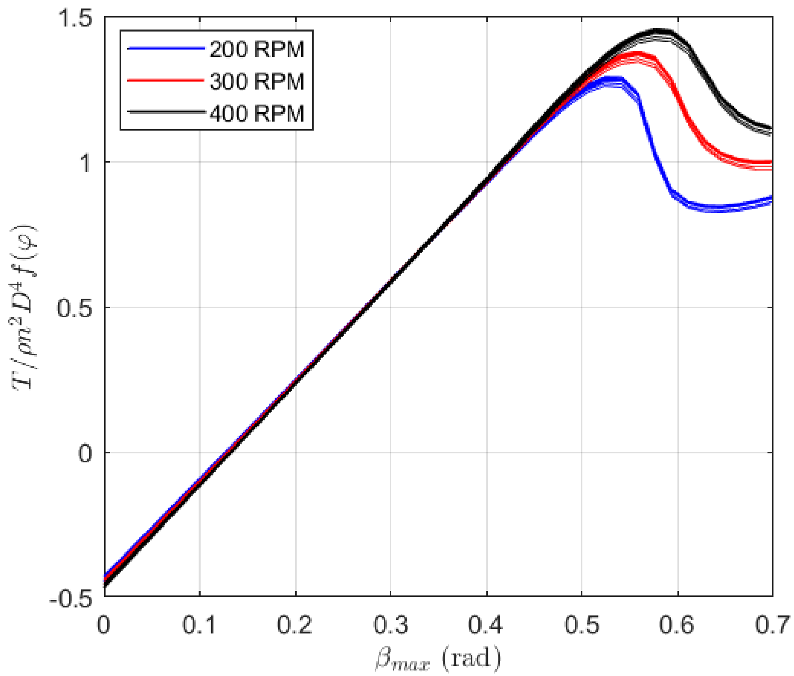

Figure 4.6. Nondimensionalized thrust magnitude vs. maximum foil pitching angle, for a range of phase angles from 0 to 90°. Top port turbine data shown at 200, 300, and 400 RPM.

Despite some nonlinearity at higher speeds for higher maximum foil pitching angles, the turbine phase angle is approximately linearly related to the corrected expression for the turbine thrust angle

$$\varphi = \frac{\Psi}{(3.3(U_{local} + W_{local})/nD) + 1} + \frac{5W_{local}}{nD} + 0.0773. \tag{4.23}$$

for the top turbines and

$$\varphi = \frac{\Psi}{(3.3(U_{local} + W_{local})/nD) + 1} + \frac{5W_{local}}{nD} - 0.0773. \tag{4.24}$$

for the bottom turbines. Therefore, given a desired turbine thrust angle, a corresponding turbine phase angle can be simply calculated as a function of the local velocities and the turbine rotation rate. This turbine phase angle can be used to solve for the maximum foil pitching angle required for a desired thrust magnitude

$$\beta_{max} = \frac{T}{a\rho n^2 D^4 f_\delta(\varphi)} - \frac{b}{a} + \frac{U_{local}\cos\varphi + W_{local}\sin\varphi}{nD} \tag{4.25}$$

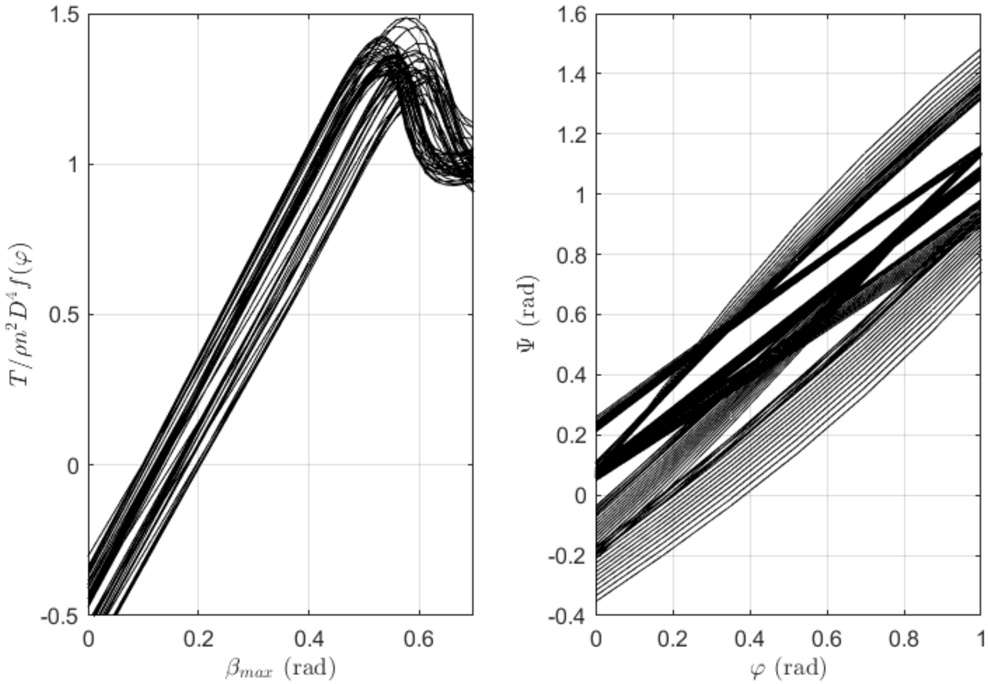

Figure 4.7. Relationships between turbine thrust and turbine actuators at 286 RPM, for combinations of local longitudinal and heave velocities from 0 to 1 m/s. Left: Nondimensionalized thrust magnitude vs. maximum foil pitching angle, for a range of phase angles from 0 to 90°. Right: Thrust direction vs. turbine phase angle, for a range of maximum foil pitching angles from 20 to 40°.

where $a = 3.5$ is the average slope of the curves shown in Fig. 4.8 in the linear region below blade stall and $b = -0.4$ is the average y-intercept value. These values are adjusted slightly in simulation to trim the vehicle.

4.3.3 Outer Loop Control Design

The NDI architecture in Fig. 4.3 uses the inner feedback linearization loop to remove nonlinearities and internal dynamics of the system, as we have discussed in the prior sections. Now the so-called "outer loop" is designed to eliminate tracking error due to external disturbances, modeling error, and other factors. The feedback linearization loop effectively linearizes the plant model, and converts it to a system of de-coupled integrators. Thus, the outer loop design can employ classical analytical methods to assign the poles of the error dynamics.

Let's begin by differentiating the output equation of the state space model:

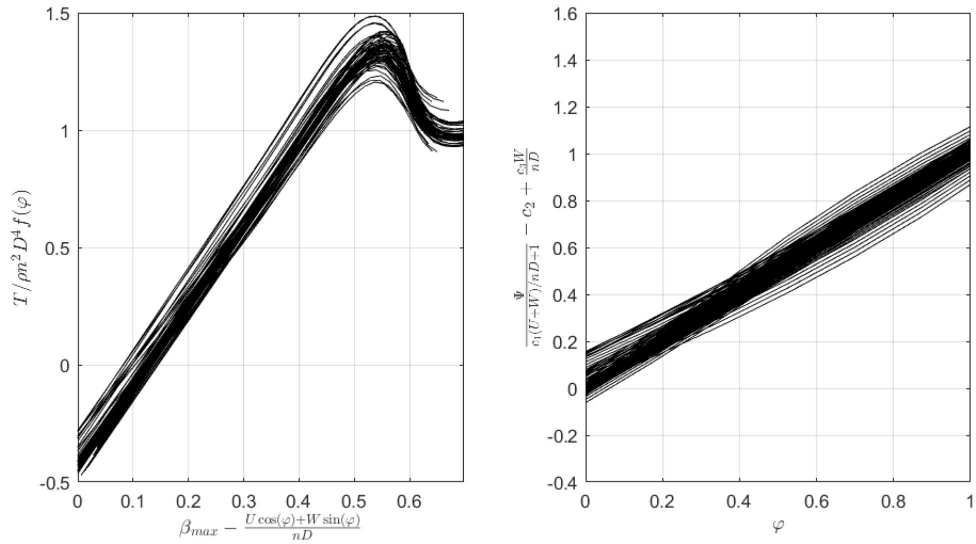

Figure 4.8. Relationships between turbine thrust and turbine actuators at 286 RPM, for combinations of local longitudinal and heave velocities from 0 to 1 m/s. Left: Nondimensionalized thrust magnitude vs. corrected maximum foil pitching angle, for a range of phase angles from 0 to 90°. Right: Corrected thrust angle vs. turbine phase angle, for a range of maximum foil pitching angles from 20 to 40°.

$$\dot{y} = \frac{\partial h}{\partial x}(x)\dot{x} = F(x) + G(x)u \tag{4.26}$$

where

$$\begin{aligned} F(x) &= \frac{\partial h}{\partial x}(x) f(x) \\ G(x) &= \frac{\partial h}{\partial x}(x) g(x). \end{aligned} \tag{4.27}$$

The feedback linearization control law is then

$$u = G^{-1}(x)[\nu - F(x)] \tag{4.28}$$

where ν is the pseudo-control vector. Substituting the control law into Eq. 4.26 yields:

$$\dot{y} = \nu. \tag{4.29}$$

The pseudo-control is defined by

$$\nu = \dot{y}_{cmd} + C(s)e \tag{4.30}$$

where $\dot{y}_{cmd}$ is the reference feedforward command and $C(s)$ is the linear compensation on the tracking error e. Combining Eqs. 4.29 and 4.30 yields

$$\dot{y} = \dot{y}_{cmd} + C(s)e. \tag{4.31}$$

The error is defined as

$$e = y_{cmd} - y \tag{4.32}$$

which is the difference between the commanded output and the actual system output. Differentiating the error equation yields

$$\dot{e} = \dot{y}_{cmd} - \dot{y} \tag{4.33}$$

Substituting Eq. 4.33 into Eq. 4.31 and accounting for system disturbances, we find the error dynamics

$$\dot{e} + C(s)e = \Delta(s) \tag{4.34}$$

where $\Delta(s)$ is a disturbance to the system.

The goal of the controller is to minimize the tracking error e. Consider a controller with a transfer function

$$\begin{aligned} C(s) &= K_P + \frac{K_I}{s} + \frac{K_{I2}}{s^2} \\ &= \frac{K_P s^2 + K_I s + K_{I2}}{s^2} \end{aligned} \tag{4.35}$$

to be applied to Eq. 4.34

$$se(s) + \frac{K_P s^2 + K_I s + K_{I2}}{s^2} e(s) = \Delta(s). \tag{4.36}$$

where the error has also been transformed using Laplace transforms. Equation 4.36 can be rearranged

$$\frac{e(s)}{\Delta(s)} = \frac{s^2}{s^3 + K_P s^2 + K_I s + K_{I2}} \tag{4.37}$$

and the roots of the error dynamics found from the polynomial

$$s^3 + K_P s^2 + K_I s + K_{I2}. \tag{4.38}$$

The gains are found by matching this characteristic polynomial with the standard polynomial for a third order system

$$(s^2 + 2\zeta\omega_n s + \omega_n^2)(s + p). \tag{4.39}$$

Thus the poles of the error dynamics can be set to a desired pair of complex poles and one real pole via

$$\begin{aligned} K_P &= p + 2\zeta\omega_n \\ K_I &= \omega_n^2 + 2\zeta\omega_n p \\ K_{I2} &= p\omega_n^2 \end{aligned} \tag{4.40}$$

The natural frequency, ω_n, determines the speed of the response, while the damping ratio, ζ, determines the shape of the response. The real pole p primarily governs the integrator action. It is selected to have a suitable frequency separation from the other two poles, and so a good rule of thumb is $p = \omega_n/5$ [76].

Controllers are designed for relative longitudinal velocity, depth, roll, pitch, and yaw. For the relative velocity, K_P and K_I in Eq. 4.40 are the proportional and integral gains on the velocity error. The constant p is set to zero since the steady-state error to a ramp input is not required for the relative longitudinal velocity control. With p equal to zero, K_{I2} is zero. The natural frequency is set to 1 rad/s and the damping ratio is set to 0.7.

For the other controllers, K_P, K_I, K_{I2} in Eq. 4.40 are actually implemented as the derivative, proportional, and integral gains respectively for the depth and the roll, pitch, and yaw attitudes. These are equivalent to K_P, K_I, K_{I2} for depth rate and roll, pitch, and yaw rates. For the depth, roll, and yaw controllers, the natural frequency is set as 2 rad/s, the damping ratio as 0.7, and the constant p as $\omega_n/5$. For the pitch controller, the natural frequency is set as 3 rad/s, the damping ratio as 1.2, and the constant p as $\omega_n/5$. The gains are summarized in Tab. 4.6.

Table 4.6. NDI outer loop controller gains.

State	K_P **(1/rad)**	K_I **(1/(rad·s))**	K_D **(1/(rad/s))**
Relative Velocity	1.6	1.28	0
Depth p_D	5.12	1.6	3.2
Roll ϕ	5.12	1.6	3.2
Pitch θ	7.8	13.32	5.4
Yaw ψ	5.12	1.6	3.2

4.4 Evaluation of Controller Performance

The performance of the controllers are assessed in simulation. The vehicle begins each simulation cruising at a 24 m depth. The simulated vehicle is moving North at 1 m/s, in a 1 m/s current moving North. The turbines are rotating at 286 RPM. The response of each controller is evaluated for individual two-second commands to speed up and slow down, vehicle dive and rise, and commands to pitch and yaw. The control commands for acceleration, and depth, pitch, and yaw rate pass through a first order command filter and then are integrated to obtain the desired trajectory, r. The command filters are

$$\text{Fil}(s) = \frac{2}{s+2} \tag{4.41}$$

using an integrator and a gain factor of 2.

Figures 4.9-4.14 show how the controllers respond to different vehicle commands. The response is mainly evaluated by comparing overshoot, OS, and settling time, t_s. For the step inputs performed here, overshoot is defined as the peak response value minus the commanded step value divided by the step value. Settling time is the time it takes for the error between the response and the steady-state response to fall to within 2% of the steady-state response.

Both controllers track commands to slow down well, i.e. there is no overshoot or steady-state error, with fast settling times. The NDI controller does not track a command to increase forward relative velocity as well as the classical controller, but settles to the desired speed with no steady state error a few seconds later. The response to depth commands (here a 1 m rise and a 0.6 m dive) are comparable between the controllers. The vehicle response differs slightly when assessing yaw

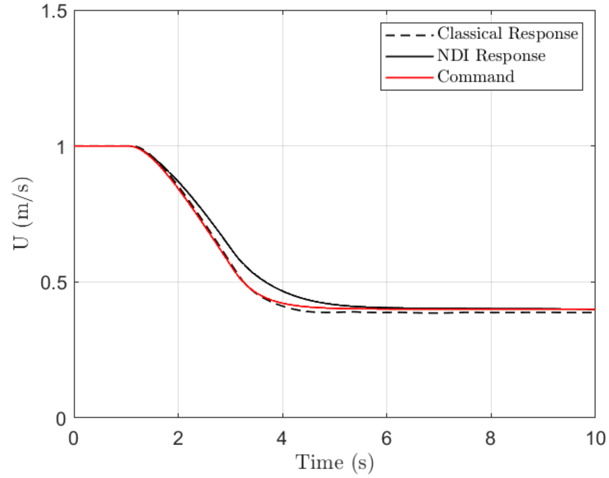

Figure 4.9. Vehicle response comparison between classical controllers and NDI controllers. Response is shown for command to slow down.

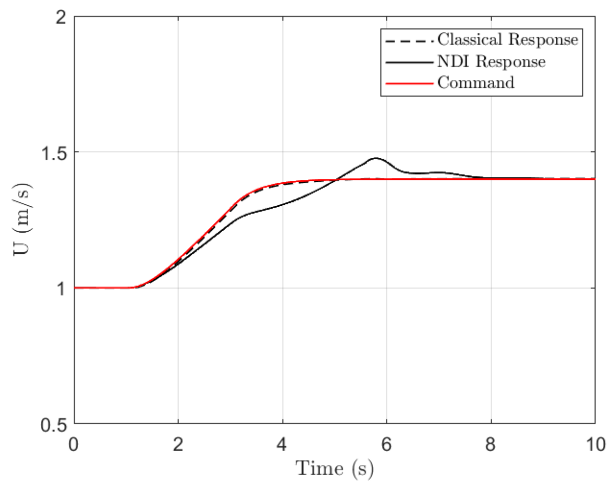

Figure 4.10. Vehicle response comparison between classical controllers and NDI controllers. Response is shown for command to speed up.

and pitch commands. The settling time for a yaw command is slightly longer for the vehicle with NDI controllers than for the vehicle with classical controllers. Additionally, the NDI-controlled vehicle has a higher pitch overshoot response and longer settling time than for the classical controller. The response of the NDI controllers are still good overall for the neutrally buoyant vehicle.

The real advantage, however, of the NDI-controlled vehicle is that it outperforms the classically-controlled vehicle in the nonlinear operating regime, i.e. for maneu-

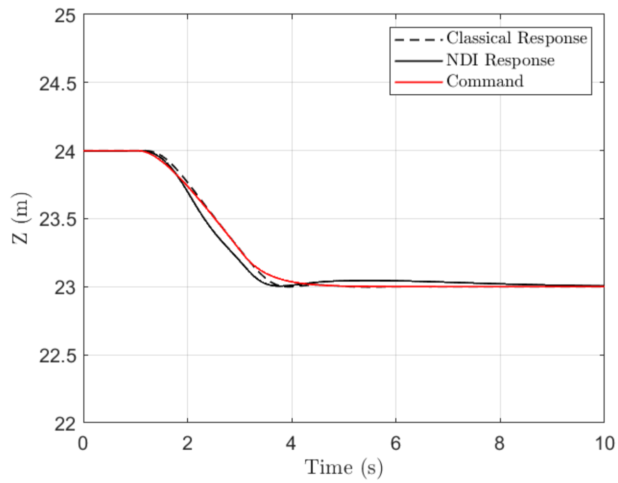

Figure 4.11. Vehicle response comparison between classical controllers and NDI controllers. Response is shown for rise command.

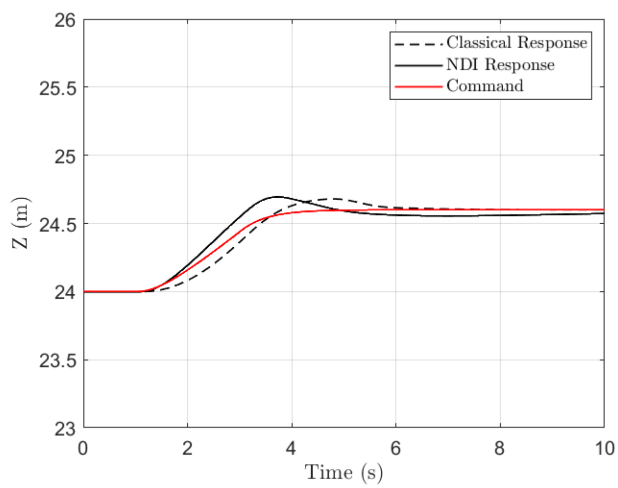

Figure 4.12. Vehicle response comparison between classical controllers and NDI controllers. Response is shown for dive command.

vers such as hover. The NDI controllers not only widen the vehicle performance window, but additionally outperform classical control for the actual SSD, that is truly negatively buoyant. Figure 4.15 shows the response of the SSD, without the added buoyancy pod, to individual commands to slow down. As the vehicle slows down to $U = 0$ m/s, the NDI controller continues to track the desired command. The classical controllers, however, start to diverge and become unstable as the command speed decreases.

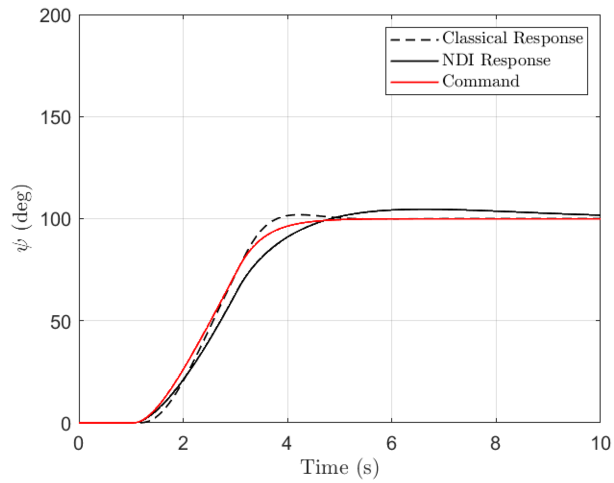

Figure 4.13. Vehicle response comparison between classical controllers and NDI controllers. Response is shown for yaw command.

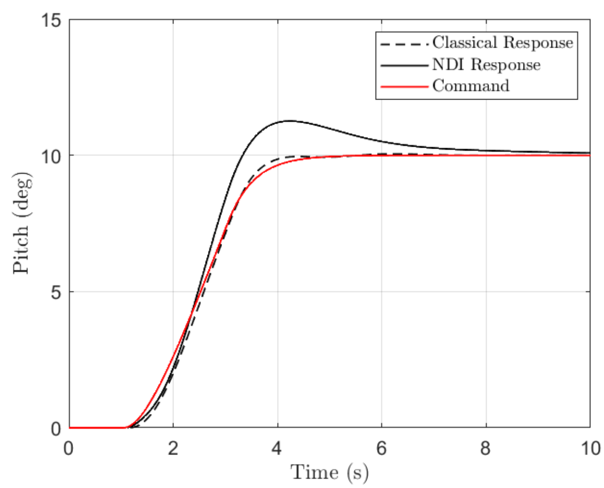

Figure 4.14. Vehicle response comparison between classical controllers and NDI controllers. Response is shown for pitch command.

Figures 4.16-4.21 show the response of the SSD to individual commands to speed up, slow down, rise, dive, yaw, and pitch. The NDI controllers track the commands with little overshoot, and fast settling times. The vehicle responds quickly to speed commands. Additionally, the controller is shown to track depth commands well. The vehicle is shown to yaw 100° in less than 4 seconds. The controller still overshoots a pitch command, with some settling time, as noted earlier.

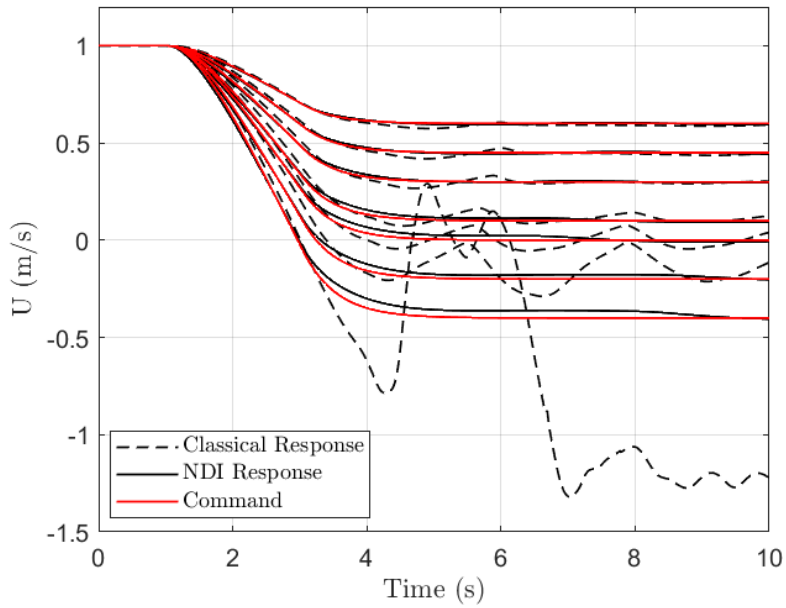

Figure 4.15. Comparison of SSD (without additional buoyancy pod) response with classical vs. NDI control. Response is shown for increasing commands for the vehicle to slow down. The vehicle starts the simulation moving North at 1 m/s, in a 1 m/s current moving North with the vehicle.

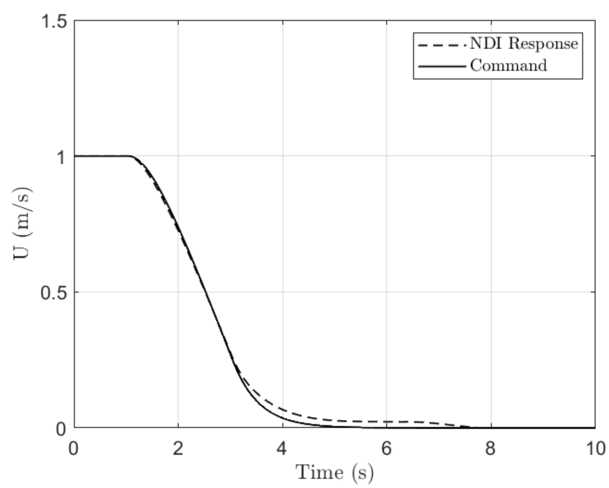

Figure 4.16. Simulated SSD response with NDI controllers. Response is shown for command to slow down.

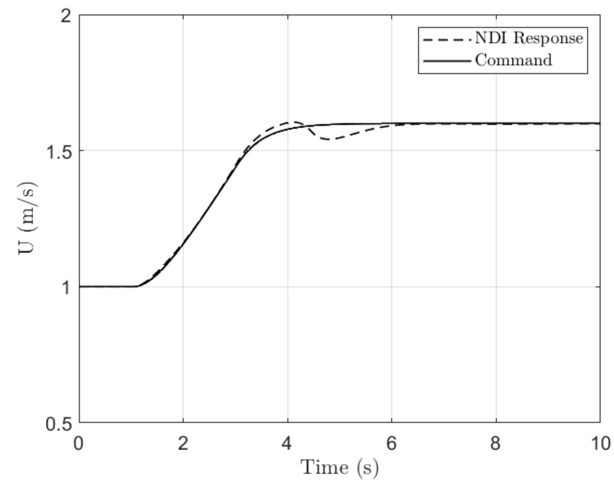

Figure 4.17. Simulated SSD response with NDI controllers. Response is shown for command to speed up.

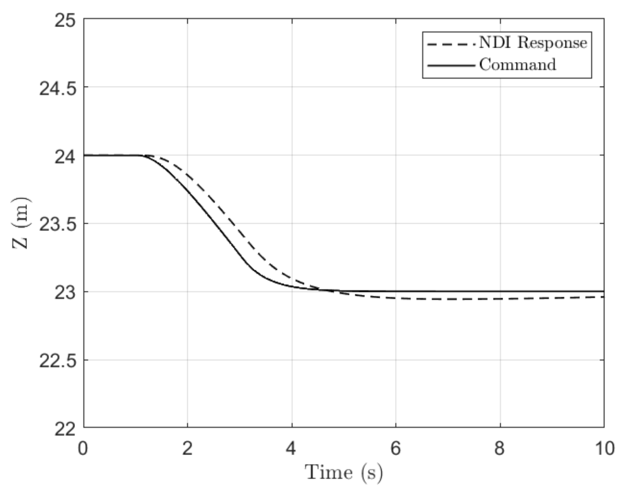

Figure 4.18. Simulated SSD response with NDI controllers. Response is shown for rise command.

It is also worth noting that the maximum foil pitching angle and phase angle for each turbine change smoothly when the vehicle decreases speed (see Fig. 4.22). For a neutrally buoyant vehicle, when the forces become small, the model has trouble resolving the turbine phase angles, resulting in rapid fluctuations. However, with a negatively buoyant vehicle, some upward force must be maintained to keep the vehicle at depth. This helps minimize the turbine phase angle changes at the hover condition.

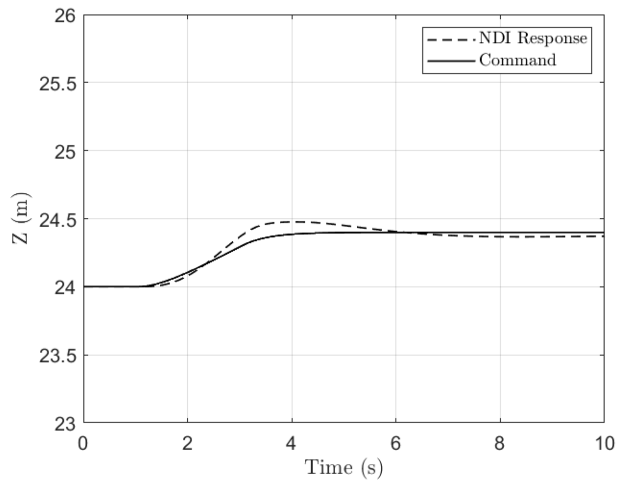

Figure 4.19. Simulated SSD response with NDI controllers. Response is shown for dive command.

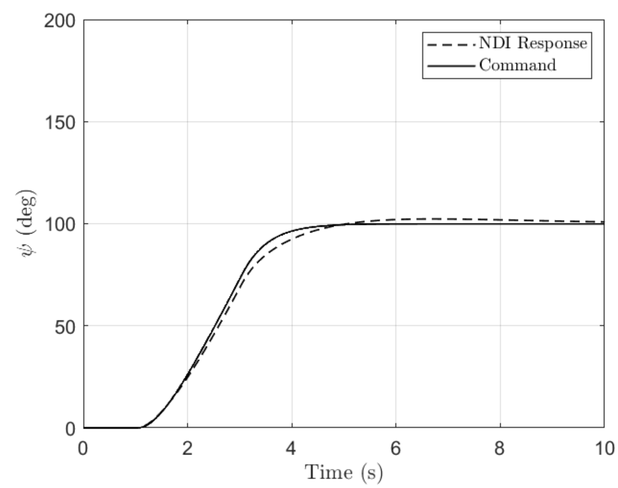

Figure 4.20. Simulated SSD response with NDI controllers. Response is shown for yaw command.

Finally, the response of the SSD (no added buoyancy pod) to an example mission is shown in Fig. 4.23. The vehicle begins the simulation at a depth of 1 m moving forward at a relative velocity of 2 m/s. The vehicle dives to 6 m over 20 s. The vehicle is then commanded to hover. The NDI controllers are able to track this velocity trajectory with little error. As the vehicle speed decreases, there is some fluctuation in the vehicle depth. The vehicle is then commanded to speed up to a relative velocity of 1 m/s and enter a yaw maneuver. The vehicle turns 180° over 2

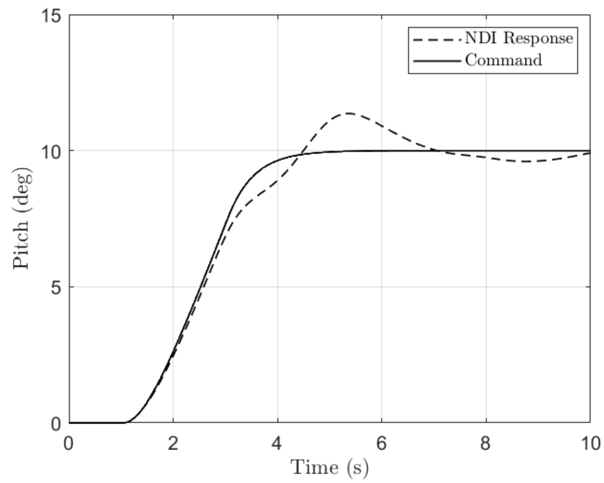

Figure 4.21. Simulated SSD response with NDI controllers. Response is shown for pitch command.

seconds: the control performance in yaw is clearly robust. Finally, the vehicle is commanded to rise to its originating depth at 1 m.

This example mission shows that the NDI controllers successfully maneuver the vehicle.

4.5 Concluding Remarks

Classical control methods are used to design controllers for an MHK cycloturbine vehicle. Classical controllers work better for a less negatively-buoyant system; these controllers fail to stabilize the original Subscale Demonstrator system at hover condition. These controllers don't account for system nonlinearities and so are not as robust as nonlinear controllers.

Nonlinear dynamic inversion is used as a basis to design more robust controllers. The control inputs are defined as the individual turbine forces in the X and Z directions. The pseudo inverse method is used to combine the control inputs into the desired vehicle forces and moments. Analytical expressions that relate the desired thrust vector for each turbine to actuator commands are found. By accounting for the nonlinearities in an inner feedback linearization loop, linear design techniques are used to create compensators for the outer loop tracking.

The NDI controller outperforms the fully classical controller in the nonlinear

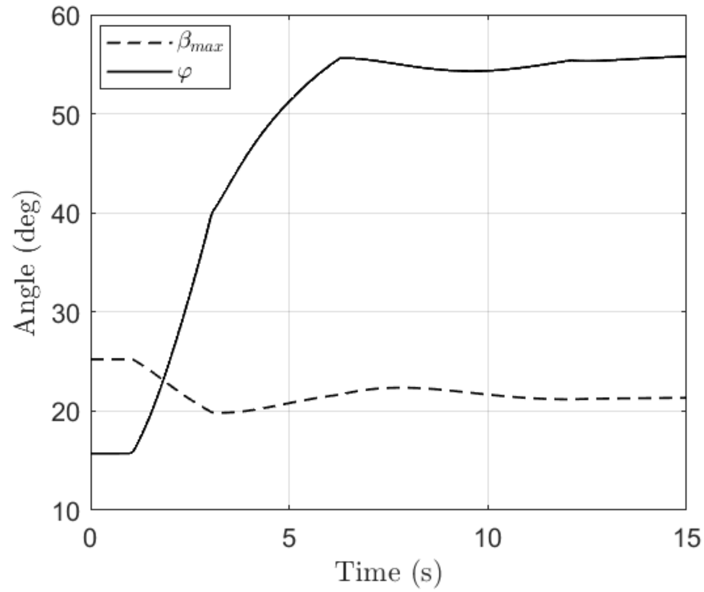

Figure 4.22. Actuator response on the top starboard turbine for command to bring SSD to a hover in simulation.

operating regime. The NDI controller allows for more complex maneuvers such as vehicle hover and station keeping.

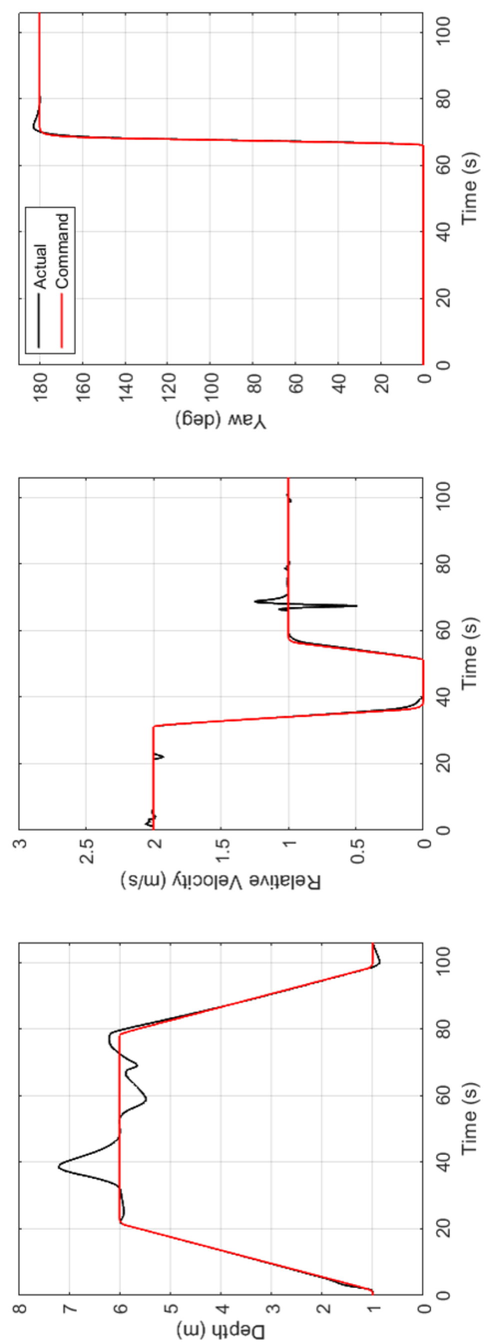

Figure 4.23. Simulation of an example mission for the SSD using NDI controllers. The vehicle is commanded to dive, hover, speed up, yaw, and rise.

5 Tonal Noise Reduction for a Marine Hydrokinetic Cycloturbine Vehicle [1]

5.1 Overview

It is anticipated that the Marine Hydrokinetic vehicle will produce and experience steady and unsteady loads due to the cyclic nature of the turbomachines. The acoustic work in this dissertation is concerned with the unsteady loads in terms of fatigue loads and radiated sound, i.e. acoustic control is important to curtail the MHK vehicle's vibrations and acoustic signature, to reduce the vehicle's fatigue for longer deployment as well as to potentially prevent harmful effects on aquatic life.

The MHK vehicle in this dissertation consists of four counter-rotating cycloturbines. Each turbine foil radiates noise equivalent to an acoustic dipole at multiples of blade rate frequency, and so the vehicle is modeled as an acoustic multipole. At blade rate frequency, the turbine size compared to its acoustic wavelength allows for the turbine to be treated as a compact source. A method of reducing the radiated acoustics of the vehicle is determined for tones at blade rate frequency and multiples, by means of clocking the blades between turbines. The effect of turbine clocking on directivity and sound power is shown. This method to reduce tonal noise at blade rate frequency and multiples is applied experimentally through testing of a Subscale Demonstrator (SSD) in ARL's Reverberant Tank facility. Fixing the SSD to a reaction frame provides the ability to measure the integrated

[1] The work presented in this chapter has been published in the Proceedings of the 2017 and 2019 ASME International Mechanical Engineering Conference and Exposition and is accepted for publication by the ASME Journal of Vibration and Acoustics.

loads using load cells. These measurements verify the effects of turbine clocking on the radiated acoustics.

5.2 Sound Radiation from a Concentrated Hydrodynamic Force

To reduce vibrations and radiated acoustics at blade rate frequency and multiples, the radiated pressure field from the MHK vehicle must first be understood. The series of steps used to obtain the compact solution will be summarized here.

Aerodynamic noise theory begins with Lighthill's formulation of the wave equation for a concentrated region of turbulent fluid motion. Lighthill's work [77–79] is unique because it considers the region as an acoustic source that drives the surrounding fluid. In the absence of mass-injection, Lighthill's formulation of the wave equation is:

$$\frac{\partial^2 \rho}{\partial t^2} - a_0^2 \nabla^2 \rho = \frac{\partial^2 T_{ij}}{\partial y_i \partial y_j} \tag{5.1}$$

where ρ is the density of the fluid, a_0 is the acoustic velocity, and

$$T_{ij} = \rho u_i u_j + (p - a_0^2 \rho)\delta_{ij} + \tau'_{ij} \tag{5.2}$$

is the Lighthill stress tensor. The first term $\rho u_i u_j$ in the tensor is the Reynolds stress, and quantifies the intensity of the turbulence in the source region. The second term $p - a_0^2 \rho$ expresses the difference between the actual pressure fluctuations and the purely isentropic density fluctuations in the medium. The final term τ'_{ij} is the viscous part of the Stokes stress tensor. Often the magnitude of the Reynolds stresses dominate the viscous stresses and so this last term may be neglected. Additionally, if the pressure fluctuations in the fluid region are everywhere isentropic with speed of sound a_0, then the second term in the Lighthill stress tensor cancels, reducing the wave equation to:

$$\frac{\partial^2 (\rho - \rho_0)}{\partial t^2} - a_0^2 \nabla^2 (\rho - \rho_0) = \frac{\partial^2 (\rho u_i u_j)}{\partial y_i \partial y_j} \tag{5.3}$$

where p_0 and ρ_0 are the pressure and density in the far-field ambient undisturbed fluid [80]. The far-field region begins at least one acoustic wavelength away from the source. It is the region where pressure and particle velocity are in phase, and energy is being radiated away from the source in the form of sound waves.

Lighthill's equation can be reformulated using Kirchhoff's equation for the fluctuating fluid density to include the acoustic phase interactions that occur between sources in a control volume when solid surfaces are not present:

$$4\pi(\rho(\mathbf{x},\mathbf{t})-\rho_\mathbf{0}) = \frac{\mathbf{1}}{\mathbf{a_0^2}}\frac{\partial^\mathbf{2}}{\partial\mathbf{x_i}\partial\mathbf{x_j}}\iiint\limits_{\mathbf{V}}\frac{\mathbf{T_{ij}}(\mathbf{y},\mathbf{t}-\frac{\mathbf{R}}{\mathbf{a_0}})}{\mathbf{R}}\mathbf{dV}(\mathbf{y}) \tag{5.4}$$

where x_i is the field point, y are the coordinates of the sources, R is the distance magnitude from the source to the field, and V is the control volume. Curle [81] extends this work to account for the effect of reflecting boundaries:

$$\begin{aligned}4\pi(\rho(\mathbf{x},\mathbf{t})-\rho_\mathbf{0}) =& \frac{1}{a_0^2}\frac{\partial^2}{\partial x_i\partial x_j}\iiint\limits_{V}\frac{[T_{ij}]}{R}dV(\mathbf{y}) \\ &-\iint\limits_{S}\frac{l_i}{R}\left[\frac{\partial(\rho u_i)}{\partial t}\right]dS(\mathbf{y}) \\ &+\frac{\partial}{\partial x_i}\iint\limits_{S}\frac{l_j}{R}[\rho u_i u_j+p_{ij}]dS(\mathbf{y})\end{aligned} \tag{5.5}$$

where l_i is the outward surface normal, and the brackets [] denote the retarded time $t - R/a_0$. The solid surface affects the sound field by causing acoustic reflections. From Curle's result, it is found that the sound pressure at each hydrofoil in the MHK vehicle is the resultant of three contributions [80]:

1. Radiation from the turbulent domain.

2. Contribution from the acceleration of the body in a direction normal to its surface.

3. Radiation from a distribution of forces acting on the region.

With respect to the turbulent radiation, Curle argues from dimensional analysis that the turbulent fluctuations compared to the surface terms scale as the square of the Mach number [82]. Therefore, this contribution to the sound pressure may be neglected for the hydrodynamic work here (since the vehicle operates at low Mach numbers). Hence, the radiated sound from the pitching foils is mainly due to

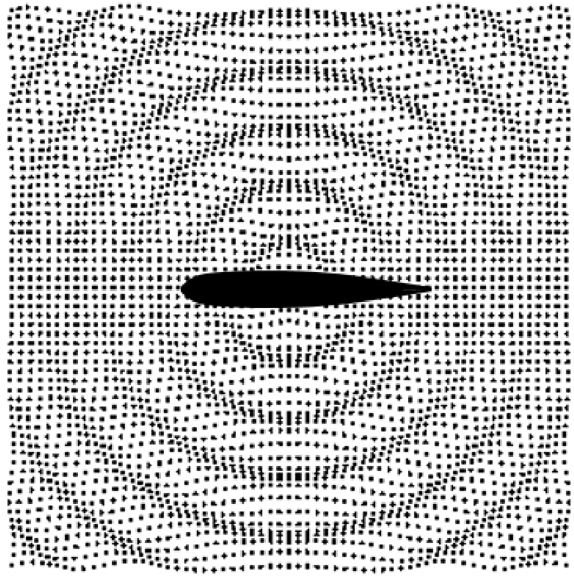

Figure 5.1. Dipole radiation from a concentrated hydrodynamic source.

direct motion of the foils and the local pressure field induced by the fluid reacting to the vibrations.

By assuming a constant fluid density in the source region, Curle's equation can be linearized. Koopmann [83, 84] transforms Curle's equation and simplifies it for rigid bodies whose dimension is less than an acoustic wavelength (compact source). Then, the radiated acoustic pressure can be related to the hydrodynamic force of the hydrodynamic structure by

$$p - p_0 = -\frac{x_i}{4\pi R^2}\left[\frac{\dot{F}_i + \rho_0 V \ddot{U}_i}{a_0} + \frac{F_i + \rho_0 V \dot{U}_i}{R}\right] \tag{5.6}$$

where the raised dot represents the time derivative [82]. The first term in this free-field equation is the far-field contribution to the radiated acoustic pressure and the second term is the near-field contribution. The following analysis focuses on the far-field radiation, and assumes that the hydrodynamic forces dominate the direct motion terms:

$$\hat{p} = -\frac{x_i}{4\pi R^2}\frac{\dot{F}_i}{a_0} \tag{5.7}$$

to obtain a simpler expression for the radiated pressure field. This equation is an equivalent form of the classical aerodynamic dipole sound from a compact source (see Fig. 5.1) [80]. Using this definition for pressure, the time-averaged intensity of the radiated pressure field is

$$I = \frac{|\hat{p}|^2}{2\rho_0 a_0} \tag{5.8}$$

because the intensity in the far-field is radial [85]. This far-field sound intensity can be integrated over an arbitrary spherical surface that completely encloses the multipole to determine the radiated sound power:

$$L_W = \frac{\pi f^2 \langle F^2 \rangle}{6\rho_0 a_0^3}. \tag{5.9}$$

Sound power is a more useful measure of the effectiveness of sound radiation than maximum intensity [86]. The corresponding omnidirectional radiated acoustic pressure as a function of distance is given by

$$\langle \hat{p}^2 \rangle = \frac{L_W \rho_0 a_0}{4\pi R^2}. \tag{5.10}$$

These pressure levels can then be compared to any environmental acoustic requirements.

5.3 Model of Vehicle Acoustics

The vehicle dynamics are simulated to assist in the design of controllers for maneuver (refer to Chapters 3 and 4). This detailed simulation solves the six degree-of-freedom rigid body equations of motion for the maneuvering MHK system subject to the hydrodynamic lift and drag forces, hydrostatic forces, and the propulsive forces from the turbines. The dynamics model relies on a simplified hydrodynamic analysis of the propulsive forces generated by the turbines, as a function of the foil pitch schedule and vehicle state. The prescribed foil pitch schedule is sinusoidal, with a maximum pitching angle and phase angle.

In addition to producing the steady thrust magnitude and direction, the turbine force model provides the time-varying foil forces in the vehicle frame. As the turbine rotates, each of the foils experiences cyclic variation in its angle of attack, resulting in cyclic variation of the lift and drag forces. An example of the foil forces over one revolution produced at a turbine RPM of 286 is shown in Fig. 5.2. The

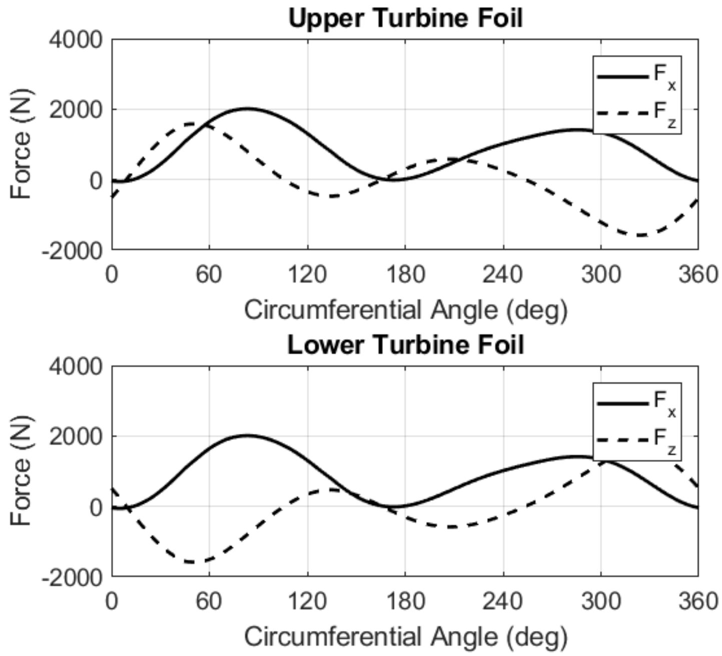

Figure 5.2. Time-varying foil forces at 286 RPM, forward thrust condition. Top: Upper turbine foil. Bottom: Lower turbine foil.

upper and lower foil forces in the X-direction are in-phase with each other, while the Z-direction forces are 180° out-of-phase. This is a result of counter-rotation between the top and bottom turbines. Additionally, there is a phase shift between the X-direction forces and the Z-direction forces for each foil. As stated, the total X- and Z-direction forces have contributions from both lift and drag, and the magnitudes of these contributions vary based on rotation of the foils.

The time-varying forces from each foil can be summed together in the vehicle frame, accounting for the 120° circumferential shift between blades (see Fig. 5.3). The total force produced from each foil is a sum of the steady force plus a fluctuating component. The fluctuating component of the forces contributes to the radiated acoustic pressure.

Since the objective of this research is to reduce tonal noise of the vehicle, it is desired to obtain the blade rate contribution to the fluctuating force component. It should be noted that the sound pressure radiation at blade rate frequency and multiples produced for each turbine is not affected by performing this force summation before calculation of the radiated pressure. In other words, computing the far-field pressure radiation from each turbine blade separately and accounting

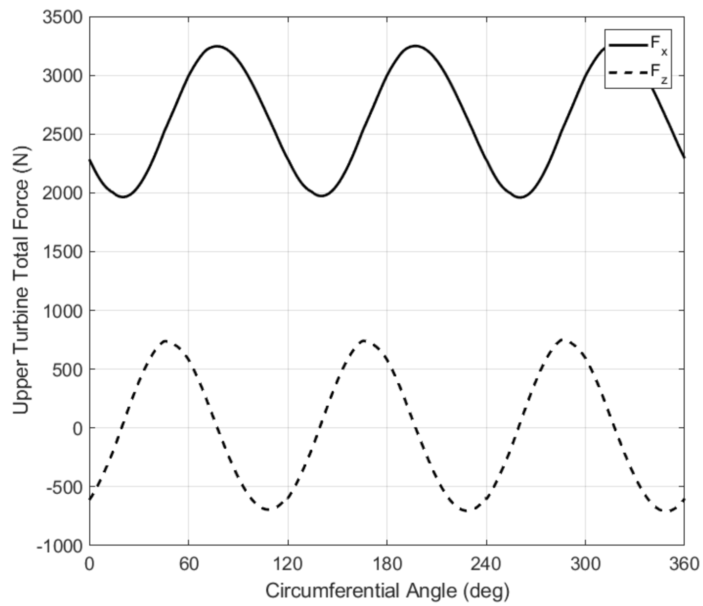

Figure 5.3. Time-varying upper turbine forces at 286 RPM, forward thrust condition.

for their relative distances to the far-field produces the same result as summing the blade forces and calculating the radiated pressure from the center of the turbine. This is because each turbine is a *compact source* as assumed in Sec. 5.2, i.e., the acoustic wavelength is larger than the turbine diameter, for the lower frequencies of interest.

The steady component of the forces is removed (see Fig. 5.4), and the fluctuating forces are converted from the time domain to the frequency domain using fast Fourier transforms (FFTs). The fluctuating force magnitudes at blade rate frequency (14.3 Hz for a 3-bladed turbine rotating at a rate of 286 RPM) and multiples are obtained. The phase angles for the fluctuating forces are also obtained from the FFT. The signals are then reconstructed with just the contribution from blade rate:

$$F_i = \sum_{n=-7, n\neq 0}^{7} \tilde{F}_{in} e^{j(2\pi n f_{bp} t + \varphi_n)} \tag{5.11}$$

the time derivative of which is

$$\dot{F}_i = \sum_{n=-7, n\neq 0}^{7} j(2\pi n f_{bp}) \tilde{F}_{in} e^{j(2\pi n f_{bp} t + \varphi_n)}. \tag{5.12}$$

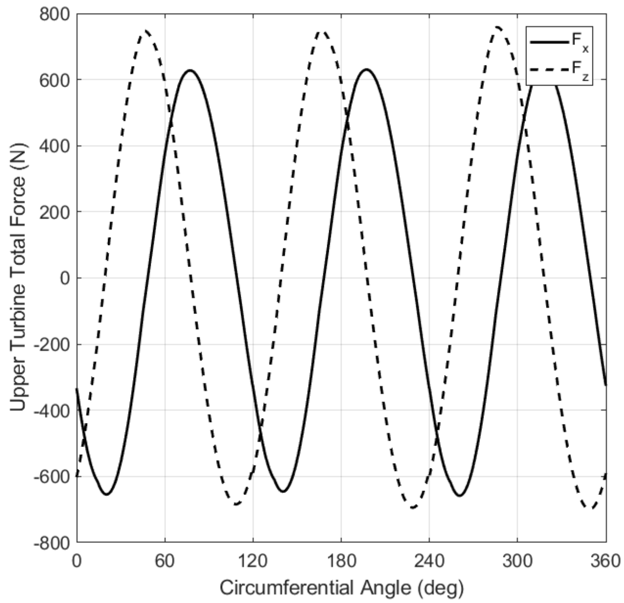

Figure 5.4. Fluctuating component of time-varying turbine forces. The case shown is at a turbine rotation rate of 286 RPM, for a forward thrust condition.

This summation is limited to an upper value of 7 times blade rate because the force output from the turbine propulsive model is negligible beyond this value. Using this expression, the radiated pressure can be determined from Eq. 5.7:

$$\hat{p} = \sum_{s=1}^{4} -\frac{x_{is}}{4\pi R_s^2}\frac{\dot{F}_{is}}{a_0} \tag{5.13}$$

for blade rate frequencies and all four turbines. The receiver location is a spherical sweep around the vehicle, centered in the vehicle:

$$\begin{aligned} \vec{r} &= x\hat{e}_x + y\hat{e}_y + z\hat{e}_z \\ x &= R\cos\theta\cos\phi \\ y &= R\sin\theta\cos\phi \\ z &= R\sin\phi \end{aligned} \tag{5.14}$$

where the distance R is large enough for the receiver to be in the far field ($kR \gg 1$). The receiver location is expressed in terms of an azimuthal angle θ from -180° to 180°, and an elevation angle ϕ from -90° to 90° (see Fig. 5.5).

Because the turbines are offset from the center of the vehicle, the distance from

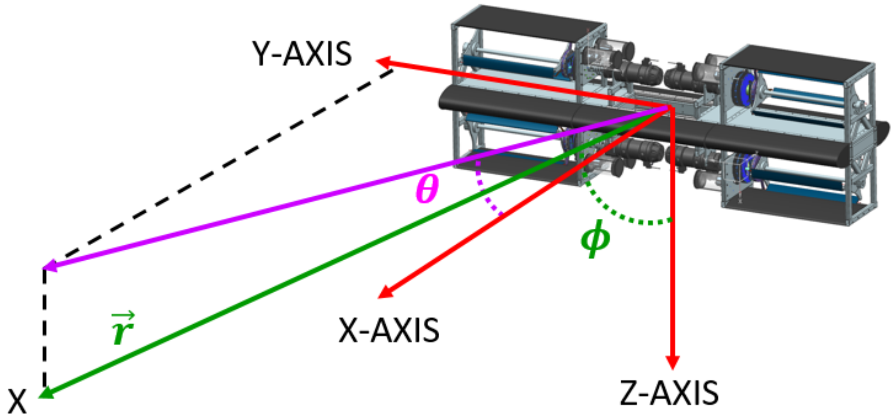

Figure 5.5. Definition of axes and angles for acoustic model.

the source to the receiver is different for each turbine:

$$R_s = \sqrt{(x - x_{0,s})^2 + (y - y_{0,s})^2 + (z - z_{0,s})^2} \tag{5.15}$$

where $x_{0,s}$, $y_{0,s}$, and $z_{0,s}$ are constants representing the offsets between the turbine sources and the center of the vehicle in the X-, Y-, and Z-directions. The magnitudes of $x_{0,s}$, $y_{0,s}$, and $z_{0,s}$ for the Subscale Demonstrator are 0 mm, 1429 mm, and 386 mm, respectively.

The time-invariant magnitude of the radiated pressure is used to compute the intensity and the sound power. The acoustic directivity of the multipole directly contributes to the radiated sound power. The directivity is affected by the alignment and polarity of the sources. This can be demonstrated for a set of sources radiating at the same frequency within a compact volume, using multipole expansions for Green's functions [85]

$$\begin{aligned} \hat{p} = S\frac{e^{ikR}}{R} - (\vec{D}\cdot\vec{\nabla})\frac{e^{ikR}}{R} + \\ \sum_{\mu,\nu=1}^{3} Q_{\mu\nu}\frac{\partial^2}{\partial x_\mu \partial x_\nu}\frac{e^{ikR}}{R} - \\ \sum_{\mu,\nu,\zeta=1}^{3} O_{\mu\nu\zeta}\frac{\partial^3}{\partial x_\mu \partial x_\nu \partial x_\zeta}\frac{e^{ikR}}{R} + \dots \end{aligned} \tag{5.16}$$

where S, D, Q, O are the monopole, dipole, quadrupole, and octopole amplitudes,

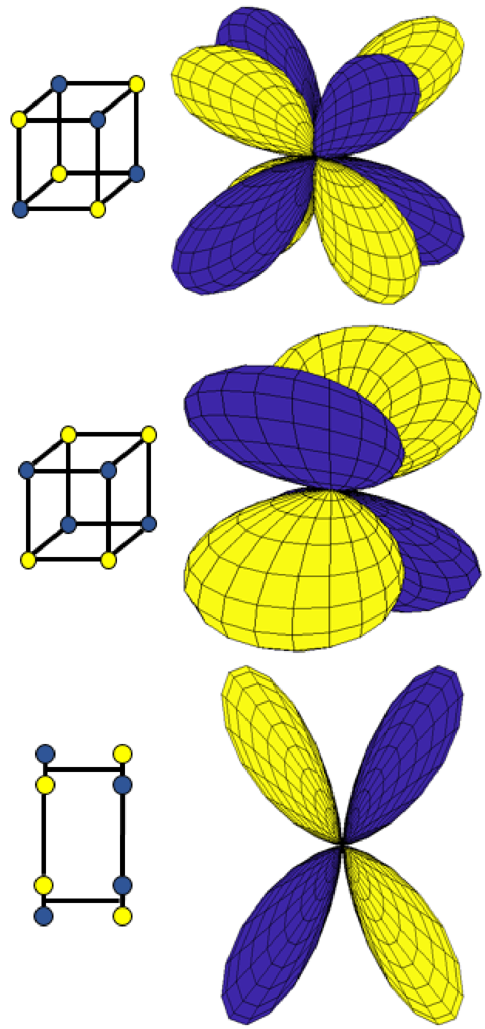

Figure 5.6. Effect of source alignment and polarity. Top: asymmetric lateral eight-pole. Middle: symmetric lateral eight-pole. Bottom: asymmetric longitudinal eight-pole.

respectively, and k is the wave number. In this expression, it is clear that the acoustic pressure field appears as a superposition of a monopole field plus a dipole field, plus a quadrupole field, plus an octopole field, etc. Depending on the alignment and polarity of the sources, different acoustic field terms become more dominant, and the contribution of their directivity affects the radiated sound power (see Fig. 5.6).

The dipole alignment is linearly related to the direction of the steady thrust (see Fig. 5.7), and independent of steady thrust magnitude (see Fig. 5.8). The polarity of each turbine source can be changed by adding an additional phase effect

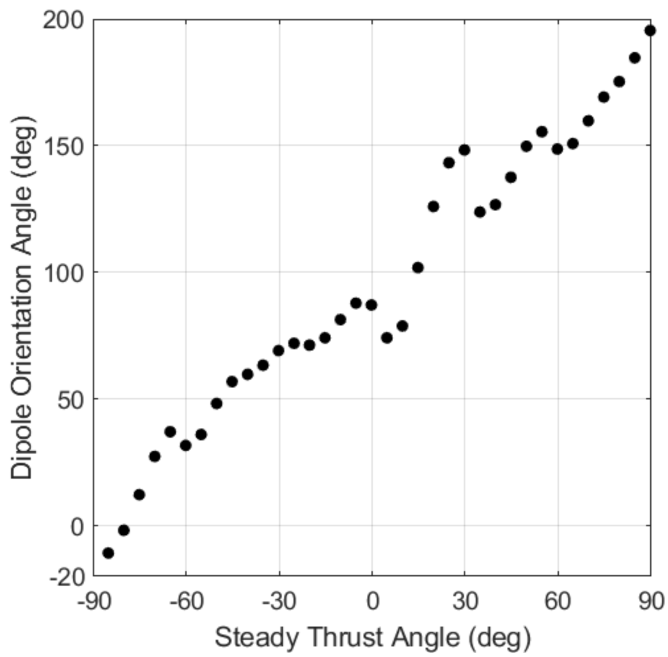

Figure 5.7. Dipole orientation angle relative to steady thrust angle at a constant magnitude of 2622 N.

into the time derivative of the fluctuating forces (for both the X- and Z-directions):

$$\dot{F}_i = \sum_{n=-7, n\neq 0}^{7} j(2\pi n f_{bp})\tilde{F}_{in} e^{j(2\pi n f_{bp} t + \varphi_n + \lambda)} \tag{5.17}$$

where λ is a constant angle between 0 and 180°. This phase effect is implemented physically by changing the relative rotational angle between turbines. Changing the rotational angle of adjacent turbines from hereon will be referred to as "turbine clocking." Figure 5.9 shows an example of turbine clocking. Iteration over all clocking options between turbines determines which clocking will minimize the sound power for a specified maneuver.

It is not only important for an acoustic controller to have information on what clocking is required to reduce the sound power, but it is also important to understand how much is gained by correcting the turbine to that clocking. For example, if the sound power in the far-field will only be reduced by 2 dB by adjusting the turbine clocking, then control may not be necessary.

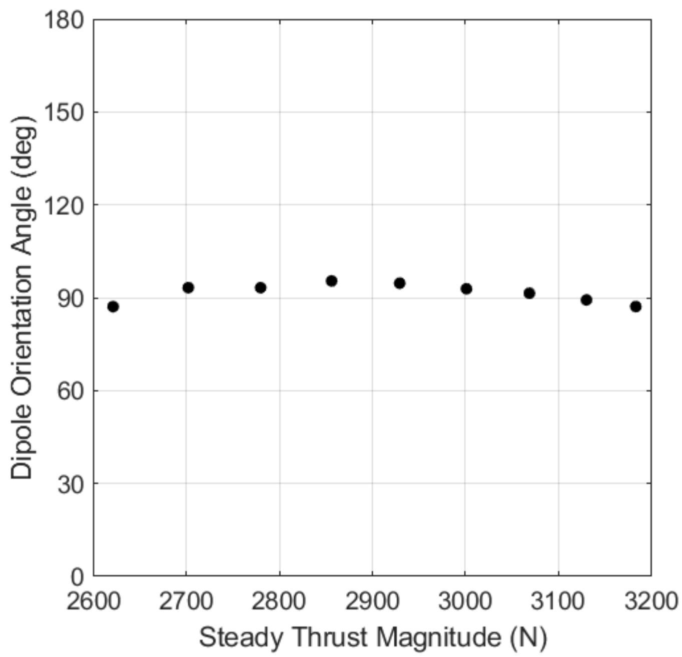

Figure 5.8. Dipole orientation angle relative to steady thrust magnitude at a constant thrust angle of 0°.

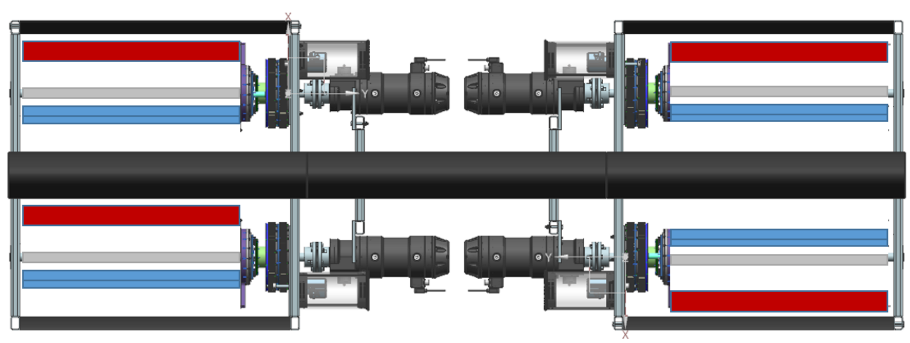

Figure 5.9. Demonstration of turbine clocking. Front view. Blade 1 highlighted in red. Upper and lower port side turbines are clocked in-phase with each other, upper and lower starboard turbines are clocked out-of-phase with each other.

5.3.1 Predicted Effect of Turbine Clocking for a Range of Vehicle Maneuvers

The turbine force model is used to create a map between the foil maximum pitching angle and phase angle, and the steady thrust magnitude and direction for a turbine rotation rate of 286 RPM (30 rad/s), for a no-current condition. This map is

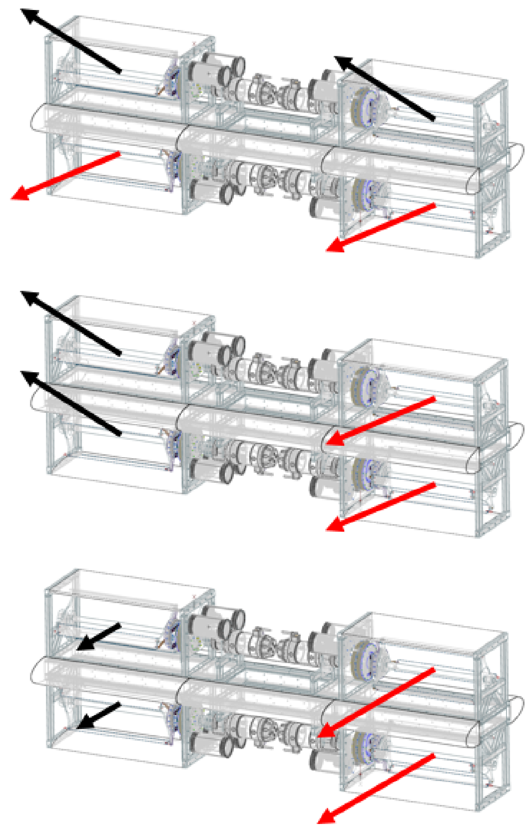

Figure 5.10. Maneuvers simulated for acoustic clocking study. Top: Scenario 1. Middle: Scenario 2. Bottom: Scenario 3.

resolved for a range of foil maximum pitching angles between 17° and 27° (high end limited by blade stall) in 0.5° increments, and a 360° sweep of phase angles in 1° increments. This map allows for many different maneuvering scenarios to be easily simulated. The subsequent analysis is for the following scenarios (refer to Fig. 5.10):

1. All turbines produce a constant thrust magnitude of 2600 N. Upper and lower turbines are separately vectored from -90 to 90° in 5° increments (1369 different maneuvers).

2. All turbines produce a constant thrust magnitude of 2600 N. Port and starboard turbines are separately vectored from -90 to 90° in 5° increments (1369 different maneuvers).

3. All turbines thrust forward. Port and starboard turbines separately sweep through a range of thrust magnitudes from 1800 to 3300 N (441 different maneuvers).

These maneuvers capture different pitch, roll, and yaw configurations. Forward and vertical thrust are also captured through these iterations.

Let us first consider the interaction between the upper and lower turbines (Scenario 1). All turbines are set to produce a constant thrust magnitude of 2600 N. The upper and lower turbines are separately vectored from -90 to 90°. For each vector configuration, the radiated pressure is computed for 9 different clocking configurations: 3 different clocking angles between the upper and lower turbines, and 3 different clocking angles between the port and starboard turbines. The clocking angles explored are 0°, 90°, and 180°. A clocking angle of 0° corresponds to turbines that are in-phase, while a clocking angle of 180° corresponds to turbines that are out-of-phase with each other. A finer resolution of clocking angles is not used because it is found not to have a significant effect on the results. Additionally, iteration over a coarse range of clocking angles reduces computation time.

From the radiated pressure, the sound intensity is determined. An example intensity in the far-field is shown for the case where the upper and lower turbines are thrusting forward at 0° (see Fig. 5.11). This case is for a clocking configuration that minimizes the sound power. Here, the turbines interact to form a quadrupole radiation pattern. Figure 5.12 shows the sound intensity field when the turbines are non-ideally clocked. It is apparent that dipole terms dominate the acoustic field.

A map of the ideal clocking between the upper and lower turbines is shown in Fig. 5.13. The optimal clocking angle between the port and starboard turbines is 180° for all vectoring cases.

The sensitivity of the radiated sound power for these combinations of vectoring is shown in Fig. 5.14. For each combination of steady thrust direction, the most sound power reduction is 42 dB, while the average sound power reduction is 39.5 dB. This reduction is significant. An acoustic controller would greatly reduce the tonal noise in cases of vehicle pitching.

Next, consider the interaction between the port and starboard turbines as outlined in Scenario 2. All turbines are set to produce a constant thrust magnitude of 2600 N. Port and starboard turbines are separately vectored from -90 to 90°. The ideal clocking between the port and starboard turbines is shown in Fig. 5.15.

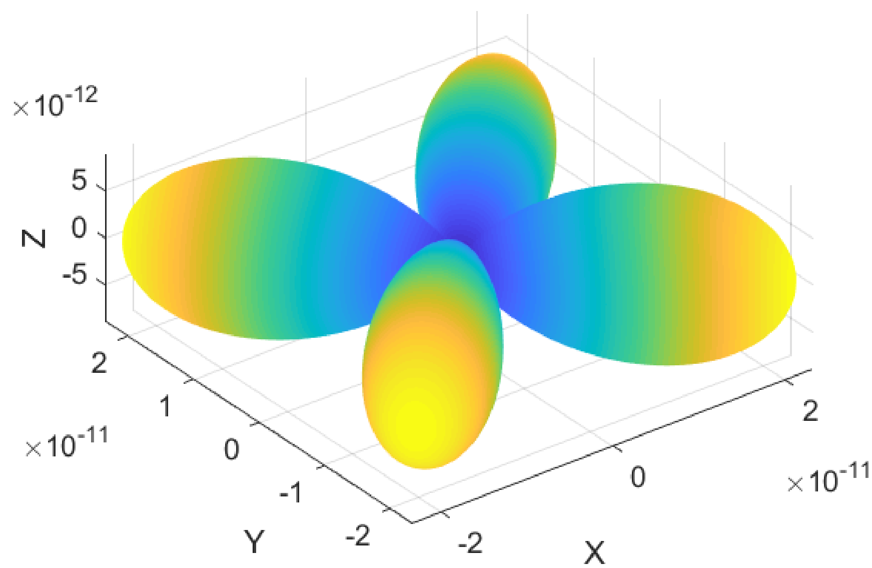

Figure 5.11. Example sound intensity for forward thrust case: optimal clocking. The turbines interact to form a quadrupole radiation pattern. Intensity in units of kg/s^3. Color range related to level of intensity.

The optimal clocking angle between the upper and lower turbines is 0° for nearly all vectoring cases, except for a few cases where it is optimal to clock the upper and lower turbines 180° out-of-phase with each other (see Fig. 5.16).

The sensitivity of the radiated sound power for these combinations of vectoring is shown in Fig. 5.17. For each combination of steady thrust direction, the most sound power reduction is 43 dB, while the least sound power reduction is 8 dB, which is still significant. Therefore, an acoustic controller would reduce the tonal noise in cases of vehicle roll, although to a lesser extent than for vehicle pitch.

Finally, consider the interaction between the port and starboard turbines as outlined in Scenario 3 for yaw configurations. All turbines thrust forward along the X-axis. Port and starboard turbines separately sweep through a range of thrust magnitudes from 1845 to 3285 N. The ideal clocking is shown in Figs. 5.18 and 5.19. The optimal clocking angle between the upper and lower turbines is 0° for

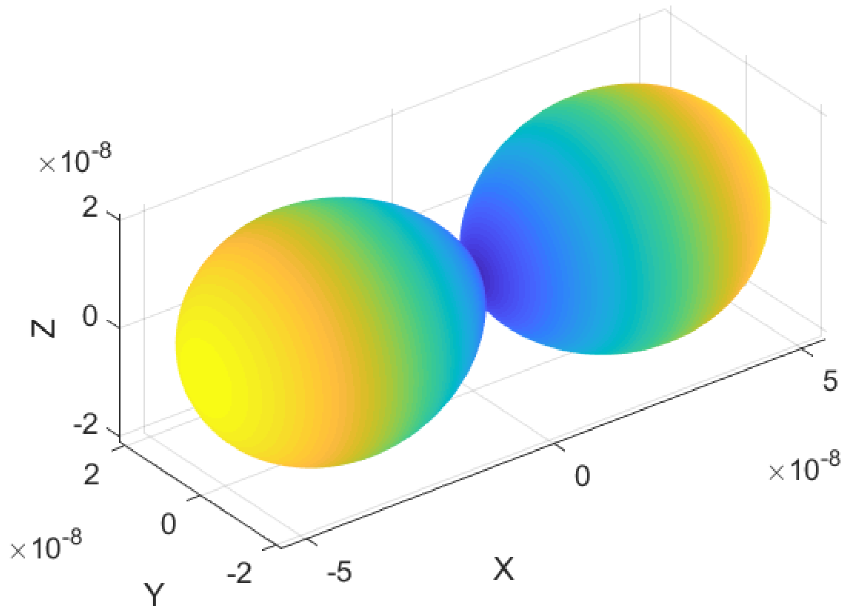

Figure 5.12. Example sound intensity for forward thrust case: nonideal clocking. The turbines interact to form a dipole radiation pattern. Intensity in units of kg/s^3. Color range related to level of intensity.

nearly all vectoring cases, except for a few cases where it is optimal to clock the upper and lower turbines 180° out-of-phase with each other. The reverse is true for clocking between the port and starboard turbines: the optimal clocking angle is 180° for nearly all vectoring cases, except for a few cases where it is optimal to clock the port and starboard turbines 0° in-phase with each other.

The sensitivity of the radiated sound power for these combinations of vectoring is shown in Fig. 5.20. For each combination of steady thrust magnitude, the most sound power reduction is 49 dB, while the least sound power reduction is 13 dB. As stated earlier, this reduction is still significant. Therefore, an acoustic controller would significantly reduce the tonal noise in cases of vehicle yaw.

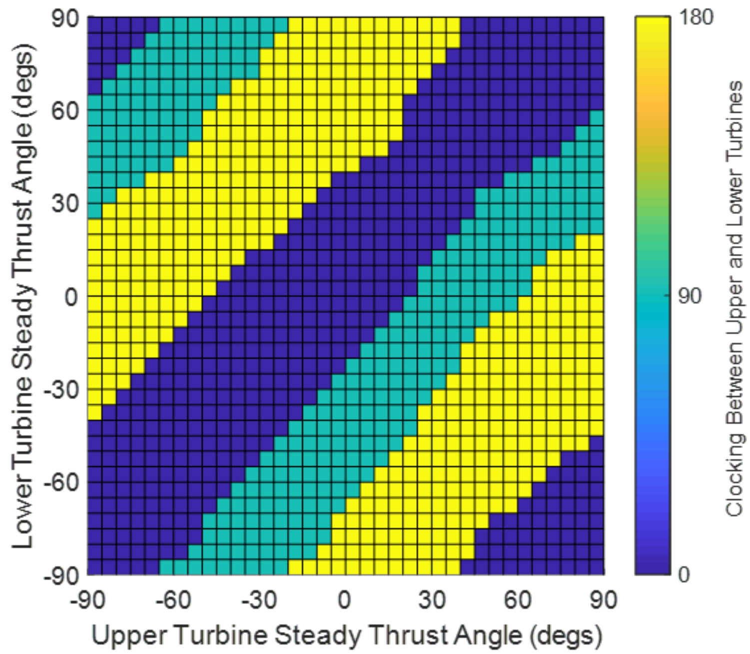

Figure 5.13. Optimal upper and lower turbine clocking for range of pitch maneuvers.

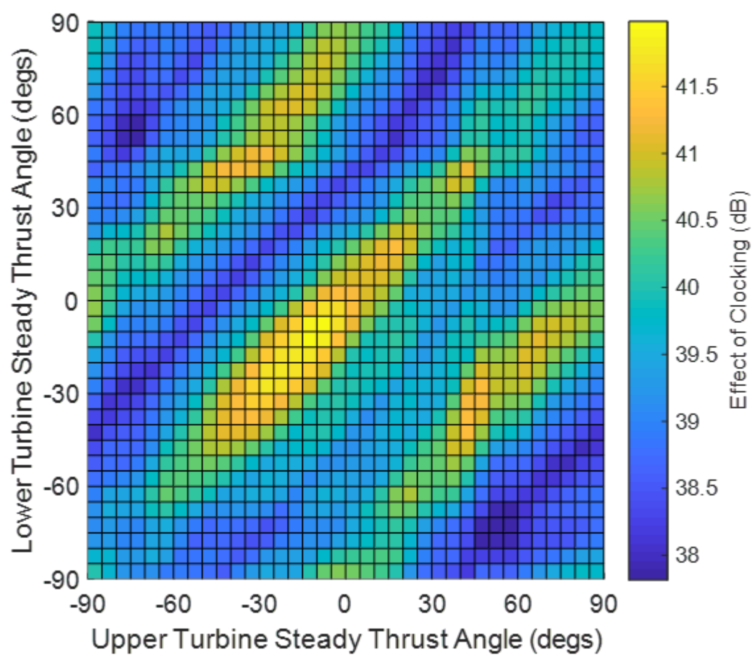

Figure 5.14. Sound power sensitivity to turbine clocking for range of pitch maneuvers. The most sound power reduction is 42 dB, while the average sound power reduction is 39.5 dB.

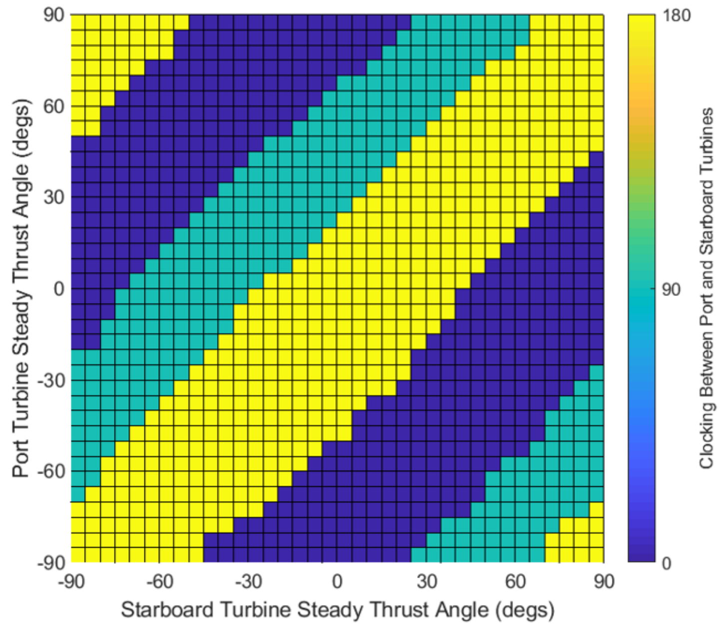

Figure 5.15. Optimal port and starboard turbine clocking for range of roll maneuvers.

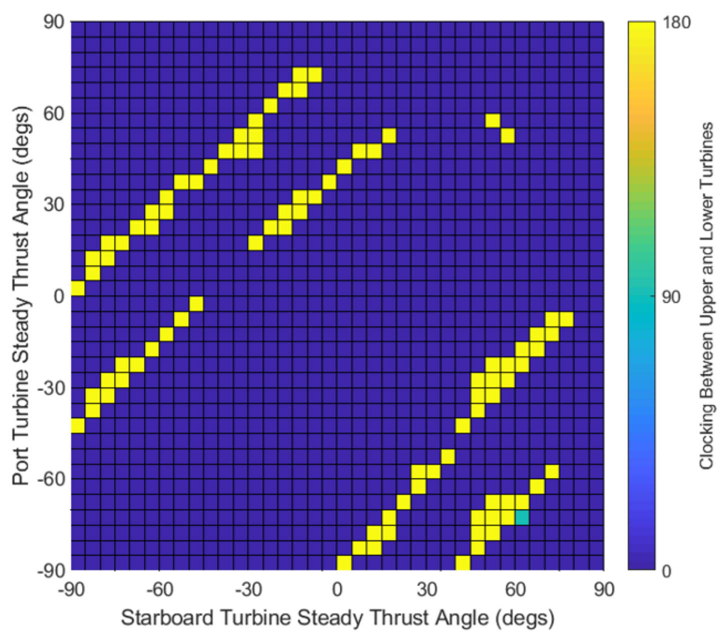

Figure 5.16. Optimal upper and lower turbine clocking for range of roll maneuvers.

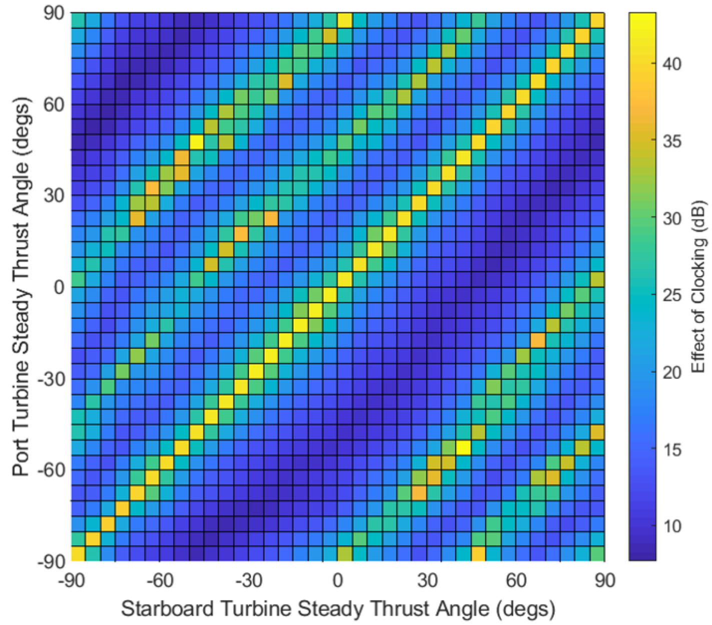

Figure 5.17. Sound power sensitivity to turbine clocking for range of roll maneuvers. The most sound power reduction is 43 dB, while the least sound power reduction is 8 dB.

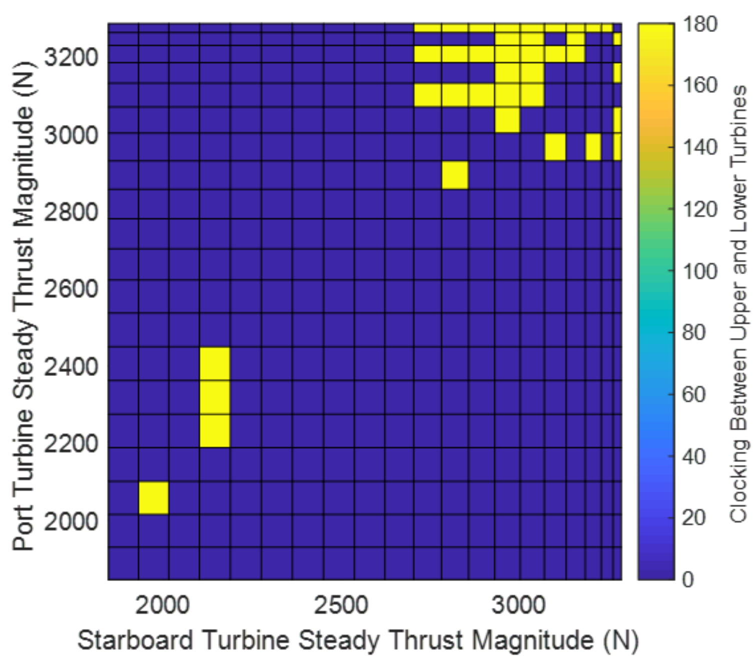

Figure 5.18. Optimal upper and lower turbine clocking for range of yaw maneuvers.

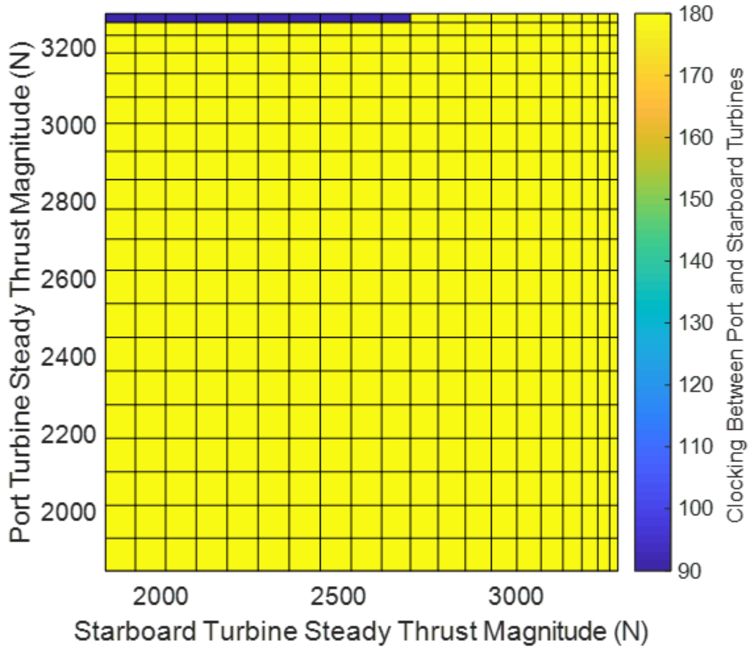

Figure 5.19. Optimal port and starboard turbine clocking for range of yaw maneuvers.

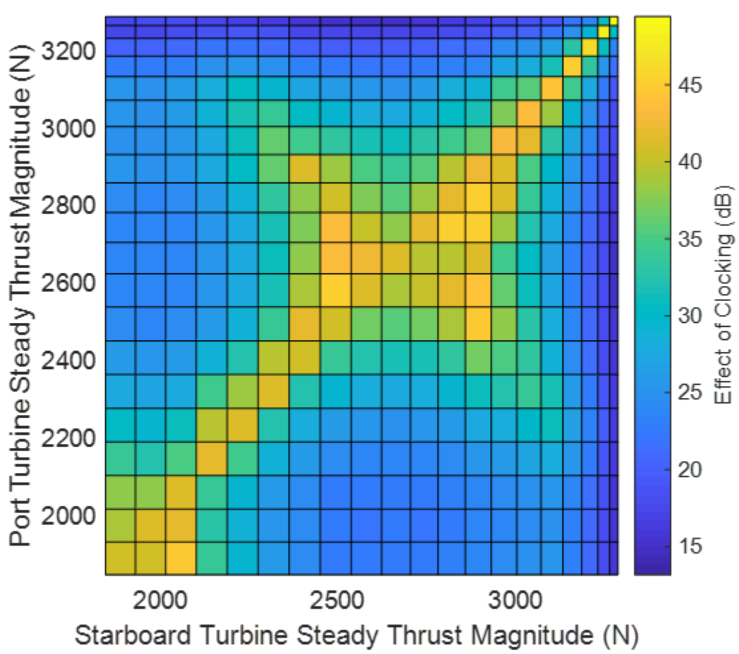

Figure 5.20. Sound power sensitivity to turbine clocking for range of yaw maneuvers. The most sound power reduction is 49 dB, while the least sound power reduction is 13 dB.

5.3.2 Predicted Effect of Turbine Clocking for Experimental Subscale Demonstrator

While the sensitivity of the sound power to turbine clocking has been evaluated for a large range of maneuvers, two cases are used for the experimental validation in this dissertation:

1. The two starboard turbines thrust forward together at 107 RPM. The maximum pitching angle of the turbines is 30°.

2. The two top turbines thrust forward together at 107 RPM. The maximum pitching angle of the turbines is 30°.

Using the theory presented, maximum noise reduction occurs when the top turbines are clocked 180° out-of-phase with each other, while the ideal clocking for the starboard turbines is to be in-phase with each other. The polarity of the dipoles for ideal clocking is shown in Fig. 5.21. The orientation of the dipoles are related to the thrust direction. For the case of the top two turbines, the sound power can be reduced by up to 30 dB re 1e-12W (compared to a non-ideal clocking case) in the far-field. While still significant, the sound power can only be reduced by 8 dB re 1e-12W for the case involving the starboard turbines. This is due to the radiation difference between a lateral quadrupole and a longitudinal quadrupole.

5.4 Experimental Work

The radiated sound performance of a single turbine Rapid Prototype Device (RPD) and a single turbine from a Subscale Demonstrator (SSD) is quantified and compared to sound pressure levels produced from other watercraft. The effects of turbine clocking to reduce tonal noise at blade rate frequency and multiples are verified experimentally on the SSD, which consists of four cycloturbines (design and discussion in Chapter 2).

The RPD and SSD are tested in the ARL Reverberant Tank (see Chapter 2 for detail on experimental setup). The tank has two movable platforms that span the width of the tank. The SSD is fixed to a steel support frame that is clamped to the platforms. The platforms are additionally clamped to the side rails of the

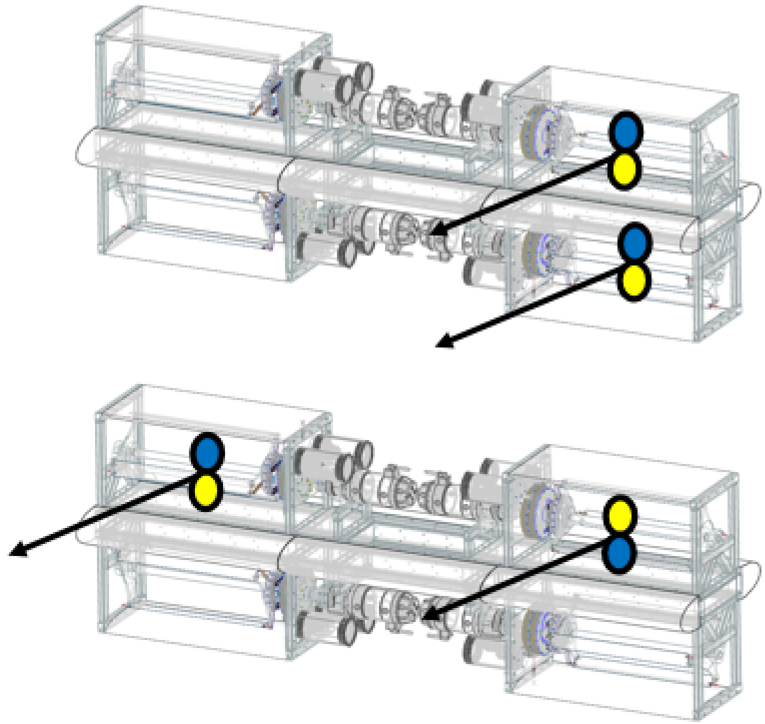

Figure 5.21. Dipole polarity for two turbines thrusting forward together. Top: starboard turbines. Bottom: top turbines.

tank to reduce vibrations. Constraining the SSD provides the ability to measure the integrated loads; a dynamometry system with six strain load cells is used to measure all force and moment components produced from the vehicle. Further discussion of this system is found in Section 5.4.4.

The test matrix for the SSD acoustic testing is documented in Tab. A.2. To provide good average values, data is taken for 300 seconds for each test condition. The motors are stopped and the water in the tank is allowed to settle for at least 1 minute between runs. The load cells are also re-zeroed between runs.

5.4.1 Sound Radiation from Single Crossflow Turbine

From the literature review in Chapter 1, Erbe et al. shows the varied and intrusive effects of watercraft noise on marine mammals. For small watercraft such as jetskis and rigid-hulled inflatable boats, source levels of 130-160 dB re 1 μPa at 1 m have been reported [51]. Source levels for large and powerful watercraft such as ferries, container ships, and icebreakers are more than 200 dB re 1 μPa at 1 m [51]. For

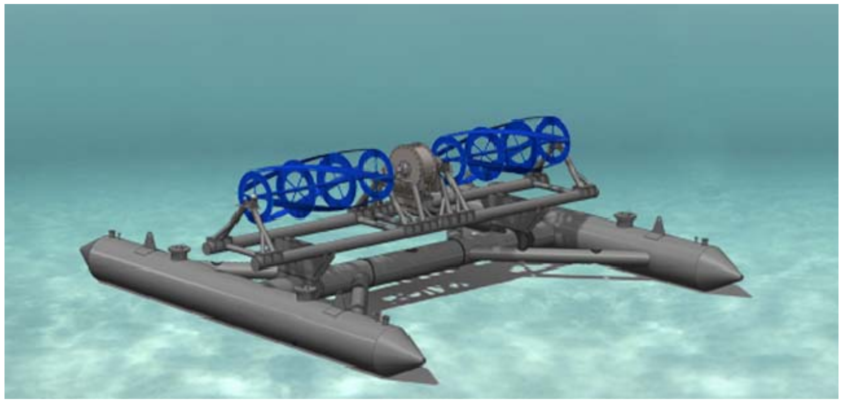

Figure 5.22. Ocean Renewable Power Company RivGen^{TM} turbine. The RivGen turbine consists of two 4.1 m long rotors situated symmetrically about a 2.8 m wide central gap containing a direct-drive generator.

comparison to a marine hydrokinetic cycloturbine, the Ocean Renewable Power Company's RivGen (see Fig. 5.22) radiates at a sound pressure level of 120 dB re 1 μPa at 1 m when rotating at 80 RPM [87]. The sound pressure level for the MHK vehicle is measured and compared to the levels of these other watercraft.

The radiated sound from the MHK vehicle is comprised of sound radiation from the crossflow turbines and sound radiation by structural vibration. It is assumed that sound radiation from the crossflow turbines dominates the sound from the structure at blade rate frequencies. The following experimental work quantifies the sound pressure level from the crossflow turbine sources.

Load cell data is acquired for both the single turbine RPD and for a single turbine on the SSD. The radiated sound pressure is computed using the dipole radiated sound prediction method described earlier for the load cell data obtained. At higher frequencies, the radiated sound pressure of the RPD is obtained using hydrophones (see experimental setup discussion in Section 2.4.3). With a reverberant volume at high enough frequencies where there is sufficient modal overlap, the acoustic pressure distribution due to an acoustic source becomes very uniform provided the distance is not too close. According to Conlon et al. the radiated power from a source within a reverberant tank is given by

$$L_{W_r} = \frac{13.82 V_{tank}}{\rho_0 a_0^2 T_{60}} \langle \hat{p}^2 \rangle_V \tag{5.18}$$

where V_{tank} is the reverberant tank volume and T_{60} is the reverberation time for

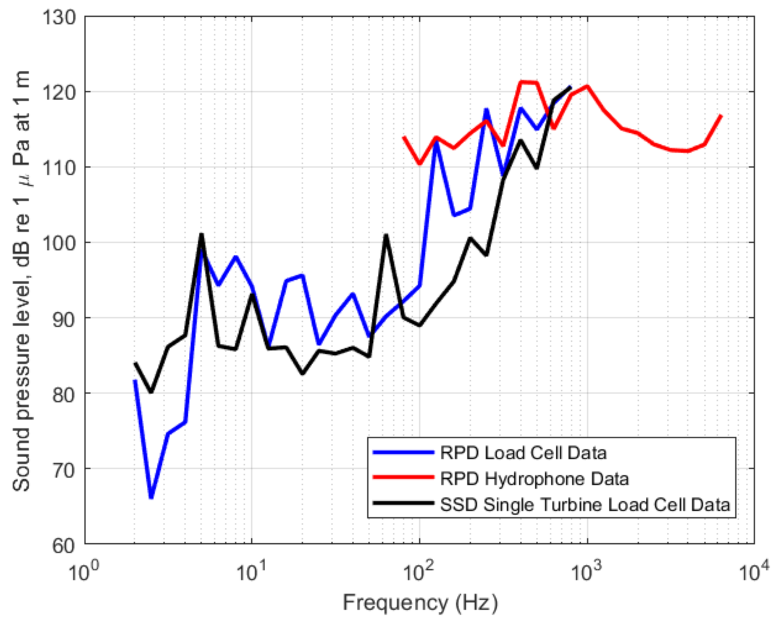

Figure 5.23. Radiated sound pressure level at 1 m in 1/3 octave bands for a single crossflow turbine operating at 107 RPM. The predictions are based on using the dipole method and the reverberant tank method.

the pressure to reduce 60 dB. The data obtained from the hydrophones in the reverberant tank are processed using this reverberant tank method.

Figure 5.23 shows the sound pressure level in 1/3 octave bands for a single turbine operating at 107 RPM. The RPD data acquired from the load cell is shown in blue. The RPD data from the hydrophones is shown in red. The hydrophone data is valid for a high frequency range, whereas the load cell data is more reliable for the low frequencies. This is why the hydrophone data is limited from 80 Hz up to 6300 Hz (where the hydrophones were noise-floor limited) while the load cell data is shown from 2-800 Hz. The data from both sets of measurements overlap between 80-800 Hz. As seen in Figure 5.23, the sound levels agree between the load cell and hydrophone data in the overlapping frequency range. The load cell data from the top starboard turbine on the SSD is shown in black for comparison. The SSD agrees with the RPD data, with some discrepancies. The SSD turbines are sandwiched between nacelles and a center structure, while the RPD is isolated beneath its barge. Additionally, the SSD turbines are supported from both ends, while the RPD is cantilevered.

Depending on the phase of the sources, one could expect a 12 dB increase in the

SSD spectrum for four turbines operating at 107 RPM. This puts the broadband levels at frequencies less than 100 Hz at around 100 dB re 1 μPa at 1 m. The narrowband levels could be as high as 113 dB re 1 μPa at 1 m. While this MHK vehicle level is quieter compared to other watercraft, reducing the tonal noise further via turbine clocking would be desirable, not only for its reduced intrusiveness on aquatic life, but also to reduce fatigue loads.

5.4.2 Sound Radiation from SSD Crossflow Turbines

To assess the effectiveness of turbine clocking on the unsteady loads, and by extension the radiated acoustics, data is collected for two scenarios: one where the two starboard turbines are thrusting in the X-direction together and one where the top two turbines are thrusting in the X-direction together, both at a commanded 107 RPM. For both cases, the maximum pitching angle is set to 30°. According to the theory presented in Section 5.3.1, it is expected that the sound power can be reduced significantly by clocking the turbines. The theory relies on a model of the turbine unsteady forces, which is compared to experimental data in Fig. 5.24. The X-direction force mean and standard deviation of 18 measurements for a single turbine thrusting forward at 107 RPM, 30° maximum pitching angle, are shown, at blade rate frequency and multiples. The predicted unsteady X-direction force from one turbine is shown for the same case. The model reliably predicts the unsteady force magnitude at 1x and 2x blade rate frequency, and loses fidelity at higher order blade rates. This is likely due to the contribution of other noise sources at higher frequencies not captured in the model, such as tonal and broadband noise from the structure. However, the forces at the first two multiples of blade rate frequency contribute the most to the total sound power.

Implementation of the clocking control in the experiment is not possible due to the lack of waterproof encoders to measure the turbine angular displacement. Furthermore, the experiments show significant slippage in the induction motors under load, and that the RPM standard variation is on the order of 5%. However, the experiment provides data to support the predictions presented in Section 5.3.1. A modulation model is fit to experimental data to show that turbine clocking effects occur in the test. The following analysis provides some validation of the noise reduction theory presented in Section 5.3.

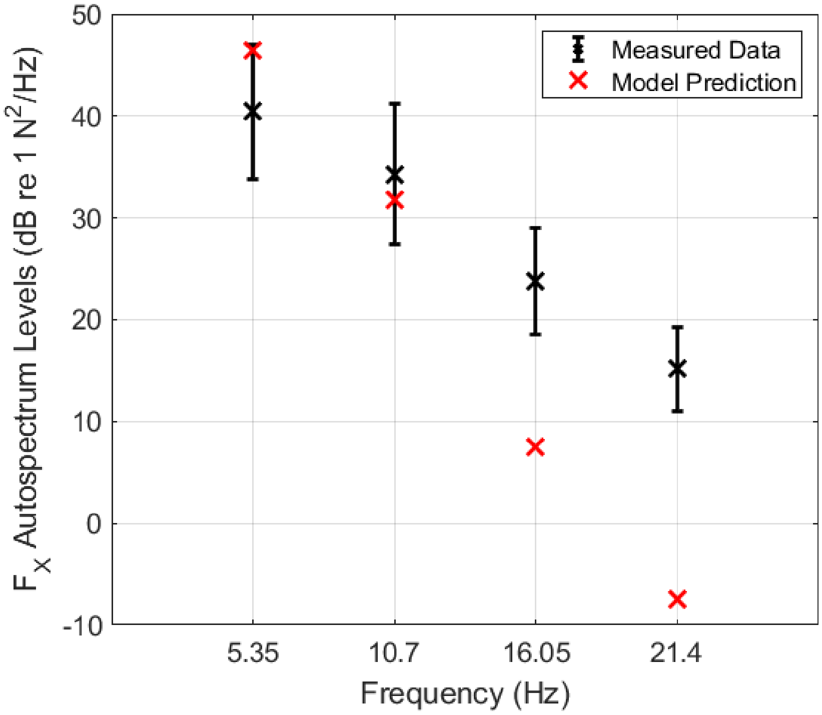

Figure 5.24. Autospectrum levels of thrust force in dB re 1 N2/Hz versus frequency. The frequencies shown correspond to multiples of blade rate.

The forces over time for the measured data are filtered using a 3rd order butterworth filter for blade rate frequencies. This filter is chosen because it is designed to have a flat frequency response in the passband. The order is selected as a compromise between computation time and frequency response character (see Fig. 5.25). The cut-on and cut-off frequencies account for the fluctuations in motor RPM. Figure 5.26 shows the mean square of the forces in the X-direction over time, filtering out data outside the region around the first blade rate frequency. A 5 second moving average filter is applied to produce the result shown.

There are significant variations in the mean square X-direction force when the two starboard turbines are thrusting together. The cause of this fluctuation could be due to a clocking effect; the variation of the RPM between turbines would affect the phasing between the turbines over the course of the five minute run. In contrast to the forces produced by the starboard turbines, the force in the X-direction from the top two turbines thrusting together shows smaller fluctuations over time.

To understand this result, consider two phasors of magnitudes $\tilde{F}_a$ and $\tilde{F}_b$

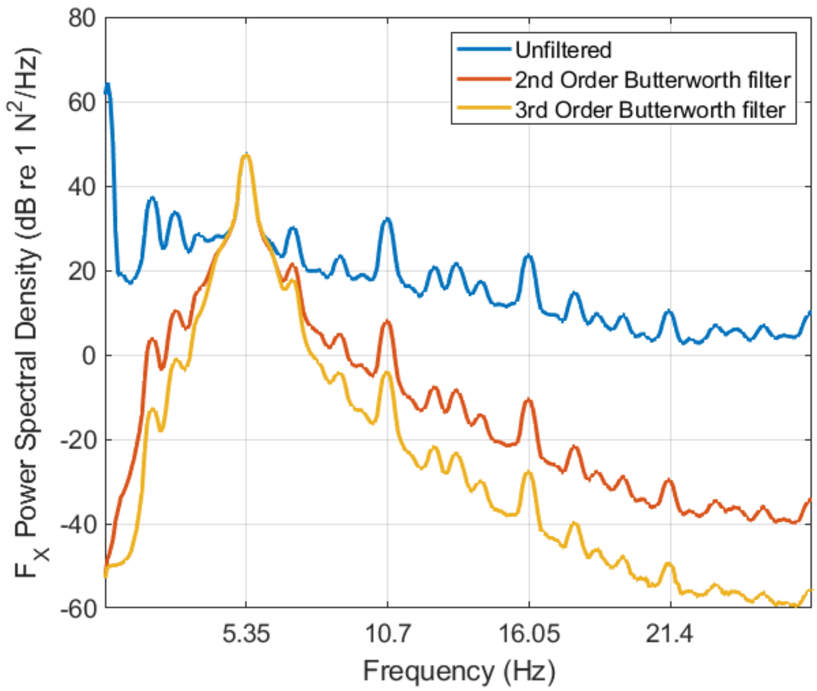

Figure 5.25. Power Spectral Density of X-direction force versus frequency. Effect of a Butterworth filter at 1x blade rate frequency. Data shown is for two starboard turbines thrusting forward at a commanded 107 RPM, 30° maximum pitching angle.

that rotate at slightly different speeds (see Fig. 5.27). The total unsteady force magnitude $\tilde{F}_c$ varies with time according to the law of cosines

$$\tilde{F}_c^2 = \tilde{F}_a^2 + \tilde{F}_b^2 - 2\tilde{F}_a\tilde{F}_b \cos \omega' t \tag{5.19}$$

where ω' is the difference in rotation rate between the phasors. The ratio of maximum to minimum force is

$$20 \log \left(\frac{F_{max}}{F_{min}} \right) = 10 \log \frac{(\tilde{F}_a + \tilde{F}_b)^2}{(\tilde{F}_a - \tilde{F}_b)^2} \tag{5.20}$$

on a decibel scale. This model is used to determine the difference in the unsteady force magnitude between turbines, as well as the difference in rotation rate.

The ratio between $\tilde{F}_a$ and $\tilde{F}_b$, as well as the rotation rate difference ω' is found by fitting to experimental data, as shown in Figures 5.28 and 5.29 for the first blade rate frequency. The values for $\tilde{F}_a$ and $\tilde{F}_b$ are found by averaging the values of experimental data peak points and valley points, respectively. The value for the

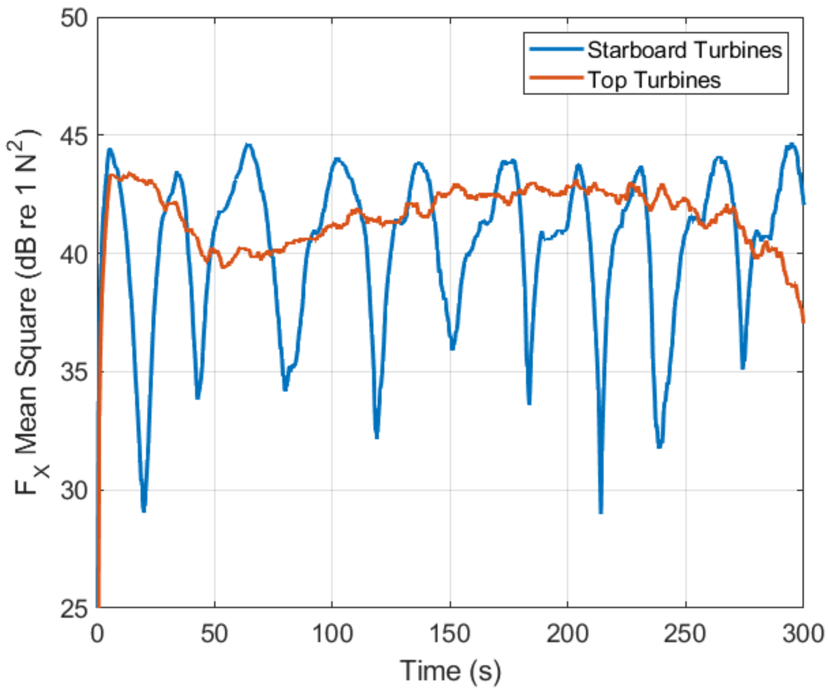

Figure 5.26. Filtered X-direction force amplitude at blade rate in dB re 1 N^2 versus time.

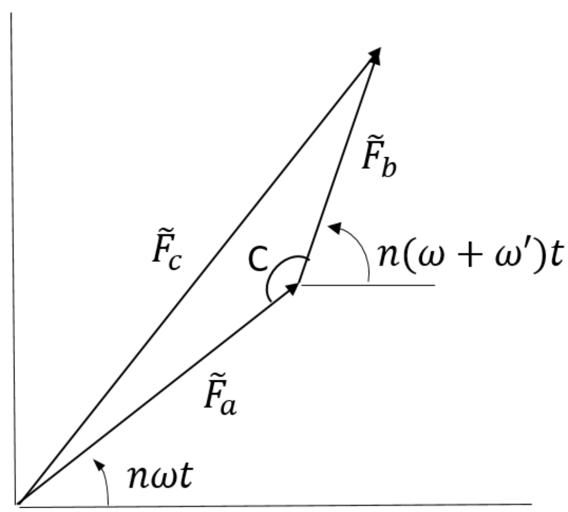

Figure 5.27. Two phasors of differing magnitudes and rotation speeds.

rotation rate difference is found by iterating over a large range of RPMs, with a small 0.01 RPM resolution, and using the least squares method to minimize the residual between the experimental data and the model.

Tables 5.1 and 5.2 show the modulation model predictions of the unsteady force

Table 5.1. Modulation Model Results for F_x Mean Square Data, Starboard Turbines Case

Multiple of BR	$\tilde{F}_b/\tilde{F}_a$	**RPM difference**
1	1.73	1.82
2	2.58	1.79
3	2.24	1.99

Table 5.2. Modulation Model Results for F_x Mean Square Data, Top Turbines Case

Multiple of BR	$\tilde{F}_b/\tilde{F}_a$	**RPM difference**
1	3.61	0.30
2	3.86	0.16
3	3.74	0.50

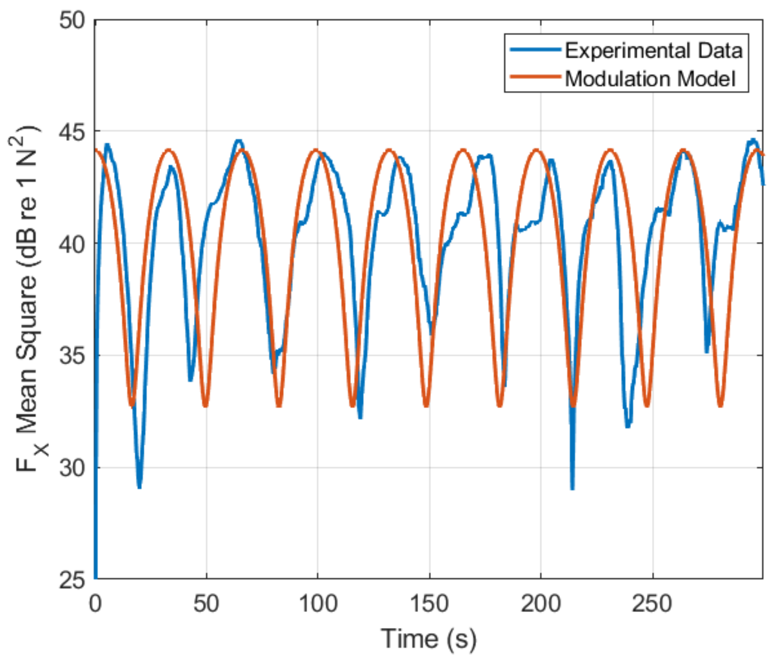

Figure 5.28. Filtered X-direction force amplitude at blade rate in dB re 1 N^2 versus time. Comparison of experimental data to modulation model for starboard turbines thrusting together at a commanded 107 RPM, 30° maximum pitching angle.

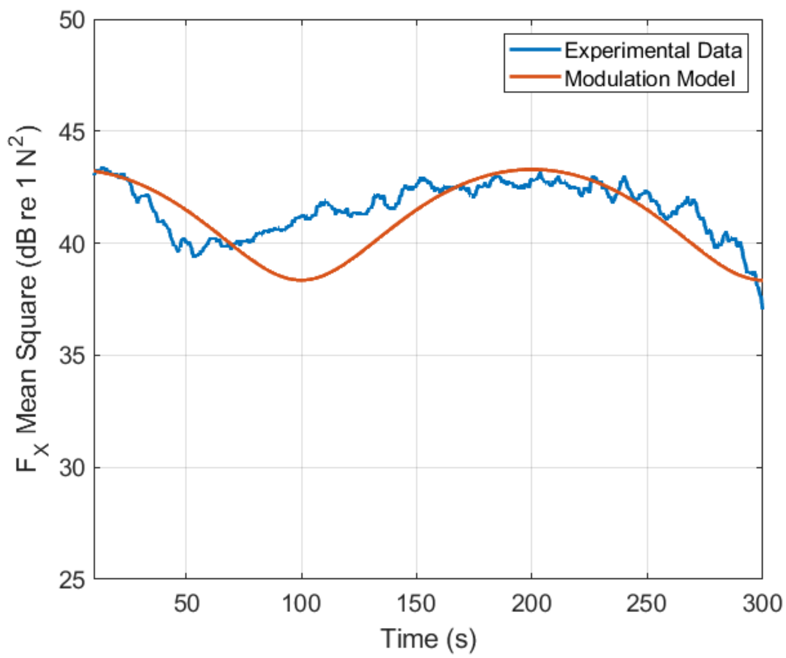

Figure 5.29. Filtered X-direction force amplitude at blade rate in dB re 1 N^2 versus time. Comparison of experimental data to modulation model for top turbines thrusting together at a commanded 107 RPM, 30° maximum pitching angle.

magnitude ratio and the rotation rate difference between turbines, as a function of blade rate frequency.

For the first blade rate frequency, the model shows that the difference in RPM between the starboard turbines is 1.8 RPM. This difference is consistent with the model prediction at 2x blade rate frequency for the same run. For the top turbine case, the model shows a difference of 0.3 RPM for 1x blade rate filtered data. The fit is not as strong at higher blade rate frequencies, which is why there is some variation in the predicted RPM difference. The RPM variation has an effect on when the turbines are clocked in-phase or out-of-phase with each other; the RPM difference explains the time between valleys in the force measurement.

Another aspect of the modulation model is the ratio between the unsteady force magnitudes $\tilde{F}_a$ and $\tilde{F}_b$. For the filtered data at 1x blade rate frequency, there is a difference in the model between the ratio $\tilde{F}_b/\tilde{F}_a$ for the case where the top turbines thrust together versus the case where the starboard turbines thrust together. For the starboard turbines, the model predicts that the ratio between the unsteady force magnitudes is 1.7 at 1x blade rate frequency, while for the top turbines, the

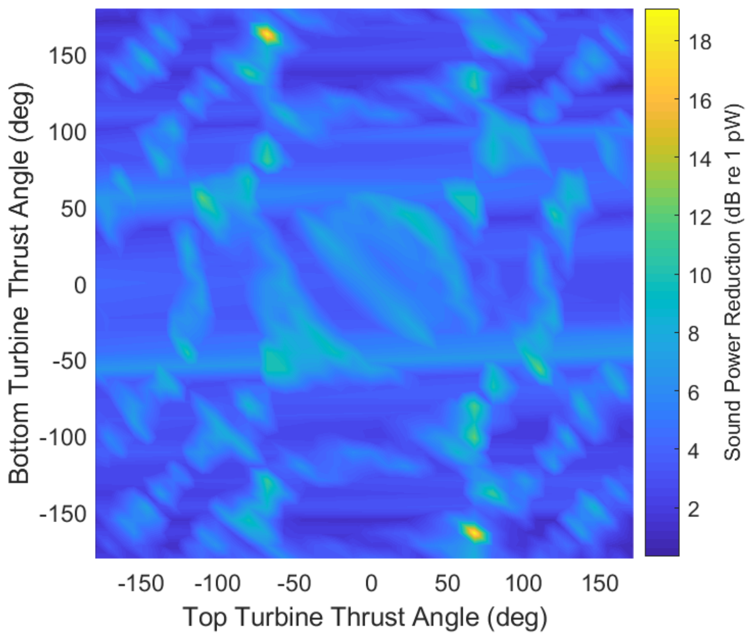

Figure 5.30. Sound power sensitivity to turbine clocking for a range of starboard turbine thrust maneuvers. Forward thrust corresponds to a thrust angle of 0°.

model predicts a ratio of 3.6. In the acoustic model discussed in Section 5.3.1, it is assumed that the unsteady force magnitudes are the same between turbines for the cases where the top and starboard turbines thrust together. When the unsteady forces are of the same magnitude, and perfectly out-of-phase with each other, the reduction in sound power is maximized (30 dB sound power reduction from clocking the top two turbines, and an 8 dB reduction by clocking the starboard turbines). If the unsteady forces are out-of-phase, but of different magnitudes, there is not as much of a reduction in sound power.

This is more clearly demonstrated by applying the unsteady force magnitude ratios found experimentally to the acoustic model. Figures 5.30 and 5.31 show a map of the sound power reduction for combinations of thrust vectoring at 107 RPM for the starboard and top turbines, respectively. Turbine clocking can reduce the sound power for the top turbines forward thrust case by roughly 4.6 dB re 1e-12W, while reducing the sound power for the starboard turbines case 6.4 dB re 1e-12W. For some combinations of thrust vectoring between the starboard turbines, turbine clocking may reduce the sound power by as much as 19 dB re 1e-12W.

In summary, the closer the ratio $\tilde{F}_b/\tilde{F}_a$ is to 1, the greater the effect on minimizing

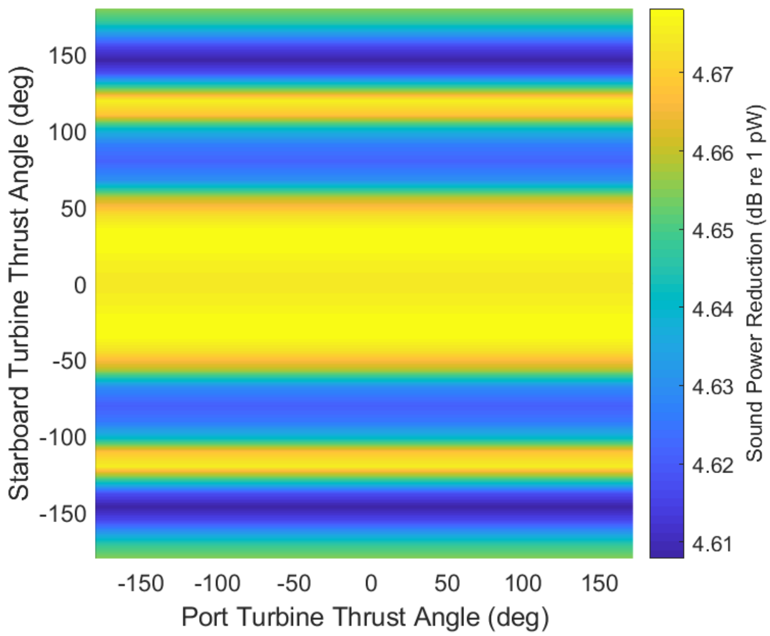

Figure 5.31. Sound power sensitivity to turbine clocking for a range of top turbine thrust maneuvers. Forward thrust corresponds to a thrust angle of 0°.

sound power. Because the ratio $\tilde{F}_b/\tilde{F}_a$ is close to 1 for the experimental case where the starboard turbines thrust together, there are larger fluctuations in the mean force. There are smaller magnitude fluctuations in the mean force for the top turbines case because the unsteady force magnitude ratio is 3.6.

The difference in the unsteady force magnitude ratio between the two cases can be attributed to flow differences in the reverberant tank. The top turbines have a larger separation distance than the starboard turbines (2860 mm versus 770 mm), and likely have different inflows.

5.4.3 Sound Radiation by SSD Structural Vibration

Sound radiation from vibrating structures is of importance to this analysis. Understanding the mechanisms of sound radiation can improve the quality of the MHK vehicle. In the following analysis, the structural modes of the vehicle are assessed, the contribution of nacelle vibration to the radiated acoustics is quantified, and the dynamometry system used for experimental work is analyzed.

5.4.3.1 Contribution of Vehicle Vibration

It is important to quantify the structural modes of the vehicle and their corresponding frequencies to understand how the structural vibration will radiate sound. Simulation of a finite element (FE) model of the Subscale Demonstrator (SSD) in-air predicts a bending mode at 14.7 Hz, a torsional mode at 16.4 Hz, and a longitudinal mode at 19.1 Hz. At 286 RPM, which is the target operating rate of the turbines, the first blade rate frequency falls at 14.3 Hz. This is very close to the finite element model's predicted bending frequency of 14.7 Hz. It is possible that with all four turbines operating at this RPM, at some thrust direction, the first bending mode could be excited. Long-term operation at this condition would increase vehicle fatigue, if not lead to vehicle failure.

To check the reliability of the finite element model, which does not include the mass and stiffness from the motors, as well as any nonlinear damping from cables, a modal tap test is performed on the SSD. The tap test is performed in air, with the vehicle modes adjusted in analysis for the submerged case. The SSD is suspended from a crane with straps for the test (see Fig. 5.32). The stiffness of the straps is assumed to be much smaller than the stiffness of the SSD, and so simulates a free-free scenario for the modal test.

A grid of 78 points (shown in Fig. 5.33) is demarcated on the SSD. These grid points are chosen to capture the bending and torsional modes that could potentially be excited by blade rate. A large force hammer with a rubber tip is used to hit the points and induce vibrations on the SSD. Five accelerometers are used to capture the response of the vehicle to the input force. Each grid point is struck 3 times for an averaged response.

ARL's Poly-reference Estimation Code (APEC) is used to identify the modes excited from the experimental data. APEC is a system-identification procedure that uses a poly-reference least-squares complex frequency domain algorithm to determine natural frequencies, loss factors, and mode shapes of experimental modal analysis data. The results of the SSD modal analysis are summarized in Table 5.4.3.1 and compared to a finite element analysis (which is simulated up to 50 Hz). The last column shows the predicted modal frequencies if the SSD is underwater.

The natural frequencies of a vibrating structure are decreased by heavy external fluids such as water. This is due to the extra force required to accelerate the fluid's inertia [88]. The frequency shifts are a function of material, thickness, and aspect

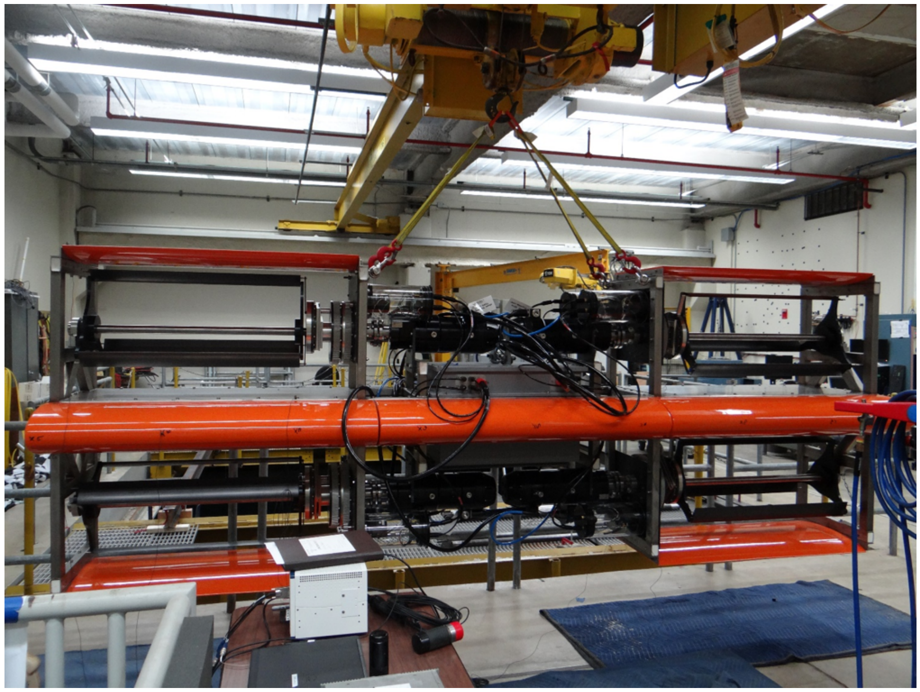

Figure 5.32. Suspended Subscale Demonstrator for modal analysis test.

ratio, and it can be approximated that the modal frequencies underwater will be 80% of the frequencies in air [89]. The first two frequencies are rigid body modes from the SSD suspension from the crane. The first bending mode is anticipated to occur underwater at 15.5 Hz. The first torsion mode is predicted to occur at 18.9 Hz.

These frequencies are higher than predicted by the finite element simulation, and also higher than the target blade rate frequency. This suggests that when operating at the target RPM of 286, acoustic radiation from structural vibrations is not a primary concern.

5.4.3.2 Contribution of Vibrating Nacelles

Another consideration is sound radiation from the vibrating nacelles. The nacelles on the SSD are the outermost orange plates. Their dimensions are 1205 mm by 560 mm, with a thickness of 60 mm. It is important to quantify this vibration to ensure that the experimental load cell measurements reflect the unsteady forces produced by the turbines, and are not contaminated by sound radiation from the structure.

The power output of a single nacelle is computed for a specified 1 m/s velocity

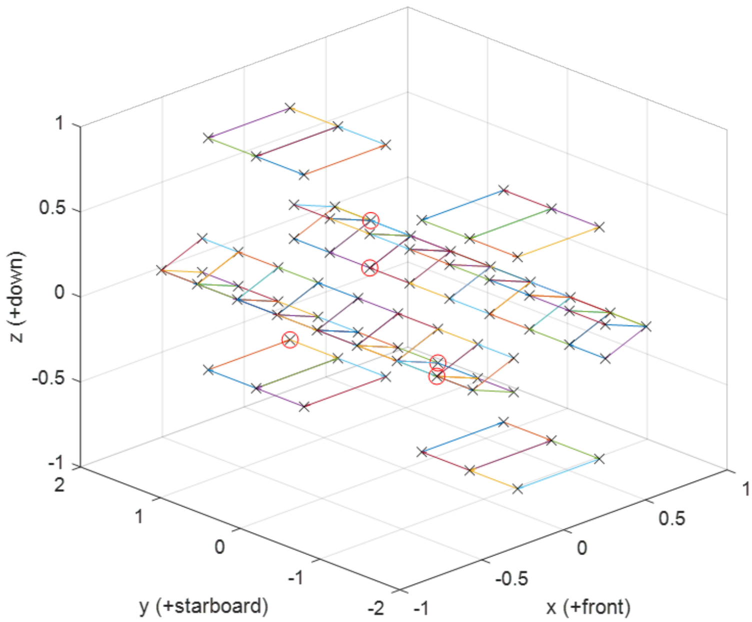

Figure 5.33. Modal analysis test grid points versus space in meters, connected as quadrilateral elements. Accelerometer locations circled in red.

in the direction normal to its surface assuming it radiates as an unbaffled piston. The computations are performed using the equivalent source techniques described by Koopmann and Fahnline [90] with the plate modeled as infinitely thin, dipole sources alone used for basis functions, and a surface mesh of 28x60 uniformly spaced rectangular elements. This can be considered an upper bound for the power output because at low frequencies where $kL \ll 1$, any phase variation in the velocity will lead to cancellation. For the computations shown, the maximum kL is

$$kL = \frac{2\pi(30\text{Hz})}{a_0}(0.56\text{m}) = 0.07 \tag{5.21}$$

which is much less than 1. The frequency is chosen to be around 6x the blade rate frequency of a turbine operating at 107 RPM.

The reference velocity for the power output is adjusted using data from the modal tap test performed in-air. From the APEC analysis, the mobility (velocity/force) of each grid point is found. The corner nacelle hit point at the largest X, Y, and Z position (refer to Fig. 5.33) has the largest mobility on the nacelle, particularly in the vehicle bending mode. This frequency-dependent mobility is converted to velocity with a defined input force. The input force used for this calculation is the measured unsteady force in the X-direction produced by the turbine as it thrusts forward: it is assumed that the unsteady forces transfer through the turbine shaft into the nacelle. The velocity is shifted in frequency to correct for the surrounding water. The power output is corrected to this predicted velocity

$$L_{W,new} = L_W + 20\log\left(\frac{V}{1\text{m/s}}\right) \tag{5.22}$$

and doubled for a second nacelle (a 6dB increase). Figure 5.34 shows the acoustic power output as a function of frequency for the vibrating nacelles. For comparison, the acoustic model predictions of the power output for two turbines rotating at 107 RPM, 30° max pitching angle, are shown. The predictions include the variation in the unsteady force magnitude between turbines found from experimental data, discussed in Section 5.4.2. The upper and lower bounds on the predictions show the effect of using turbine clocking to minimize the sound power.

At 1x and 2x blade rate frequency, the sound power produced by the unsteady turbine forces are much higher than the power output from the nacelles. There is low risk of structural contamination on the measurements at these frequencies. At 3x blade rate frequency, the structural vibration is a larger contributor to the power output.

5.4.4 Effect of SSD Dynamometry System on Experimental Unsteady Loads

The hydrodynamic loads of the Subscale Demonstrator (SSD) are measured within ARL's Reverberant Tank. A dynamometry system consisting of a frame of links containing strain load cells is shown in Fig. 5.35. This analysis provides suitability of the dynamometry system, provides a transfer matrix between the link loads and the SSD principal coordinate system, and determines the rigid body natural frequencies.

It is assumed that the dynamometry system behaves as a truss where only axial loads are allowed through each link. It is further assumed that the node displacements are small, and that the SSD itself acts as a rigid body. Finally, it is

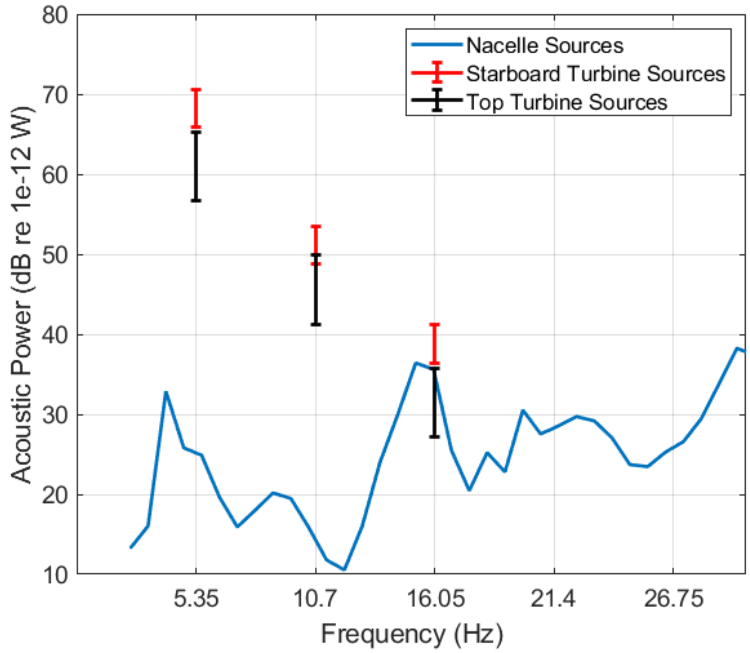

Figure 5.34. Radiated sound power in dB re 1 pW versus frequency.

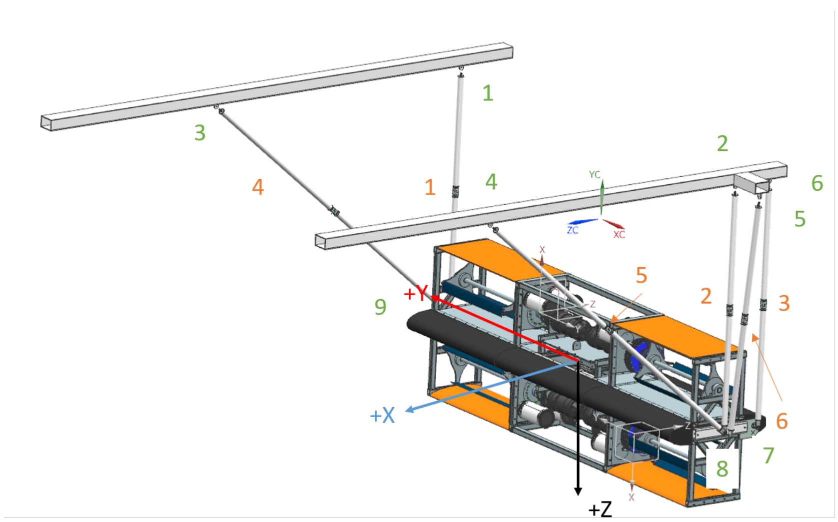

Figure 5.35. Links and nodes of Subscale Demonstrator dynamometry system. Links are numbered with orange text and nodes are numbered with green text.

assumed that the back of the back support of the dynamometry is held rigidly.

Figure 5.35 shows the nodes in green and the links in orange. The coordinate system shown corresponds to the center of gravity of the SSD. Only Nodes 1 through

4 are allowed to be displaced and their position is dictated by

$$\vec{x} = \Phi\vec{q} \tag{5.23}$$

where $\vec{q}$ corresponds to the rigid body translations and rotations. The matrix Φ is a 12x6 matrix relating the two systems. The stiffness of the deflections are found from

$$K_\delta = \frac{EA_{tube}}{L_{tube,i}} \tag{5.24}$$

where E is the Young's modulus of steel, A_{tube} is the cross-sectional area of the tubing, and $L_{tube,i}$ is the length of each of the six tubes.

The stiffness matrix is subsequently found by

$$K_q = \Phi' B' K_\delta B \Phi \tag{5.25}$$

where the matrix B relates the link deflection to the coordinate system. The natural frequencies are found from the eigenvalues of the moment of inertia matrix divided by the stiffness matrix. The moment of inertia matrix is populated with values determined from swing tests (tabulated in Tab. 2.8). The lowest natural frequency occurs at 19.4 Hz.

At the experimental operating RPM of 107, the frequencies of concern are the lower blade rate frequencies at 5.35 Hz, 10.7 Hz, and 16.05 Hz. The natural frequencies of the dynamometry system are above these frequencies. The dynamometry system is not expected to influence the unsteady force measurements at the first few blade rate frequencies.

5.5 Concluding Remarks

An acoustic model of a novel marine hydrokinetic cycloturbine vehicle is presented. Further, noise is reduced at blade rate frequency and multiples via a new method of turbine clocking, whereby the phase angle between turbines is varied.

A small-scale vehicle is built and tested in ARL's Reverberant Tank facility. The unsteady forces are measured using load cells. Data from these tests show fluctuations in the mean square force in the X-direction at blade rate frequencies.

It is demonstrated that the fluctuations in mean square force in the thrust direction are a result of the turbines moving in and out-of-phase relative to one another.

The experimental modulations in force data are modeled, quantifying the differences in unsteady force magnitude and RPM between turbines. This modulation model fits well with the measured data, ultimately indicating that the clocking angle between turbines in a marine hydrokinetic cycloturbine vehicle has a significant effect on the vehicle forces and by extension the radiated acoustics.

Further, the structural vibration of the vehicle and its nacelles is shown to not significantly contribute to the radiated sound power compared to the crossflow turbines. The experimental unsteady loads are also not affected by the dynamometry system. The crossflow turbines are the main source of the sound radiation at blade rate frequency and multiples.

In future work, classical control methods can be used to design an acoustic controller that tracks the relative phase angle between turbines using waterproof encoders.

Table 5.3. Mode Shapes and Natural Frequencies of Subscale Demonstrator

Mode Shape	FE Expected Natural Frequency In-Air (Hz)	Measured Natural Frequency In-Air (Hz)	Expected Natural Frequency Underwater (Hz)
Rigid Body (heaving)	-	4.8	3.8
Rigid Body (bobbing)	-	12.1	9.7
1st Bending	14.7	19.4	15.5
1st Torsion	16.4	23.6	18.9
2nd Torsion	44.2	25.0	20.0
2nd Bending	23.3	29.3	23.4
3rd Bending	-	36.5	29.2
3rd Torsion	-	38.8	31.0

6 | Conclusions and Recommendations for Future Work

6.1 Conclusions

The work presented in this dissertation has focused on the design, control, and validation of a Marine Hydrokinetic (MHK) cycloturbine vehicle. This vehicle has the capability to power subsea networks and also provide logistical support to subsea assets. The device generates electricity from moving water, and it can also propel itself through the water. The assessment of the vehicle design and control has been accomplished through experimental studies and computational simulations. These studies have furthered the understanding of the mechanical, dynamic, and acoustic behavior of the vehicle.

Chapter 2 defined a notional system layout for a controllable and stable MHK vehicle design. The analysis determined that a four-turbine configuration with stacked counter-rotating cycloturbines provided the best control of the vehicle, particularly in pitch, as well as additional benefits for power generation. A 1/5.56 scale single turbine Rapid Prototype Device (RPD) and Subscale Demonstrator (SSD) were designed and built for experimental testing, with consideration for a thrust vectoring mechanism to control the propulsive forces from the vehicle cycloturbines. Experimental work included operation of these devices in a reverberant tank under stationary conditions over a variety of shaft speeds.

Chapter 3 introduced a nonlinear dynamics model to determine the forces and moments produced on and by the MHK cycloturbine vehicle. This model combined hydrodynamic and hydrostatic forces and moments with flat-earth vector equations of motion for an MHK vehicle in six degrees-of-freedom. The model included modeling of the inflow through the turbines as a single streamtube, which contributed to determination of the turbine forces and moments. The turbine force model was tuned to two-dimensional and three-dimensional CFD, and further to experimental data, with good agreement. The vehicle dynamics model also included a hydrodynamic model of the vehicle, which accounted for blockage effects. This model included lift, induced drag, and form drag. Lift forces were predicted from two-dimensional CFD and adjusted for three-dimensional effects. Drag forces were calculated from theory. Hydrostatic forces such as the vehicle's buoyancy force was also included in the model. This dynamics model was used to design vehicle controllers.

In Chapter 4, classical control methods were initially used to design controllers that tracked the vehicle state, in order to maneuver the vehicle underwater. Classical controllers were limited, however, to a neutrally-buoyant system; the controllers failed to stabilize the system when there was cross-coupling in the control derivative matrix. Additionally, these controllers did not account for system nonlinearities and so would not be as robust as nonlinear controllers. Nonlinear dynamic inversion (NDI) was therefore used as a basis to design more robust controllers. It was shown that the NDI controller outperformed the fully classical controller. The NDI controller allowed for more complex maneuvers such as vehicle hover and station keeping.

Lastly, in Chapter 5 an acoustic model of the MHK cycloturbine vehicle was presented, where each cycloturbine was modeled as a compact source. The analysis presented in this Chapter showed that the cycloturbines were the main source of the sound radiation at blade rate frequency and multiples. From the model presented, it was determined that tonal noise at blade rate frequency and multiples could be reduced via a new method of turbine clocking, whereby the phase angle between cycloturbines is varied. This theory was tested on a Subscale Demonstrator in a reverberant tank. The experimental modulations in force data from two turbines were modeled, quantifying the differences in unsteady force magnitude and RPM between turbines. The modulation model fit well with the measured data, ultimately indicating that the clocking angle between turbines in an MHK cycloturbine vehicle has a significant effect on the vehicle forces and by extension the radiated acoustics.

6.2 Recommendations for Future Work

To further the research and create opportunities for advancement in the field, the following suggestions are made for future work:

1. In March of 2020, the Ocean Renewable Power Company (ORPC) tested the Subscale Demonstrator at the University of Maine Advanced Structures and Composites Center. Testing of the Subscale Demonstrator at the University of Maine facility included submergence and buoyancy tests, forward flight, controlled turns, 360° turns under joystick control, testing with waves, and diving tests. The data from these tests can be used to further advance the dynamics and turbine force models and the NDI controllers. For example, the current model does not include added mass effects, which could potentially be characterized. The drag values of the model could also be tuned given data from the University of Maine testing.

2. The Ocean Renewable Power Company intends to test the Subscale Demonstrator in open water at its federally funded Cobscook Bay project site in Maine. Implementation of the NDI controllers in this free field testing would validate their effectiveness, particularly for maneuvers such as hover.

3. Acoustic control of tonal noise at multiples of blade rate frequency is important to reduce fatigue loads as well as to reduce the environmental impact of the MHK vehicle underwater. While turbine clocking was shown to effectively reduce this noise experimentally, an acoustic controller should be designed and tested to implement this method. Acoustic control could be implemented using the turbine RPM–turbines can be clocked by slowing one turbine relative to another for a short period of time. Classical control methods can be used to design an acoustic controller that tracks the relative phase angle between turbines using waterproof encoders.

Appendix A
Experimental Test Matrices

Table A.1. Reverberant Tank RPD Bare Shaft Test Matrix. Hydrophone data acquired for this test.

Test Date	Test Number	Run Number	RPM
5/3/2017	CFTurb0047	2	22
5/3/2017	CFTurb0047	3	43
5/3/2017	CFTurb0047	4	65
5/3/2017	CFTurb0047	5	86
5/3/2017	CFTurb0047	6	107
5/3/2017	CFTurb0047	7	0

Table A.2. Reverberant Tank SSD Acoustic Test Matrix

		Top Starboard		Top Port		Bottom Starboard	
Test	Test Date	β_{max} [°]	φ [°]	β_{max} [°]	φ [°]	β_{max} [°]	φ [°]
1	5/6/2019	30	110			30	-80
2	5/6/2019	30	110			30	-80
3	5/6/2019	30	110			30	-80
4	5/6/2019	30	110			30	-80
5	5/6/2019	30	110			30	-80
6	5/6/2019	30	110			30	-80
7	5/6/2019	30	110			30	-80
8	5/6/2019	30	110			30	-80
9	5/6/2019	30	110			30	-80
10	5/9/2019	30	0			30	-175
11	5/9/2019	30	110			30	-80
12	5/9/2019	30	155			30	-45
13	5/9/2019	30	110	30	-100		
14	5/10/2019	30	110	30	-100		
15	5/10/2019	30	110	30	-100		
16	5/10/2019	30	110	30	-100		

Table A.3: Reverberant Tank RPD Single Turbine Test Matrix. Hydrophone data acquired for test number 52.

Test Date	Test Number	Run Number	RPM	β_{max} [°]
4/14/2017	CFTurb0025	1	0	30
4/14/2017	CFTurb0025	2	22	30
4/14/2017	CFTurb0025	3	43	30
4/14/2017	CFTurb0025	4	65	30
4/14/2017	CFTurb0025	5	86	30
4/14/2017	CFTurb0025	6	107	30
4/14/2017	CFTurb0025	7	65	30
4/19/2017	CFTurb0030	1	0	30
4/19/2017	CFTurb0030	2	22	30
4/19/2017	CFTurb0030	3	0	30
4/19/2017	CFTurb0030	4	43	30
4/19/2017	CFTurb0030	5	65	30
4/19/2017	CFTurb0030	6	86	30
4/19/2017	CFTurb0030	7	107	30
4/19/2017	CFTurb0030	8	65	30
4/19/2017	CFTurb0030	9	0	30
4/21/2017	CFTurb0037	1	22	30
4/21/2017	CFTurb0037	2	43	30
4/21/2017	CFTurb0037	3	65	30
4/21/2017	CFTurb0037	4	86	30
4/21/2017	CFTurb0037	5	107	30
4/21/2017	CFTurb0037	6	0	30
4/21/2017	CFTurb0037	7	22	30
4/21/2017	CFTurb0037	8	43	30
4/21/2017	CFTurb0037	9	65	30
4/21/2017	CFTurb0037	10	86	30
4/21/2017	CFTurb0037	11	107	30
4/21/2017	CFTurb0037	12	0	30
4/24/2017	CFTurb0039	1	22	30
4/24/2017	CFTurb0039	2	43	30
4/24/2017	CFTurb0039	3	65	30
4/24/2017	CFTurb0039	4	86	30
4/24/2017	CFTurb0039	5	107	30
4/24/2017	CFTurb0039	6	0	30
6/5/2017	CFTurb0048	1	22	30
6/5/2017	CFTurb0048	2	22	30
6/5/2017	CFTurb0048	3	43	30
6/5/2017	CFTurb0048	4	65	30
6/5/2017	CFTurb0048	5	86	30
6/5/2017	CFTurb0048	6	107	30
6/5/2017	CFTurb0048	7	0	30
6/6/2017	CFTurb0050	1	0	30
6/6/2017	CFTurb0050	2	22	30
6/6/2017	CFTurb0050	3	43	30
6/6/2017	CFTurb0050	4	65	30
6/6/2017	CFTurb0050	5	86	30
6/6/2017	CFTurb0050	6	107	30
6/6/2017	CFTurb0050	8	86	30
6/6/2017	CFTurb0050	9	65	30
6/6/2017	CFTurb0050	10	43	30
6/6/2017	CFTurb0050	11	22	30
7/6/2017	CFTurb0052	1	0	30

Continued on next page

Table A.3 – continued from previous page

Test Date	Test Number	Run Number	RPM	β_{max} [°]
7/6/2017	CFTurb0052	2	22	30
7/6/2017	CFTurb0052	3	43	30
7/6/2017	CFTurb0052	4	65	30
7/6/2017	CFTurb0052	5	86	30
7/6/2017	CFTurb0052	6	107	30
7/6/2017	CFTurb0052	7	107	30
7/6/2017	CFTurb0052	8	86	30
7/6/2017	CFTurb0052	9	65	30
7/6/2017	CFTurb0052	10	43	30
7/6/2017	CFTurb0052	11	22	30
7/6/2017	CFTurb0052	12	0	30
7/12/2017	CFTurb0061	1	0	30
7/12/2017	CFTurb0061	2	22	30
7/12/2017	CFTurb0061	3	43	30
7/12/2017	CFTurb0061	4	65	30
7/12/2017	CFTurb0061	5	86	30
7/12/2017	CFTurb0061	6	107	30
7/12/2017	CFTurb0061	7	127	30
7/12/2017	CFTurb0061	8	107	30
7/12/2017	CFTurb0061	9	86	30
7/12/2017	CFTurb0061	10	65	30
7/12/2017	CFTurb0061	11	43	30
7/12/2017	CFTurb0061	12	43	30

Table A.4: Reverberant Tank SSD Single Turbine Test Matrix

Test	Test Date	Configuration	RPM	β_{max} [°]	φ [°]
1	5/1/2019	Top Starboard Turbine Response	22	30	90
2	5/1/2019	Top Starboard Turbine Response	65	30	90
3	5/1/2019	Top Starboard Turbine Response	107	30	90
4	5/1/2019	Top Starboard Turbine Response	107	30	80
5	5/1/2019	Top Starboard Turbine Response	107	30	100
6	5/1/2019	Top Starboard Turbine Response	107	30	90
7	5/1/2019	Top Port Turbine Response	107	30	100
8	5/1/2019	Top Port Turbine Response	107	30	90
9	5/1/2019	Top Port Turbine Response	107	30	-100
10	5/1/2019	Bottom Starboard Turbine Response	107	30	-90
11	5/1/2019	Bottom Starboard Turbine Response	107	30	-80
12	5/1/2019	Top Port Turbine Response	65	30	-100
13	5/1/2019	Top Port Turbine Response	22	30	-100
14	5/1/2019	Top Port Turbine Response	43	30	-100
15	5/1/2019	Top Port Turbine Response	86	30	-100
16	5/1/2019	Top Port Turbine Response	65	30	-115
17	5/1/2019	Top Port Turbine Response	86	30	-115
18	5/1/2019	Top Port Turbine Response	107	30	-115
19	5/1/2019	Top Port Turbine Response	65	30	-130
20	5/1/2019	Top Port Turbine Response	86	30	-130
21	5/1/2019	Top Port Turbine Response	107	30	-130
22	5/1/2019	Top Port Turbine Response	65	30	-145
23	5/1/2019	Top Port Turbine Response	86	30	-145
24	5/1/2019	Top Port Turbine Response	107	30	-145
25	5/1/2019	Top Port Turbine Response	65	30	-85
26	5/1/2019	Top Port Turbine Response	86	30	-85
27	5/1/2019	Top Port Turbine Response	107	30	-85
28	5/1/2019	Top Port Turbine Response	65	30	-70

Continued on next page

Table A.4 – continued from previous page

Test	Test Date	Configuration	RPM	β_{max} [°]	φ [°]
29	5/1/2019	Top Port Turbine Response	86	30	-70
30	5/1/2019	Top Port Turbine Response	107	30	-70
31	5/1/2019	Top Port Turbine Response	65	30	-55
32	5/1/2019	Top Port Turbine Response	86	30	-55
33	5/1/2019	Top Port Turbine Response	107	30	-55
34	5/1/2019	Top Port Turbine Response	65	30	-100
35	5/1/2019	Top Port Turbine Response	65	20	-100
36	5/1/2019	Top Port Turbine Response	86	20	-100
37	5/1/2019	Top Port Turbine Response	107	20	-100
38	5/1/2019	Top Port Turbine Response	65	9	-100
39	5/1/2019	Top Port Turbine Response	86	9	-100
40	5/1/2019	Top Port Turbine Response	107	9	-100
41	5/1/2019	Top Port Turbine Response	65	0	-100
42	5/1/2019	Top Port Turbine Response	86	0	-100
43	5/1/2019	Top Port Turbine Response	107	0	-100
44	5/3/2019	Top Port Turbine Response	107	30	-100
45	5/3/2019	Top Starboard Turbine Response	107	30	100
46	5/3/2019	Top Starboard Turbine Response	107	30	110
47	5/3/2019	Top Starboard Turbine Response	107	30	110
48	5/3/2019	Bottom Starboard Turbine Response	107	30	-80
49	5/6/2019	Top Starboard Turbine Response	107	30	110
50	5/6/2019	Top Port Turbine Response	107	30	-100
51	5/6/2019	Top Port Turbine Response	107	30	-175
52	5/6/2019	Top Port Turbine Response	107	30	-160
53	5/6/2019	Top Port Turbine Response	107	30	-145
54	5/6/2019	Top Port Turbine Response	107	30	-130
55	5/6/2019	Top Port Turbine Response	107	30	-115
56	5/6/2019	Top Port Turbine Response	107	30	-100
57	5/6/2019	Top Port Turbine Response	107	30	-85
58	5/6/2019	Top Port Turbine Response	107	30	-70
59	5/6/2019	Top Port Turbine Response	107	30	-55
60	5/6/2019	Top Port Turbine Response	107	30	-40
61	5/6/2019	Top Port Turbine Response	107	30	-25
62	5/6/2019	Top Port Turbine Response	107	30	-10
63	5/6/2019	Top Port Turbine Response	107	30	5
64	5/6/2019	Top Port Turbine Response	107	30	20
65	5/6/2019	Top Port Turbine Response	107	30	35
66	5/6/2019	Top Port Turbine Response	107	30	50
67	5/6/2019	Top Port Turbine Response	107	30	65
68	5/6/2019	Top Port Turbine Response	107	30	80
69	5/6/2019	Top Port Turbine Response	107	30	95
70	5/6/2019	Top Port Turbine Response	107	30	110
71	5/6/2019	Top Port Turbine Response	107	30	125
72	5/6/2019	Top Port Turbine Response	107	30	140
73	5/6/2019	Top Port Turbine Response	107	30	155
74	5/6/2019	Top Port Turbine Response	107	30	170
75	5/7/2019	Top Starboard Turbine Response	107	30	110
76	5/7/2019	Top Starboard Turbine Response	107	30	115
77	5/7/2019	Top Starboard Turbine Response	107	30	112
78	5/7/2019	Top Port Turbine Response	107	30	-100
79	5/8/2019	Top Starboard Turbine Response	107	30	112
80	5/8/2019	Bottom Starboard Turbine Response	107	30	-175
81	5/8/2019	Bottom Starboard Turbine Response	107	30	-160
82	5/8/2019	Bottom Starboard Turbine Response	107	30	-145
83	5/8/2019	Bottom Starboard Turbine Response	107	30	-130
84	5/8/2019	Bottom Starboard Turbine Response	107	30	-115
85	5/8/2019	Bottom Starboard Turbine Response	107	30	-100

Continued on next page

Table A.4 – continued from previous page

Test	Test Date	Configuration	RPM	β_{max} [°]	φ [°]
86	5/8/2019	Bottom Starboard Turbine Response	107	30	-85
87	5/8/2019	Bottom Starboard Turbine Response	107	30	-70
88	5/8/2019	Bottom Starboard Turbine Response	107	30	-55
89	5/8/2019	Bottom Starboard Turbine Response	107	30	-40
90	5/8/2019	Bottom Starboard Turbine Response	107	30	-25
91	5/8/2019	Bottom Starboard Turbine Response	107	30	-10
92	5/8/2019	Bottom Starboard Turbine Response	107	30	5
93	5/8/2019	Bottom Starboard Turbine Response	107	30	20
94	5/8/2019	Bottom Starboard Turbine Response	107	30	35
95	5/8/2019	Bottom Starboard Turbine Response	107	30	50
96	5/8/2019	Bottom Starboard Turbine Response	107	30	65
97	5/8/2019	Bottom Starboard Turbine Response	107	30	80
98	5/8/2019	Bottom Starboard Turbine Response	107	30	95
99	5/8/2019	Bottom Starboard Turbine Response	107	30	110
100	5/8/2019	Bottom Starboard Turbine Response	107	30	125
101	5/8/2019	Bottom Starboard Turbine Response	107	30	140
102	5/8/2019	Bottom Starboard Turbine Response	107	30	155
103	5/8/2019	Bottom Starboard Turbine Response	107	30	170
104	5/8/2019	Top Starboard Turbine Response	107	30	110
105	5/8/2019	Top Starboard Turbine Response	107	30	115
106	5/8/2019	Top Starboard Turbine Response	107	30	112
107	5/8/2019	Bottom Starboard Turbine Response	107	30	-80
108	5/8/2019	Bottom Starboard Turbine Response	107	30	-85
109	5/8/2019	Bottom Starboard Turbine Response	107	30	-82
110	5/9/2019	Top Port Turbine Response	22	30	-100
111	5/9/2019	Top Port Turbine Response	43	30	-100
112	5/9/2019	Top Port Turbine Response	65	30	-100
113	5/9/2019	Top Port Turbine Response	86	30	-100
114	5/9/2019	Top Port Turbine Response	107	30	-100
115	5/9/2019	Top Port Turbine Response	129	30	-100
116	5/9/2019	Top Port Turbine Response	150	30	-100
117	5/9/2019	Top Port Turbine Response	170	30	-100
118	5/9/2019	Top Port Turbine Response	190	30	-100

Table A.5: Reverberant Tank SSD Multiple Turbine Test Matrix

		Top Starboard		**Top Port**		**Bottom Starboard**	
Test	**Test Date**	β_{max} [°]	φ [°]	β_{max} [°]	φ [°]	β_{max} [°]	φ [°]
1	5/3/2019	30	110	30	-110		
2	5/3/2019	20	110	30	-110		
3	5/3/2019	9	110	30	-110		
4	5/3/2019	0	110	30	-110		
5	5/3/2019	0	110	20	-110		
6	5/3/2019	0	110	9	-110		
7	5/3/2019	9	110	20	-110		
8	5/3/2019	30	110	20	-110		
9	5/3/2019	30	110			30	-80
10	5/3/2019	20	110			30	-80
11	5/3/2019	9	110			30	-80
12	5/3/2019	0	110			30	-80
13	5/3/2019	0	110			20	-80
14	5/3/2019	0	110			9	-80
15	5/3/2019	9	110			20	-80
16	5/3/2019	30	110			20	-80
17	5/6/2019	30	65	30	-55		

Continued on next page

Table A.5 – continued from previous page

Test	Test Date	Top Starboard β_{max} [°]	Top Starboard φ [°]	Top Port β_{max} [°]	Top Port φ [°]	Bottom Starboard β_{max} [°]	Bottom Starboard φ [°]
18	5/6/2019	30	80	30	-55		
19	5/6/2019	30	95	30	-55		
20	5/6/2019	30	110	30	-55		
21	5/6/2019	30	125	30	-55		
22	5/6/2019	30	140	30	-55		
23	5/6/2019	30	155	30	-55		
24	5/6/2019	30	125	30	-85		
25	5/6/2019	30	140	30	-70		
26	5/7/2019	30	112	30	-100		
27	5/7/2019	30	102	30	-110		
28	5/7/2019	30	97	30	-115		
29	5/7/2019	30	92	30	-120		
30	5/7/2019	30	87	30	-125		
31	5/7/2019	30	82	30	-130		
32	5/8/2019	30	115			30	-85
33	5/8/2019	30	120			30	-80
34	5/8/2019	30	130			30	-70
35	5/8/2019	30	140			30	-60
36	5/8/2019	30	145			30	-55
37	5/8/2019	30	160			30	-40
38	5/8/2019	30	175			30	-25
39	5/8/2019	30	100			30	-100
40	5/8/2019	30	115			30	-85

Table A.6: Reverberant Tank SSD Bare Shaft Test Matrix

Test	Test Date	Top Starboard Turbine RPM	Top Port Turbine RPM	Bottom Starboard Turbine RPM
1	5/13/2019	22	0	0
2	5/13/2019	43	0	0
3	5/13/2019	65	0	0
4	5/13/2019	86	0	0
5	5/13/2019	107	0	0
6	5/13/2019	129	0	0
7	5/13/2019	150	0	0
8	5/13/2019	170	0	0
9	5/13/2019	190	0	0
10	5/13/2019	0	22	0
11	5/13/2019	0	43	0
12	5/13/2019	0	65	0
13	5/13/2019	0	86	0
14	5/13/2019	0	107	0
15	5/13/2019	0	129	0
16	5/13/2019	0	150	0
17	5/13/2019	0	170	0
18	5/13/2019	0	190	0
19	5/13/2019	0	0	22
20	5/13/2019	0	0	43
21	5/13/2019	0	0	65
22	5/13/2019	0	0	86
23	5/13/2019	0	0	107
24	5/13/2019	0	0	129
25	5/13/2019	0	0	150
26	5/13/2019	0	0	170

Continued on next page

Table A.6 – continued from previous page

Test	Test Date	Top Starboard Turbine RPM	Top Port Turbine RPM	Bottom Starboard Turbine RPM
27	5/13/2019	0	0	190

Appendix B MATLAB Diagrams

Figure B.1 shows the interface used to understand and evaluate the pitch balance of different vehicle configurations in typical operating conditions.

Figures B.2, B.3, and B.4 show the MATLAB Simulink diagrams that are used for simulating the MHK vehicle, and evaluating controller performance.

The MATLAB Guided User Interface (GUI) shown in Fig. B.5 and subsequent code is used for controlling the SSD during Reverberant Tank testing. In Fig. B.5, the commands for maximum pitching angle and phase angle for each turbine are input in the blocks on the left. The state of each stepper motor is also provided. The main motor RPMs are input in the block on the right. The code also allows for dithering of the motor commands, to attempt clocking control.

Figure B.8 shows the diagram of the code used specifically for the stepper motors. The top block on the left for each stepper motor determines what the stepper setpoint should be based on the commanded degree. The bottom block on the left for each stepper motor determines the current position of the motor in degrees to output to the GUI. The blocks on the right for each stepper form and send all the CAN messages. This is what does the initialization of the motors (programming limits, homing, etc.). It also handles forming the CAN messages for the position commands once the motor is in the operational state. The main difference between the functionality of the phase and amplitude control is that the amplitude setpoint is relative to the setpoint of the phase motor. That is why there are two setpoints summed together to get the actual setpoint for the amplitude motor.

While ultimately joystick controllers were not used for the Reverberant Tank testing, the code shown in Fig. B.9 and B.10 was written in order to use joysticks

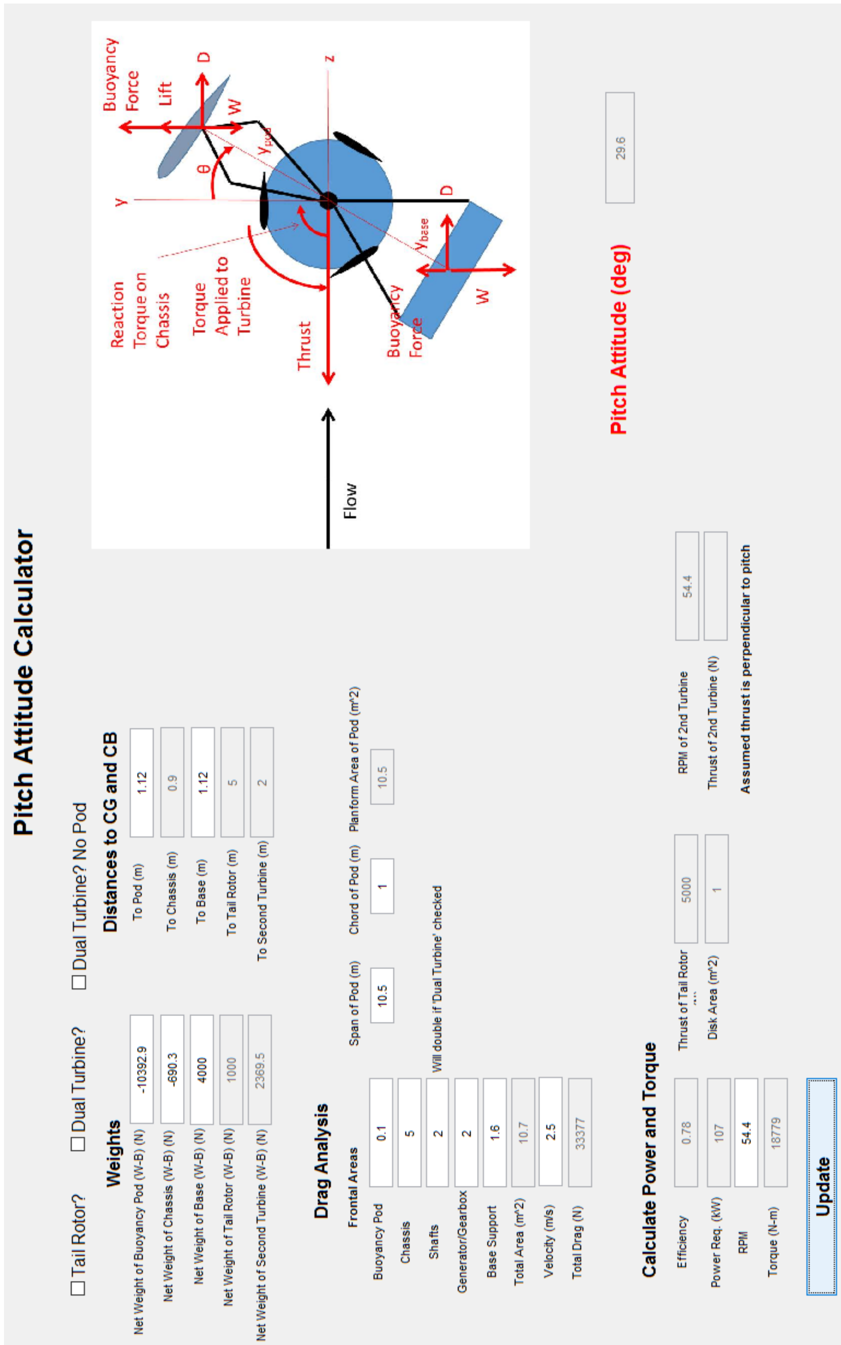

Figure B.1. MATLAB GUI used to solve for vehicle pitch attitude. User manipulates weights, distances to vehicle components, and drag values. The tool calculates the power, torque, and pitch attitude based on the given inputs.

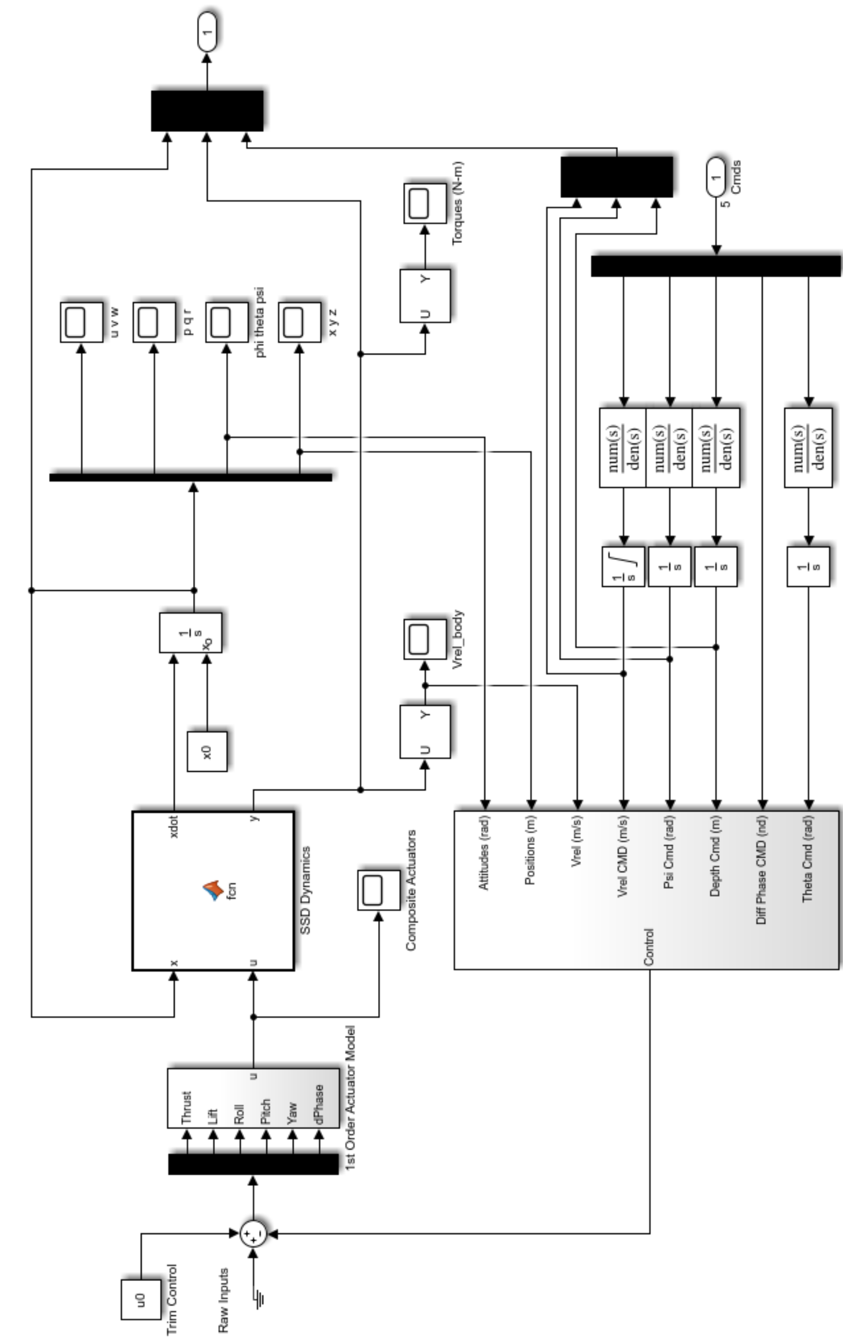

Figure B.2. MATLAB Simulink diagram for the classical controller model.

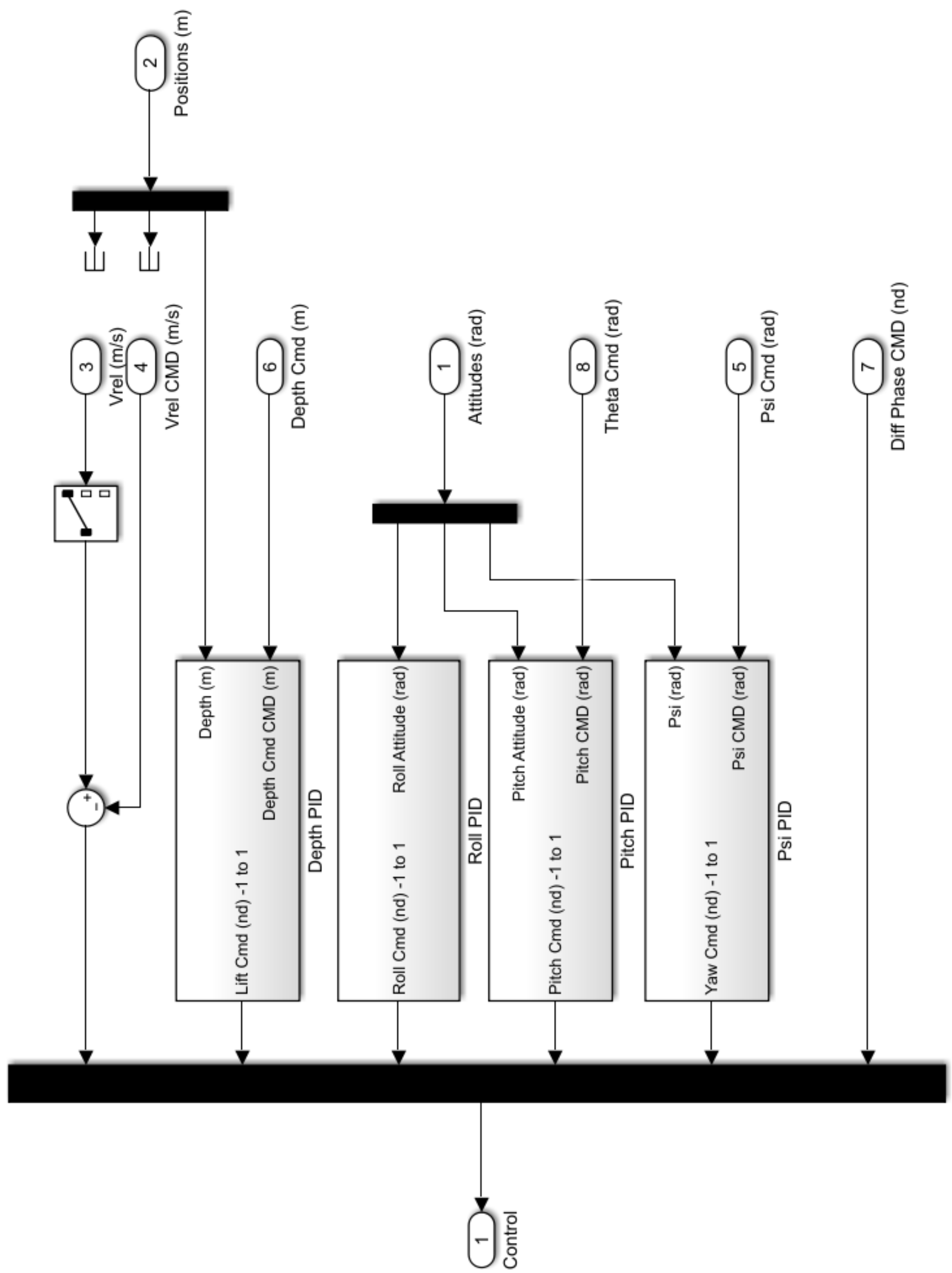

Figure B.3. Autopilot in the MATLAB Simulink diagram for the classical controller model.

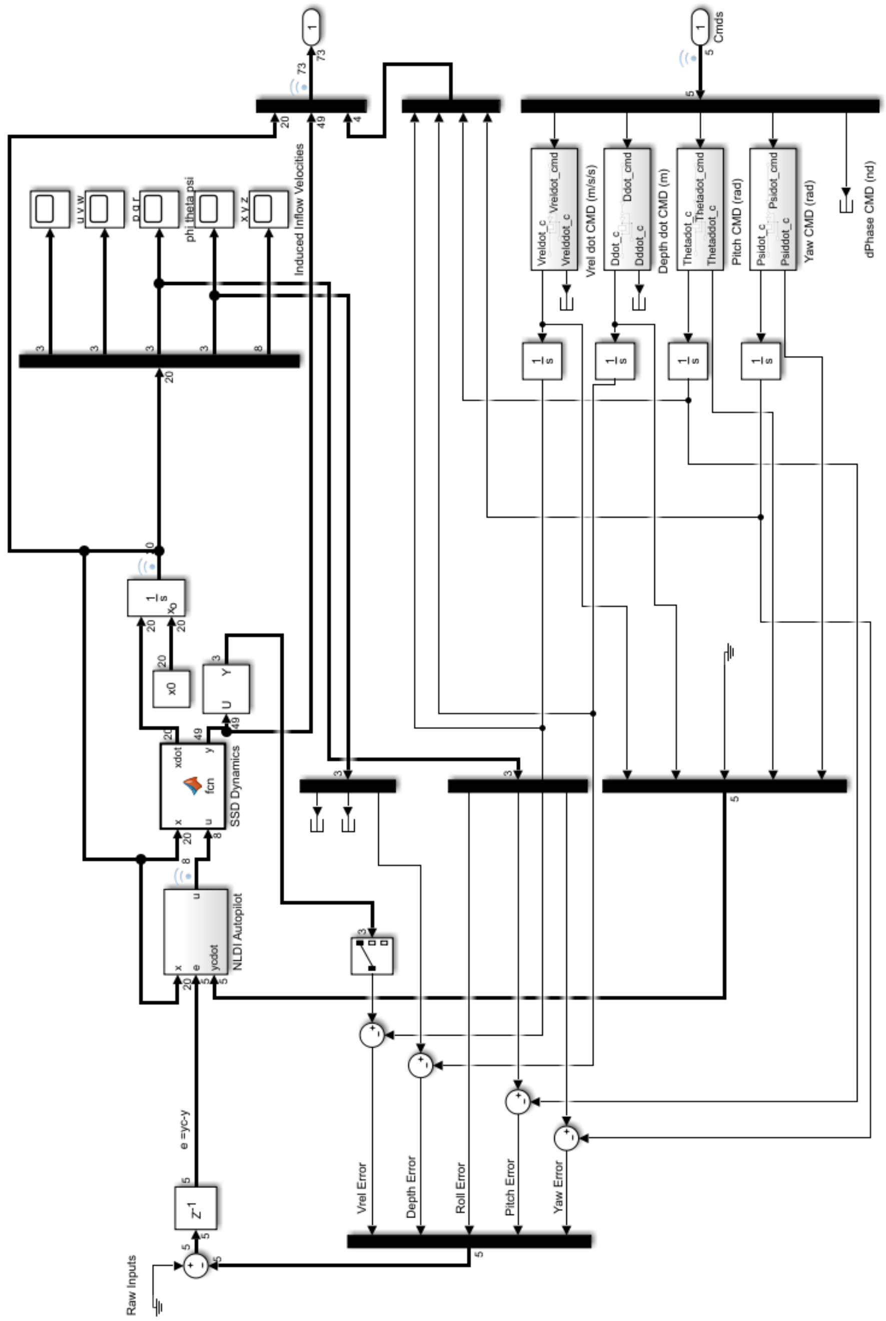

Figure B.4. MATLAB Simulink diagram for the NDI controller model.

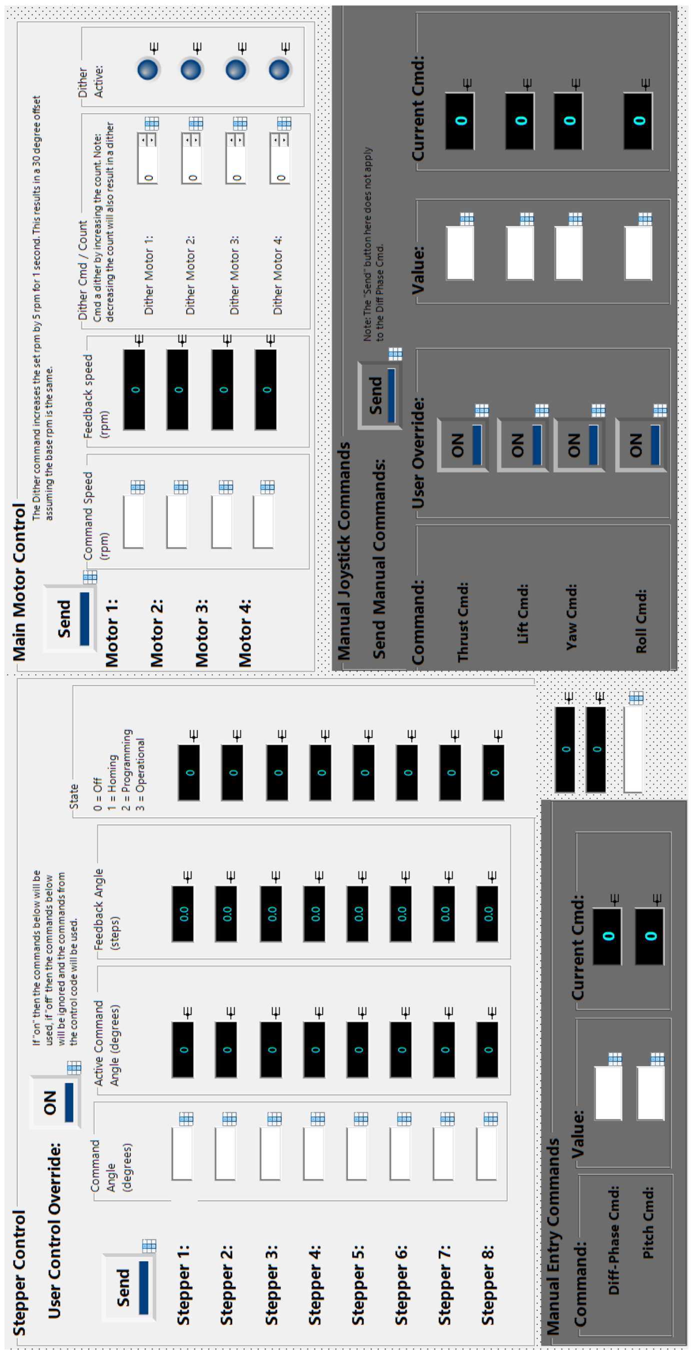

Figure B.5. MATLAB Guided User Interface (GUI) for controlling the SSD during Reverberant Tank testing.

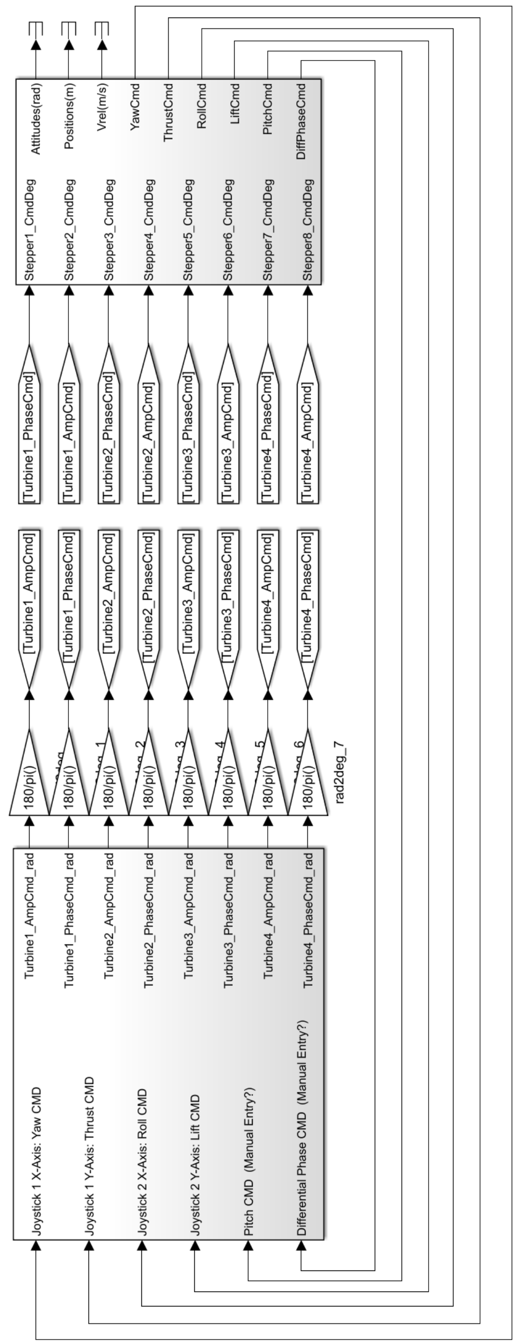

Figure B.6. MATLAB Simulink diagram for the SSD controller code wrapper.

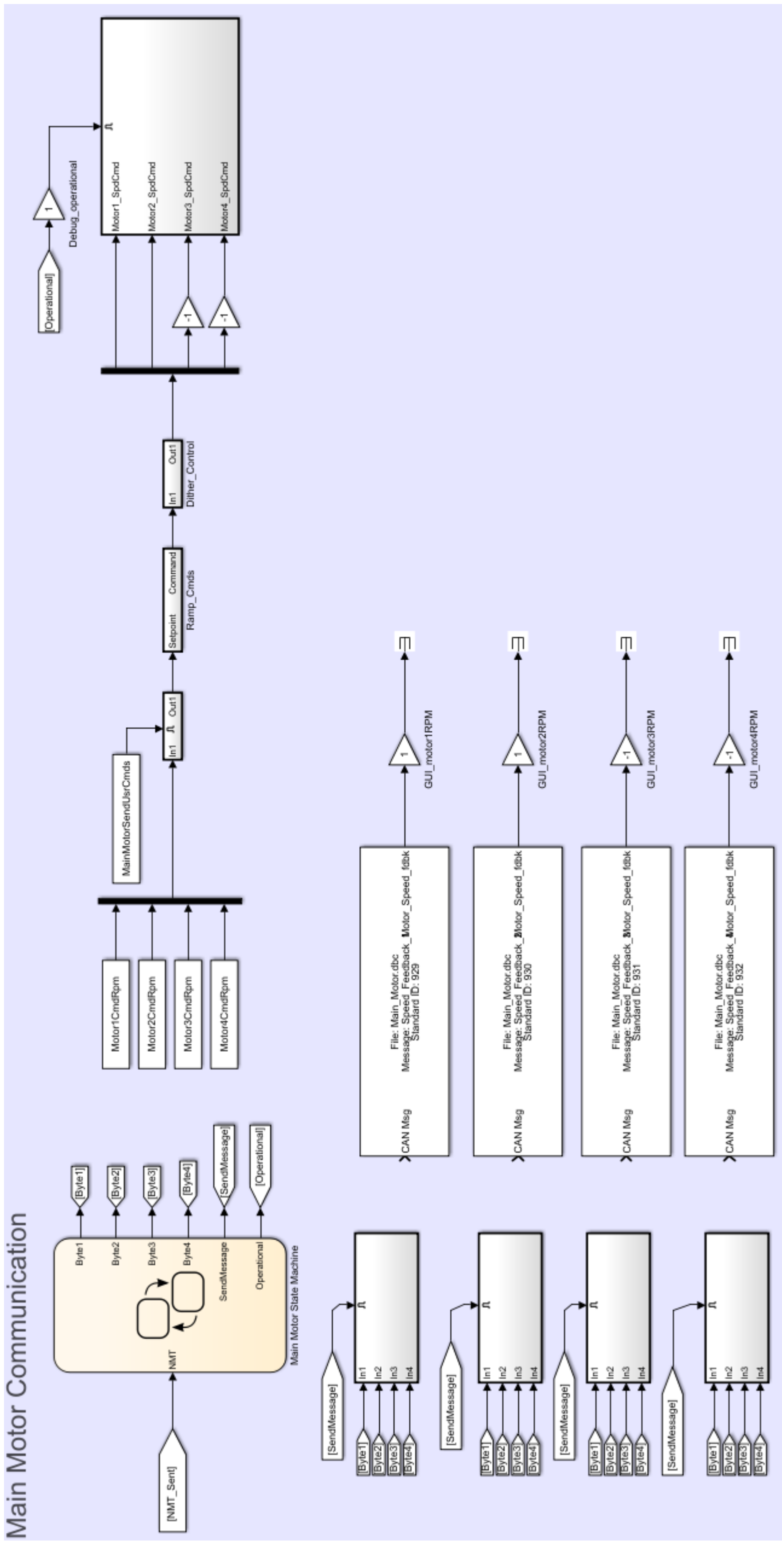

Figure B.7. MATLAB Simulink diagram for the SSD main motors.

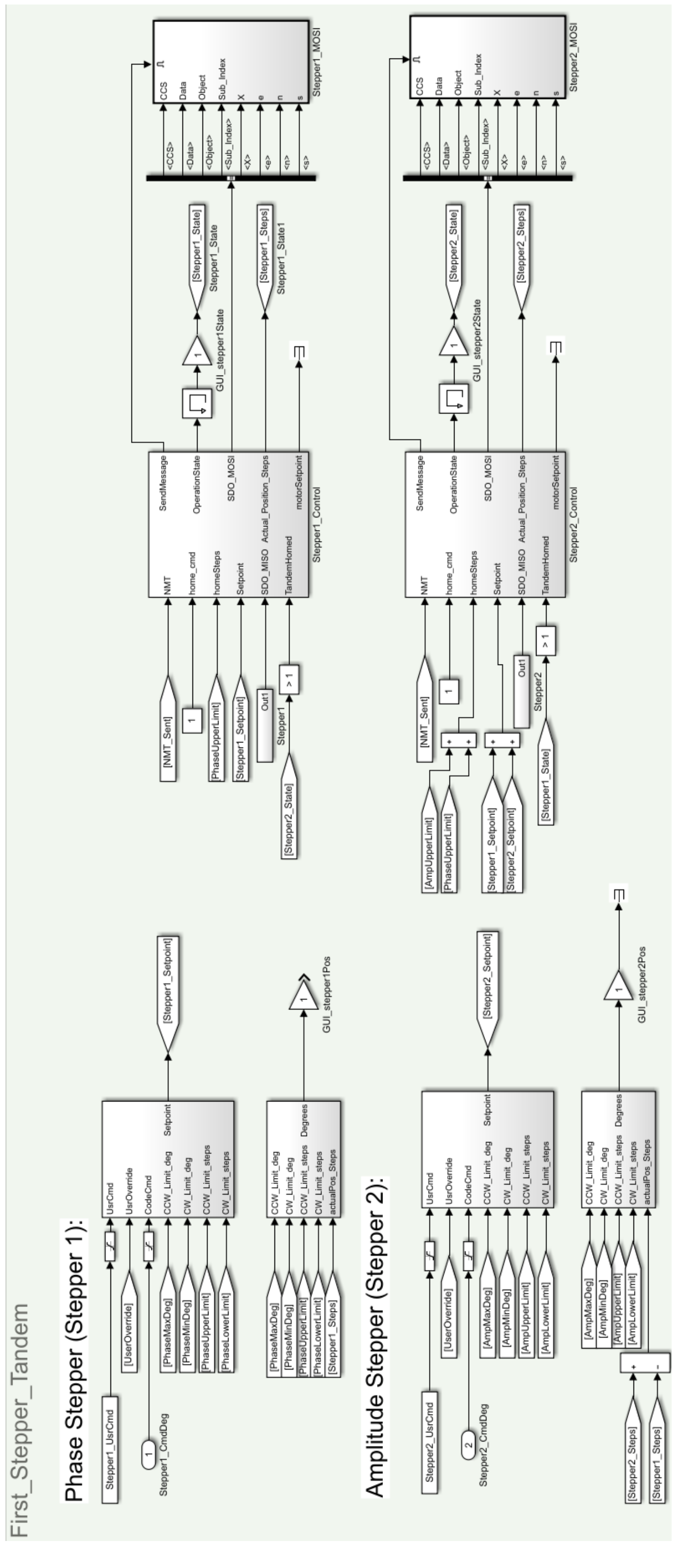

Figure B.8. MATLAB Simulink diagram for the SSD stepper motors.

for thrust vectoring from the turbines.

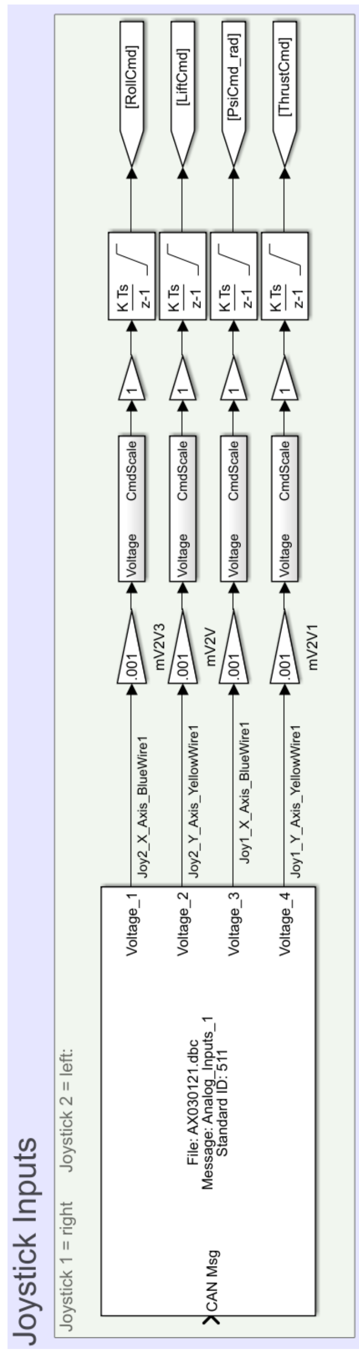

Figure B.9. MATLAB Simulink Diagram for the SSD Joystick Controllers

Figure B.10. MATLAB Simulink Diagram for the SSD Joystick Controllers: Internal Control Mixing

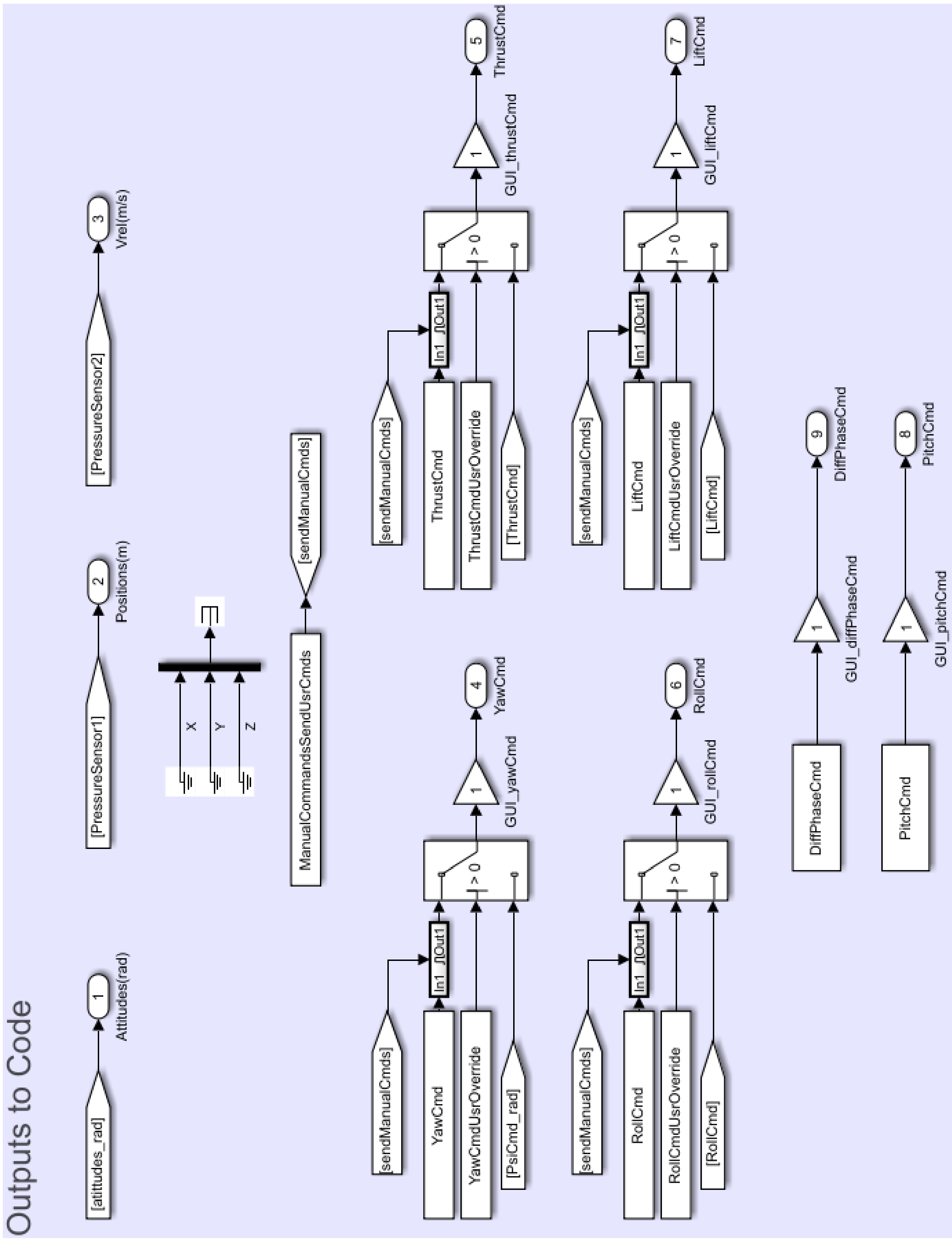

Figure B.11. MATLAB Simulink Diagram for the SSD Controller Code Output

Bibliography

[1] International Energy Agency. Energy Access Outlook 2017: From Poverty to Prosperity. International Energy Agency, 2017.

[2] A. Fischer, L. de Almeida, and A. Beluco. Converting Energy from Ocean Currents. *International Journal of Research in Engineering and Technology*, 5(3):220–227, 2016.

[3] M. I. Yuce and A. Muratoglu. Hydrokinetic Energy Conversion Systems: A Technology Status Review. *Renewable and Sustainable Energy Reviews*, 43:72–82, 2015.

[4] C. Boirum and S. Post. Review of Historic and Modern Cyclogyro Design. *45th AIAA/ASME/SAE/ASEE Joint Propulsion Conference and Exhibit*, AIAA Paper 2009–5023, Aug. 2009.

[5] Ocean Renewable Power Company. `http://www.orpc.co/orpcpowersystem_turbinegeneratorunit.aspx`. Accessed: 2017-09-28.

[6] A. Bahaj and L. Myers. Fundamentals Applicable to the Utilisation of Marine Current Turbines for Energy Production. *Renewable Energy*, 28(14):2205–2211, 2003.

[7] M. Khan, G. Bhuyan, M. Iqbal, and J. Quaicoe. Hydrokinetic Energy Conversion Systems and Assessment of Horizontal and Vertical Axis Turbines for River and Tidal applications: A Technology Status Review. *Applied Energy*, 86(10):1823–1835, 2009.

[8] C. Sauer and J. McEntee. TidGen Power System Commercialization Project. Technical report, ORPC Maine, 2013.

[9] J. Johnson and D. Pride. River, Tidal, and Ocean Current Hydrokinetic Energy Technologies: Status and Future Opportunities in Alaska. Technical report, Prepared for the Alaska Energy Authority by the Alaska Center for Energy and Power, 2010.

[10] Blue Water Energy BlueTec Tidal Energy Converter. `http://www.bluewater.com/bluetec`. Accessed: 2017-11-07.

[11] Kepler Energy Transverse Horizontal Axis Water Turbine. `http://www.keplerenergy.co.uk/about-html.php`. Accessed: 2017-11-07.

[12] VectRA 3000 Series Tugs, Italy. `http://www.ship-technology.com/projects/vectra-3000-series-tugs/vectra-3000-series-tugs1.html`. Accessed: 2017-11-03.

[13] iVSP: Controlling a Virtual Voith Schneider Propeller. `http://voith.com/corp-en/drives-transmissions/voith-schneider-propeller-vsp.html`. Accessed: 2017-11-20.

[14] H. Sachse. Kirsten-Boeing Propeller. Technical Report NACA-TM-351, NASA, Feb. 1926.

[15] T. van Terwisga, F. Quadvlieg, and H. Valkhof. Steerable Propulsion Units: Hydrodynamic Issues and Design Consequences. *Paper written on the occasion of the 80th anniversary of Schottel GmbH & Co*, Aug. 2001.

[16] A. Bruckner, J. Lee, and S. Musi. The Boeing Aerodynamical Chamber and its Impact on Aeronautics Education at the University of Washington. *54th AIAA Aerospace Sciences Meeting*, AIAA Paper 2016–1397, Jan. 2016.

[17] B. Roesler, M. Francsiquez, and B. Epps. Design and Analysis of Trochoidal Propulsors Using Nonlinear Programming Optimization Techniques. *ASME 2014 33rd International Conference on Ocean, Offshore and Arctic Engineering*, OMAE Paper 2014–24093, June 2014.

[18] M. Benedict. *Fundamental Understanding of the Cycloidal-Rotor Concept for Micro Air Vehicle Applications*. PhD thesis, University of Maryland, College Park, 2010.

[19] M. Benedict, T. Jarugumilli, and I. Chopra. Effect of Rotor Geometry and Blade Kinematics on Cycloidal Rotor Hover Performance. *Journal of Aircraft*, 50(5):1340–1352, 2013.

[20] M. Benedict, V. Lakshminarayan, J. Pino, and I. Chopra. Fundamental Understanding of the Physics of a Small-Scale Vertical Axis Wind Turbine with Dynamic Blade Pitching: An Experimental and Computational Approach. *54th AIAA/ASME/ASCE/AHS/ASC Structures, Structural Dynamics, and Materials Conference*, AIAA Paper 2013–1553, Apr. 2013.

[21] M. Benedict and I. Chopra. Design and Development of an Unconventional VTOL Micro Air Vehicle: The Cyclocopter. *SPIE Micro- and Nanotechnology Sensors, Systems, and Applications IV*, SPIE 8373(83731F–1), May 2012.

[22] T. Jarugumilli, M. Benedict, and I. Chopra. Experimental Optimization and Performance Analysis of a MAV Scale Cycloidal Rotor. *49th AIAA Aerospace Sciences Meeting including the New Horizons Forum and Aerospace Exposition*, AIAA Paper 2011–821, Jan. 2011.

[23] E. Shrestha, M. Benedict, and I. Chopra. Autonomous Hover Capability of Cycloidal-Rotor Micro Air Vehicle. *51st AIAA Aerospace Sciences Meeting including the New Horizons Forum and Aerospace Exposition*, AIAA Paper 2013–0121, Jan. 2013.

[24] E. Shrestha, D. Yeo, M. Benedict, and I. Chopra. Development of a Micro-scale Cycloidal-rotor Aircraft for Micro Air Vehicle Application. *International Journal of Micro Air Vehicles*, 9(3):218–231, 2017.

[25] A. Mills, M. Benedict, and I. Chopra. Investigation of the Effect of Blade Kinematics and Reynolds Number on the Aerodynamic Performance of a Small-Scale Vertical Axis Wind Turbine with Dynamic Blade Pitching. *54th AIAA Aerospace Sciences Meeting*, AIAA Paper 2016–0137, Jan. 2016.

[26] I. Hwang, C. Hwang, S. Min, I. Jeong, C. Lee, Y. Lee, and S. Kim. Design and Testing of VTOL UAV Cyclocopter with 4 Rotors. *American Helicopter Society 62nd Annual Forum*, May 2006.

[27] I. Hwang, S. Min, C. Lee, and S. Kim. Experimental Investigation of VTOL UAV Cyclocopter with Four Rotors. *48th AIAA/ASME/ASCE/AHS/ASC Structures, Structural Dynamics, and Materials Conference*, AIAA Paper 2007–2247, Apr. 2007.

[28] I. Hwang, Y. Lee, and S. Kim. Optimization of Cycloidal Water Turbine and the Performance Improvement by Individual Blade Control. *Applied Energy*, 86(9):1532–1540, 2009.

[29] S. Kim, C. Yun, D. Kim, Y. Yoon, and I. Park. Design and Performance Tests of Cycloidal Propulsion Systems. *44th AIAA/ASME/ASCE/AHS Structures, Structural Dynamics, and Materials Conference*, AIAA Paper 2003–1786, Apr. 2003.

[30] C. Yun, I. Park, I. Hwang, and S. Kim. Thrust Control Mechanism of VTOL UAV Cyclocopter with Cycloidal Blades System. *Journal of Intelligent Material Systems and Structures*, 16:937–943, 2005.

[31] I. Paraschivoiu, O. Trifu, and F. Saeed. H-Darrieus Wind Turbine with Blade Pitch Control. *International Journal of Rotating Machinery*, 2009(505343), 2009.

[32] B. Kirke and L. Lazauskas. Enhancing the Performance of Vertical Axis Wind Turbine using a Simple Variable Pitch System. *Wind Engineering*, 15(4):187–195, 1991.

[33] A. Schönborn and M. Chantzidakis. Development of a Hydraulic Control Mechanism for Cyclic Pitch Marine Current Turbines. *Renewable Energy*, 32(4):662–679, 2007.

[34] J. Boschma. Cycloidal Propulsion for UAV VTOL Applications. Technical report, Bosch Aerospace Inc., Nov. 1998.

[35] H. Yu, L. Bin, and H. Rong. The Research on the Performance of Cyclogyro. *6th AIAA Aviation Technology, Integration and Operations Conference*, AIAA Paper 2006–7704, Sep. 2006.

[36] K. Taniguchi. *Studies on a Trochoidal Propeller*. PhD thesis, Tokyo University, 1960.

[37] J. van Manen. Results of Systematic Tests with Vertical Axis Propellers. Technical Report 235b, The Netherlands Ship Model Basin, Dec. 1966.

[38] M. Mendenhall and S. Spangler. Theoretical Analysis of Cycloidal Propellers. Technical report, Nielsen Engineering and Research, Inc., June 1973.

[39] W. Haberman and E. Harley. Performance of Vertical Axis (Cycloidal) Propellers Calculated by Taniguchi's Method. Technical Report 1564, David Taylor Model Basin, 1961.

[40] B. Stevens, F. Lewis, and E. Johnson. *Aircraft Control and Simulation: Dynamics, Controls Design, and Autonomous Systems*. John Wiley & Sons, 2016.

[41] P. Smith and A. Berry. Flight Test Experience of a Non-linear Dynamic Inversion Control Law on the VAAC Harrier. *AIAA Atmospheric Flight Mechanics Conference*, AIAA Paper 2000–3914, 2000.

[42] G. Walker, S. Wurth, and J. Fuller. F-35B Integrated Flight-Propulsion Control Development. *AIAA AVIATION Forum*, AIAA Paper 2013–4243, Aug. 2013.

[43] O. Fritsch, P. De Monte, M. Buhl, and B. Lohmann. Quasi-static Feedback Linearization for the Translational Dynamics of a Quadrotor Helicopter. In *Proceedings of the 2012 American Control Conference*, pages 125–130, 2012.

[44] V. Mistler, A. Benallegue, and N. M'Sirdi. Exact Linearization and Noninteracting Control of a 4 Rotors Helicopter via Dynamic Feedback. In *Proceedings of the IEEE International Workshop on Robot and Human Interactive Communication*, pages 586–593, 2001.

[45] J. Wang, F. Holzapfel, and F. Peter. Comparison of Nonlinear Dynamic Inversion and Backstepping Controls with Application to a Quadrotor. In *Proceedings of the EuroGNC 2013, 2nd CEAS Specialist Conference on Guidance, Navigation, and Control*, pages 1245–1263, 2013.

[46] J. Denenberg and J. Charry. Energy Savings Through the Use of Active Noise Cancellation. The Guide To The Energy Policy Act of 1992, 1992.

[47] A. Hawkins and A. Popper. Effects of Noise on Fish, Fisheries and Invertebrates in the U.S. Atlantic and Arctic from Energy Industry Sound Generating Activities. *U.S. Department of the Interior*, 2012.

[48] R. Dooling, M. Leek, and A. Popper. Effects of Noise on Fishes: What we can learn from humans and birds.

[49] A. L. Graham and S. J. Cooke. The Effects of Noise Disturbance from Various Recreational Boating Activities Common to Inland Waters on the Cardiac Physiology of a Freshwater Fish, the Largemouth Bass (Micropterus Salmoides). *Aquatic Conservation: Marine and Freshwater Ecosystems*, 18(7):1315–1324, 2008.

[50] D. R. Ketten. Marine Mammal Auditory System Noise Impacts: Evidence and Incidence. In *The Effects of Noise on Aquatic Life*, pages 207–212. Springer, 2012.

[51] C. Erbe, S. Marley, R. Schoeman, J. N. Smith, L. Trigg, and C. B. Embling. The Effects of Ship Noise on Marine Mammals—A Review. *Frontiers in Marine Science*, 6:606, 2019.

[52] S. Kamiyoshi and S. Kaji. Tone Noise Reduction of Multi-stage Fan by Airfoil Clocking. *6th AIAA Aeroacoustics Conference and Exhibit*, AIAA Paper 2000–1992, June 2000.

[53] J. Blaszczak. Noise Reduction and Efficiency Improvement through Vane Indexing of a Two-Stage Turbine. *12th AIAA/CEAS Aeroacoustics Conference and Exhibit*, AIAA Paper 2006–2578, May 2006.

[54] D. Kovalev, V. Saren, and R. Shipov. Influence of Mutual Circumferential Shift of Stators on the Noise Generated by System of Rows Stator-Rotor-Stator of the Axial Compressor. In *Unsteady Aerodynamics, Aeroacoustics and Aeroelasticity of Turbomachines*, pages 261–273. Springer, 2006.

[55] K. Auman. Reduction of Discrete Blade Rate Tones Via Slowly Rotating Stator, 2017.

[56] J. Blaszczak. Performance Improvement and Noise Reduction through Vane and Blade Indexing of a Two-stage Turbine. *14th AIAA/CEAS Aeroacoustics Conference (29th AIAA Aeroacoustics Conference)*, AIAA Paper 2008–2941, May 2008.

[57] D. Forbush, B. Polagye, J. Thomson, B. Fabien, J. Donegan, and J. McEntree. Characterization and Control of Cross-flow Turbine in Shear Flow. In *3rd Marine Energy Technology Symposium*, 2015.

[58] T. Fossen. *Handbook of Marine Craft Hydrodynamics and Motion Control*. John Wiley & Sons, 2011.

[59] R. Medvitz, M. Jonson, J. Dreyer, and J. McEntee. Parameterization of a Multi-Directional Tidal Turbine Performance Using Computational Fluid Dynamics. *ASME 2015 34th International Conference on Ocean, Offshore and Arctic Engineering*, OMAE Paper 2015–41035, June 2015.

[60] M. Jonson. Preferred Vehicle Scaling. In *ASME 2007 International Mechanical Engineering Congress and Exposition*, pages 63–69, 2007.

[61] R. Norton. *Design of Machinery: An Introduction to the Synthesis and Analysis of Mechanisms and Machines*. McGraw-Hill, 2001.

[62] Parker/Compumotor. *Chapter 6. Hardware Reference*, page 185, 2009.

[63] S. C. Conlon, S. A. Hambric, and W. K. Bonness. Evaluation of a Reverberant Water Tank for Radiated Power Measurements. In *Noise-Con National Conference on Noise Control Engineering*, 2004.

[64] A. Malipeddi and D. Chatterjee. Influence of Duct Geometry on the Performance of Darrieus Hydroturbine. *Renewable Energy*, 43:292–300, 2012.

[65] F. Ponta and G. Dutt. An Improved Vertical-axis Water-current Turbine Incorporating a Channelling Device. *Renewable Energy*, 20(2):223–241, 2000.

[66] Y. Hu, K. Lim, and W. Hu. The Research on the Performance of Cyclogyro. In *6th AIAA Aviation Technology, Integration and Operations Conference (ATIO)*, page 7704, 2006.

[67] B. McCormick. *Aerodynamics, Aeronautics, and Flight Mechanics*. John Wiley Sons, Inc., 1995.

[68] S. Hoerner and H. Borst. *Fluid-Dynamic Lift*. Mrs. Liselotte A. Hoerner, 1975.

[69] J. Leishman. *Principles of Helicopter Aerodynamics*. Cambridge University Press, 2006.

[70] R. Chen. A Survey of Nonuniform Inflow Models for Rotorcraft Flight Dynamics and Control Applications. *NASA TM-102219*, 64:1–67, 1989.

[71] D. Peters and N. HaQuang. Dynamic Inflow for Practical Application. *Journal of the American Helicopter Society*, 33(4), 1988.

[72] R. Sheldahl and P. Klimas. Aerodynamic Characteristics of Seven Symmetrical Airfoil Sections Through 180-Degree Angle of Attack for Use in Aerodynamic Analysis of Vertical Axis Wind Turbines. *Sandia National Laboratories*, SAND 80-2114, March 1981.

[73] J. Wright and J. Cooper. *Introduction to Aircraft Aeroelasticity and Loads*. John Wiley & Sons, 2007.

[74] R. Beard and T. McLain. *Small Unmanned Aircraft: Theory and Practice*. Princeton University Press, 2012.

[75] S. Snell, D. Enns, and W. Garrard. Nonlinear Inversion Flight Control for a Supermaneuverable Aircraft. *Journal of Guidance, Control, and Dynamics*, 15(4):976–984, 1992.

[76] J. Horn. Non-Linear Dynamic Inversion Control Design for Rotorcraft. *Aerospace*, 6(3):38, 2019.

[77] M. Lighthill. On sound generated aerodynamically, I., General theory. *Proc. R. Soc. London, Ser. A*, 211:564–587, 1952.

[78] M. Lighthill. On sound generated aerodynamically, II., Turbulence as a source of sound. *Proc. R. Soc. London, Ser. A*, 222:1–32, 1954.

[79] M. Lighthill. Sound generated aerodynamically. *Proc. R. Soc. London, Ser. A*, 267:147–182, 1962.

[80] W. Blake. *Mechanics of Flow-Induced Sound and Vibration*. Academic Press, Inc., 1986.

[81] N. Curle. The influence of solid boundaries upon aerodynamic sound. *Proc. R. Soc. London, Ser. A*, 231:505–514, 1955.

[82] M. Jonson. *Sound Power Reduction of Structures with Nearly Degenerate Modes by Material Tailoring*. PhD thesis, The Pennsylvania State University, 1998.

[83] G. Koopmann. Periodic Flow Noise Reduction Using Flow-excited Resonators: Theory and Application. Technical Report DFVLR-FB 83-29, DVFLR Institit fur Experimentelle Stromungsmechanik Abt. Turbulenforschung, 1983.

[84] G. Koopmann. *Wind Induced Vibrations and Their Associated Sound Fields*. PhD thesis, Catholic University of America, Washington, D.C., 1969.

[85] A. Pierce. *Acoustics: An Introduction to Its Physical Principles and Applications*. Acoustical Society of America, 1989.

[86] F. Fahy. *Sound and Structural Vibration: Radiation, Transmission and Response*. Academic Press, 1985.

[87] Brian Polagye. Acoustic characterization of a hydrokinetic turbine. 2015.

[88] M. Shepherd, J. Fahnline, T. Dare, S. Hambric, and R. Campbell. A Hybrid Approach for Simulating Fluid Loading Effects on Structures Using Experimental Modal Analysis and the Boundary Element Method. *The Journal of the Acoustical Society of America*, 138 3073–3080, 2015.

[89] U. Lindholm, D. Kana, W. Chu, and H. Abramson. Elastic Vibration Characteristics of Cantilever Plates in Water. *J. Ship Res.*, 9, no. 1, 11–22, Jun. 1965.

[90] G. Koopmann and J. Fahnline. *Designing Quiet Structures: a Sound Power Minimization Approach*. Elsevier, 1997.

Vita

Margalit Zipora Goldschmidt

Margalit Goldschmidt received her B.S. and M.S. in Aerospace Engineering from The Pennsylvania State University in May 2012 and August 2014, respectively. Her M.S. thesis was titled "Unsteady Force Measurement Using Small Piezoelectric End Sensors," which focused on designing a unique pressure sensor distribution to capture unsteady forces traveling across a propeller blade. Margalit Goldschmidt is currently a researcher at the Applied Research Laboratory (ARL), and has 6 years professional experience in the Fluid Dynamics and Acoustics Office. As a researcher, she has worked on experimental and analytical acoustics research and development programs for the Navy and other Department of Defense organizations. Her technical background includes broad work in unsteady dynamometry, spectral data analysis, and signal processing, with a research focus on flow acoustics and controls. Additionally, Margalit Goldschmidt serves on the ARL Diversity Committee, awarded in 2017 for her work championing women and underrepresented minorities in engineering and organizing K-12 STEM outreach events.